

**The Significance of Passive Acoustic
Array-Configurations on Sperm whale Range
Estimation when using the Hyperbolic Algorithm.**

Jonathan Vallarta Hernández

Thesis submitted for the degree of
Doctor of Philosophy

Heriot-Watt University
School of Engineering & Physical Sciences

February 2009

The copyright in this thesis is owned by the author. Any quotation from the thesis or use of any information contained in it must acknowledge this thesis as the source of the quotation or information

ABSTRACT

In cetacean monitoring for population estimation, behavioural studies or mitigation, traditional visual observations are being augmented by the use of *Passive Acoustic Monitoring (PAM)* techniques that use the creature's vocalisations for localisation.

The design of hydrophone configurations is evaluated for sperm whale (*Physeter macrocephalus*) range estimation to meet the requirements of the current mitigation regulations for a safety zone and behaviour research.

This thesis uses the *Time Difference of Arrival (TDOA)* of cetacean vocalisations with a three-dimensional hyperbolic localisation algorithm. A MATLAB simulator has been developed to model array-configurations and to assess their performance in source range estimation for both homogeneous and non-homogeneous sound speed profiles (SSP). The non-homogeneous medium is modelled on a Bellhop ray trace model, using data collected from the Gulf of Mexico. The sperm whale clicks are chosen as an exemplar of a distinctive underwater sound.

The simulator is tested with a separate synthetic source generator which produced a set of TDOAs from a known source location. The performance in source range estimation for *Square*, *Trapezium*, *Triangular*, *Shifted-pair* and *Y-shape* geometries is tested. The Y-shape geometry, with four elements and aperture-length of 120m, is the most accurate, giving an error of $\pm 10\text{m}$ over slant ranges of 500m in a homogeneous medium, and 300m in a non-homogeneous medium. However, for towed array deployments, the Y-shape array is sensitive to angle-positioning-error when the geometry is seriously distorted. The Shifted-pair geometry overcomes these limits, performing an initial accuracy of $\pm 30\text{m}$ when the vessel either moves in a straight line or turns to port or starboard. It constitutes a recommendable array-configuration for towed array deployments.

The thesis demonstrates that the number of receivers, the array-geometry and the array-aperture are important parameters to consider when designing and deploying a hydrophone array. It is shown that certain array-configurations can significantly improve the accuracy of source range estimation. Recommendations are made concerning preferred array-configurations for use with PAM systems.

ACKNOWLEDGEMENTS

First of all, the author of this thesis would like to thank to Ron McHugh and Paul Record for their supervision and comments made on this work during the period of the PhD course. Thanks are also offered to Jonathan Gordon for opening the opportunity of field experience work in the Gulf of Mexico in 2003, and also for promoting an interest on the underwater-acoustics field during the beginning of this research work. The author's thanks also go to Aaron Thode for sharing his knowledge on passive acoustic localisation methods and for offering hospitality at his home in San Diego, California in 2005. His genuine interest and advice on this work really generated motivation to go ahead.

The author would also like to thank Magnus Wahlbergh and John Spiesberger for providing advice on their important contribution to the algebraic solution of the source localisation method, Peter Madsen for facilitating appropriate electronic literature, Alec Duncan for making available the code of the acoustic propagation model, and Douglas Biggs and Luke Rendell for their contribution with real data that helped to simulate different underwater acoustic scenarios.

Special thanks are offered to Jeshua Vallarta for his contagious inspiration and his expertise on the design and image composition. It helped to communicate scientific knowledge through some of the figures shown on this thesis and posters presented at three different conferences in America, Europe and Africa respectively. Without his willingness and suggestions, this work would not have been completed.

Big thanks go to Carmen Torres-Sanchez, Denis Carrigan and Jorge Vallarta for their friendship and continuous encouragement during the most critical moments. I cannot leave without mentioning Gerry Toner and all the staff of SCHOLAR's for their unconditional support. People like Isobel Morrison, Colin Rodie, Sandrine Sienche and Adam King also deserve the author's acknowledgement for their precious time and dedicated work on the revision of this thesis.

Finally, the author of this thesis would like to express his most sincere acknowledgement and love to the people to whom he is deeply indebted for their invaluable support throughout his whole life -*mis padres, Jorge y Silvia*.

DECLARATION STATEMENT

(Research Thesis Submission Form should be placed here)

TABLE OF CONTENTS

ABSTRACT	ii
ACKNOWLEDGEMENTS.....	iii
DECLARATION STATEMENT.....	iv
LIST OF TABLES	ix
LIST OF FIGURES	x
CONFERENCES AND POSTERS.....	xiv
1 Introduction	1
1.1 Underwater Sound.....	2
1.1.1 Natural Sources of Sound.....	2
1.1.2 Anthropogenic Sources of Sound	2
1.2 Cetacean Order.....	4
1.2.1 Marine Mammal Hearing and Mitigation Measures.....	6
1.2.2 Sperm whale.....	9
1.3 Monitoring of Marine Life.....	11
1.3.1 Visual Monitoring.....	11
1.3.2 Passive Acoustic Monitoring (PAM).....	12
1.3.3 Advantages.....	13
1.3.4 Disadvantages	13
1.4 PAM Structure	14
1.4.1 Detection	14
1.4.2 Recognition	15
1.4.3 Localisation.....	16
1.5 Field Work	18
1.5.1 Material and Methods	19
1.5.2 Results.....	23
1.5.3 Discussion	23
1.6 Problem and Motivation.....	25
1.7 Main Contribution.....	27
1.8 Thesis Description.....	27
1.8.1 Thesis Organization	28
2 PAM Localisation.....	29
2.1 Passive SONAR	29
2.1.1 Brief History	31
2.1.2 Array-configurations	32
2.1.3 Hyperbolic Technique.....	36
2.1.4 Model-based Techniques	38
2.1.5 Signal-Frequency Techniques.....	39
2.1.6 Multipath Technique	42
2.1.7 Source-Motion Techniques	43
2.2 Active SONAR	45
2.3 PAM Localisation Software.....	46

2.4 Discussion and Summary	49
3 Hyperbolic Localisation Algorithm	53
3.1 Underwater Modelling	53
3.1.1 Ray Theory	57
3.1.2 Highly Idealized Medium	58
3.2 Geometric Hyperbolic Surfaces	58
3.2.1 Hyperbola	58
3.2.2 Hyperboloid	60
3.3 Matlab Simulator	62
3.3.1 Synthetic TDOA Data Generation	62
3.4 Localisation Algorithm Methodology	63
3.4.1 Stage One	64
3.4.2 Stage Two	66
3.4.3 Stage Three	66
3.4.4 Stage Four	67
3.5 Discussion and Summary	68
4 Array Optimization.....	69
4.1 Number of receivers	69
4.1.1 Two Receivers	69
4.1.2 Three Receivers	71
4.1.3 Four Receivers and more	71
4.2 Array-Geometry	73
4.2.1 Linear-Array	73
4.2.2 Planar-Array	74
4.2.3 Volumetric-Array	75
4.3 Array-Aperture	76
4.4 Simulation Settings	78
4.4.1 Highly Idealized Scenario	78
4.4.2 Table Settings	80
4.5 Square-Array	83
4.5.1 Short Aperture (L)	83
4.5.2 Long Aperture (16 L)	86
4.5.3 Comparison Short Vs Long Aperture	88
4.6 Y-shape-Array	89
4.6.1 Short Aperture (L)	89
4.6.2 Long Aperture (16 L)	92
4.6.3 Comparison Short Vs Long Aperture	95
4.7 Comparison Square Vs Y-shape	96
4.8 Other Array-Configurations	99
4.8.1 Trapezium-Array	99
4.8.2 Triangular-Array	101
4.8.3 Shifted-pair-Array	103
4.8.4 Circular-Array	106
4.8.5 Summary	107

4.9 Choice of Pair Combinations	109
4.9.1 Square Geometry	110
4.9.2 Triangular Geometry	110
4.9.3 Trapezium Geometry	111
4.9.4 Shifted-pair Geometry	111
4.9.5 Y-shape Geometry	112
4.9.6 Summary	113
4.10 Source Tracking Simulations	113
4.10.1 Sperm whale dive profile	114
4.10.2 Short-Square Array	115
4.10.3 Short-Y-shape Array	117
4.10.4 Short-Shifted-pair Array	119
4.10.6 Long-Y-shape Array	122
4.10.7 Long-Shifted-pair Array	124
4.10.8 Discussion	126
4.11 Array Positioning-Error	127
4.11.1 Offset-Positioning-Error (OpE)	127
4.11.2 Angle-Positioning-Error (ApE)	130
4.11.3 Array Depth-Motion	141
4.11.4 Gaussian Array Depth-Motion	148
5 Non-Homogeneous Medium	153
5.1 Acoustic Propagation Model	153
5.1.1 Model Integration	153
5.1.2 Sound Speed Profile (SSP)	154
5.1.3 Bellhop Model	155
5.1.4 Modelling Settings	157
5.2 Experimental Modelling for a Hyperbolic Localisation Algorithm	158
5.2.1 Short Aperture	159
5.2.2 Long Aperture	161
5.2.3 The use of different SSP	165
5.2.4 Sperm whale dive profile	168
5.3 Discussion and Summary	180
6 Conclusions and Further Work	181
Appendix A	187
Underwater Acoustic Concepts	187
A.1 SOUND	187
A.1.1 Sound Speed	187
A.1.2 Transmission Loss	189
A.1.3 Ambient Noise	192
A.1.4 Directionality and Source Level	193
A.1.5 Signal-to Noise Ratio	194
A.1.6 Sonar Equations	195

Appendix B	197
Algebraic Solution of the Source Location Problem	197
B.1 Synthetic TDOA.....	197
B.2 Algebraic Solution.....	198
Appendix C	201
Matlab Graphical User Interfaces (GUI).....	201
C.1. Simulator	201
C.1.1 Settings	201
C.1.2 Receivers	202
C.1.3 Control Panel	203
C.1.4 Results	206
C.1.5 Plots	207
C.2 Acoustic Propagation Model	208
References	210

LIST OF TABLES

Table 3.1	Domains of applicability of underwater acoustic propagation models.
Table 4.1	Ideal Apertures for Different Frequencies.
Table 4.2	Specifications for Exemplar Simulation.
Table 4.3	Simulation Specifications for Short-Square-Array.
Table 4.4	Synthetic source values of R_H and R_D used for experimental simulations.
Table 4.5	Simulation Specifications for Long Aperture.
Table 4.6	Comparison table of Short Vs Long Aperture for the Square Geometry.
Table 4.7	Simulation Specifications for Short Aperture.
Table 4.8	Simulation Specifications for Long Aperture.
Table 4.9	Comparison table of Short Vs Long Aperture for the Y-shape Geometries.
Table 4.10	Comparison table of Square Vs Y-shape Geometries.
Table 4.11	Summary of the Simulation Results for the Trapezium Geometry.
Table 4.12	Summary of the Simulation Results for the Triangular Geometry.
Table 4.13	Summary of the Simulation Results for the Shifted-pair Geometry.
Table 4.14	Simulation Specifications for a Circular array.
Table 4.15	Summary of Maximum and Minimum Accurate Source Ranges.
Table 4.16	Summary of Maximum and Minimum Partially-Accurate Source Ranges.
Table 4.17	Source Tracking Simulation Specifications.
Table 4.18	Simulation Specifications with Array Positioning-Error.
Table 4.19	Simulation Specifications with Array Depth-Motion.
Table 4.20	Combination of Different Experimental Simulations.
Table 4.21	Summary of the Accurate Combinations for Array Depth-Motion.
Table 4.22	Accurate Combinations for Array Depth-Motion of a Towed Y-shape Array.
Table 4.23	Gaussian Array Depth-Motion Simulation Specifications.
Table 4.24	Ultimate Summary Table on the Accuracy of Array Optimization.
Table 5.1	Synthetic source values of R_H and R_D used for experimental simulations.
Table 5.2	Experimental Specifications for two Array-Configurations.
Table 5.3	Summarised table of results correspondent to a Short-Square-Array.
Table 5.4	Summarised table of results correspondent to a Short-Y-shape-Array.
Table 5.5	Summarised table of results correspondent to a Long-Square-Array.
Table 5.6	Summarised table of results correspondent to a Long-Y-shape-Array.
Table 5.7	Experimental Specifications of four source positions (A, B, C & D).

LIST OF FIGURES

Figure 1.1	The Pacific Ocean is the largest ocean.
Figure 1.2	Taxonomic tree of the Sperm whale (<i>Physeter macrocephalus</i>).
Figure 1.3	Examples of cetacean auditory thresholds.
Figure 1.4	Monopulsed sperm whale click with its Spectral Frequency.
Figure 1.5	Power Spectral Density of the monopulsed sperm whale click.
Figure 1.6	Visual observer (left). Manual bearing device (right).
Figure 1.7	General diagram of a PAM system.
Figure 1.8	Azimuth and elevation angles represented on a 3D plane.
Figure 1.9	Research vessel Gyre and Sperm whale with drill rig.
Figure 1.10	Acoustic Monitoring Station.
Figure 1.11	Stereo towed hydrophone array built by Ecologic Ltd.
Figure 1.12	Portable Acoustic System.
Figure 1.13a	Scenario A. Semi-horizontal Array.
Figure 1.13b	Scenario B. Vertical Array.
Figure 1.14	Two hydrophone array deployment at the stern of the vessel.
Figure 1.15	TDOA computation.
Figure 1.16	Circle intersection by using two pingers.
Figure 1.17	Geometry of the circle intersection.
Figure 2.1	TDOA scenario.
Figure 2.2	SC (left) and MB (right) Tubes Devices.
Figure 2.3	Watkins and Schevill 4-hydrophone-array.
Figure 2.4	Three relatively simple methods of estimating source levels.
Figure 2.5	Simple diagram of a hydrophone array-configuration.
Figure 2.6	Isodiachron versus Hyperbola.
Figure 2.7	DIFAR Sonobuoy Diagram.
Figure 2.8	Beamforming Schematic.
Figure 2.9	Different multipath sound reflections.
Figure 2.10	TMA visualisation of a vessel.
Figure 2.11	Typical scenario of a SURTASS LFA and passive array deployment.
Figure 2.12	Ishmael's screen. Signal waveform and spectrogram.
Figure 2.13	Rainbow Click screen.
Figure 3.1	Summary of the theoretical approaches for propagation modelling.
Figure 3.2	Hyperbola Geometry.
Figure 3.3	Hyperboloid of two sheets reduced to one half.
Figure 3.4	Hyperboloid scenario resulting from two receivers array.
Figure 3.5	Intersection of three hyperboloid geometric surfaces.
Figure 3.6	Intersection in a single point.
Figure 3.7	Synthetic TDOA computation in 3D.
Figure 3.8	Block diagram of the simulator algorithm.
Figure 3.9	Algorithm Diagram and its four stages.
Figure 3.10	Tolerance Localisation Error based on sperm whale.

Figure 4.1a	Broadside scenario is the result of a TDOA equals to zero.
Figure 4.1b	Endfire scenario is the result of a TDOA equals to TDOR.
Figure 4.2	3D Graphical SV Location, with bearing and range included.
Figure 4.3a	Semi-horizontal array deployment.
Figure 4.3b	Vertical array deployment.
Figure 4.4	The right/left ambiguity of source location.
Figure 4.5	Planar-Array Geometry.
Figure 4.6	Common Planar-Array Geometries.
Figure 4.7	Volumetric-Array Geometry.
Figure 4.8	Typical Power Spectral Density of a Sperm whale.
Figure 4.9	A 3D graphical scenario for Experimental Simulations.
Figure 4.10	A general representation of the Slant Ranges in 3D.
Figure 4.11	Polar representation of the hundred Source positions (Sv).
Figure 4.12	Polar representation of an exemplar array simulation.
Figure 4.13	Superior view of a square array of 4 elements.
Figure 4.14	Short-Square-Array ($4LR_H$ to $32LR_H$).
Figure 4.15	Long-Square-Array ($4LR_H$ to $128LR_H$).
Figure 4.16	Short Vs Long aperture of a Square array ($16LR_H$ at $8LR_D$).
Figure 4.17	Superior view of a planar Y-shape array of 4 elements.
Figure 4.18	Short-Y-Array ($2LR_H$ to $16LR_H$).
Figure 4.19	Short-Y-Array ($32LR_H$).
Figure 4.20	Long-Y-Array ($1LR_H$ to $32LR_H$).
Figure 4.21	Long-Y-Array ($64LR_H$).
Figure 4.22	Short Vs Long aperture of a Y-shape array ($32LR_H$ at $16LR_D$).
Figure 4.23	Comparison of a Square Vs Y-shape array ($16LR_H$ at $8LR_D$).
Figure 4.24	Five typical array geometries of elements.
Figure 4.25	Superior view of a planar <i>Trapezium</i> array of 4 elements.
Figure 4.26	Trapezium-Array ($2LR_H$ to $16LR_H$).
Figure 4.27	Superior view of a planar <i>Triangular</i> array of 4 elements.
Figure 4.28	Triangular-Array ($2LR_H$ to $16LR_H$).
Figure 4.29	Superior view of a planar <i>Trapezium</i> array of 4 elements.
Figure 4.30	Short Shifted-pair ($16LR_H$ to $64LR_H$).
Figure 4.31	Comparison of a Short Vs Long Array-Aperture ($64LR_H$ at $8LR_D$).
Figure 4.32	Superior view of a planar Circular array of 5 elements.
Figure 4.33	Long-Circular-Array ($128LR_H$ at $8LR_D$).
Figure 4.34	Pair-Combination Comparison of the Square Geometry.
Figure 4.35	Pair-Combination Comparison of the Triangular Geometry.
Figure 4.36	Pair-Combination Comparison of the Trapezium Geometry.
Figure 4.37	Pair-Combination Comparison of the Shifted-pair Geometry.
Figure 4.38	Choice Comparison of pair-combinations with Y-shape ($4LR_H$ at $8LR_D$).
Figure 4.39	Pair-Combination Comparison of the Y-shape Geometry.
Figure 4.40	Typical Sperm Whale Dive Profile.
Figure 4.41	Typical Synthetic Source Dive Profile.
Figure 4.42	Effects of a Short-Square Array on a Source Dive Profile (a, b, c).
Figure 4.43	Additional simulations with a different azimuth angle.
Figure 4.44	Effects of a Short-Square Array on two Source Dive Profiles.

Figure 4.45	Effects of a Short-Y-shape Array on a Source Dive Profile.
Figure 4.46	Effects of a Short-Shifted Array on a Source Dive Profile.
Figure 4.47	Effects of a Long-Square Array on a Source Dive Profile.
Figure 4.48	Effects of a Long-Square Array with a second Source Dive Profile.
Figure 4.49	Effects of a Long-Y-shape Array on a Source Dive Profile.
Figure 4.50	Effects of a Long-Y-shape Array with a second Source Dive Profile.
Figure 4.51	Effects of a Long-Shifted-pair Array on a Source Dive Profile.
Figure 4.52	Effects of a Long-Shifted-pair Array with a second Source Dive Profile.
Figure 4.53	Scenario of a Towed Shifted-pair Array with OpE (0 to $\pm 30m$) on XY axes.
Figure 4.54	Effects of $\pm 30m$ OpE on the performance of a Shifted-pair array
Figure 4.55	Scenario of a Towed Y-shape-pair Array with OpE (0 to $\pm 30m$) on XY axes
Figure 4.56	Effects of $\pm 30m$ OpE on the performance of a Y-shape array.
Figure 4.57	Three Different Scenarios of a Towed Array.
Figure 4.58a	Exemplar diagram of the angle-positioning-error (ApE).
Figure 4.58b	Length between vessel and first receiver position.
Figure 4.59	Scenario with Shifted-pair array towed to a vessel moving in a Straight line.
Figure 4.60	Scenarios with a Shifted-pair array towed to a vessel turning to Port.
Figure 4.61	Scenarios with a Shifted-pair array towed to a vessel turning to Starboard.
Figure 4.62	1 st series -scenarios with Y-shape array towed and moving in a straight line.
Figure 4.63	2 nd series -scenarios with Y-shape array towed and moving in a straight line.
Figure 4.64	Scenarios with a Y-shape array towed to a vessel turning to Port.
Figure 4.65	Scenarios with a Y-shape array towed to a vessel turning to Starboard.
Figure 4.66	Y-shape Array Geometry.
Figure 4.67	Array Depth-Motion scenario.
Figure 4.68	Four scenarios with depth-motion in ONE receiver.
Figure 4.69	Six scenarios with depth-motion in TWO receivers.
Figure 4.70	Four scenarios with depth-motion in THREE receivers.
Figure 4.71	Towed array of three lines for a Y-shape geometry.
Figure 4.72	Experimental simulations with synthetic aberrations. Y-shape array.
Figure 4.73	Experimental simulations with synthetic aberrations. Shifted-pair array.
Figure 5.1	Generation of Simulation Data.
Figure 5.2	Three different sound speed profiles of the Gulf of Mexico.
Figure 5.3	Sound speed profile and associated ray trace.
Figure 5.4	Short-Square-Array (16LR _H & 8LR _D).
Figure 5.5	Short-Y-shape-Array (8LR _H & 8LR _D).
Figure 5.6	Long-Square-Array (4L-16LR _H , 8LR _D)
Figure 5.7a	Long-Y-shape (32LR _H , 8LR _D).
Figure 5.7b	Long-Y-shape (64LR _H , 8LR _D).
Figure 5.8	Scenario with different sound speed profiles and source positions.
Figure 5.9	Long-Square-Array (32LR _H).
Figure 5.10	Long-Y-shape-Array (32LR _H).
Figure 5.11	Comparison of a Long-Square Array in two different mediums.
Figure 5.12	2D views of a Long-Square Array tracking a synthetic Source Profile.
Figure 5.13	Comparison of a Long-Y-shape Array in two different mediums.
Figure 5.14	2D views of a of a Long-Y-shape Array tracking a synthetic Source Profile.

Figure 5.15	Comparison of a Long-Shifted Array in two different mediums.
Figure 5.16	2D views of a of a Long-Shifted Array tracking a synthetic Source Profile.
Figure 5.17	Comparison of a Long-Y-shape Array with two different SSP.
Figure 5.18	Typical array depth-motion on TWO or more receivers.
Figure 5.19	Typical array depth-motion on ONE receiver.
Figure 5.20	Typical XY array-motion on the FOUR receivers.
Figure 6.1	Scenarios of two linear arrays towed by a vessel in the Gulf of Mexico
Figure 6.2	Y-shape Array-Configuration, with an aperture-length of $32L$.
Figure A.1	Typical sound–speed profile.
Figure A.2	TL as a function of range.
Figure A.3	TL as function of range and receiver depth.
Figure A.4	Representation of the different TL calculations.
Figure A.5	Knudsen spectra.
Figure C.1	Matlab GUI Simulator.
Figure C.2	Settings and TDOAs.
Figure C.3	Receivers Position.
Figure C.4	3D Receiver Array.
Figure C.5	Control Panel Sections.
Figure C.6	Synthetic source position and its hyperbolic approaching location.
Figure C.7	3D plot of the intersection of three hyperboloid geometric surfaces.
Figure C.8	Zoom in window showing the hyperboloid intersection.
Figure C.9	Propagation Model Parameters.
Figure C.10	Acoustic Propagation Modelling Techniques.
Figure C.11	Bellhop Setting Parameters.

CONFERENCES AND POSTERS

Conference Paper:

- The Effect of Different Array-Configurations on the Accuracy of Passive Acoustic Location of Cetaceans.
Vallarta J., McHugh R. and Record P.
Proceedings of the Institute of Acoustics Fourth International Conference on Bio-Acoustics, Vol. 29, pp. 141-148, Loughborough, UK, April 2007.

Posters:

- 3D Passive Acoustic Localisation Homogeneous Vs Non-Homogeneous Medium.
Vallarta J., McHugh R.
17th Biennial Conference on the Biology of Marine Mammals,
Cape Town, South Africa, December, 2007
- The Effect of Passive Acoustic Array-Configuration and Element Aberrations on Cetacean Localisation.
Vallarta J., McHugh R.
16th Biennial Conference on the Biology of Marine Mammals,
San Diego, USA, December, 2005

Chapter 1

Introduction

"The ocean is a precious resource shared by all the world's peoples"

- Jean Michael Cousteau

The earth is unique among the planets of the solar system, since it is largely covered by water. One of the astronauts of the Apollo 8 moon flight commented: "In the whole universe, wherever we looked, the only bit of colour was back on the earth. There we could see the royal blue of the seas, the tans and browns of the land, and the whites of the clouds. . . ." [161]. When photographed from outer space, our beautiful blue planet looks as if it should be called Water, not Earth. Indeed, if the world's water evenly covered the surface of the planet, it would form a global ocean 1.5 miles (2.5 km) deep. All of the earth's land surfaces could fit into the Pacific Ocean, with room to spare [162].

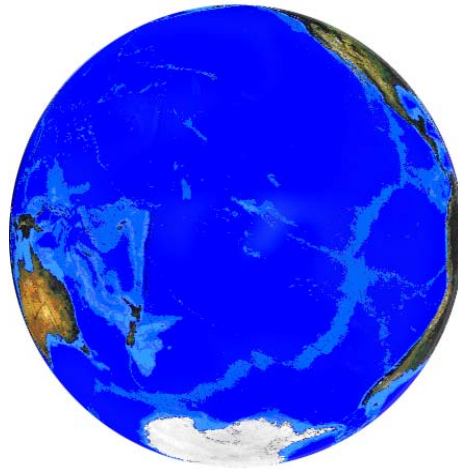


Figure 1.1: The Pacific Ocean is the largest ocean

Life in the oceans can be found from the surface to the extreme environments at the bottom of the deepest submarine trench. It is not surprising that the oceans represent over 99% of the living space on Earth; we are indeed living on what is truly an ocean planet. Today our knowledge of the ocean is rapidly evolving, such that we are coming to understand more fully the role that each parameter plays in our lives.

1.1 Underwater Sound

Sound is known as “a disturbance in pressure that propagates through a compressible medium” [105]. Unlike light, sound is transmitted very efficiently through water. Although from the outside the oceans seem a quiet place, in reality they are not. The efficiency of underwater sound propagation (see Appendix A) allows animals to use it as a primary method of communication.

1.1.1 Natural Sources of Sound

When a natural underwater object vibrates, it creates sound-pressure waves that alternately compress and decompress the water molecules as the sound wave travels through the water. Sound waves radiate in all directions away from the source. The physical transitions associated with sound waves can be detected by hydrophones, and their audio output can be detected as auditory sensations on the ear at determined frequencies. Among the most common natural sources of sound in the oceans are waves interacting, waves breaking, wind noise transmitted directly into the water, rain, snow and spray falling onto the water. In frozen areas, sources are ice rubbing and cracking. Thunder, cosmic rays, and earthquakes are other kinds of unanimated sources of sound [69]. On the other hand, the marine mammals represent the most important group of animated sources of underwater sound. They are extremely vocal.

1.1.2 Anthropogenic Sources of Sound

In the ocean, a wide range of sounds are generated by humans. The vast expanse of the oceans was free of significant human impact until the intentional introduction of sound into the oceans. Although considerable advances have been made in terrestrial communications such as electromagnetic techniques in recent decades, there was also wide interest in underwater acoustic techniques [16, 17, 23, 107, 164]. As engineers and scientists learned to appreciate the properties of acoustic propagation in the sea, they introduced sound sources to communicate and to detect objects in the oceans. At some point, as humans use the oceans more and increase anthropogenic sound in the oceans, the conflict with the sound-sensing systems of marine animals seemed

inevitable. The intentional and unintentional introduction of sound in the oceans associated with activities beneficial to humans has known deleterious effects on individual marine mammals [70].

The major source classes of anthropogenic sound [108] with their respective *Received Levels (RLs^{*})* measured in the oceans are:

- **Active Sonar** – military sonar (RLs 130-150 dB re 1 μ Pa).
- **Marine Construction** - drilling and detonations (RLs 140-179 dB re 1 μ Pa).
- **Seismic Exploration** – seismic survey air guns (RLs 115-170 dB re 1 μ Pa).
- **Shipping** – whale-watching vessels (RLs 115-138 dB re 1 μ Pa).
- **Synthetic Acoustic Signals** – acoustic deterrent and harassment devices (RLs 107-164 dB re 1 μ Pa).

^{*}For more details on RL and acoustic measures, please see appendix A, equation A.7.

If cetacean monitoring is performed from a vessel, two types of background noise are found, self noise and ambient noise. The three major classes of self noise are ship machinery noise, propeller noise and hydrodynamic noise. The noise level from shipping that has increased during the past decade could also be included as ambient noise if the cetacean monitoring is performed from a noiseless platform. Other sources of ambient noise come from the offshore oil industry and wind farm constructions. Pile-driving activities are an example of other contributors to the distress imposed on marine mammals. Among the most extremely loud anthropogenic sources are the seismic surveys. They use airgun blasts which are conducted during oil exploration and often extend over large areas and periods of time.

Anthropogenic sound has a significant adverse impact on marine species. Since they are dependent upon hearing, the concern over noise impacts is particularly important. Hearing comprises a simple chain of events: sound energy is converted by bio-mechanical transducers (middle and inner ear) into electrical signals (neural impulses) that provide a central processor (brain) with acoustic data [70].

In March 2000, 17 whales were reported stranded along the Providence Channels of the Bahamas Islands [74]. Seven whales died. Haemorrhages were found in the inner ears and some cranial spaces. These pathologies were consistent with stress and pressure-

related trauma that may have compromised hearing. The observed cause of death in the whales was the physical consequences of stranding. The investigations concluded that “the sound field created by the combination of ocean state, topography, and the use of multiple tactical mid-range frequency sonar during the exercise, was an important factor in the stranding event” [74]. Two months later, a mass stranding of cetaceans was reported along the Madeira Archipelago [72]. Several observations were consistent with the Bahamian pathologies. The coincidence of pathology and the stranding patterns in both sites raised the concern that similar causes contributed to strandings in both sites [72].

With regard to non-auditory effects, the hypothesis exists that “acoustic exposure may produce nitrogen bubbles in blood or other tissues” [128]. Although there is much well-documented literature [36, 37, 62, 71, 72, 108, 128], there still remain many *unknowns*, such as when and how these acoustic changes translate into biologically significant effects –effects that have repercussions for the animal’s ability to engage in essential activities, and effects that have potential consequences at the population level.

So far, these may be only the first early warnings or “tip of the iceberg” with respect to sound and its possible harmful effect on marine mammals [107]. Although we have to be careful in separate factual information from newspaper stories, there is no doubt that the impact of underwater sound is related to the environmental and political perspective in today’s society.

1.2 Cetacean Order

Marine mammals are grouped into three different orders: sirenians, pinnipeds, and cetaceans. Cetacean use underwater sounds as a primary method of communication with each other. The Cetacea order (Figure 1.2) is divided into two suborders: Odontoceti (Toothed whales) and Mysticeti (Baleen whales). The main biological distinction between the two suborders is the presence of teeth [119]. The Mysticeti do not have teeth. Instead they have keratin baleen plates, suspended from the roof of the mouth. The Odontoceti do have teeth. Their number of teeth varies from 2 in some beaked whales to more than 250 in some dolphin species [34, 75, 96, 119]. The

cetaceans vary in their capability of vocalising at different frequency ranges. Unlike the mysticetes which collectively use lower frequencies (7 Hz to 22 kHz) [73], odontocetes use intermediate to very high frequencies (1 kHz to 100+kHz) [6, 121]. For instance, some species, like the fin whale (*Balaenoptera physalus*), are able to vocalise at low frequencies (10-30 Hz) [32, 166]; other species, like the pygmy sperm whale (*Kogia breviceps*), vocalise at higher frequencies (60-200 kHz) [121, 122].

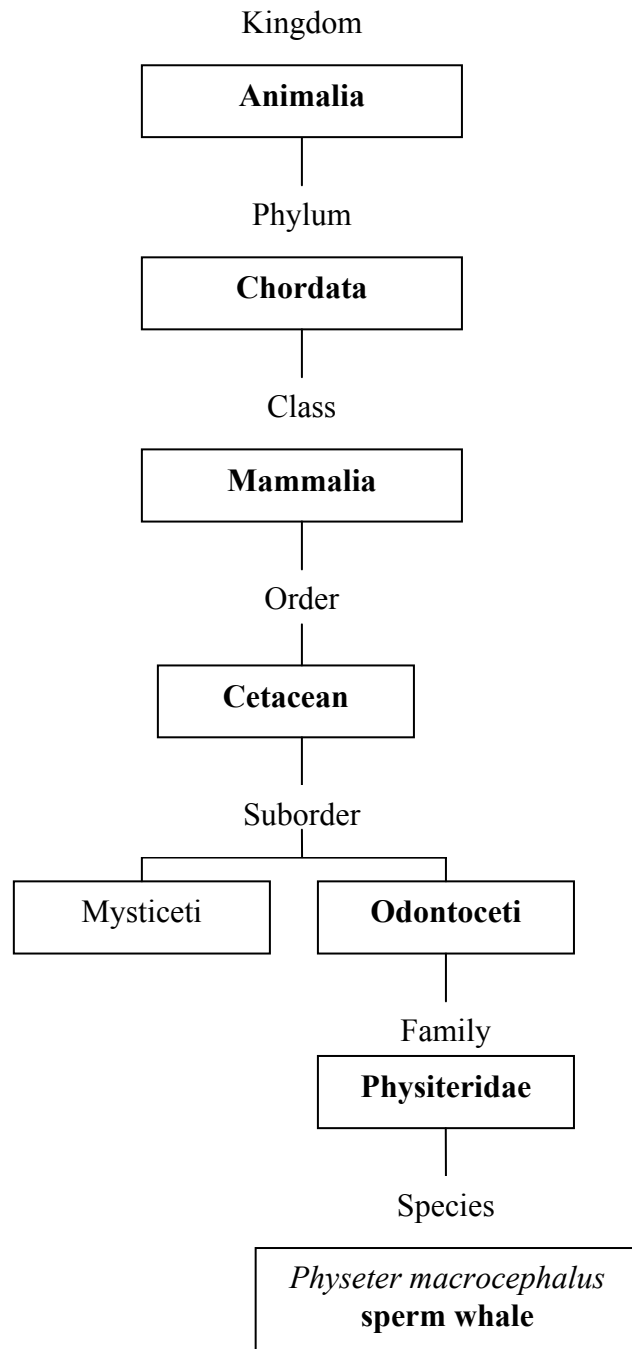


Figure 1.2: Taxonomic tree of the sperm whale (*Physeter macrocephalus*)

1.2.1 Marine Mammal Hearing and Mitigation Measures.

The marine mammals also vary in their capability to detect sound. Figure 1.3 shows a general scenario of a marine mammal audiogram, based on six different species.

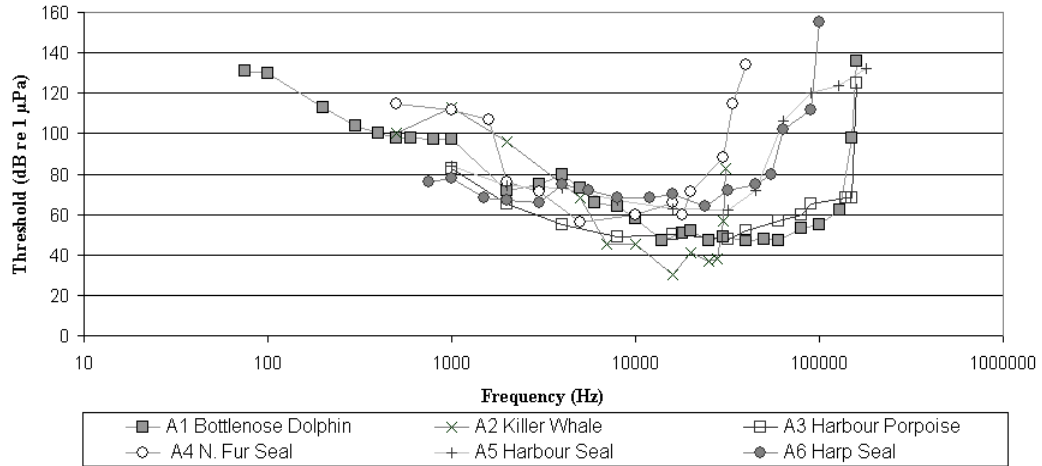


Figure 1.3: Examples of marine mammal auditory thresholds [93]. The audiogram represents the minimum sound level of a pure tone that marine species can hear in a noiseless environment. Bottlenose dolphin [67, 83], Killer whale [52] Harbour porpoise [3] Northern Fur seal [104], Harbour seal [101], Harp seal [140].

The conservation status and biology of most marine mammals are poorly understood. Many populations are threatened; quite a few are endangered; all are susceptible to humankind's interference with marine ecosystems. The effects of acoustic emissions on marine life depend on four critical factors [46], and knowledge of each is required for estimating damage:

- **received power level** – source level, range to subject, propagation conditions.
- **exposure time** – tracking of subject, gaps between multiple exposures.
- **the subject of exposure** – species classification, age, activity.
- **the nature of the signal** – rise time, duration, transmitting frequency/bandwidth

According to Richardson *et al.* [121], there are four zones of noise influence. The zone of audibility, in which the animal is able to detect the sound; the zone of responsiveness, in which the animal reacts behaviourally or physiologically; the masking zone, in which noise is strong enough to interfere with detection of other sounds; and the zone of

hearing loss, the area near the noise source where the received sound level is high enough to cause tissue damage resulting in hearing losses. The damage is classified as either permanent (PTS) or temporary threshold shifts (TTS), a change of the hearing threshold as a result of noise exposure [71, 93].

In 2007, the US Navy issued a Programmatic Environmental Assessment/Overseas EA (First EA) in conjunction with the recommendations of the National Marine Fisheries Service (NMFS). The First EA proposed a PTS Level A of between 195 to 215 dB, a TTS level B threshold of between 190 and 195 dB, and a sub-TTS or non-behavioural disturbance level of 190 dB or less. However, since some marine mammals may react to Mid-Frequency Sonar (MFA) at levels lower than those previously thought, NMFS required mitigation measures above and beyond those that the Navy had originally proposed, and recommended a sub-TTS level of 173 dB [41]. Long or repeated exposure to TTS sounds can induce PTS, and cause direct physical harm with behaviours that may lead to physiological harm, stranding, or, potentially, death. Damage is directly related to the power spectrum of the sound and the sensitivity of the ear. At low levels, noise and TTS hearing loss do not pose a significant problem, but at higher powers, they can interfere in several important ways:

- Missed Communication: marine mammals simply are not able to hear the other members of their species in the area, possibly interfering with migration, mating, and other social interactions.
- Poor echolocation: marine mammals are not able to hunt effectively.
- Stress: marine mammals are susceptible to stress hormone levels associated with noise exposure, causing erratic behaviour that could interfere with migration, mating, or cause stranding and death [70, 128].

Recent studies use “available marine mammal TTS data and precautionary extrapolation procedures based on terrestrial mammal data to estimate exposures associated with PTS” [108, 128]. The latest literature on mitigation measures [128] present a summary of behavioural responses by cetaceans exposed to multiple pulses. These studies indicate that there are behavioural responses to sounds with RLs of 110-180 dB re 1 μ Pa for species of low frequency, and RLs of 100-180 dB re 1 μ Pa for species of middle frequency. Southall *et al.*, recommend more comprehensive and calibrated

measurements of the properties of natural and anthropogenic sound sources. It also highlights the need for a study of their propagation and received characteristics in different environments. Continued effort is still needed on the simultaneous and residual physiological effects of noise exposure on marine mammal hearing.

A report of the “*Effects of offshore wind farm noise on marine mammals and fish*” published in July 2006 [146] states a regulatory approach of a zone of potential TTS of 1,800m for all odontocetes, regardless of the studies in two species. The report also recommends that “studies on frequency dependant TTS are urgently needed to derive more solid conclusions on the effects of sound on toothed whales”. The behavioural effects can take many forms, and will depend on whether the interfering sound causes PTS, TTS, or if it is merely audible in the same frequency band as the communications or echolocation signals of the marine mammal (Figure 1.3).

Nowadays, there are many reported mitigation procedures in place worldwide [11, 12, 41, 68]. However, in February of 2008, the Court in the USA pointed out the importance of Navy conducting effective training while taking greater precautions. The Navy was also required to take a hard look at the impacts of its high-intensity MFA sonar by adhering to additional mitigation measures to protect marine mammals. The mitigation measures for a safety zone included:

1. Reducing sonar transmissions levels by at least 6dB whenever a marine mammal is detected within 1,500 metres of the transmitting vessel.
2. Reducing levels by at least 10 dB for any marine mammal detected within 750 metres.
3. Ceasing transmissions of all sonar when a marine mammal is detected within or close to within 500m of the sonar dome.

1.2.2 Sperm whale

In this thesis the cetacean species target is the sperm whale (*Physeter macrocephalus*) which belongs to the suborder Odontoceti (Figure 1.2) and is well known as the largest toothed whale in the world [87]. The average size of an adult reaches 15m in length [48, 85]. They are oceanic [163] and make deep dives of 400 to 1200m that last for an average of at least 45 minutes, followed by about 8 minutes on the surface [2, 48, 49]. During bouts of foraging behaviour, they seem to spend all of their time either diving or recovering on the surface [98, 139].

Sperm whales are extremely vocal and produce sharp, impulsive, broadband sounds called clicks [4, 8, 57]. These clicks have a frequency range of 100 Hz to 30 kHz, the majority of energy of which is in the 2 to 4 kHz and 10 to 16 kHz ranges [8, 81, 121, 165]. The clicks are transient signals whose duration is short compared with that of the observation interval. Figure 1.4 shows a monopulsed sperm whale click [103] together with its spectrogram.

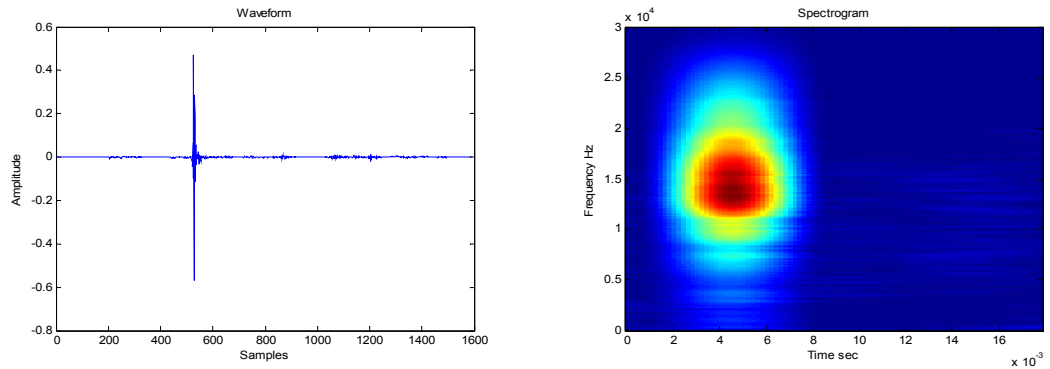


Figure 1.4: Monopulsed sperm whale click and spectral frequency range up to 30 kHz
(computed with Matlab software, data obtained by Peter Madsen [103]).

The Power Spectral Density (PSD) represents the distribution of energy in the signal as a function of frequency [115]. Figure 1.5 shows the PSD of the monopulsed sperm whale click described above.

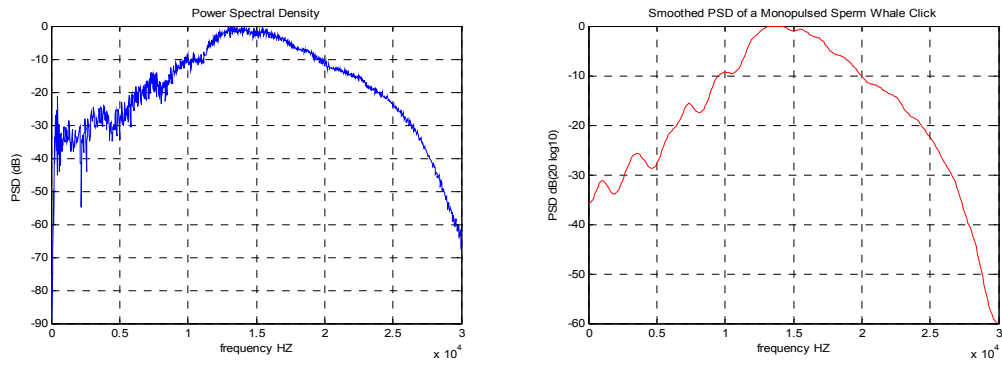


Figure 1.5: Power Spectral Density of the monopulsed sperm whale click with a higher energy at 15 kHz (computed with Matlab software, data obtained by Peter Madsen [103]).

Clicks can be produced with a variety of repetition rates, these being assigned to four main categories. “Usual clicks”, the most commonly heard sound, have an *InterClick Interval* (ICI) of about 0.5 to 1 s; "slow clicks" have an ICI of about 5 to 7s [169]; "buzzes" are a series of very rapid clicks with up to 220 clicks per second [47]; and "codas" are short, patterned series of clicks with irregular repetition rates [57, 167].

Sperm whales use *echolocation* to navigate and find prey at ranges greater than is possible with aquatic vision [172]. Echolocation involves emitting a succession of tone bursts or other transient signals, and listening for reflections [105]. Echoes of clicks from the surface are frequently detectable [142]. These vocalisations seem to function both for echolocation and communication, although direct evidence for these is lacking [8, 47, 169].

In summary, sperm whales rely heavily on acoustic modality. This means that sound equipment and underwater acoustic methods can offer efficient means of finding and tracking sperm whales [47, 172]. Sperm whale vocalisations can very easily be recorded, if necessary, by no specialists or remotely, and there is considerable scope for automated analysis [43]. Of all the cetaceans, sperm whales are most amenable to acoustic detection and survey methods.

1.3 Monitoring of Marine Life

Given that most the marine mammal behaviours occur under water, where they are difficult to document, and that makes it particularly hard to estimate the effects of a short-term exposure as they ripple through the lifetime of an individual, or as the effects on different individuals ripple through the population. Even extreme effects, including death, are often not necessarily visually observed. Continuous monitoring is important in order to determine whether or not a sound source is affecting the behaviour of marine mammals. The monitoring techniques are based on either visual observations or passive acoustics.

1.3.1 Visual Monitoring

Visual observations of marine mammals can provide detailed information on the behaviour, movement, and abundance of these animals in the wild. Changes in the animals' behaviour and abundance can be used to infer how the animals are affected by sound. Visual observation studies involve trained observers watching for marine animals of interest. Each observer is responsible for surveying a particular area of water. Once an animal is spotted, the observer takes note of the bearing (position angle), gives an estimate of the number of animals present and tries to identify the species (Figure 1.6). Then, depending upon the aims of the project, animals can be photographed for identification purposes, filmed for behaviour study, or tracked for a period of time.

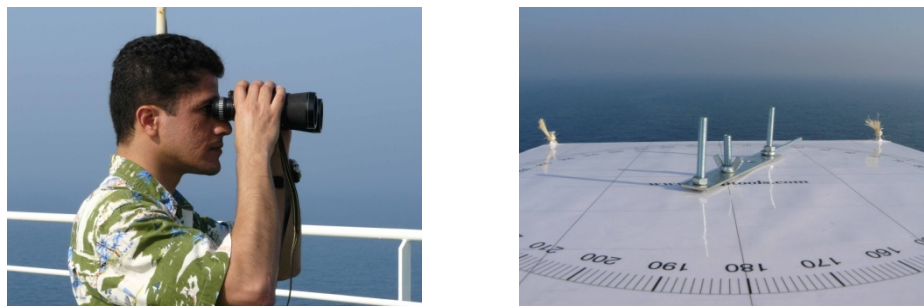


Figure 1.6: Visual observer (left). Manual bearing device (right)

For many years the use of visual cues has been an established mitigation technique. Such mitigation is required when operators are likely to create high levels of anthropogenic noise in the sea. If creatures are observed within the recognised exclusion zones of the sound source, legislation demands that the work has to be stopped until such time as the creatures are seen to have dispersed from the area [41].

1.3.2 Passive Acoustic Monitoring (PAM)

Nowadays, an essential and powerful tool called Passive Acoustic Monitoring (PAM) has emerged recently to help with the concern of marine life in important issues such as behaviour, population estimation, mitigation and monitoring studies of how the cetaceans are affected by the anthropogenic noise in the sea. This technique uses the animal's own vocalisations for detection and location purposes. Mechanical vibrations are received in a piezoelectric element (hydrophone) and transformed into electrical pulses, which are amplified and then transmitted to an acoustic station to be digitised by using a Data Acquisition Card (DAC). The signal is sampled at least twice the highest analogue frequency component, according to the Nyquist theorem. Then, the signal is ready to be processed through mathematical algorithms for detection, recognition and localisation purposes (Figure 1.7).

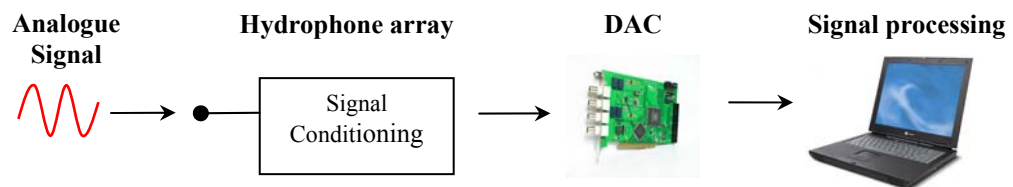


Figure 1.7: General diagram of a PAM system

Currently, PAM is still in its infancy. Legislation is moving towards PAM being accepted, and it is being adopted as an additional tool for the visual surveys. PAM is effective only for studying animals that are vocalising, but the absence of vocalisations does not necessarily mean that animals are not present. PAM can also be used to track animals from a distance and to measure patterns of movement and sound production.

1.3.3 Advantages

PAM techniques have a number of advantages over visual ones.

- They are less affected by meteorological conditions, and are often more predictable and consistent in their performance than human observers who are dependant totally of their own judgment and visual errors.
- They can observe many individuals at once and are suitable for continuous monitoring applications for 24 hours a day.
- They work when animals are hidden from view, such as at night or when submerged.
- Not only do they allow for the detection of marine animals outside the visual range of the observers, but can also provide information as to the location of the animals relative to the observation vessel.
- They are also readily automated using modern signal processing techniques which are based on increased availability of low cost, yet efficient computers [42].

1.3.4 Disadvantages

- PAM is effective only in the study of animals that are vocalising.
- The accuracy of PAM depends on the array-configuration and algorithm used.

1.4 PAM Structure

PAM relies heavily on advances in recording and data processing technology. The recent explosion in fast, inexpensive personal computers and electronics has created tremendous growth potential in the field. PAM has been developed to gather specialized or common data for particular or general scenarios. The structure of PAM is classified according its three different uses: Detection, Recognition and Localisation.

1.4.1 Detection

Detection is the step where the vocalisations of interest are located within the recording. Standard PC sound card technology can detect dominant components of most cetaceans within the range of 20 Hz to 20 kHz [121]. More specialized recording equipment is used to detect sounds below and above such a range.

Frequency and time series data are processed using a Fast Fourier Transform (FFT) to produce spectrograms of the calls. The technique generally works with an energy detector that exploits the frequency/time characteristics of the signal. Nevertheless, the problem with detection is the wide range of species, since each species produces different sounds with different duration and source level [151]. Also, the frequency contours of cetacean vocalisations can be complex and nonlinear [91].

A simple philosophy is to attempt to detect all sound occurrences that deviate from the background noise. However, fundamental calls may be obscured by louder ambient noise. Hence, in order to better quantify the nature and variability of the calls, matched filters are used to maximise the signal-to-noise-ratio (SNR) of the output by condensing the amplitude of the signal into the output peak. A matched filter may be implemented by the correlated part of a known signal (kernel) with input data from the channel to produce peaks in the output, indicating the presence of an animal call. The kernel can be either real or synthetic [95]. The success of a specific matched filter depends on the variation of animal calls and the ambient noise characteristics from the channel [137]. Other techniques for detecting marine mammals with a wide variety of sounds use a

power-law integrator and a Page's test. The power-law integrator is robust against varying signal bandwidth and the Page's test detector is a robust detector for signals with an unknown duration [151]. Some others use an edge detector on the smoothed spectrogram of vocalisations [44].

Nevertheless, in biologically realistic environments, signals are highly diverse and often only partially known. The problem of detection and estimation of real signals is often dependent upon a fully parametric signal model and large and high-quality datasets for determining the statistical distributions of the parameters [91].

1.4.2 Recognition

Once detection is made, it is important to know whether it is man-made or biological [151]. A chain of recognition steps is followed to parameterize the signal using specific features. The signal is then classified by decisions based on these features. The automatic recognition exploits the time-frequency complexity of an animal vocalisation [95]. It is also a challenging problem in signal processing, since difficulty arises from the non-stationary nature of the signals involved; from the highly variable nature of animal sounds at the individual, intraspecific, and interspecific levels of analysis, and from the characteristics of the noise environments encountered in field recordings. Recognition is divided into two stages: *characterisation* and *classification*.

Characterisation is the process of extracting a few descriptive features from the detected vocalisations. The characterisation step is necessary because the dimensionality of a detected vocalisation is usually too great to apply classification directly. However, for low-dimensional detections such as clicks, it is possible to skip the characterisation step and instead force the classification step to learn what to base the class decision on.

Classification is the final stage of the recognition chain. The aim is to identify which pre-defined class the vocalisation belongs to, based on the features of the vocalisation [66]. Two popular types of classification methods for transient signals are Statistical Analysis of time series and Pattern Recognition in Time-Frequency plots [151].

Statistical analysis measures a number of characteristics from the sound, and uses these in statistical classifiers [40, 76, 112]. The time-frequency plots must be isolated by following a processing scheme of normalisation, thresholding and clustering. Then, in order to classify a detected sound, the measured features of a cluster are compared with those of the typical sounds produced: clicks, moans, whistles and sweeps [151].

Various techniques have been used for automatic recognition of animal calls. Among the different techniques often used to compute the time-frequency distribution are *Short-Time FFT processing (STFT)*, *Wavelet processing* and *Cochlea processing*. STFT cuts the time-series of the transient into short segments, which are analysed specially by means of an FFT [151]. Colchea processing is a technique based on the human ear. The technique is very suitable for the identification of human speech and seems suitable for the identification of marine mammal sounds [151]. Wavelet processing adapts the time frequency resolution to the signal and this is then classified [1].

Other techniques use neural networks, typically using spectrogram values as input; they perform well on noisy data [95, 117, 149]. Some others use frequency-modulated vocalisations that are broken into sequences of linear chirps. Speech methods have also been applied [116]. Recently normalized lofargrams from a broadband beamformer and time-based techniques have also been used [151]. Parametric modelling techniques use AutoRegressive Moving-Average (ARMA) models which are appropriate for narrowband signals in noise [66]. Spectrogram matched filtering or cross-correlation of the spectrograms are perhaps the most common methods used for classifying and comparing animal sounds [18, 21].

1.4.3 Localisation

Localisation, as defined in acoustics, is “the perception by a listener that a sound is coming from a certain direction”; however, it is also known as “the process of judging the direction of a source” [103]. For purposes of accuracy, the direction must include bearing (azimuth and elevation angle) and range. Since localisation is performed in a three-dimensional space, it may also be called *spatial discrimination*.

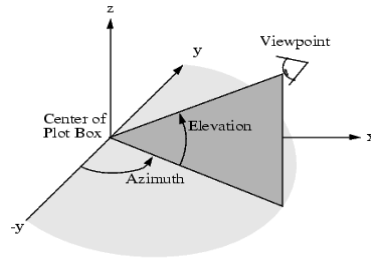


Figure 1.8: Azimuth and elevation angles represented on a Cartesian XYZ plane

Spatial discrimination requires the use of a number of individual receivers. PAM can use hydrophone arrays to record marine sounds and determine where they come from. A simple hydrophone array consists of at least two hydrophones deployed at known locations. The hydrophone geometry may vary, as will be discussed in chapter four.

The majority of algorithms used to determine the localisation fall under the general headings of hyperbolic fixing, optimization, model-based approaches and bearing triangulation [79, 80, 92, 106, 124, 126, 147, 157, 157, 174]. All these different algorithms will be analyzed in detail in the next chapter.

The degree of difficulty in accomplishing each of the steps in PAM is a function of the acoustic characteristics of the calls, the ambient noise background, the instrumentation configuration and sensitivity, the performance of the localisation algorithms, and the precision required for localisation in two or three dimensions. This thesis uses a particular *three-dimensional PAM localisation algorithm*; detection and recognition are not a concern of this thesis.

1.5 Field Work

Within the first year of this work the author of this thesis was involved in field experiments. From the 31st of May to the 21st of June 2003 a cruise was performed in the Gulf of Mexico. It was conducted by the Sperm Whale Seismic Study (SWSS), a programme to study sperm whales and their response to seismic exploration [64, 65]. SWSS was sponsored by the U.S. Minerals Management Service and involved researchers from Texas A&M University, Oregon State University, Woods Hole Oceanographic Institution, the University of Durham, and Ecologic in coordination with the International Association of Geophysical Contractors. The cruise was led by Dr Jonathan Gordon from the Sea Research Mammal Unit at St Andrews, and Dr Douglas Biggs from Texas A&M University. The work plan consisted of three types of activities involving ship work and subsequent analysis and interpretation. The programme was classified on *Habitat Characterisation and Sperm Whale Survey* and *Photo-Identification* activities aboard the *R/V Gyre*. Specific acoustic equipment was developed to obtain recordings from the sounds produced by the sperm whales. This cruise represented a unique opportunity to work with the key researchers in marine mammal studies.

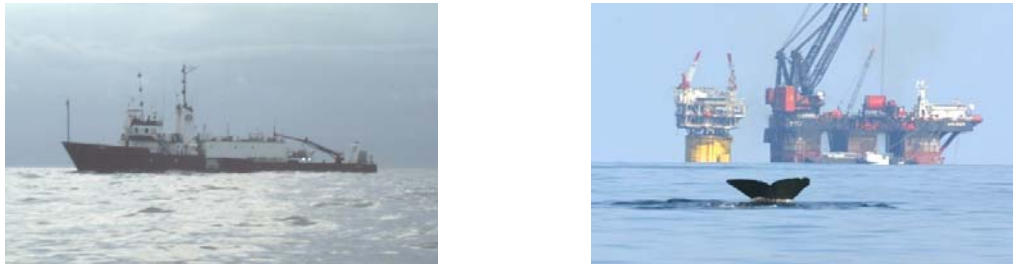


Figure 1.9: Research vessel Gyre (left). Sperm whale and drill rig by C. Richter (right).

One of the primary tasks was to be responsible for monitoring sperm whales round the clock and tracking them. Also, there were opportunities for making multi-track recordings from the two hydrophone arrays which were used to investigate how one could use simple array geometry to calculate the location of sperm whales. To assist with precise alignment array it was necessary to incorporate a sound source in one of the arrays. Additional responsibilities included some recordings of a drill rig by deploying two single hydrophones from *Rigid Hulled Inflatable Boats (RHIB)* with a completely portable system.

1.5.1 Material and Methods

Two acoustic systems were implemented to record the sperm whale sound. A permanent acoustic monitoring station and an alternative portable system were developed by the Ocean Systems Laboratory (OSL). The acoustic monitoring station was established in a dry computer room. A team of four acoustic monitoring personnel (monitors) provided 24-hour coverage for all of the time that the ship was at sea and off the continental shelf.



Figure 1.10: Acoustic Monitoring Station

Each of the two computers was connected to an independent *towed hydrophone linear array* to generate stereo sound recordings. Each linear hydrophone array consisted of two acoustic elements (receivers) mounted about 3m apart and housed in a 10m-long reinforced polyurethane tube. These elements were connected to low-noise pre-amplifiers (30dB gain) which incorporated a 100Hz high-pass filter to remove low frequency water noise. In addition, a pressure sensor was placed in both tubes to measure the depth of the hydrophones below the surface with an accuracy of $\pm 0.05\text{m}$. The two tubes were filled with castor oil (Castrol R30) as this has acoustic properties similar to those of seawater. Each tube was connected to a cable extension of 390m. The stereo towed hydrophone arrays were built by Ecologic Ltd.



Figure 1.11: Stereo towed hydrophone array built by Ecologic Ltd.

The portable system was used at the RHIB to make recordings of sperm whales near drill rigs, and in temporal occasions was connected to the towed arrays from the acoustic monitoring station.

The portable system comprised a set of two hydrophones that were connected to a pre-amplifier box and then to a conditioning signal box where the signals were filtered and amplified to be digitised by a versatile high speed Data Acquisition Card (DAC) model AD136 and FreeVIEW maker with resolution of 12-bits at up to 625kHz. The system also used a personal computer and FreeView software for the processing and analysis of all captured data (Figure 1.12). A post analysis of the sperm whale recordings was done using Cool Editor Pro software (Syntrillium, Inc.).



Figure 1.12: Portable Acoustic System

The portable system had the advantage of adding more channels to the DAC. Each channel was set with an independent sample rate of 44.1 kHz.

The detection process used Rainbow-Click as the main software and Ishmael as a monitoring screen in real time for the cetacean vocalisations. For further detailed discussion on PAM software, see chapter two, section 2.3. The localisation took place from the azimuth bearings given by Rainbow-Click. In order to eliminate the left-right ambiguity, a *Target Motion Analysis* method was used. Logger software with a *Global Positioning System (GPS)* and a geographic map integrated were also used together with the help of some visual observers. Basically, the cycle consisted of four main steps: detecting the whale call; establishing its location on the XY plane; tracking the whale; and waiting until the whale reached the surface for photo- ID, skin collection, satellite-tagging.

A linear array of two hydrophones was towed at each extreme of the stern. For the array deployment, there were two different scenarios which were applied either for only one linear array or two arrays at the time. The first one showed a linear hydrophone array being towed by the vessel. However, owing to hydrophone buoyancy and vessel speed, scenario A was represented as a semi-horizontal line (Figure 1.13a). Scenario B corresponded to a static vessel with the towed linear array in vertical position (Figure 1.13b).

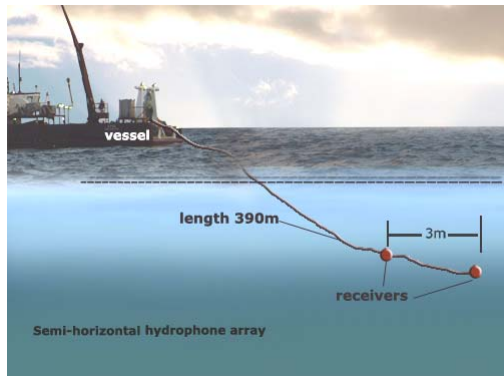


Figure 1.13a: Scenario A.
Semi-horizontal Array.

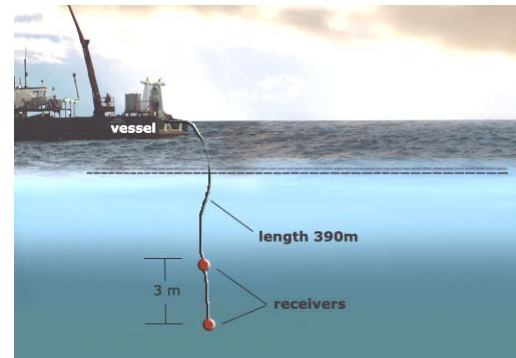


Figure 1.13b: Scenario B.
Vertical Array.

To investigate the effects of different array geometries on the final source localisation, several experiments were attempted. During the evenings, usually after recovering the RHIB's and before trawling, there were some occasions when the port side and starboard linear arrays were deployed at the same time, performing recordings of up to 4 channels simultaneously, as shown in Figure 1.14. The aperture of both linear arrays was increased according to scenarios A and B. There were also times when the length of the starboard array was changed.

On particular occasions, one of the two hydrophones located at the port side was used as a pinger to establish the distance separation within both linear arrays. The Time-Difference-Of-Arrival (TDOA) of the signal received by the other hydrophone (starboard) was measured and multiplied by the average sound speed (1500m/s) (Figure 1.15).

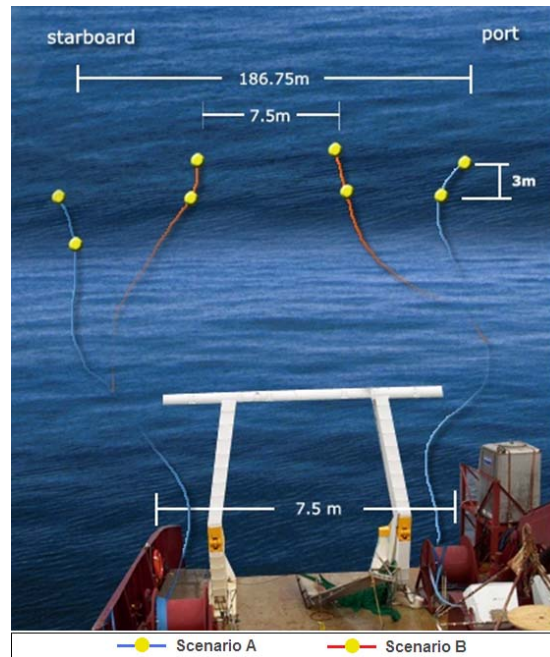


Figure 1.14: Towed hydrophone array deployment at the stern of the vessel. Scenario A is presented in blue and scenario B in red. Only one hydrophone of the port side was used as a pinger.

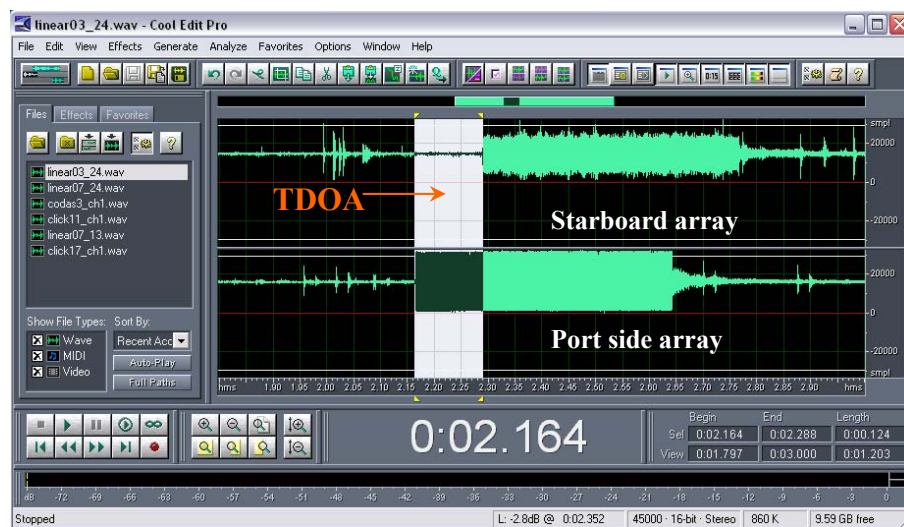


Figure 1.15: TDOA computation. The port side array generates a pinger recording which is received by the starboard array with a delay time or TDOA (*computed by Cool Editor Pro software*).

1.5.2 Results

Although not all the data were useful, a few relevant data gathered during the cruise offered the following results. A group of several TDOA pinger recordings gave an estimate of the variability found when the vessel was moving at a certain speed. For instance, when the two linear arrays were at different depths (54m and 28m) and the vessel speed was 3.8 knots (1.9m/s) it was found that for scenario A (semi-horizontal), the arrays had a distance separation of 187m average with a standard deviation of ± 1.5 m. On the other hand, for scenario B (vertical-array), the linear arrays kept a distance separation of 7.5m.

1.5.3 Discussion

The uncertainty of using one pinger lay on the unknown xy -position for each receiver of the starboard linear array. If two pingers were used instead of one on the port linear array, the Cartesian coordinates of the hydrophones on the starboard linear array could be known. By doing so, two TDOAs would be measured and two circumferences would be generated. They would intersect at two points, pointing to two possible solutions but resulting in the obvious solution correspondent to the starboard side, as shown in Figure 1.16.

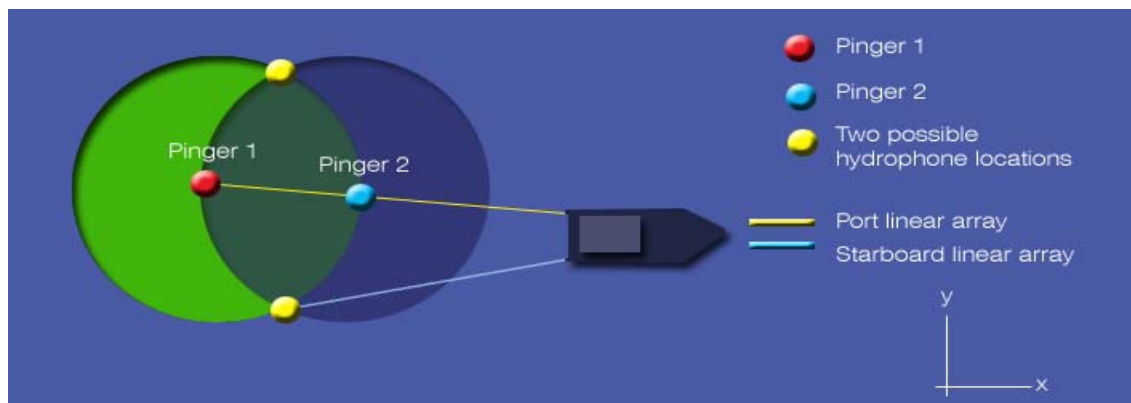


Figure 1.16: Circle intersection by using two pingers. The use of two pingers along the port linear array would help to obtain the Cartesian coordinates of one of the receivers (circles in yellow).

The xy position of each receiver could be known computing the following formulas based on the intersection of two circles (Figure 1.17).

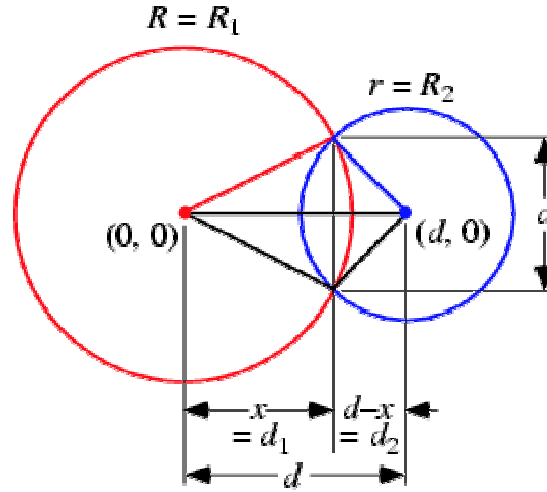


Figure 1.17: Geometry of the Circle intersection [170]

The equations for the two circles are:

$$x^2 + y^2 = R^2 \quad (1.1)$$

$$(x - d)^2 + y^2 = r^2 \quad (1.2)$$

where d is the separation distance between the pingers, R is the radius of the red circle with the first pinger in the centre at the origin coordinates $(0, 0)$ and r the radius of the blue circle with a second pinger at the centre $(d, 0)$.

The equation for the entire intersection cord length is

$$a = 2y \quad (1.3)$$

Solving for y from equation (1.1)

$$y^2 = R^2 - x^2 \quad (1.4)$$

Substituting (1.4) in (1.2)

$$(x - d)^2 + (R^2 - x^2) = r^2 \quad (1.5)$$

Solving for x results in (1.5)

$$x = \frac{d^2 - r^2 + R^2}{2d} \quad (1.6)$$

Substituting (1.6) in (1.4) and solving for y

$$y = \frac{\sqrt{4d^2 R^2 - (d^2 - r^2 + R^2)^2}}{2d} \quad (1.7)$$

Substituting (1.7) in (1.3)

$$a = \frac{1}{d} \sqrt{(-d + r - R)(-d - r + R)(-d + r + R)(d + r + R)} \quad (1.8)$$

Therefore the two solutions for the relative position of the receiver are given by the Cartesian coordinates $\left(x, \frac{a}{2}\right)$ or $\left(x, -\frac{a}{2}\right)$.

The pinger experiment highlighted the importance of the use of at least two pingers to continue monitoring the relative position of each receiver in the linear arrays.

The general problem faced in this cruise consisted on the lack of accuracy in obtaining some important variables needed for the computation of the source location. Without an accurate knowledge of the receiver position, the hydrophone array configuration became uncertain, complicating the source localisation problem. The valuable information gathered on this cruise highlights the CTD (Conductivity Temperature Density sensor) measurements which contain the different sound speed profiles for several locations of the Gulf of Mexico, and which were used in the simulations that will be described in chapter five.

1.6 Problem and Motivation

The overall scope of study addressed by this thesis is to assess the performance of typical hydrophone array-configurations in source range estimation. The experience obtained on PAM trials in the Gulf of Mexico had considerable relevance to the author's work. Contrary to the normal sequence of activities in a research project, the first-year fieldwork set up the scenario for the studies presented in this thesis. It helped

to establish the ideas relating to the passive acoustic localisation algorithms and assisted in the understanding of the necessary variables in posterior experiments. Although small details in the experimental plan seemed not to have so much relevance at the time, the experience of witnessing the PAM techniques used to locate and track whales was very helpful. Attending the trials greatly helped in the author's understanding of the kinds of problems biology and acoustic researchers face in the field.

Currently, there is a limited number of automated passive acoustic systems for detection, recognition and localisation of cetaceans, and these are to be found mostly in the military sphere [68, 106]. PAM is reliant on continuous acoustic activity (vocalisations) from the source. Therefore, precise and accurate information from the source location becomes essential if tracking the source is required. Most of the cetacean vocalisations are recorded by using a simple linear hydrophone array that can contain two or more receivers. Although it is possible to achieve ambiguous computations of the source range estimation in two-dimensions, it is not adequate when marine mammal studies demand a three-dimensional source range and when there is still a lack of knowledge on PAM capabilities within the scientific marine community. Today it is very common to hear questions such as:

- What source localisation method has the best accuracy?
- How many hydrophones (receivers) should an array have?
- What array-geometry is the most appropriate?
- What aperture-array is the most accurate/appropriate for a particular task?
- What is the maximum range for source estimation?
- What is the difference of source range estimation when the receivers are affected by array-motion?
- How are the source range estimations affected by sound speed variations?
- Does a sound propagation model give more accurate results?

The importance of such questions is of great relevance in the interest of cetacean monitoring for the abundance, distribution and behavioural studies of endangered species. On the other hand, mitigation measures for a safety zone demand that accurate source locations be met. The main motivation for this thesis therefore comes from

investigating the significance of the hydrophone array-configuration and of the underwater sound channel for a geometric hyperbolic localisation algorithm.

1.7 Main Contribution

Since the array configuration constitutes the major factor controlling performance under the control of scientists, a major contribution of this thesis relies on a set of guidelines on the *design and deployment of a hydrophone array-configuration* for sperm whale range estimation and its correspondence with mitigation measures for a safety zone. Among the most important issues to consider are the number of receivers, the array geometry and the array aperture.

To investigate the accuracy of several array-configurations, the development and application of a simulator was indispensable. One of the great assumptions of the research community on the typical localisation algorithms (e.g. hyperbolic technique) is the presence of a homogeneous medium where the sound speed is constant and there is no transmission loss. Then, the integration of a *sound propagation model* into the software simulator resulted in a medium for resolving such assumptions.

1.8 Thesis Description

This thesis uses the Time Difference of Arrival (TDOA) of sperm whale clicks to investigate the significance of various *hydrophone array-configurations* in source range estimation for a particular *three-dimensional hyperbolic localisation algorithm*. It also studies their relationship with the propagation of the underwater sound and of the mitigation measures for a safety zone. It focuses on the sperm whale (*Physeter macrocephalus*) because of its extensive acoustic modality and high source level, which facilitates acoustic monitoring.

1.8.1 Thesis Organization

The first chapter examines the high concern relating to marine mammal life. It introduces the concept of PAM on cetacean localisation. It also includes a summary of the fieldwork in the Gulf of Mexico.

Chapter two reviews the different underwater acoustic localisation methods and shows why the author decided to focus on hyperbolic localisation techniques. It also discusses the general assumptions of this thesis.

Chapter three introduces the mathematical models of the sound propagation channel. It describes in detail the three-dimensional geometric hyperbolic localisation algorithm. The source localisation algorithm is based on the intersection of virtual hyperboloids projected by the difference of time received on the hydrophone-array, and is better known in the acoustic community as the hyperbolic technique.

Chapter four examines different array configurations assuming a homogeneous medium. Although many other array-configurations were attempted, the main array-configurations investigated in this thesis were the Square, Shifted-pair and Y-shape arrays.

Chapter five uses the integration of the simulator and a sound propagation model to include the effects associated with a non-homogeneous medium. The array configurations are tested simulating a synthetic source diving profile.

The last chapter discusses the findings; these include a compilation of practical recommendations on the design and deployment of a hydrophone array-configuration. It finishes with suggestions for further research to give continuity to the current work.

The thesis also has three appendixes. Appendix A defines the basic underwater acoustic principles used in this thesis. Appendix B shows an algebraic solution of the source location problem. Appendix C describes the Matlab GUI simulator and the acoustic propagation model used.

Chapter 2

PAM Localisation

For many years the use of Passive Acoustic Monitoring (PAM) multidisciplinary scientific research has undertaken studies on the biology, behaviour, conservation, and ecology of a variety of cetaceans. With the fast development of electronic and computer technology, the setting up of PAM systems is becoming increasingly available and spreading rapidly.

This chapter presents the most relevant work of PAM cetacean localisation techniques since its early beginnings. It also discusses the advantages and disadvantages of the different approaches, and concludes with the reasons for the author choosing hyperbolic localisation as the main technique to focus on this thesis.

2.1 Passive SONAR

Most acoustic localisation techniques are based on SONAR (SOund NAvigation and Ranging), and for the same reason can be categorised into two main types, namely *active* and *passive*. Passive sonar systems are not restricted to water applications only. Nowadays, passive systems are being used in related fields of acoustics. Some of the applications are:

- Target Motion Parameter estimation [84].
- Localisation and characterisation of knocks and taps on a glass window [110].
- Effective Measurement of pipes diameter containing flowing fluids [29].
- Measurement of gravel sediment transport in very shallow water [90].
- Creation of tangible computer interfaces [111].
- Bird sound locations, by using a tomography technique [130, 132, 133].

To comply with those applications, passive acoustic systems require a basic knowledge of the Time Difference Of Arrival (TDOA) and the sound speed in the medium.

The problem of source location from TDOA measurements occurs in a range of applications from wireless communication networks to electronic warfare positioning. For example, in wireless communication, the TDOA is applied in signals with a noisy channel of a popular method of signal modulation for mobile telephony, namely GSM [89]. Electronic Warfare Communication Systems use two intercept receivers to eavesdrop on the transmitted signal with no knowledge of waveforms or position [35]. Other applications are indoor positioning [13] and the implementation of tangible acoustic interfaces for computer-human interaction in the field of air passive acoustics [178]. However, the problem of source location from TDOA measurements is not restricted to the water only. Underwater applications have also made an important contribution to cetacean localisation.

The history shows that the use of *Time Difference Of Arrival (TDOA)* has enabled researchers to compute mathematical algorithms for locating underwater active sources. For instance, when sound is received by two hydrophones-elements at different arrival times, the TDOA is the most accessible information from the source location (Figure 2.1).

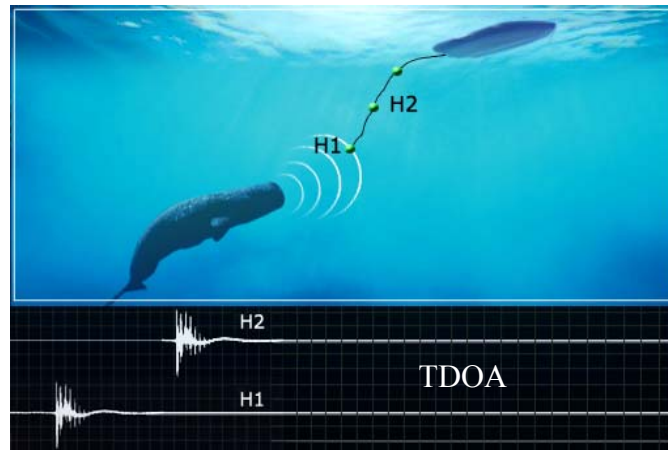


Figure 2.1: TDOA scenario. A towed hydrophone array that uses the *Time Difference Of Arrival (TDOA)* of a vocalising source to determine its location.

Correlation analysis of a transmitted signal to two receivers is used to compute a TDOA variable. With more than two receivers, more complex array geometries can be deployed and an improvement on the source localisation accuracy can be accomplished.

2.1.1 Brief History

An understanding of passive underwater acoustics began with Leonardo da Vinci and his underwater listening tube [16, 86]. Then Lord Rayleigh [118] made significant contributions to the field of acoustics. He concluded that if direction can be estimated by using the phase difference caused by the separation of our ears, then the sensitivity should be improved by increasing the separation between the primary sensors. This observation gave rise to the development of binaural listening devices for determining bearing (Figure 2.2). A typical aircraft listening device consisted of a pair of large acoustic horns, each connected to one of the operator's ears by means of a tube and stethoscope earpiece. By rotating the pair of horns until the sound seemed equal in both ears, the operator determined bearing [16].

An early successful passive detection and localisation system was the American SC [16]. This device was a direct descendant of Da Vinci's original listening tube. Instead of placing one tube in the water, two tubes were used, with their sensitive bulbs separated by approximately 5 ft. The bulbs were connected to the ears by air tubes that terminated in stethoscope-type earpieces. Later, a natural extension of the SC listening device was the MB Tube, with six rubber bulbs on each side of a rotational tube [16]. This improved the sensitivity and the angular resolution of the SC device. These devices were deployed external to the ship's hull and generally could only be used at low speed. To avoid this problem, the MV Tube consisted of a flush-mounted array of bulbs on the hull [16]. The acoustic shielding provided by the ship's hull permitted resolution of the left-right ambiguity normally associated with a single-line array. It reached ranges of 1,800 metres while travelling at 20 knots [16].

However, the most successful of the towed systems was the U-3 Tube, developed in 1918 [16]. Twelve equally spaced hydrophones were housed in a flexible rubber tube 12 metres long. This line array of hydrophones was called an "eel". The U-3 Tube system consisted of two eels towed approximately 90 to 150 metres behind the ship, with about 3.5 metres of separation between the horizontal arrays. The electrical signals were brought onboard by means of a multi conductor cable, and compensated for different signal arrival angles by means of an electrical compensator [16].

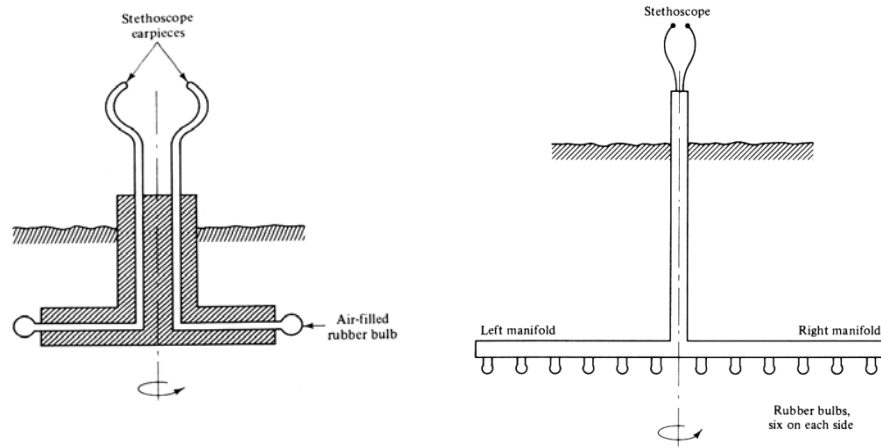


Figure 2.2: SC (left) and MB (right) Tubes Devices [16]

Passive systems such as the SC, MV, and U-3 Tube systems had reasonable success in detecting submerged sources. Nevertheless, their performance in terms of localisation accuracy was not sufficient.

2.1.2 Array-configurations

The earliest recorded use of PAM using a hydrophone array for cetacean monitoring was in 1963 when Walker [159] used three hydrophones to track sources of 20-Hz pulses. By 1964, Cummings *et al.* [26] used three hydrophones at the corners of an equilateral triangle to determine the locations and source levels of sounds from fish and invertebrates. In 1972, Watkins and Schevill [164] arranged an experiment with a four-hydrophone array to give a three-dimensional position for sources (Figure 2.3).

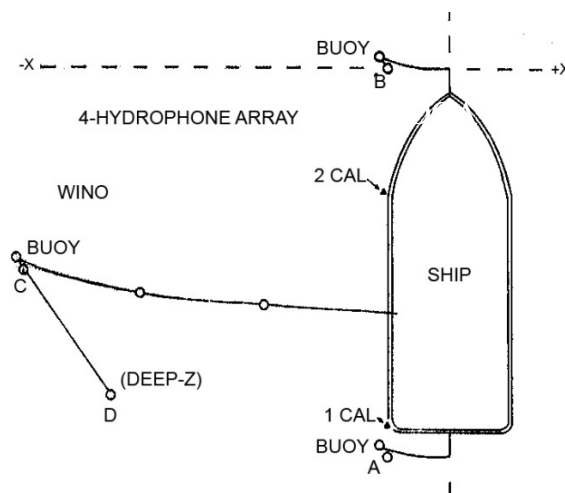


Figure 2.3: Watkins and Schevill 4-hydrophone-array [164]

Many applications made use of measurements of source direction in combination with visual information to locate sources. For example, in 1978, Winn and Winn [176] used a ship mounted passive SONAR array to determine the direction of singing humpback whales so that they could be approached and then located visually. Since the 1980s, combined PAM methods with the traditional visual census technique described in section 1.3.1 have also been used. However, for most of the surveys, PAM methods have relied on *array-configurations* of hydrophones.

In 1980, Clark [19] described a compact three hydrophone system and associated processing, which provided a real time estimate of source direction to identify sources in a study of right whale behaviour. In 1985 and 1987, Cummings and Holliday [23, 24] located and tracked bowhead whales using a nearly linear array of three widely spaced sonobuoys. In 1993, Freitag and Tyack [39] used up to six hydrophones to track dolphins over short ranges. Since then, more elaborate methods have been used to locate and track whales [20, 25, 138].

By 1998, Cato [17] had described three relatively simple methods of estimating source levels of marine animal sounds by estimating the source distance acoustically, using one or two hydrophones (Figure 2.4). The first method uses time lags and levels of the signals received at two hydrophones from one source. If the positions of the two hydrophones are known, the source position can also be estimated with the left-right ambiguity. The second method does not determine the position of the source, other than that it lies on the surface of a sphere defined by a circle. It used the difference in received levels only and required the hydrophone spacing to be known. The third method takes into account that if the direct and surface reflected arrivals are known, the source level can be determined with a single hydrophone and the refraction of a virtual one. Although that simplifies the hydrophone array-configuration, the source position on a circle ambiguity remains.

Back in 2000, Janik *et al.* [56] presented the localisation accuracy of a three-element hydrophone array with a triangular geometry to study different aspects of cetacean vocal behaviour. Mohl *et al.* [100] explored three different array-configurations (linear, triangular and an overdetermined array). They broke with the traditional cabled array system, and instead they used moving platforms equipped with radio links and Global Positioning System (GPS). That led to the advantage of the range being restricted only

by the signal-to-noise ratio (SNR) of the sounds and not by the array itself. However, each of the platforms presented logistics problems, and the system was considered inadequate for use in real-time tracking.

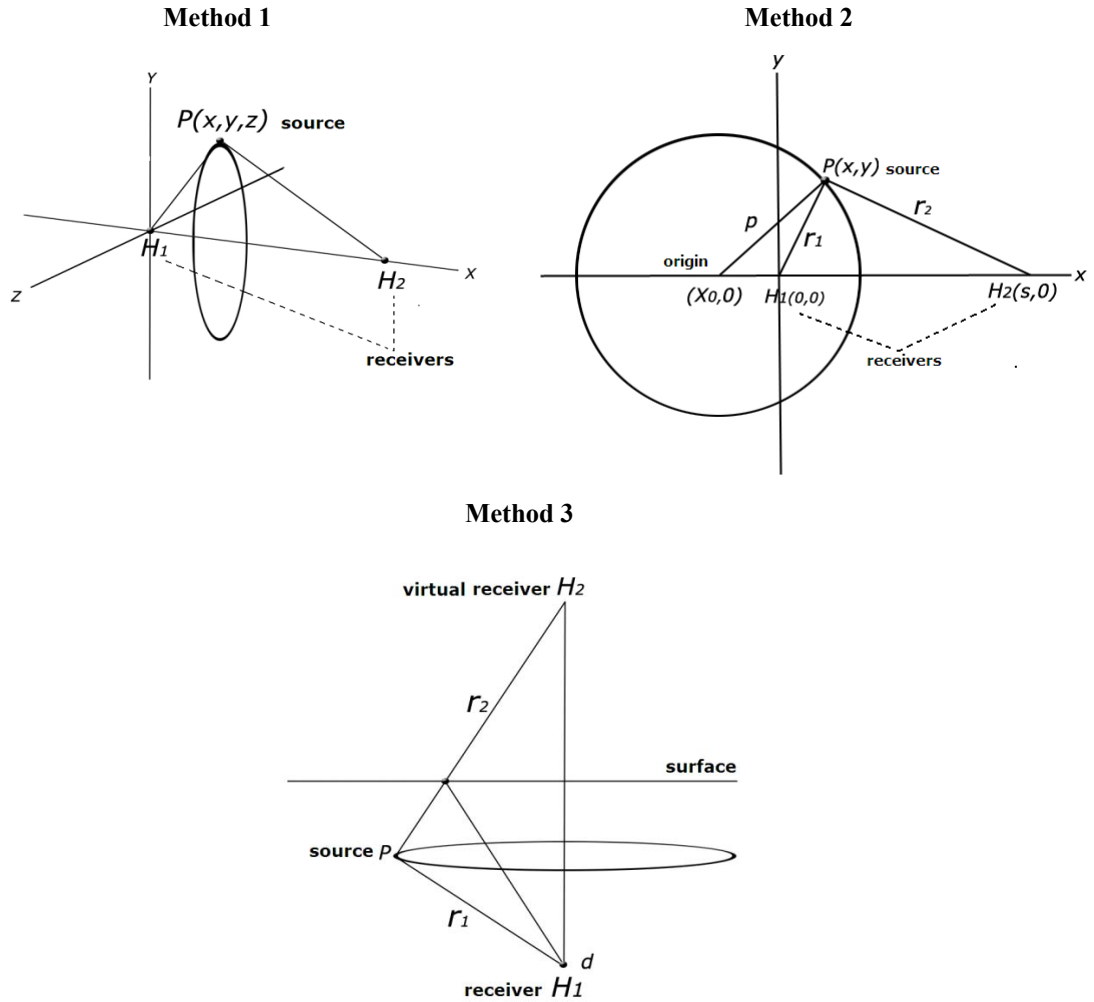


Figure 2.4: Three relatively simple methods of estimating source levels of marine animals by using one or two hydrophones described by Cato [17].

In 2001, Wahlbergh *et al.* [158] published an array-configuration that consisted of three-free-floating or moving platforms, each equipped with a hydrophone at a depth of 30 metres, and two additional hydrophones lowered from one of the platforms to depths of 100 and 460 metres, as shown in Figure 2.5.

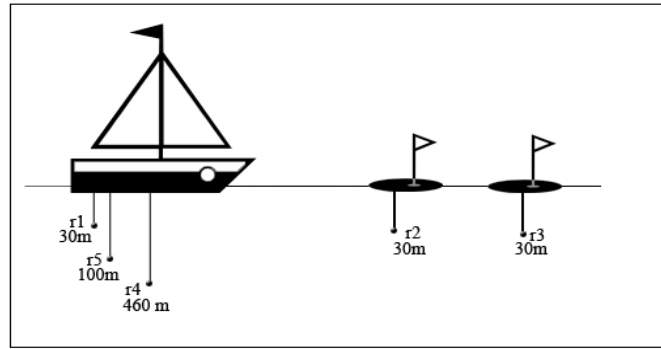


Figure 2.5: Simple diagram of a hydrophone array-configuration used by Wahlbergh *et al.* [158]. Three free-floating platforms were each equipped with a hydrophone at 30m depth (r_1 , r_2 , r_3) and two additional hydrophones were lowered at 100 and 460 m (r_4 , r_5).

In 2004, Simard *et al.* [124] published the use of a square configuration and an arc shape named a U-configuration. In the same year, Simons *et al.* [126] presented an array of five hydrophones forming a square (14 by 14km) with one hydrophone in the centre. Laplanche *et al.* [79] used a virtual large vertical four hydrophone array, whereby the direct-path source signal is received by one real hydrophone, and its three delayed echoes are interpreted as different signals received by three virtual hydrophones creating a large vertical array. Recently, more geometry arrays have been explored. In 2006, Giraudet *et al.* [45] and White *et al.* [171] used an array of five widely-spaced bottom-mounted hydrophones. Also in 2006, Morrissey *et al.* [106] divided an array into hexagon-shaped hydrophone sub-arrays.

In 2007, Dobbins [30] published a method using acoustically small sensors for passive azimuth localisation. The system is based on a linear vertical array of eight hydrophones suspended from a single buoy. It also has a horizontal array at the top of three hydrophones (“triplet”) equally spaced around a circle. Such array design helps to overcome the left/right ambiguity of azimuth localisation. It also helps to detect vocalisations to a range greater than is possible using a single hydrophone.

In summary, the literature reviewed highlights the following points:

- Most researchers use an array-configuration of *three* receivers. Only a few decide to use more than five receivers.
- *Linear*, *Triangle*, and *Square* are among the most popular array geometries used. Others prefer to use a random scattered geometry.

- *Towed-arrays* and *Floating-platforms* (e.g. sonobuoys) are among the most common array deployments.
- The aperture-array varies from a *few* metres to *hundreds* of metres.

As can be seen, many array-configurations have been used, and although most researchers provide detailed description related to the array-configuration used in their experiments, they rarely explain why that particular array-configuration was chosen.

2.1.3 Hyperbolic Technique

The hyperbolic technique is based on the intersections of different hyperbolas that are computed by assuming a constant sound speed, and use a TDOA for each pair of hydrophones in the array.

In 1972, Watkins and Schevill [164] were the first to publish a source localisation technique by means of TDOA measurement and computing calculation of the geometric hyperboloid solutions in a three-dimensional plane. The receiver position relative to each other was calculated from the arrival times of two sound pulses put into the water. A system of matching signal traces on a delayed second-sweep oscilloscope was used to measure the time difference between the two sweeps. The same methodology was followed with subsequent signals from the other hydrophones. Once they computed the TDOA for each pair of hydrophones, it was used as the main variable in the hyperbolic method. Finally, the position of the sound source was indicated with reference to the XYZ coordinate system.

It is worth noting that by that time Watkins and Schevill recognized that their method was limited by certain number of factors such as suitability of the source vocalising, sound recordings, size of the array, and measurement errors. They recommended that sounds must begin abruptly or have some sharply defined component, they must be relatively isolated in time or frequency from sounds, and they must have sufficient intensity above background noise to be measured. They also recommended the use of a very “large spatial array” to create large times for good resolution (usually limited to a tolerance error of 0.05 to 0.1 msec) of the calculated position.

In 1990, Spiesberger and Fristrup [130] revised the hyperbolic method proposed by Watkins and Schevill [164]. Their work was based on animal localisation, ignoring environmental fluctuations and receiver-position errors, and assuming that the speed of sound was constant. From this revision, several conclusions were obtained. The equipment required to implement the method was readily available. The costs of multiple-channel recordings were modest. According to Spiesberger and Fristrup [130], the localisations of calling animals were significantly improved when the changes of the underwater acoustic environment and the receiver-position uncertainties were modelled rather than ignored.

Janik *et al.* [56] published a 2D hyperbolic localisation algorithm that calculates the form of the hyperbola for each time delay. It was found that sometimes the hyperbolas' intersection formed a triangle rather than one point, so a localisation error was present. By early 2001, an algebraic solution [134, 158] for the source location problem was published (see Appendix B.2). This was a synthesis between the methods used by Watkins and Schevill [164] and those used by Spiesberger and Fristrup [130]. The algebraic solution uses a system of identical sets of equations, and it has the advantage of giving the same mathematical form for the two- and three-dimensional array systems. The inconvenience of using an algebraic solution lies in the fact that it requires at least five receivers for a three-dimensional geometry to avoid any ambiguous solutions for the source location [134]. These ambiguities are explained in chapter four under the section 'Number of receivers'. Wahlbergh *et al.* [158] concluded that the source localisation accuracy depends on the precision of the measurements of the TDOAs, sound speed, receiver positions and the array-geometry.

Simard *et al.* [124] used a 2D hyperbolic localisation algorithm made in Matlab, which rejected delays that were larger than the maximum travel time between hydrophone pairs. The *rms* error relative to the observed TDOAs is estimated, and the hyperbolic uncertainty is obtained by converting the time error into distance error by multiplying by the constant sound speed. Simard *et al.* stated that "precise estimation of TDOAs is critical for accurate localisation" [124]. They also agreed that hydrophone positions, sound speed and the array-geometry are variables that have a direct effect on the source localisation accuracy. More recently, in 2006, Morrissey *et al.* [106] used a sound speed profile in conjunction with 2D and 3D hyperbolic localisation algorithms

developed by Vincent [152] to compute the location of sperm whale species in real-time.

During recent decades, the algorithms and methodology for the hyperbolic acoustic localisation method have had slight variations [99]. Nevertheless, the main principles, based on the use of TDOA and a pair of hydrophones, still remain, with the only difference that they employ different techniques to estimate the TDOAs. The low cost (hardware and software), and basic assumptions as straight-paths from the source to the receivers, and a constant sound speed facilitate the use of such a technique.

2.1.4 Model-based Techniques

Unlike the hyperbolic technique, the model-based techniques assume the effects of a sound propagation model. Spiesberger and Wahlberg [131] introduced a new geometrical shape, called an isodiachron. It can be defined as the surface along which the locus of points has the same difference in travel time between two points in a non-homogeneous space. Unlike a hyperbola that extends to infinity, an isodiachron (Figure 2.6) is confined to a finite region of space when the sound speed differs between the animal and each of two receivers.

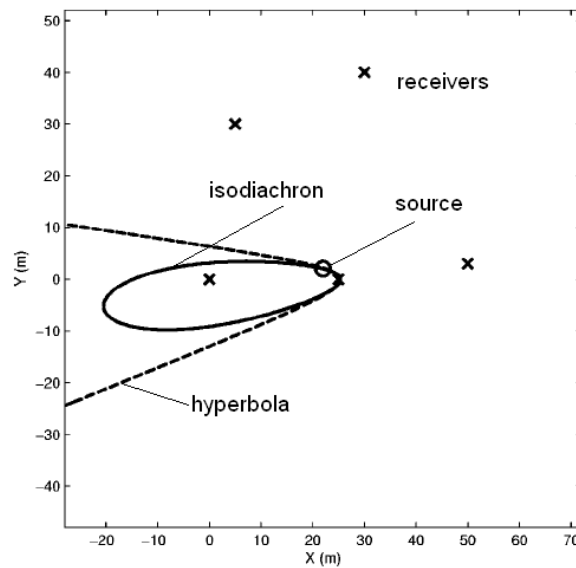


Figure 2.6: Isodiachron versus Hyperbola. Comparison of a source localisation scenario by a single *Isodiachron* and *hyperbola* geometrical shapes. Unlike a hyperbola that extends to infinity, an isodiachron is confined to a finite region of space [135].

The main problem with the isodiachron method is that it relies on the need of *prior* probability density functions to estimate a collection of valid sound speeds that coincide with valid receiver array configurations [131, 135, 136]. Differences in sound speed are significant, and researchers have had to adopt models for locations that allow the inclusion of them [152, 153, 154].

Tiemann and M. B. Porter [147] developed a model based on an acoustic propagation model to account for variations in sound speed and multipath effects when estimating travel time from hypothesized source positions. The model provides increased accuracy over indirect path scenarios, such as in shallow water environments or at long ranges. It uses a ray-tracing model Bellhop with Gaussian beam-spreading to include indirect paths in the location estimates (see chapter five). The model-based localisation algorithm consists of two main components: spectral pattern correlation to calculate time lags, and ambiguity surface construction to generate a location estimate. The model uses comparisons between predicted and measured time-lags for widely spaced receivers to build an ambiguity surface showing the most probable whale position in a horizontal plan view around the array. The output of the algorithm is a graphical display that easily conveys mammal location and confidence, being suitable for real-time implementation without user interaction. The only disadvantage of this method arises when modelling a range-dependent replica. Although it can improve localisation accuracy, it requires 100 times more computation time [147].

2.1.5 Signal-Frequency Techniques

Bearings from Directional-Frequency-Analysis and Recording (DIFAR) sensors have also been used by some researchers [51, 92] to determine 2D positions. DIFAR sonobuoys (Figure 2.7) have been used by the Navy for many decades, providing magnetic bearings to low frequency (less than 4 kHz) sound sources from a single sensor.

A DIFAR sensor makes use of particle motion in the sea water, caused by acoustic wave propagation, allowing for a compact sensor which indicates horizontal direction to each sound source present [92]. Thus, for the species which call below 200 Hz,

sonobuoys and fixed hydrophones have significant advantages over towed hydrophones, which suffer from flow noise and ship noise. Using DIFAR sensors also has the advantage of not depending on a constant sound speed approximation. Nevertheless, a disadvantage when compared with common hydrophones is that it requires three times the data bandwidth [92]. For instance, Wiggins *et al.* [174] used four DIFAR sonobuoys and hyperbolic localisation software in order to evaluate the normal-mode range estimate modelling. The method provides both source range and depth estimates from a single sensor.

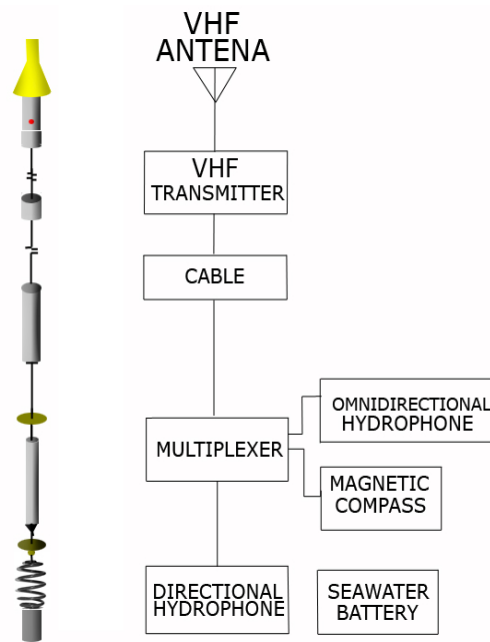


Figure 2.7: DIFAR Sonobuoy Diagram

Cetacean localisation, speed and direction of travel can also be determined through *Beamforming*. This method can be used to determine the azimuth direction of cetacean from the ship [179]. In the same way as the Fourier transform of time is frequency, the Fourier transform of space is wave-number. Beamforming is done in the wave-number domain where it can also be interpreted as a direction/bearing. The ability of a beamforming-array (Figure 2.8) to locate cetacean bearing will depend on the number of elements, distance between array and animal, and spacing of elements versus frequency of animal vocalisations.

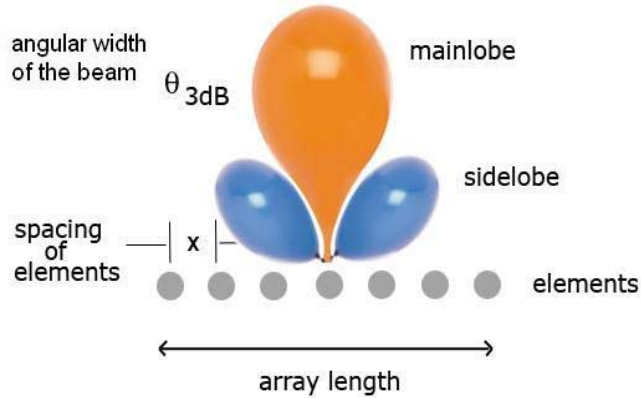


Figure 2.8: Beamforming Schematic

According to Thode *et al.* [145] a major disadvantage of beamforming occurs when “the spacing between adjacent hydrophones exceeds half an acoustic wavelength at a given frequency, and the beamformer cannot distinguish between the true signal bearing (the mainlobe) and multiple false bearings”. For instance, “beamforming on a 10-kHz pure tone (15-cm wavelength) with hydrophones spaced 5 metres apart generates over 60 grating lobes, making mainlobe identification impossible” [145]. Although array spacing can be changed mechanically, the highest frequency of towed systems is generally limited by the cable, acquisition, processing and recording bandwidths of the overall system. On the other hand, the very low frequency range of some cetaceans also presents a problem for towed arrays, which are often contaminated with very high flow noise at such frequencies.

Other signal-frequency techniques are *Matched-Field Processing (MFP)* [143] and *Matched-Beam Processing (MBP)* [120]. To sample the entire water column, the ideal array-geometry for these methods is a vertical linear array. However, such techniques are applicable mainly to low frequency signals.

If high frequency components of the source are detected, the source range may be inferred by a different technique based on the *Sound Pressure Level* and its *Spectral Content* [120]. These techniques require the knowledge of the source spectrum and the propagation characteristics of the environment. Other ways to infer the source range may be by inspecting the degree of *Signal Distortion* over the propagation paths from the source to the receiver [120].

Vertical Direct Passive Ranging (VDPR) gives also the source range by using a vertical array. *Horizontal Direct Passive Ranging (HDPR)* and *Range-Focused Beamforming (RFB)* exploit the curvature of the arriving acoustic signals. They require wideband signals and high signal-to-noise ratio (SNR). For scenarios where there is more than one cetacean vocalising, some have opted to use them as active sources in a *Multistatic System*; nevertheless, this may present a challenge for the detection problem [120, 127].

2.1.6 Multipath Technique

Recently, more elaborate methods have been used. These have included other variables which in the past were ignored. That is the case of *multipath analysis*. For wideband signals, such as the “click” vocalisation from sperm whales, it is often possible to determine the range and depth of the animal by examining the multi-path structure of the complete signal [78, 79]. The various arrivals of one single sperm whale click correspond to the various paths of a signal that has been reflected by the surface and the bottom. The correspondent paths are: direct path, surface bounce, bottom bounce, surface-bottom bounce, bottom-surface bounce (Figure 2.9). Refraction is ignored, and the time differences between arrivals are associated with the geometry of those paths and the sound speed in water. It is assumed that the sound speed is constant with depth. The final source location is then achieved by a set of non-linear equations.

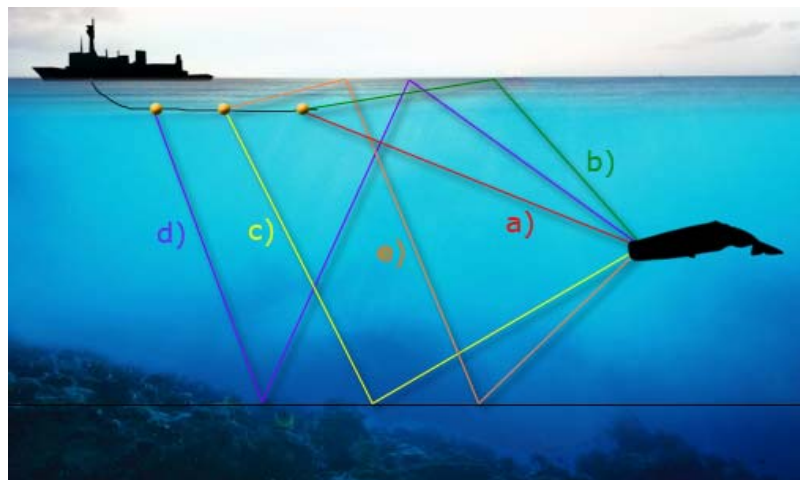


Figure 2.9: Different multipath sound reflections: a) direct path, b) surface bounce, c) bottom bounce, d) Surface-bottom bounce, e) bottom-surface bounce.

In 2002, Aaron Thode [144] developed a passive acoustic method for tracking sperm whale dive profiles. Multipath reflections of underwater biological sounds, such as surface-reflected or bottom-reflected paths, are used to reduce the number of physical hydrophones required to acquire a position. Two or three hydrophones deployed as either vertical or large-aperture (hydrophone separations on the order of 120m are assumed) towed array, can be used [141, 142]. The relative arrival times between the direct and surface reflected acoustic paths are used to obtain ranges and depths of the cetaceans with respect to the array, simplifying automation of the data processing.

The technique is most stable whenever the cetaceans “are directly ahead or behind the towing vessel, the hydrophones are relatively deep, and the animal range is less than a few hydrophone depths” [142]. The technique is least accurate whenever “the hydrophones are shallow and the cetacean is nearly equidistant from both hydrophones” [142]. Also, common situations such as a rough sea and multiple vocalising sources generally prevent this method from working well.

In multipath effects, surface-reflections are included as they have been observed, even when the ocean surface is agitated. However, bottom arrivals are not assumed because they are difficult to detect with automated software whenever they are present; they are also difficult to associate with a particular direct arrival whenever more than one animal is acoustically active.

2.1.7 Source-Motion Techniques

Target Motion Analysis (TMA) is used to determine the range of cetacean from the ship [27]. If the source is stationary and a ship moves over time by towing a horizontal line array, it would collect bearing estimates for the source location and the source would lie in the area intersected by the group of beams. The accuracy of this method is related to the width of the beams and the number of different bearing measurements. Linear arrays have a right/left ambiguity. This can be broken if the vessel performs a manoeuvre between the compared beams. For a non-stationary source, the problem becomes more complicated.

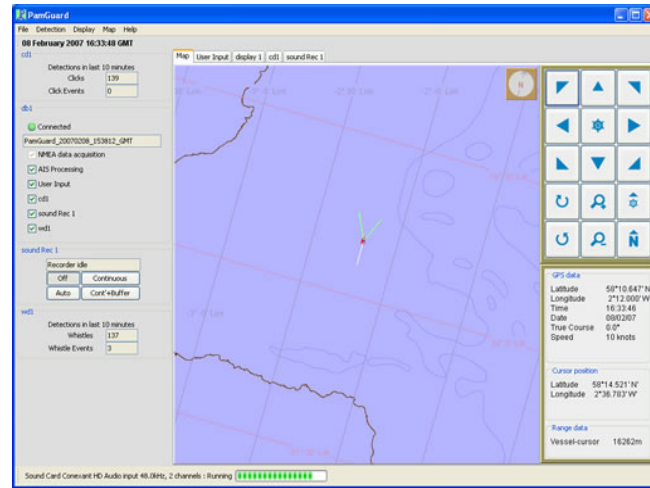


Figure 2.10: TMA visualisation of a vessel performing a manoeuvre between the two compared beams highlighted in green colour (Pamguard GUI screenshot [181]).

The limitations for this method are based on the fact that the contact with a specific cetacean must be maintained over the manoeuvre time, and also all contacts must be assumed to come from the same cetacean over the manoeuvre time. If the cetacean vocalise sporadically or stop vocalising, the method does not have a good performance [4].

GPS Localisation and tracking is a technique that helps to monitor the movement or migratory patterns of a wild animal remotely using GPS and optional environmental sensors or automated data-retrieval technologies, such as Argos satellite uplink, mobile data telephony and a range of analytical software tools. A GPS-enabled device will normally record and store location data at a pre-determined interval or on interrupt by an environmental sensor. These data may be stored pending recovery of the device, or relayed to a central data store or internet-connected computer using an embedded cellular (GPRS), radio, or satellite modem [9]. The animal's location can then be plotted against a map or chart in near real-time or, when analyzing the track later, using a software package.

While GPS localisation and tracking present the problem of high cost and logistical performance when attaching the device on the animals; it also can place additional constraints on size and weight, and may not allow for post-deployment recharging or replacement of batteries or correction of attachments.

2.2 Active SONAR

Unlike *passive* SONAR, which does not transmit any signal, *active* SONAR uses a sound transmitter and a receiver. In simple terms, active sonar is used to measure distance through water between two SONAR transducers or a combination of a hydrophone. In terms of active acoustic localisation systems, active SONAR is more comprehensive and might detect animals other than just those vocalising or on the surface.

The Navy [68] has developed a Surveillance Towed Array Sensor System (SURTASS) low Frequency Active (LFA) SONAR [10]. They use SURTASS LFA during routine training and testing as well as during military operations. The SONAR system operates in the low frequency band, between 100 and 500 Hz. It has both active and passive components. The active component of the system, LFA, is set with acoustic transmitting source elements suspended by cable from underneath a ship. These projectors produce the active SONAR signal or “ping”. A “ping” can last between 6 and 100 seconds. The time between transmissions is typically from 6 to 15 minutes. The SURTASS LFA SONAR signal is not a continuous tone, but rather a transmission of various waveforms that vary in frequency and duration. The duration of each continuous frequency sound transmission is never longer than 10 seconds. The signals are loud at the source, but levels diminish rapidly over the first kilometre. The passive component of the system is SURTASS. It detects returning echoes from submerged objects, such as threat submarines, through the use of TDOAs from hydrophones on a receiving array that is towed behind the ship. The SURTASS LFA ship maintains a minimum speed of 5.6 kph (3 knots) through the water to tow the horizontal line hydrophone array (Figure 2.11).

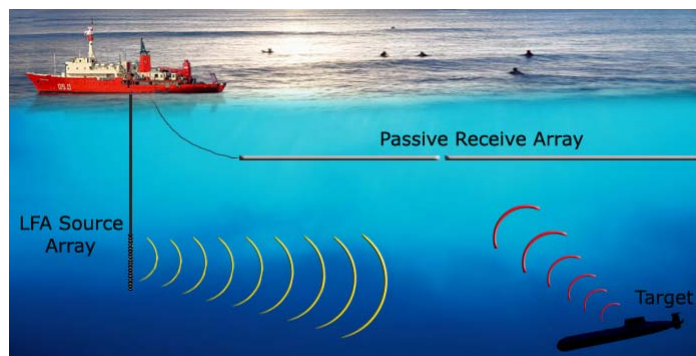


Figure 2.11: Typical scenario of a SURTASS LFA and passive array deployment.

SONAR systems are commercially available and may improve active monitoring. Nevertheless, we should not forget that, as with any active SONAR, adverse environmental effects are possible. Military sonars often produce intense sounds, with source levels above 210 dB re 1 μ Pa at 1m [108]. For instance, Miller *et al.* [97] found that humpback whales lengthened their songs during playbacks of SURTRASS LFA system as a medium to counter interference from sonar signals. Maximum RLs at the whales ranged between 130 and 150 dB re 1 Pa rms [108]. As discussed in chapter one, there is growing evidence of a possible link between military sonar exercises and strandings of cetaceans [36, 37, 38, 62, 63].

2.3 PAM Localisation Software

PAM software is already available in several formats. Some of them are openly available through the internet from some charity organizations like the International Fund for Animal Welfare (IFAW). There are also several commercial software packages manufactured by research institutes and private companies. Such is the case of CIBRA, University of Pavia, Italy and NAUTA research and consulting. For sperm whale localisation, a brief description of the most relevant PAM software is presented here.

ISHMAEL, written by David Mellinger [94] of Oregon State University (USA), is a program for acoustic analysis. It is a software package with a variety of acoustic detection and display functions. It contains a spectrogram viewer, three acoustic localisation methods, three methods for automatic call detection, real-time sound recording, a beamformer and a log file annotation feature. The most basic operation in Ishmael is viewing a spectrogram. A spectrogram shows time on one axis (in Ishmael, the horizontal axis) and frequency on the other axis.

Ishmael's capabilities are primarily aimed at processing large amounts of sound data quickly and relatively easily. The sound can be a collection of sound files, or a signal arriving in real time from one or more microphone(s) or hydrophone(s).

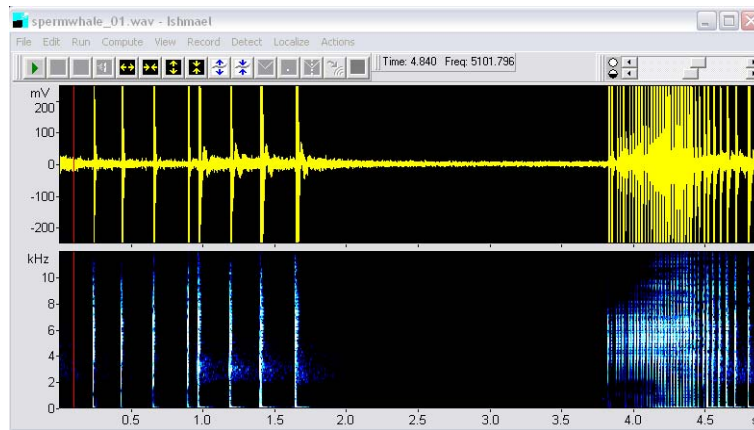


Figure 2.12: Ishmael's screen. Signal waveform and spectrogram

Ishmael can determine the location of a sound source in either one dimension (1D) or two dimensions (2D). For 1D, it calculates a bearing angle and requires at least two channels of sound (two simultaneously operating hydrophones). For 2D, it calculates an X-Y position and requires at least three channels. Ishmael can capture data across up to 32 channels. Ishmael is not particularly well-suited to sound exploration—taking an unknown sound and examining it in detail to find out and measure its characteristics. Its primary aim is to be used for real-time analysis of acoustic data sets.

RAINBOWCLICK, initially developed by D. Gillespie and R. Leaper [43], is a program designed for the detection and analysis of sounds made primarily by sperm whales. IFAW has made it freely available for marine conservation and protection projects. This program is designed to detect and analyse medium frequency (100 Hz – 22 kHz) clicks typically produced by sperm and pilot whales in real-time. The program receives data through an ADC board or a soundcard. The first stage in the analysis is to remove as much noise from the signal as possible. Much of this is low frequency (<1 kHz); e.g. engine noise and noise reduction is achieved by using any of a number of digital filtering functions written into the program. Putative clicks are identified from the background noise by applying detection trigger thresholds. These thresholds are adjusted dynamically in response to changes in the ambient noise level. Once the clicks have been identified, they are plotted against time.

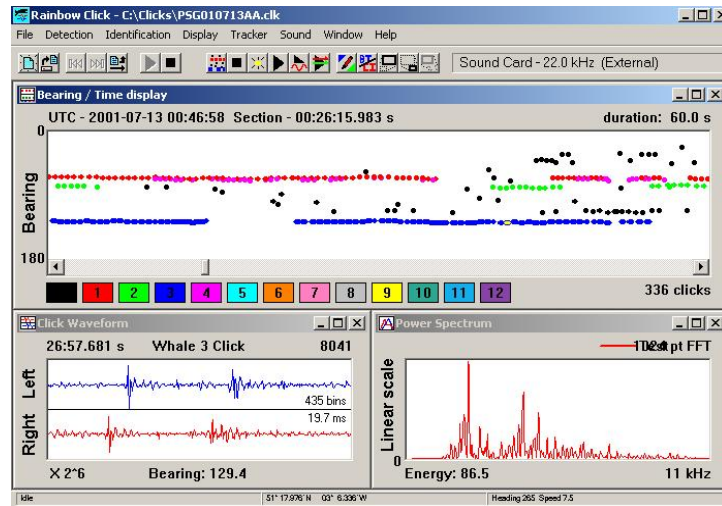


Figure 2.13: RainbowClick screen

If a two-element array is used, then the bearings to the clicks can be determined. This is achieved by measuring the TDOA of the signal at each of the hydrophone-elements. The program cross-correlates the click waveforms, and then a TDOA is calculated. By using this time difference and the distance between the elements, the bearing of the click relative to the hydrophone can be calculated [82].

RainbowClick is possibly the most popular PAM detection programs used by scientists and marine mammal observers. It is easy to install and it does not require very much experience. Its main problem is based on the use of a two-elements array which generates a left-right ambiguity on the source position. This is because the clicks in fact lie on a hemi-cone. Trains of clicks from a single cetacean will tend to move steadily astern as the animal is passed by the vessel. If the program receives position information from the National Marine Electronics Association (NMEA), a server program, then the track of the vessel can be plotted in a separate window. If bearings to clicks are plotted, then the approximate position of the whale is where these bearings intersect. The only range given is the one that the user can estimate from the current vessel position to the intersection point.

The NMEA server was written for collecting data from a GPS unit - or any NMEA device such as echo sounders, wind gauges, etc. The NMEA server program makes these data available to other programs running on the same computer.

PAMGUARD [181] is a recent open source development which provides a flexible, modular software framework with basic application functionality comparable to the existing PAM software (e.g. Ishmael, Rainbow Click). It was implemented in Java modules, is capable of working on multiple operating systems (e.g. Windows/Linux), and has the ability to incorporate new modules as they are developed to include additional detection, classification, localisation, and sound visualisation functionalities. Its versatile software/hardware interface enables flexibility in the configuration of underwater equipment (number of receivers, sensitivities, aperture and geometry).

2.4 Discussion and Summary

As shown in this chapter, the PAM cetacean localisation techniques used fall under the general headings of hyperbolic localisation, bearing triangulation, multipath and model-based approaches. There is no single PAM localisation methodology that can include the vast number of acoustic scenarios. These rely on particular events and specific assumptions rather than on the group of different source scenarios that can occur.

For instance, the direct path assumption is valid only in shallow environments. A multipath propagation model must be used for larger ranges than a few kilometres. The bearing triangulation and TMA techniques are strictly dependent on the manoeuvre of the vessel to track the different scenarios of the vocalising sources. One might take as an example the ability of some cetaceans to reach greater depths, diving in shallow waters or stopping vocalising at certain depths and on particular occasions. In addition, depending on the aims of the project and the physics of the environment, some of the PAM localisation methodologies need to be adapted in order to make a timely decision. For example, cetacean mitigation measures depend on the fast acquisition of accurate source locations within the exclusion zone.

Hyperbolic localisation continues to be the main technique used by many researchers because of its simplicity and strong dependence on three main variables TDOAs, receiver positions and sound speed of the medium. TDOAs are easily obtained by different cross-correlation methods, and by use of the great variety of PAM software

available. Receiver positions can be recorded by using GPS location sensors in each of the receivers. Sound speed is measured by deploying CTD sensors.

Another advantage of the hyperbolic technique is its adaptability into a broad range of scenarios. By using adequate detection and recognition methods, TDOA measurements may cover cetacean vocalisations of a wide frequency range from 10 Hz to 200 kHz, including calls that vary in nature from clicks to groans, buzzes, chirps and whistles. If a two-dimensional location is needed, the hyperbolic technique may be used in shallow and depth underwater scenarios.

One of the major disadvantages of the hyperbolic technique is the gross assumption of a constant sound speed. This includes the assumption of a straight-line sound propagation from the source to the receivers, where the ray refraction effects are neglected. However, in some scenarios such direct paths do not exist, leading to inaccurate locations. Even though those assumptions could be valid, and no TDOA measurements errors were included, the geometry of the hydrophone array is another important aspect affecting the accuracy of source range estimation.

Although the hyperbolic technique has helped to monitor the localisation performance of several surveys, little progress has been made on the significance of the hydrophone array-configurations on the accuracy of the source localisation problem. Although most researchers have used several array-configurations, they rarely explain the influence and effects of the array on source range estimation.

The latter is of great relevance when surveys (e.g. mitigation) demand meeting with accuracy specific source range locations. Unlike other external factors, such as the source, sea currents, ambient noise, etc., where the observer does not have control over them at all, the array-configuration constitutes a major and unique factor where the observer does have control. The attributes of the array-configuration are the number of receivers, array-geometry, and aperture-array.

According to the literature, the general scenario of array-configurations used by PAM cetacean researchers can be divided into three groups: towed-arrays, floating-platforms (e.g. sonobuoys) and fixed hydrophones (e.g. bottom-mounted sensors). Although deploying bottom-mounted sensors on the sea bed provide significant signal gain for

locating cetaceans in the vicinity, their fixed location limits their location range. Furthermore, in terms of logistical operations, they are restricted to working in environments to which only humans have access. The floating-platforms or towed-arrays have the characteristic of offering a major flexibility to variable scenarios which are in a sense, dictated by the animal position. A towed-array can be used either as a static or moving platform. For instance, with linear towed-arrays, a moving platform (e.g. vessel) becomes essential so the right/left ambiguity can be broken when using hyperbolic or TMA techniques. Nevertheless, moving platforms suffer from flow noise and ship noise. Static platforms avoid such a noise, a good thing for species calls below 200 Hz, and facilitate the logistic of the deployment of different array-geometries.

Since the study of the underwater scenario for cetacean localisation is complicated (see Appendix A.1), the author has considered making the following assumptions when using the hyperbolic technique in this thesis:

- No multipath effects (reverberation) are included. Multipath occurs more often in shallow scenarios, owing to the reflection between surface and seabed. This thesis will focus on deep scenarios, where the boundaries of the medium are dismissed.

Source and receivers are considered static. Doppler effects are ignored. The Doppler effect is a shift in acoustic frequency caused by the relative motion between source and receiver. Therefore, if the velocity of the source and observer are not significant, the emitted frequency can be assumed as equal to the received frequency [16, 105].

- Presence of only one single vocalising source in alignment with the receiver hydrophone array. In chapter four, straight-path rays between source and receiver are assumed. In chapter five, bending-paths rays are assumed instead, owing to the effects of the sound propagation channel.
- Omnidirectional response on each receiver of the array. A response that does not vary with the direction of the incident source signal [105].

- Precise knowledge of the receiver positions of the array. Chapters four and five discuss the effects of varying the receiver positions.

Performing experiments at sea in order to evaluate array performance - even for a small array of hydrophone elements - is a complex and costly business. In order to assess the performance of typical hydrophone array-configurations, a MATLAB-based array-simulator with a full 3D simulation environment was developed.

A simulator that uses a 3D hyperbolic localisation algorithm is even more representative because it provides directional and slant range information. The integration of a sound propagation model also offers an excellent opportunity to compare the results of a non-homogeneous medium with the common assumptions of the existence of a highly idealized homogeneous medium.

The main aim is to investigate the significance of the array configurations under the scheme of the hyperbolic localisation technique. A detailed description of the hyperbolic localisation algorithm of the simulator is given in the following chapter, by taking into account all the issues and assumptions previously discussed.

Chapter 3

Hyperbolic Localisation Algorithm

As reviewed in the previous chapter, in the hyperbolic localisation technique the TDOA constitutes the first link to estimate the source location. Assuming a highly idealized medium, this chapter explains how synthetic TDOA data are used in a geometric hyperbolic algorithm, developed by the author, to solve the localisation problem.

3.1 Underwater Modelling

To simplify things in this chapter and the following one, the hyperbolic localisation technique is considered under a highly idealized medium. However, a brief review of the principles of underwater modelling is presented in this section.

The theoretical basis underlying all mathematical models of acoustic propagation is the wave equation [33]. The wave equation is derived from the more fundamental equations of state, continuity and motion. Formulations of acoustic propagation models generally begin with the three-dimensional, time-dependent wave equation. Depending upon the governing assumptions and intended applications, the exact form of the wave equation can vary considerably. For most applications, a simplified linear, hyperbolic, second-order, time-dependent partial differential equation is used:

$$\nabla^2 \Phi = \frac{1}{c^2} \frac{\partial^2 \Phi}{\partial t^2} \quad (3.1)$$

where ∇^2 is the Laplacian operator $(\partial^2 / \partial x^2) + (\partial^2 / \partial y^2) + (\partial^2 / \partial z^2)$, Φ is the potential function, c is the speed of sound, t the time, and x, y, z are the spatial dimensions. Subsequent simplifications incorporate a harmonic solution in order to obtain the time-independent Helmholtz equation. Specifically, a harmonic solution is assumed for the potential function Φ

$$\Phi = \phi e^{-i\omega t} \quad (3.2)$$

where ϕ is the time-independent potential function and ω the source frequency ($2\pi f$). Then the wave equation reduces to

$$\nabla^2 \phi + k^2 \phi = 0 \quad (3.3)$$

where $k = \omega/c = 2\pi/\lambda$ is the wave number and λ the wavelength.

Various theoretical approaches are applicable to the Helmholtz equation. The approach used depends upon the specific geometrical assumptions made for the propagation and the type of solution chosen for assumptions made for ϕ .

Although acoustic propagation models can be classified according to the theoretical approach employed, the cross-connections that exist among the various approaches complicate a strict classification scheme. The literature [33] gives a generalized classification scheme that has been constructed using five categories corresponding to the five canonical solutions of the wave equation.

- Ray theory
- Normal mode
- Multipath expansion
- Fast field
- Parabolic equation techniques

Within these five categories, a further subdivision can be made according to range-independent and range-dependent types.

Range independence means that the model assumes a cylindrical symmetry for the environment (i.e. a horizontally stratified ocean in which properties vary only as a function of depth). However, if the range-independent ocean waveguide is represented by an increasing number of homogeneous layers, a numerical solution based on the field representation for homogeneous layers will converge toward the correct solution. The basic physics of deep-ocean waveguide propagation can be addressed by simpler methods owing to the fact that the spatial scales of the horizontal variability in most cases are much larger than the scales of the vertical variability. The layers must be less

than one quarter of a wavelength thick. Also, it is much more convenient to divide the deep ocean into a relatively few number of layers with depth-varying properties in a form that allows for an analytic solution to the wave equation within each layer [61].

Range dependence indicates that some properties of the ocean medium are allowed to vary as a function of range (r) and azimuth (θ) from the receiver, in addition to a depth (z) dependence. Real sound-speed profiles have depth dependence and consequently need to be represented by a combination of layering and variable sound speed within the layers. The ocean environment varies in all spatial coordinates as well as time. The complexity of the acoustic modelling depends on the nature of the spatial variability. Thus, since the deep ocean has variation in sound speed with depth and range, it cannot be represented by a homogeneous fluid layer.

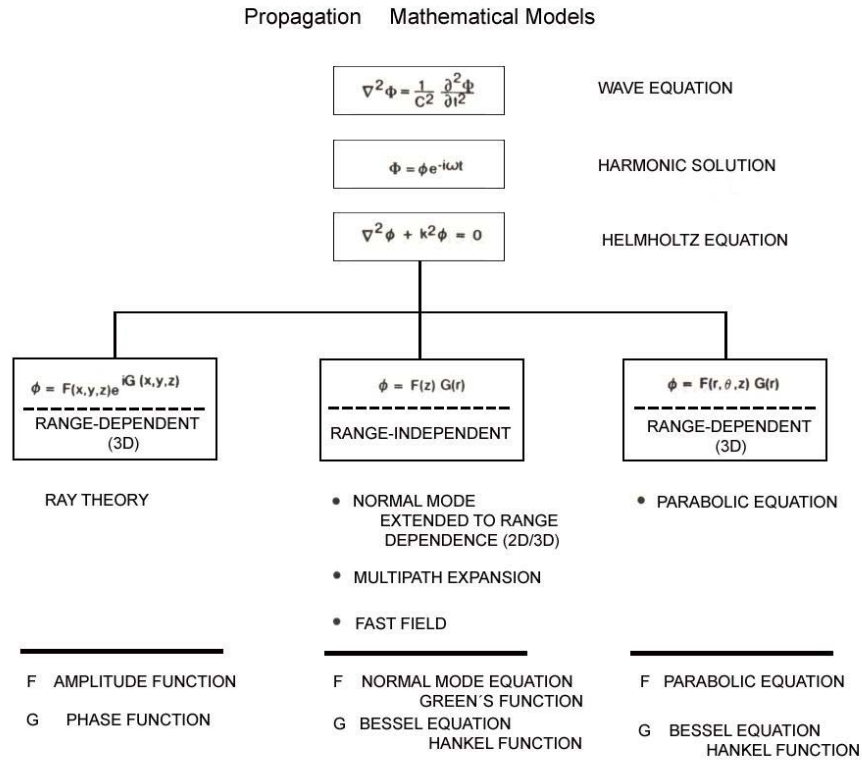


Figure 3.1: Summary of the theoretical approaches for propagation modelling.
(Published by [59] and adapted by [33])

The Acoustic Propagation Models are used extensively in the operational environment where speed is a critical factor and environmental uncertainty poses much more severe constraints on the attainable accuracy. The scheme of Figure 3.1 serves as a useful road

map to illustrate the relationships of the five approaches used to solve the wave equation.

The modelling of sound propagation in the ocean is complicated because the environment varies laterally – i.e. is range dependent - and all environmental effects on sound propagation are dependent on acoustic frequency in a rather complicated way. In sonar design and operation problems, the analyst is normally faced with a decision matrix involving water depth (deep versus shallow), frequency (high versus low) and range dependence (range-independent versus range-dependent ocean environments). A scheme of the five main modelling approaches is presented in Table 3.1.

MODEL TYPE	APPLICATIONS							
	SHALLOW WATER				DEEP WATER			
	Low Frequency		High Frequency		Low Frequency		High Frequency	
	RI	RD	RI	RD	RI	RD	RI	RD
Ray Theory	-	-	X	XX	X	X	XX	XX
Normal Mode	XX	X	XX	X	XX	X	X	-
Multipath Expansion	-	-	X	-	X	-	XX	-
Fast Field	XX	-	XX	-	XX	-	X	-
Parabolic Equation	X	XX	-	-	X	XX	X	X

Low frequency (< 500 Hz)

RI: Range-Independent Environment

High frequency (>500 Hz)

RD: Range-Dependent Environment

XX Modelling approach is both applicable (physically) and practical (computationally)

X Limitations in accuracy or in speed execution

- Neither applicable nor practical

Table 3.1: Domains of applicability of underwater acoustic propagation models.
(Published by [60] and adapted by [33])

Since this thesis focuses on sperm whale, the *Ray Theory* approach was chosen as being the most appropriate. The environment is characterized as the one with the greatest deep sea conditions, with a full range-dependence factor and source signals above the 500 Hz. Shallow water always presents a challenge for marine detection because of its multipath issues. Thus, shallow water is discarded in this thesis.

3.1.1 Ray Theory

Ray theory originally emerged from the study of optics, where it was used to understand the propagation of light even before the more fundamental equations for light propagation were known [47]. Ray theory starts with the Helmholtz equation. The solution for ϕ is assumed to be the product of a pressure amplitude function $\phi = A e^{ip}$. Substituting this solution into the Helmholtz equation (3.3) and separating real and imaginary terms yields

$$\frac{1}{A} \nabla^2 A - [\nabla P]^2 + k^2 = 0 \quad (3.4)$$

With the assumption that the fractional change in the sound speed gradient over a wavelength is small compared with the gradient $\frac{c}{\lambda}$, it follows that

$$\frac{1}{A} \nabla^2 A \ll k^2 \quad (3.5)$$

then under this approximation, equation (3.4) reduces to

$$[\nabla P]^2 = k^2 \quad (3.6)$$

as the eikonal equation. Surfaces of constant phase are the wavefronts, and the normals to these are rays. Eikonal refers to the acoustic path length as a function of the path end points. Such rays are referred to as eigenrays of the source and receiver positions [33].

Ray theory is useful in deep water, where a small number of rays transmit most of the acoustic energy from a source to a receiver, where there is a direct path from source to receiver, and where only a limited number of surface and bottom-reflected paths contribute. Hence, the important ray paths are either refracted-refracted or refracted-surface-reflected. Typical deep-water environments are found in all oceans at depths exceeding 2000 metres. A further simplification of ray tracing is achieved if the environment is horizontally stratified, in which case range and travel time can be calculated directly, using Snell's law. The initial step is to divide the sound speed

profile into layers of constant linear gradient, and develop an algorithm to follow, by means of Snell's law, the arcs of rays leaving the source at different angles. However, besides being unable to handle diffraction, the basic ray-tracing technique breaks down in the vicinity of focal points and caustics. To overcome these difficulties, a hierarchy of modifications has been introduced, allowing ray tracing to be extended to lower frequencies, accounting to some extent for caustics and diffraction. Variants of this technique have also been developed. [61].

3.1.2 Highly Idealized Medium

In the idealized homogeneous medium, where all properties of this medium are constant, the boundaries are sufficiently remote, such that they may be ignored. Reflection and refraction are not included. The sound speed is considered as constant (1500m/s). Any inaccuracies in TDOAs and receiver position measurements are also ignored. A common assumption is a high sound source directionality with straight-path rays between source and receivers. In a lossless homogeneous medium, the power density or intensity does not diminish with range. In simple terms, there is *no attenuation* for the source signal. Although that is appreciated as a gross simplification, chapter five will take into account the effects associated with sound propagation in a non-homogeneous medium.

3.2 Geometric Hyperbolic Surfaces

Since the hyperbolic localisation technique is based on the geometrical surface called a *hyperbola*, it is important to review the mathematical principles to get into a detailed study and achieve better understanding.

3.2.1 Hyperbola

A *hyperbola* is defined as a conic section, defined as the locus of a point that moves so that the numerical difference of its distances from two fixed points (called foci) is a

constant. The equation for a hyperbola with semi-major axis a parallel to the x-axis and semi-minor axis b parallel to the y-axis is given by

$$\frac{x^2}{a^2} - \frac{y^2}{b^2} = 1 \quad (3.7)$$

To understand Equation 3.7, consider Figure 3.2 which shows a hyperbola on a Cartesian plane XY . P represents any point along the hyperbola. F_1 and F_2 are the respectively foci of the hyperbola. The difference between the two vectors F_1P and F_2P is a constant K , which is also defined by $2a$. The half distance between the foci is given by c and the value of b is defined as $c^2 - a^2$. However, the most interesting of the hyperbola geometry is that, to trace all the different points that P can take, the only elements needed are F_1 , F_2 , and the constant K .

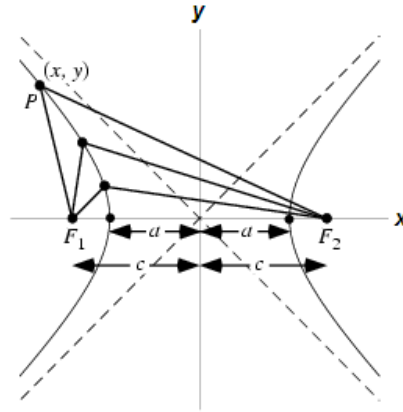


Figure 3.2: Hyperbola Geometry [15]

In the source localisation problem, the *source vocalising* (S_V) is the variable unknown P on the hyperbola geometry. Each of the foci points (F_1 F_2) represents a different *hydrophone receiver*. The difference of the arrival times of one same signal to the pair of hydrophones is the TDOA. By multiplying the TDOA by the *Sound Speed* in the medium, a constant K - better known as *range difference* - is obtained. Such information is necessary to trace its correspondent hyperbola. However, since in reality the environment is in three planes, it has been necessary to translate the problem into a three-dimensional (3D) surface for a more realistic scenario.

3.2.2 Hyperboloid

The correspondent geometric surface in 3D for the well known hyperbola is the *hyperboloid*. A hyperboloid is a quadratic surface which may be one or two sheets. The one-sheeted hyperboloid is a surface of revolution obtained by rotating a hyperbola about the perpendicular bisector to the line between the foci, while the two-sheeted hyperboloid is a surface of revolution obtained by rotating a hyperbola about the line joining the foci [53]. For underwater localisation purposes, the use of a two-sheeted hyperboloid is the most appropriate. If it is oriented along the z-axis, also called the depth-axis, the hyperboloid has the following Cartesian equation

$$\frac{x^2}{b^2} + \frac{y^2}{b^2} - \frac{z^2}{a^2} = -1 \quad (3.8)$$

By taking only one half of the two-sheets its 3D visualisation is shown as follows

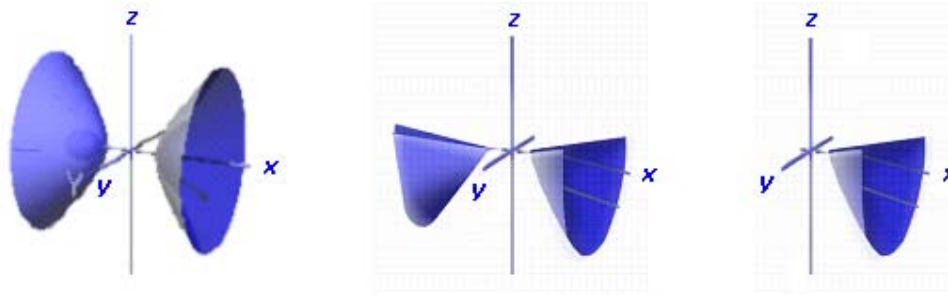


Figure 3.3: Hyperboloid of two sheets reduced to one half

Translating that into our underwater scenario, a towed hydrophone array of two elements would generate a *virtual hyperboloid*, such as the one illustrated in Figure 3.4.

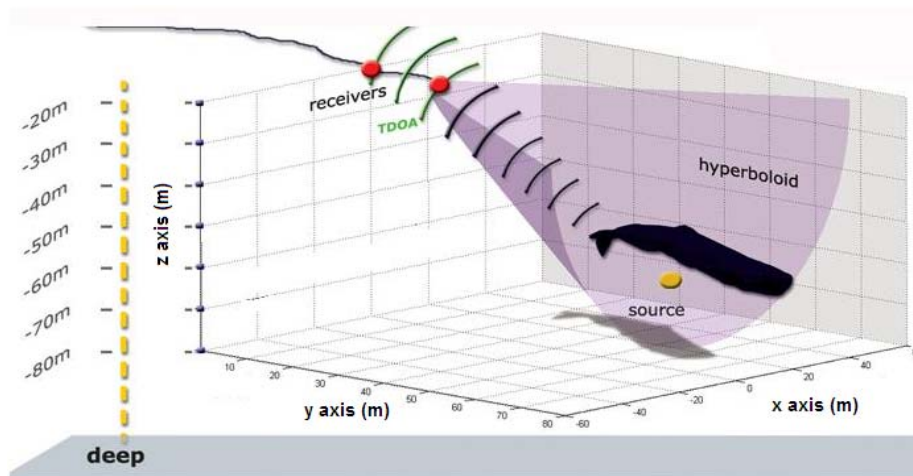


Figure 3.4: Hyperboloid scenario resulting from two receivers array

The 3D geometric hyperbolic localisation method is based on the use of several receivers to generate a sufficient number of hyperboloids that intersect ideally in a single point location. The intersection provides us with either the source location in the Cartesian plane xyz or slant range and directional (azimuth/elevation) information of the receiver-source (Figures 3.5 and 3.6).

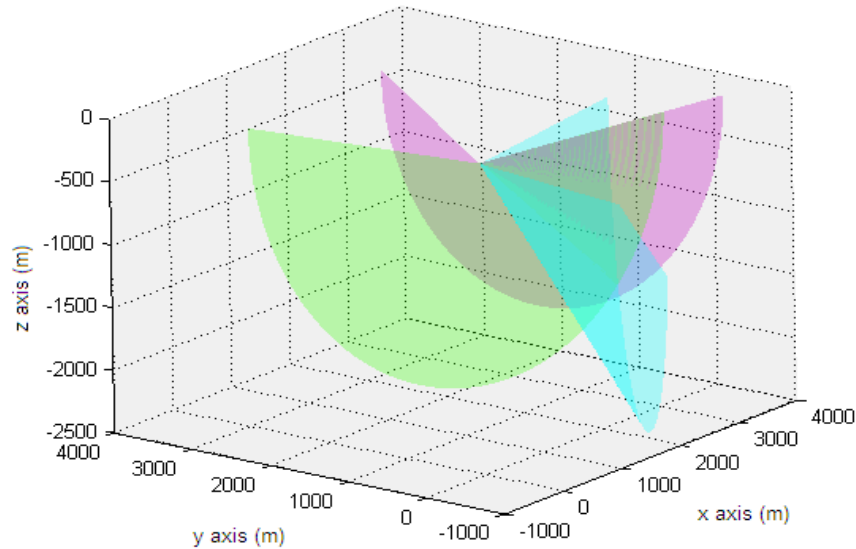


Figure 3.5: Intersection of three hyperboloid geometric surfaces. Plot generated by the MATLAB Simulator.

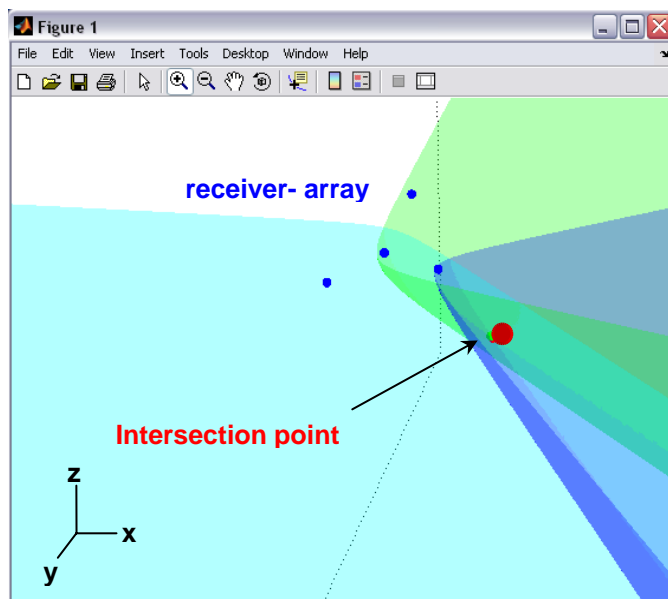


Figure 3.6: Intersection in a single point. Plot generated by the MATLAB Simulator.

3.3 Matlab Simulator

In order to perform different scenarios where the hyperbolic method is used, a full 3D simulation environment was developed using MATLAB Version 7.0 (Mathworks, Inc). The simulator is divided into two essential sections: (a) data generation and (b) localisation computation. The *data generation* refers to TDOA data, which can be taken from real measurements or computed from the array configuration, sound speed and source position proposed by the user. The user is able to set the receiver position in the Cartesian plane (x, y, z) for 2 or more elements in size via a Graphical User Interface (GUI). The *localisation computation* uses a geometric hyperbolic method as the main localisation algorithm to identify the source location. The final result is given in a 3D graphical representation in the Cartesian plane (x, y, z). For more details of the Matlab GUI simulator, see Appendix C.

3.3.1 Synthetic TDOA Data Generation

Straight line geometry was used to compute the TDOA parameters from a known source location by assuming constant sound speed (ss). Synthetic data generation is essential to model the different scenarios of the source location problem. The TDOA computation is based on the equation for distance d_{sr} between two points, source ($s_x s_y s_z$) and receiver ($r_x r_y r_z$).

$$d_{sr} = \sqrt{(r_x - s_x)^2 + (r_y - s_y)^2 + (r_z - s_z)^2} \quad (3.9)$$

By dividing d_{sr} over ss , the *time-of-arrival* (TOA) is computed. The difference between the two TOAs is known as the TDOA (Figure 3.7). Straight and direct line paths, a constant sound speed, a static receiver position and TDOA measurements without error are major assumptions on the computation of synthetic data. For a completely mathematical reference, please see Appendix B.

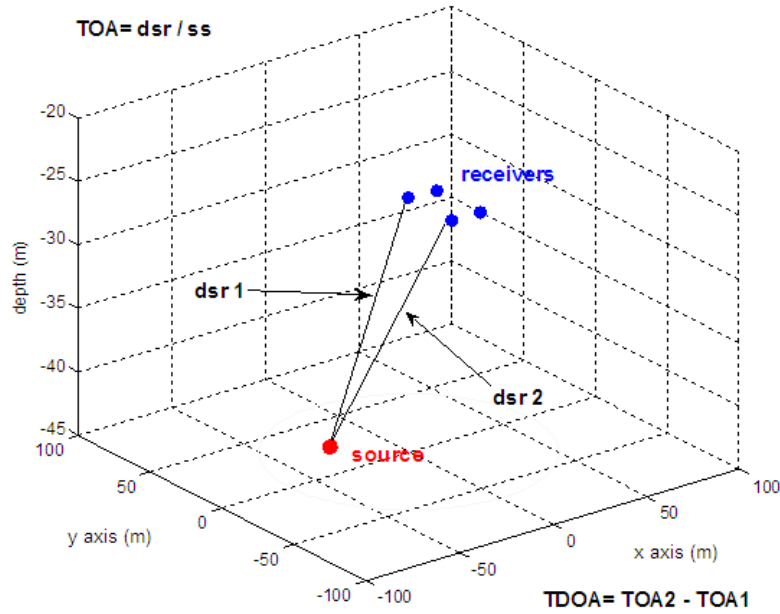


Figure 3.7: Synthetic TDOA computation in 3D. Based on the distance difference between source and receivers. Plot generated by the MATLAB Simulator.

3.4 Localisation Algorithm Methodology

The simulator algorithm uses the TDOA data to generate a 3D graphic surface of one half of a two-sheeted hyperboloid for each pair of receivers set by the user. Then it uses the range differences of each grid point to each pair of receivers to match such information with their correspondent TDOA values. The matching value corresponds to the intersection point of the total number of geometric surfaces and the final source location is given. The algorithm used can be represented in four main stages (Figure 3.8).

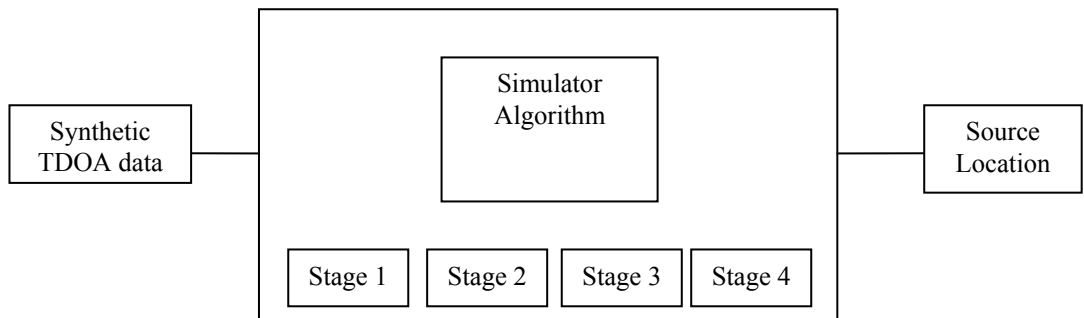


Figure 3.8: Block diagram of the simulator algorithm

3.4.1 Stage One

The first stage consists of producing a half two-sheeted hyperboloid for each two-element-pair oriented along the z-axis. The main variables known are:

A , which denotes the *receiver matrix* for a 3D position system of the receiver-array

$$A = \begin{bmatrix} r_x(1), r_x(2), \dots, r_x(n) \\ r_y(1), r_y(2), \dots, r_y(n) \\ r_z(1), r_z(2), \dots, r_z(n) \end{bmatrix}$$

where (r_x, r_y, r_z) are the Cartesian coordinates of n number of receivers;

D , which denotes the *distance* between each pair of receivers ($r_{12}, r_{13}, \dots, r_{1-n}$)

$$D = [d_{12} \ d_{13} \ \dots \ d_{1n}]$$

T , which denotes the *TDOA* for each pair of receivers

$$T = [\tau_{12} \ \tau_{13} \ \dots \ \tau_{1n}]$$

R , denotes the *source-receiver range difference* vector. It is the result of multiplying T by the sound speed SS

$$R = [g_{12} \ g_{13} \ \dots \ g_{1n}]$$

X , Y and Z are the three vectors that define the three coordinate axes

$$X = [x_1, x_2, \dots, x_{128}]$$

$$Y = [y_1, y_2, \dots, y_{128}]$$

$$Z = [z_1, z_2, \dots, z_{128}]$$

The parametric equations [50] that describe the two-sheeted hyperboloid are

$$\begin{aligned} x &= b \sinh v \cos u \\ y &= b \sinh v \sin u \\ z &= a \cosh v \end{aligned} \tag{3.10}$$

where

$$a = \frac{g_{1(i+1)}}{2}, b = \sqrt{c^2 - a^2}, c = \frac{d_{1(i+1)}}{2}, \quad i = 1, 2, \dots, n-1$$

$$\text{for } u \in \left(\frac{-\pi}{2}, \frac{\pi}{2} \right) \text{ and } v \in [0, -2\pi)$$

Then, the parametric equations are computed for each pair of receivers ($r_{12}, r_{13}, \dots, r_{1-n}$) and are grouped in one *hyperboloid matrix* (of dimensions 3×128)

$$H_{Ij} = \begin{pmatrix} h_{x1}, h_{x2}, \dots, h_{x128} \\ h_{y1}, h_{y2}, \dots, h_{y128} \\ h_{z1}, h_{z2}, \dots, h_{z128} \end{pmatrix}$$

where

$$j = 2, 3, \dots, n,$$

The following computations are:

- Hyperboloid matrix rotation on X axis (azimuth)
- Hyperboloid matrix rotation on Z axis (elevation)
- Hyperboloid matrix translation
- Hyperboloid matrix transpose
- Loop cycle of a hundred times π

The total group of grid points defines the hyperboloid geometric surface to be plotted. At this point, the possible S_V location vector (s_{vx}, s_{vy}, s_{vz}) corresponds to any vector (h_x, h_y, h_z) of the hyperboloid matrix H_{Ij} .

3.4.2 Stage Two

A second stage does a cross-correlation of each of the H_{I_j} matrixes into a unique ${}^{\text{new}}H$ matrix of dimensions $m \times 3$, where m represents the number of possible S_V location vector solutions (s_{vx}, s_{vy}, s_{vz}) . Then, each vector of the ${}^{\text{new}}H$ matrix is transformed into a new vector which contains the *range difference* between each position vector and each pair of receivers. This new matrix ${}^{\text{new}}R$ has dimensions $m \times n$, where n represents the total number of receivers of the array.

$${}^{\text{new}}R = \begin{pmatrix} g_{12} g_{13} \dots g_{1n} \\ g_{22} g_{23} \dots g_{2n} \\ \dots \dots \dots \dots \\ g_{m2} g_{m3} \dots g_{1n} \end{pmatrix}$$

3.4.3 Stage Three

Each row from ${}^{\text{new}}R$ is compared with the original R *range difference* vector. Although ideally there is “one unique solution”, owing mainly to the curvature nature of the hyperboloid geometric surfaces, ${}^{\text{new}}R$ could have more than one grid point that approximate to the original R vector. So, when there is more than one possible solution that matches the R vector, the mean of the several approximation vectors provides an *estimate value*. The weighting given to such estimate value is based on a small delta factor (δ) added to the R vector. The value of $\pm\delta$ is 0.015 m, the equivalent to $10\mu\text{s}$ assuming a constant sound speed of 1500m/s. If there is no matching vector, the algorithm increases the δ value n times until one or more points match a vector. The final result is an estimate vector with an additional error of n times $\pm\delta$.

3.4.4 Stage Four

Once a final matching vector has been found, a fourth stage looks up the correspondent position vector in the hyperboloid matrix ${}^{new}H$ of stage two and a final *source location vector* is given. The diagram on Figure 3.9 summarizes the computation algorithm, including each of its stages.

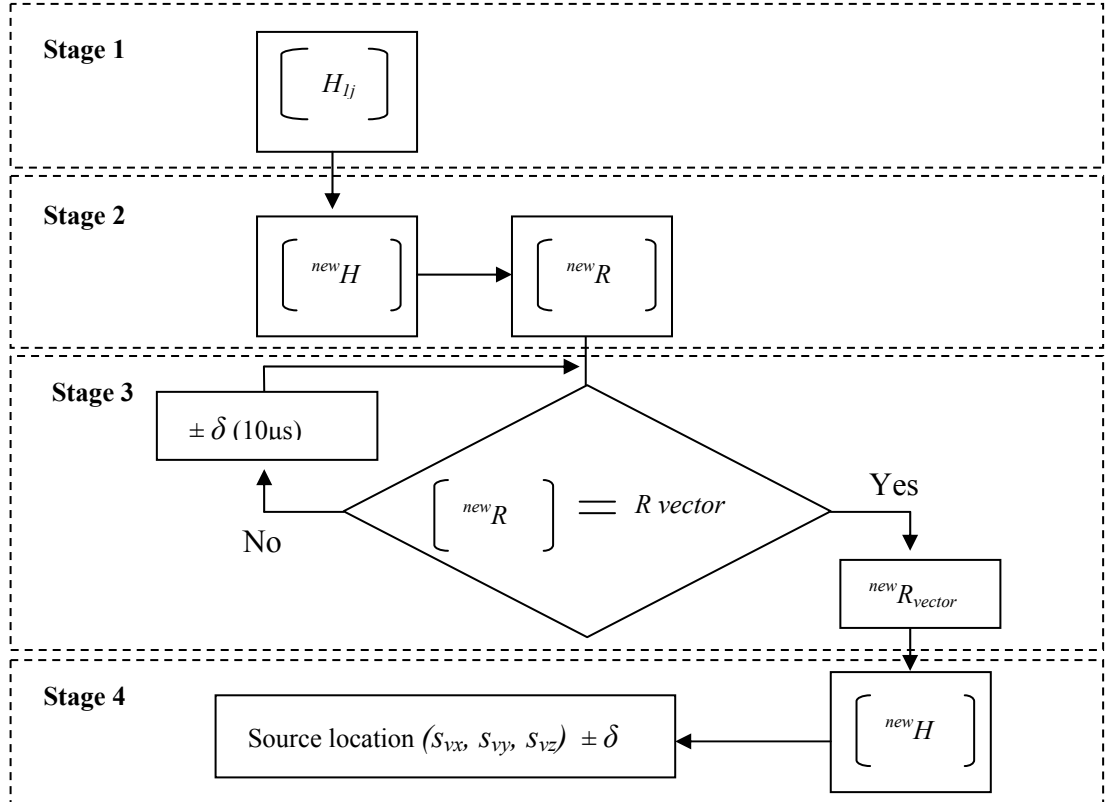


Figure 3.9: Algorithm diagram and its four stages.

3.5 Discussion and Summary

The geometric hyperbolic localisation algorithm presented in this thesis is based exclusively on the generation of 3D geometry surfaces, called hyperboloids that are produced mainly by individual TDOAs. Although it is possible to locate a source in 2D, in the real world, the scenarios are presented in 3D. For instance, consider the scenario in which a 2D hyperbolic method is used for a source that is supposed to be on the same plane of the receivers, but could be along a third axis. In such a case, the 2D location would be just an approximation. It is in this sense that the 3D hyperbolic localisation is superior to the traditional hyperbolic algorithm in 2D, because it includes complete range (horizontal and depth) and bearing information (angle). In a highly idealized medium, a constant sound speed, direct source ray paths, omnidirectional receivers, non-signal attenuation, a static deployment of the receiver array, and a single source vocalising per each set of TDOAs are assumed. For simulation purposes, synthetic TDOA data are computed from a known source position and used as the main input of the geometric hyperbolic localisation algorithm, which is divided into four stages. The weighting given to the estimate value error is determined by δ equivalent to $\pm 10\mu\text{s}$ added to the set of TDOAs, if a constant sound speed of 1500m/s is also assumed.

The following chapter discusses the importance and the relationship between array-configuration and source range estimation.

Chapter 4

Array Optimization

One of the essential elements in PAM cetacean localisation is the transducer sensor array which is used to receive the signals from the source. An array of acoustic underwater transducers is also known as a hydrophone array. The number of hydrophones and the way in which these are deployed and distributed along the array constitute the *array-configuration*. Since the array-configuration has a direct effect on location accuracy [109] and it is a major factor controlling performance under the control of the scientists [123], the consideration of array optimization is of prime importance in this thesis. The following attributes of the array-configuration are also considered: *number of receivers*; *geometry* and *overall aperture*. Concerning the several issues that are associated with this concept, this chapter describes how the Matlab simulator allows the user to explore quantitatively two different array configurations in 3D using a geometric hyperbolic localisation algorithm, and following the gross assumption of a highly idealized medium. It also helps to establish the existing relationship between array-configuration and source position.

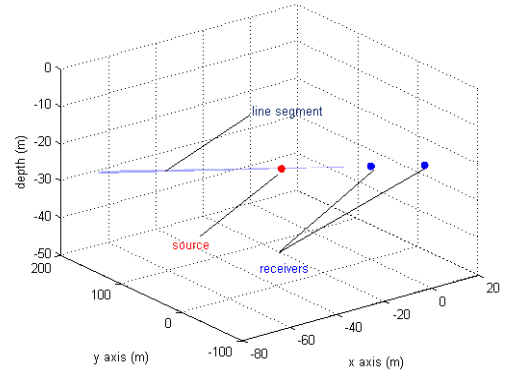
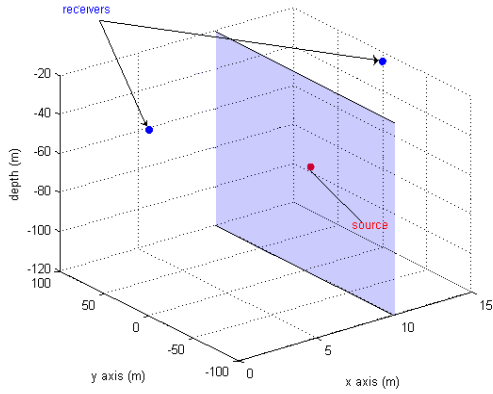
4.1 Number of receivers

Before moving onto an analysis of the capabilities of different array-configurations, it is important to consider how many receivers are needed for accurate 3D hyperbolic localisations.

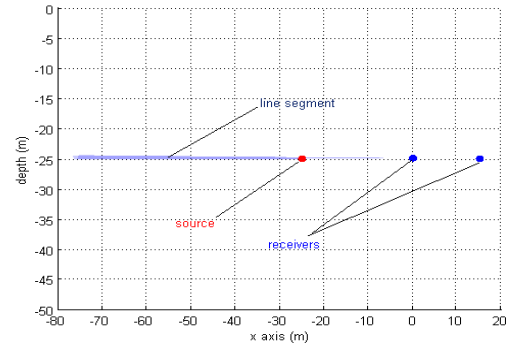
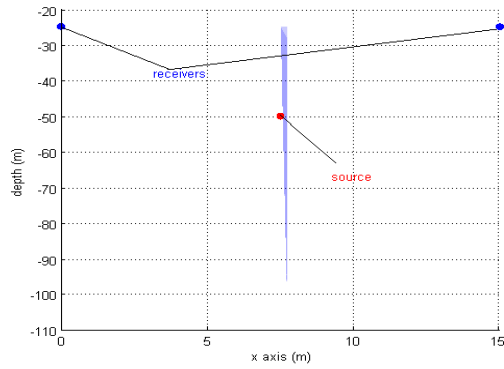
4.1.1 Two Receivers

Currently, automated detection systems based on two receivers are used in cetacean monitoring [43]. These can give only instantaneous ambiguous bearing (port/starboard), without *depth* and *slant range* information available. When using the 3D hyperbolic technique, the location of the source can be assumed to lie on a geometric hyperboloid surface, except for two scenarios (see Figures 4.1a and 4.1b).

XYZ – Cartesian plane



XY – Cartesian plane



XZ – Cartesian plane

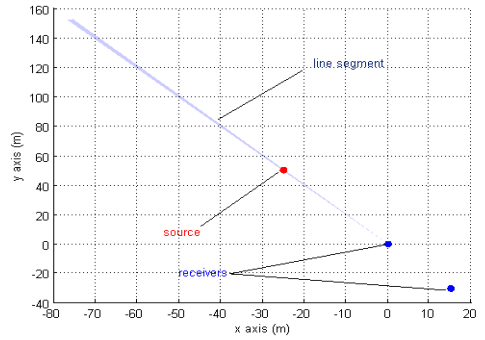
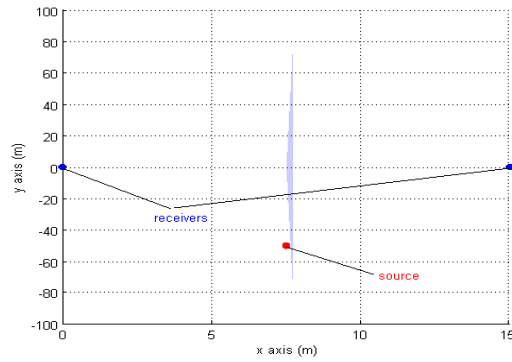


Figure 4.1a: *Broadside* scenario is the result of a TDOA equal to zero.

Figure 4.1b: *Endfire* scenario is the result of a TDOA equal to TDOR.

The first scenario (Figure 4.1a) results when a vocalisation sound is received in such a way that the TDOA is zero. This scenario is better known when the source is *broadside* to the receiving pair, and for this special case the hyperboloid becomes a flat surface.

The second scenario (Figure 4.1b) occurs when the vocalisation sound results in a TDOA such that the delay is equivalent to the time taken for sound to propagate directly between the two receivers or *time-difference-of-receivers* (TDOR). This scenario is better known when the source is *endfire* to the receiving pair, converting the hyperboloid into a straight line [130].

The *endfire* and *broadside* scenarios are worthy of note as they constitute particular scenarios where there is limited localisation capability. The importance of such scenarios relies on the effects associated with the final source range estimation.

4.1.2 Three Receivers

By using three receivers, a source location is inferred through the intersection of hyperboloid surfaces from three pairs of receivers (r1, r2), (r1, r3), (r2, r3). Each pair of receivers defines a TDOA and a hyperboloid surface. However, the pair (r2, r3) represents one linear combination of the other two pairs (r1, r2) and (r1, r3),

$$TDOA_{13} - TDOA_{12} = TDOA_{23} \quad (4.1)$$

An array of three receivers is able to produce an approximation of the source location in a two-dimensional Cartesian plane XY only. In two-dimensional localisations, the TDOAs are assumed to come from a source located at the same plane. Hence when the source vocalising is out of the plane of the receivers, the final result is an estimation of the source range with errors that could be significant [134].

4.1.3 Four Receivers and more

If the receiver number one (r_1) is chosen as the main reference, it is found that four receivers generate three independent TDOAs from the three following pair of receivers: (r1, r2), (r1, r3), (r1, r4). Four receivers are also sufficient to give a desirable directional (azimuth and elevation) and slant range information of the source location (Figure 4.2).

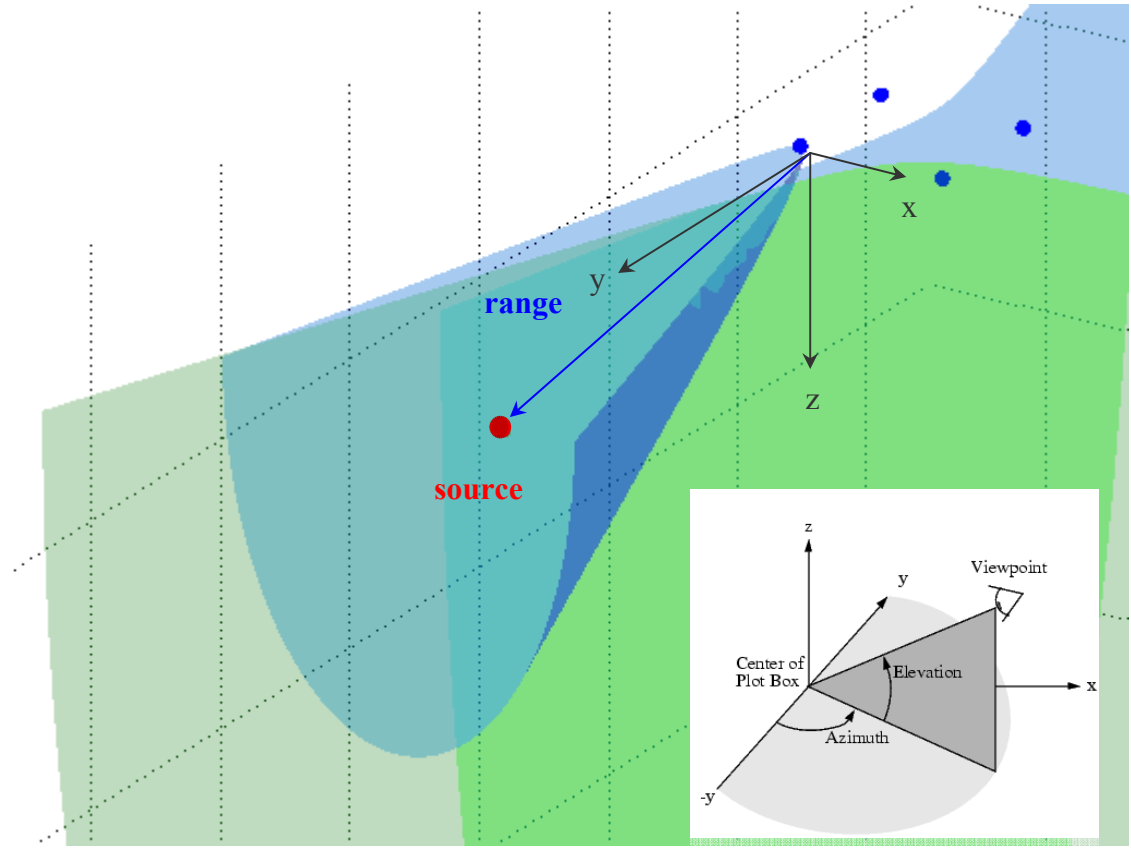


Figure 4.2: 3D Graphical Source Location, with bearing (azimuth and elevation) and range included.
Plot generated by the MATLAB Simulator.

However, if the hyperbolic method is used in scenarios where the source may occupy areas that contain ambiguous regions -i.e the air- an ambiguous source location solution may occur. That is, the hyperboloids intersect at two points instead of only one [134]. In such a case, three hyperboloids would not be sufficient for three-dimensional localisation, and the use of more than four receivers would be necessary to increase the number of independent TDOAs. Nevertheless, in our particular scenario, the ocean becomes a physical barrier that prevents the animals from occupying aerial areas, ensuring that ambiguous locations on such regions cannot occur.

4.2 Array-Geometry

The array-geometry can be divided into three big general groups: linear, planar and volumetric [109]. Each group can have several different geometries or receiver-distributions according to the number of elements and their position in the array plane.

4.2.1 Linear-Array

The *linear-array* is one in which the elements are deployed along a straight line segment [54]. It can be deployed in a horizontal or vertical line. In the particular case of an array towed by a vessel travelling at certain speed, the array-geometry becomes *semi-horizontal* depending on the distance between receivers (Figure 4.3a). On the other hand, static vessels or small boats tend to keep a *vertical* array-geometry. For instance, consider the passive sonobuoys [80]. These are inflatable surface buoys with a radio transmitter that remains on the surface while one or more hydrophones and stabilizing equipment descend below the surface to a certain depth (Figure 4.3b).

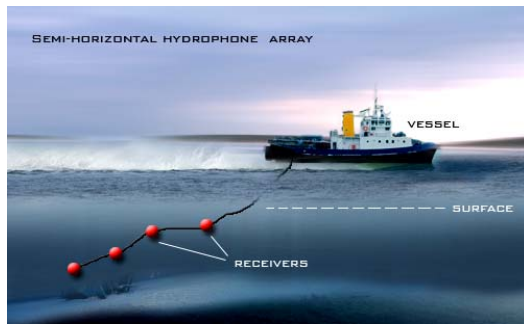


Figure 4.3a: Semi-horizontal array deployment

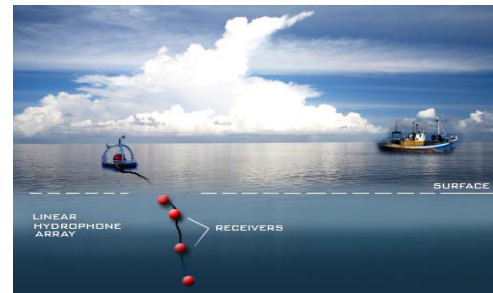


Figure 4.3b: Vertical array deployment

The use of a linear-array with hyperbolic techniques is not always favourable. Since the linear-array falls under the one-dimensional category, a source localisation suffers the effects of the right/left ambiguity (Figure 4.4).

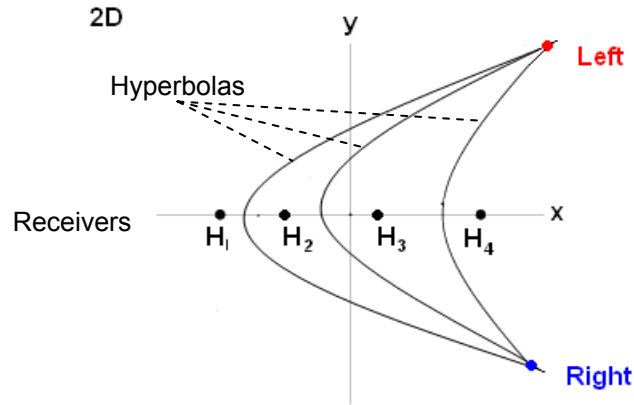


Figure 4.4: The right/left ambiguity source location occurs when the *linear array-geometry* is used in conjunction with the hyperbolic technique.

As discussed in chapter 2, researchers have applied *Target Motion Analysis (TMA)* techniques over time to break such ambiguity; however, it cannot be resolved for instant bearings. The linear-array is more often used with beam-forming techniques [77, 143].

4.2.2 Planar-Array

The *planar-array* is one in which all the elements are deployed along a 2D plane. Therefore, for any array of receivers located at the same depth the correspondent geometry is the planar-array. It is also used for practical deployments, assuming a static receiver-position.

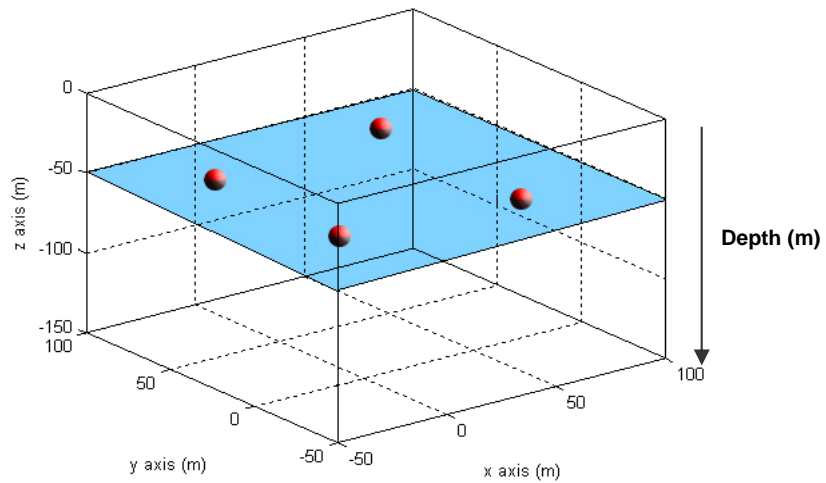


Figure 4.5: Planar-Array Geometry

A planar-array offers a great variety of planar geometries on the horizontal Cartesian plane. Depending on the number of elements, several different planar-array geometries can be deployed (Figure 4.6).

Square, rectangular and triangular are some of the most common of these; however, the number of possible planar array-geometry combinations may vary from a small group to several more.

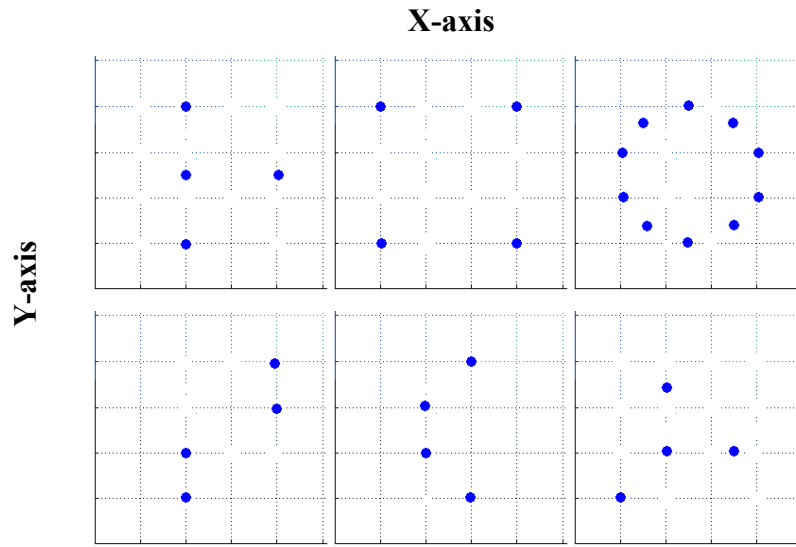


Figure 4.6: Common Planar-Array Geometries. Superior view. From left to right: Triangular, Square, Circular, Shifted-pair, Trapezium and Y-shape.

In this thesis the planar geometry is applied in most of the simulations. In reality, owing to current aberrations and other issues, it is difficult to keep the position of all the elements at the same depth. This situation introduces another type of geometry.

4.2.3 Volumetric-Array

The *volumetric-array* is one in which the elements are deployed along a 3D plane. The linear and planar arrays are usually represented in 2D; on the other hand, the *volumetric-array* geometry must always be represented in 3D. Each element has a unique position on the Cartesian plane XYZ.

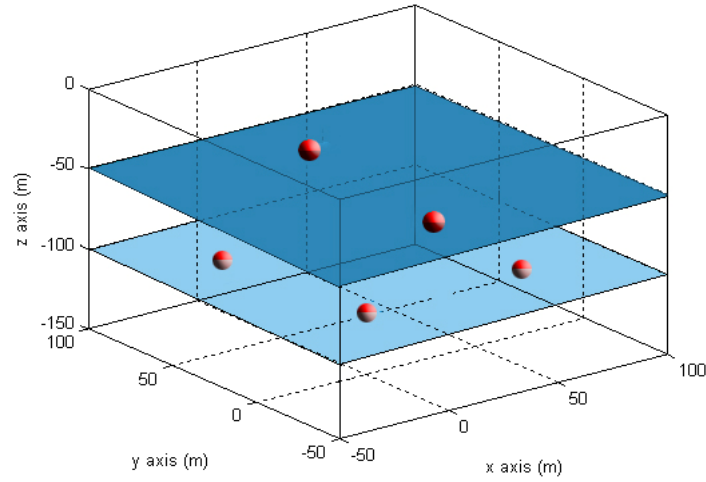


Figure 4.7: Volumetric-Array Geometry. Plot generated by the MATLAB Simulator.

The volumetric-array geometry is the closest to the reality. The accuracy of a volumetric-array relies mainly on an appropriate receiver-distribution. In comparison with the planar-array, the volumetric-array can take a vast number of possible combinations. A further section in this chapter analyses the implications of receivers at different depth positions.

4.3 Array-Aperture

The array-aperture has always been a relative measurement for hydrophone array deployments. For instance, while Møhl and Wahlberg [100] used a long-aperture array of at least more than 1km in their experiments, Watkins and Schevill [164] used a short-aperture array of 30m. Thode [142, 144] defined an array of two elements separated by 170m as a short-aperture and a long-aperture array between 200 and 300m. Others have used apertures of 115m and 205m [28].

Following Rayleigh's [118] principle for direction of maximum response, the *ideal* separation distance of two elements to receive a minimum low frequency of a Sperm whale click ($f=100$ Hz) in the ocean ($c=1500$ m/s) applying Nyquist theorem ($\lambda/2$ criterion) is 7.5 metres [16]. It is expressed as

$$\lambda = \frac{c}{2f} \quad (4.2)$$

This separation represents half of the Sperm whale wavelength. Table 4.1 presents a model of the different apertures between two elements for the distribution of energy in a typical click (on-axis) of sperm whale as a function of its frequency (Figure 4.8).

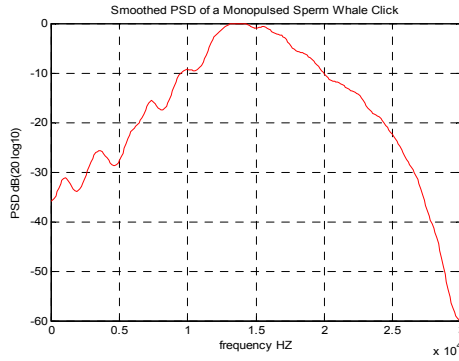


Figure 4.8: Typical Power Spectral Density of a sperm whale click (*computed by Matlab software*)

Frequency (kHz)	Aperture (metres)
0.1	7.5
2	0.375
4	0.188
10	0.150
16	0.469
30	0.025

Table 4.1: Ideal Apertures for Different Frequencies

Therefore, assuming acoustic plane wave propagation in a homogeneous medium, the ideal aperture of two elements to receive the lowest frequency produced by a sperm whale can be considered to be $L=7.5m$ (see equation 4.2). Any aperture superior to the L assures the inclusion of the complete frequency range of a sperm whale [16].

The notation used in this thesis is that a *short aperture-array* is defined as one with the length L . A “short” is the most common aperture used in small vessels for towed arrays. A *long aperture-array* is defined as an array having a distance separation equivalent to $16L$. Unlike the short, a “long” aperture is more often used from floatable platforms [158]. For matters of simplicity, the term L is mentioned repeatedly in this thesis to make reference to any distance.

4.4 Simulation Settings

Since each array-geometry has a direct effect on the final source range estimation, different array-geometries, including a range of scenarios, are simulated. To find out how the aperture and geometry of the array are related with the variation of a source range estimation, the source position is varied in both planes, the horizontal (XY) and the vertical (Z).

In the real underwater world, the *Source Vocalising* (S_V) position is unknown. In this thesis, each S_V is known *a priori*. Each experimental simulation has been programmed to include a hundred selected S_V positions around the receiver-array. Then, each simulation runs the hyperbolic geometric algorithm to compute a S_V location. The *localisation error* (4.3) is defined as the absolute difference between the *synthetic source position* (S_{Vs}) and the *computed source location* (S_{Vc}) –see sections 3.4.3 and 3.4.4. The following section sets the general scenario for all the simulations computed and shown in this thesis.

$$\mathcal{E} = |S_{Vs} - S_{Vc}| \quad (4.3)$$

4.4.1 Highly Idealized Scenario

This chapter is based on a highly idealized 3D graphical scenario (Figure 4.9). It uses a straight ray approximation, static receiver and source positions. A planar square array-geometry with four receivers is chosen as an exemplar array. The centre of the array geometry is set at the coordinates (0, 0, z). These are used as a *reference point* (P_0) in the Cartesian coordinate system XYZ. Then, a hundred S_V positions are chosen and placed at a determined *Horizontal Range* (R_H) which is used to represent the distance between P_0 and S_V on the horizontal coordinate system XY. *Depth Range* (R_D) is also used to represent the distance between P_0 and S_V on the vertical coordinate system ZY or ZX. *Slant range* (R_S) represents the *source range* in the 3D space between P_0 and S_V . From the Pythagoras formula, the *slant range* (R_S) is the square root of the sum of the squares of *depth range* (R_D) and *horizontal range* (R_H). If R_H and R_D keep constant, R_S could also be represented as a rendered cone of radius R_H and altitude R_D (Figure 4.10).

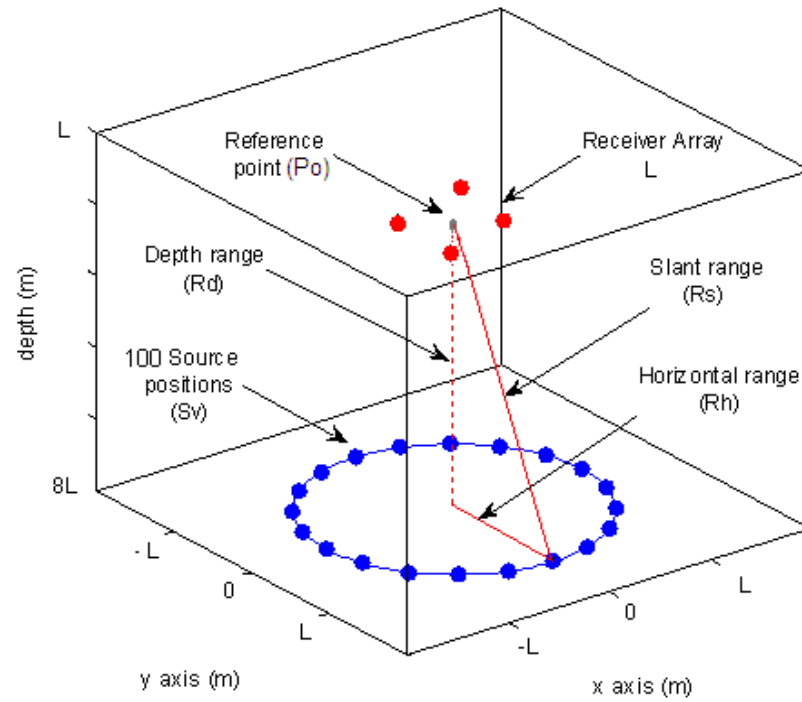


Figure 4.9: A 3D graphical scenario for Experimental Simulations. Plot generated by the MATLAB Simulator.

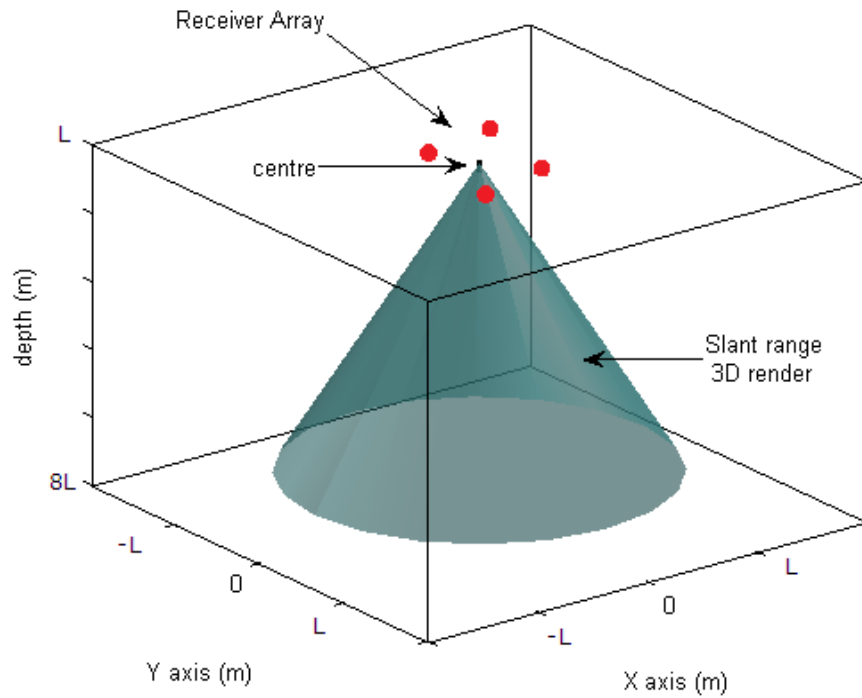


Figure 4.10: A general representation of the *Slant Ranges* results into a 3D rendered cone. Plot generated by the MATLAB Simulator.

Because of the imprecision of the geometric hyperbolic method, the ideal cone becomes deformed and such errors are significant. For a friendly display of the results obtained, the author presents here a set of plots in the Polar coordinate system (2D). All the experimental simulations follow the same pattern of settings to facilitate the analysis of other array configurations.

4.4.2 Table Settings

The specifications for each group of simulations are shown in a table format that contains the type of geometry, aperture length, number of receivers, depth at which the receivers are deployed, number of the suggested source positions, horizontal range and depth range. The relevant variations between each simulation are highlighted in bold font.

Array-Configuration		Exemplar
Geometry		Square-planar
Aperture length	A	L
Num. receivers	i	4
Receivers depth	r_d	L
Num. sources	S_V	100
Horizontal Range	R_H	16L
Depth Range	R_D	8L

Table 4.2: Specifications for Exemplar Simulation

For instance, on this first exemplar simulation the array geometry chosen is a square-planar, the aperture length is L and the number of receivers is four. The initial horizontal range for the source position is sixteenth times the aperture length ($16L R_H$), which creates a satisfactory way to compare the relationship between aperture and source range location. The initial value for depth range of eight times the aperture length ($8L R_D$) has to do with the vocalising activity of the source and the receiver array depth position (r_d) at 7.5m. According to some of the literature, there is reduced vocal source activity when the cetaceans are at or near the surface [4, 31, 87, 168]. Therefore, by placing a synthetic source at an initial depth of 67.5m, or its equivalent R_D of 8L, the presence of active vocalising sources can be assumed.

4.4.3 Exemplar Plots

The use of 2D Cartesian graphs implies that we discard the existence of a third axis, which in most cases is the Z axis or depth axis, according to the underwater scenario discussed here. When that is the case, the receivers and source are assumed to be located at the same plane or depth. However, since the TDOA data contain important information that places the S_V position at a different plane of the receivers, the final source location in the 2D Cartesian plane is only an approximation and an implicit error is included [134].

To avoid such a problem, a good solution may be the use of 3D plots. Nevertheless, 3D planes are difficult to show on paper. Thus, a 2D plot (Figure 4.11) in a Polar coordinates system is suggested as a better representation of the slant range (or source range). The advantage of using this type of polar plots lies in their ability to represent the slant range in a 2D plane. Rather than relying on a 2D approximation as many do, the slant range gives a most trustable value of the distance between receiver and source.

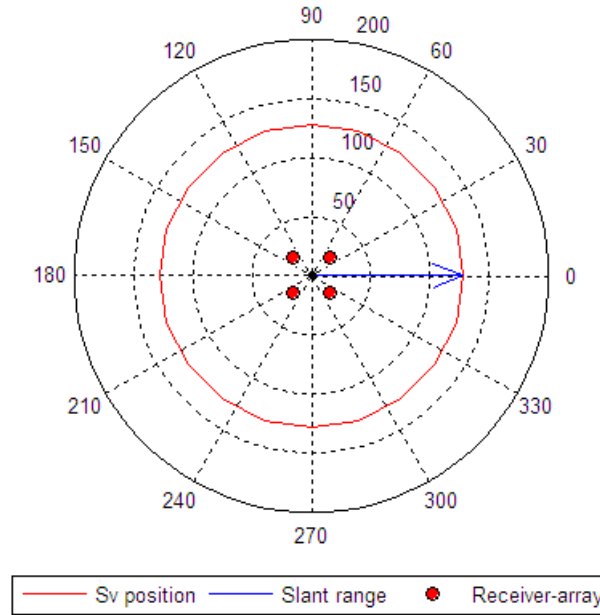


Figure 4.11: Polar representation of the hundred *Source positions* (S_V)

Figure 4.11 shows a 2D graphical representation of the *slant range* plotted in the Polar coordinate system. The red circle represents the source-tracking line assuming a spatial under sampling of a hundred points. Each point corresponds to an individual synthetic source position located at a constant *slant range* (blue arrow) from the centre of the array. The *slant range* is predetermined by the values of R_H and R_D . When the aim of

the simulation is to see the effects of the source moving on a horizontal plane, R_D is fixed to a certain depth, while R_H varies. On the other hand, when the source is moving on the vertical plane, R_H is fixed to a certain distance, whereas R_D continues increasing.

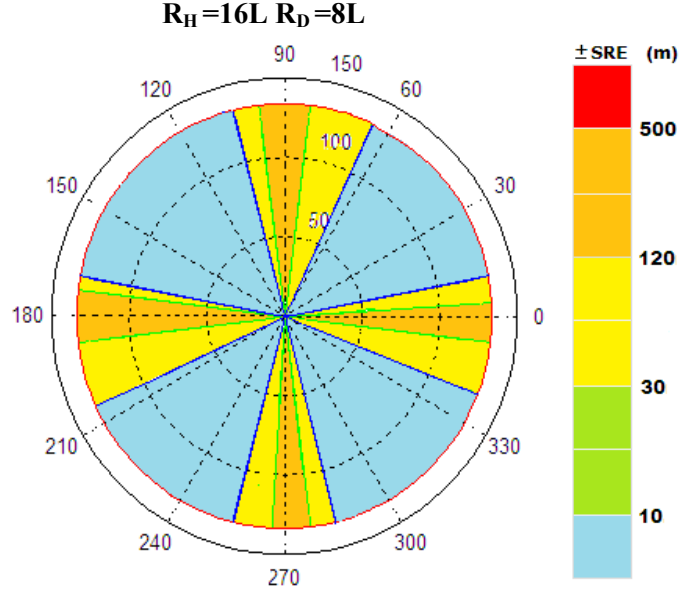


Figure 4.12: Polar representation of an exemplar array simulation, highlighting the *Slant Range Error (SRE)* variation in terms of L (7.5m)

To distinguish between accurate and inaccurate source locations, a plot is shown in Figure 4.12. The coloured bar highlights the *Slant Range Error (SRE)* or source range estimation defined by equation (4.3). A minimal $SRE < \pm 10m$ is defined by the colour blue. A maximum $SRE > \pm 500m$ is represented in red. The different colours represent the variation of the SRE for different source bearings. The polar representation of this plot helps to visualize the bearings where the array configuration is more accurate. Although an array-configuration can be completely accurate for 360° at a particular slant range, this is not always the case.

In this thesis the following considerations are assumed. If the SRE is within $\pm 10m$ for the 100% of S_V positions covering the 360° at a particular slant range, the array would be considered *completely accurate*. If the same SRE covers more than 80% but less than the 100% of the total S_V positions, the array would be considered *partially accurate*. Finally, if the same SRE covers less than the 80%, the array would be considered *inaccurate*. This plot gives the user a degree of confidence regarding the accuracy of a particular array-configuration.

4.5 Square-Array

The square-array is one of the simplest planar geometries used in practice with four receivers. Among its main features are the same distance separation L for each pair of receivers, as shown in Figure 4.13.

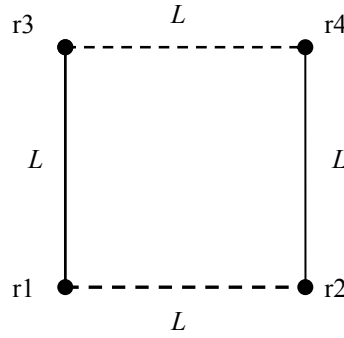


Figure 4.13: Superior view of a *square* array of 4 elements

4.5.1 Short Aperture (L)

The first aim of these experimental simulations (see specifications on Table 4.3) is to investigate the behaviour of a short-aperture array by choosing a source position with a fixed R_D at an initial value of $8L$ and increasing R_H by the power of 2^n times L (see Table 4.4). These series of experimental simulations are the result of moving the source along a horizontal range of $\sim 1\text{km}$ and a depth range of $\sim 0.5\text{km}$. The results obtained are plotted following the same pattern of the exemplar plots shown previously (Figure 4.14).

Square-Array		$n = \{0, 1, \dots, 7\}$ $m = \{3, 4, \dots, 6\}$
Aperture length	A	Short (L)
Num. receivers	i	4
Receivers depth	r_d	L
Num. sources	S_V	100
Horizontal Range	R_H	$2^n L$
Depth Range	R_D	$2^m L$

Table 4.3: Simulation Specifications for Short-Square-Array

Depth Range	Horizontal Range						
8LR _D	LR _H	2LR _H	4LR _H	8LR _H	16LR _H	32LR _H	64LR _H
16LR _D	LR _H	2LR _H	4LR _H	8LR _H	16LR _H	32LR _H	64LR _H
32LR _D	LR _H	2LR _H	4LR _H	8LR _H	16LR _H	32LR _H	64LR _H
64LR _D	LR _H	2LR _H	4LR _H	8LR _H	16LR _H	32LR _H	64LR _H

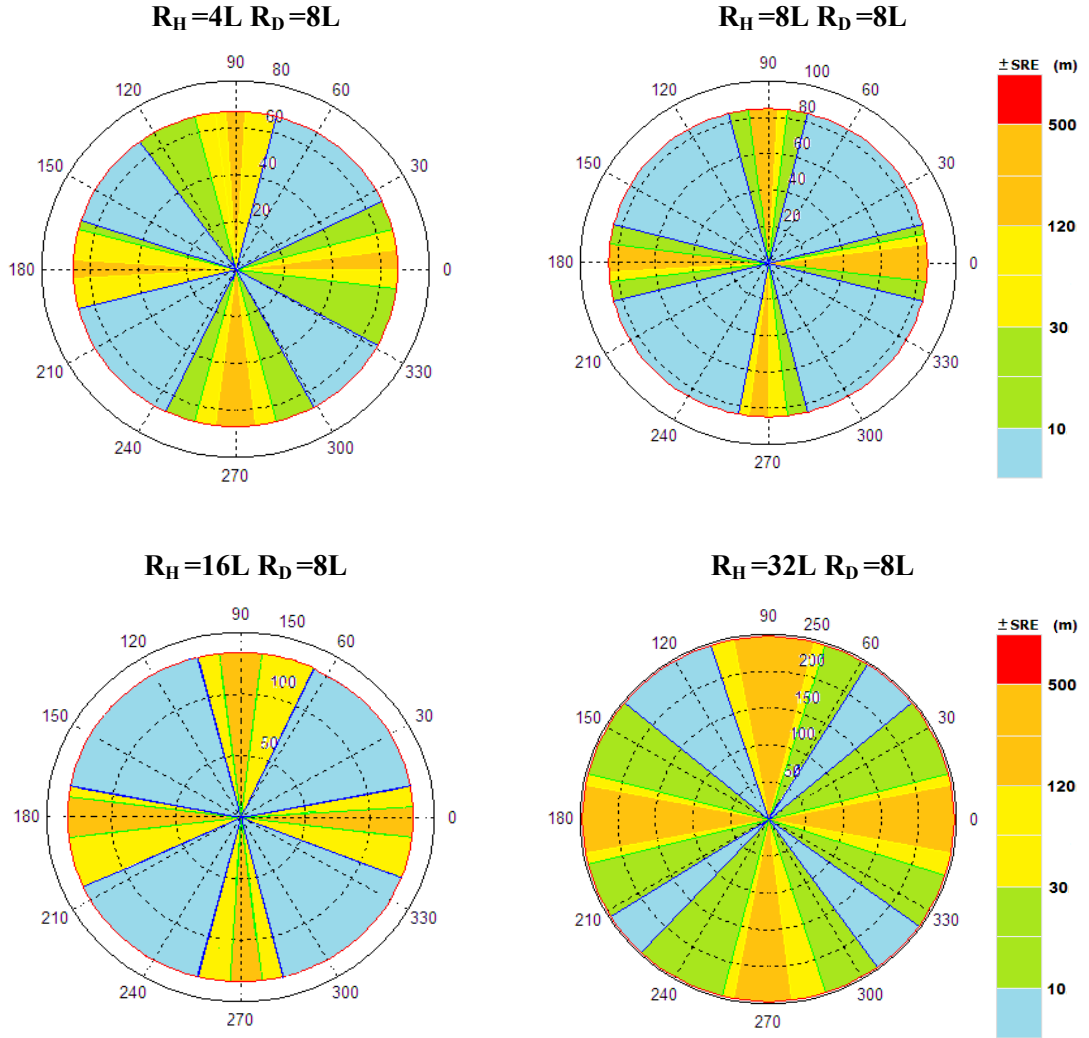
Table 4.4: Synthetic source values of R_H and R_D used for experimental simulations

Figure 4.14: Short-Square-Array ($4LR_H$ to $32LR_H$). The array was found to be partially accurate for horizontal ranges from $4L$ ($30m$) up to $16L$ ($120m$) and inaccurate for horizontal ranges of $32L$ ($240m$) and over.

When the source is located at either $1L$ or $2L$ from the centre of the array, the TDOAs are too small (on the range of microseconds). That produces numeric noise in the

geometric hyperbolic algorithm and it makes the array geometry totally inaccurate for locating the source at such ranges.

On the other hand, when the source is located at a horizontal range of $4L$ and onwards, there is a characteristic pattern that occurs on the square geometry. There are four clear areas where the array geometry is totally inaccurate. These inaccuracies are the result of a broadside condition from at least one of the hydrophone pairs. As mentioned before, when a broadside condition occurs the TDOA becomes zero, converting the hyperboloid into one plane and making the intersection with the rest of the hyperboloids inaccurate. These effects are repeated and increased for horizontal source ranges of $8L$, $16L$ and $32L$ respectively, as shown in Figure 4.14.

The square geometry finds it difficult to determine the slant range for more than 80% of the total source positions. The accurate bearings are reduced to small angles and the broadside uncertainties are widely increased. Therefore, the array is considered inaccurate for such horizontal ranges. For source positions at horizontal ranges of $64L$ and $128L$, the short square array geometry is also considered to be inaccurate. All the source range estimations are out of the tolerance error.

The second aim of these experimental simulations was to investigate the behaviour of a short-aperture array by varying the depth range R_D by the power of 2^n times L (see Table 4.3). A first attempt at depth ranges of $16L$ R_D failed completely. Additional simulations were performed and it was noticed that these only maximise the error found. Overall, the array geometry was not sufficiently accurate to reach deep source positions.

In summary, the short square array geometry was found to be inaccurate for any horizontal range. This first group of simulations show a complete scenario of the slant range error expected when using a square geometry with short aperture. It also introduces a series of simulations that was applied to different array configurations.

4.5.2 Long Aperture (16 L)

The second group of experimental simulations includes the same array geometry but with a longer aperture (16L). This is sixteen times longer than the short aperture discussed previously. By varying R_D and R_H by the power of 2^n times L, a series of experimental simulations were performed as it was shown in Table 4.4. The general specifications for each of the long-aperture experimental simulations are shown in Table 4.5.

Square-Array		$n = \{0, 1, \dots, 7\}$ $m = \{3, 4, \dots, 6\}$
Aperture length	A	Long (16L)
Num. receivers	i	4
Receivers depth	r_d	L
Num. sources	S_V	100
Horizontal Range	R_H	$2^n L$
Depth Range	R_D	$2^m L$

Table 4.5: Simulation Specifications for Long Aperture

As in the previous section, these series of simulations show the effect of a moving source along the horizontal range (Figure 4.15). With the exception of the broadside inaccuracies, the long square array is partially accurate to locate sources at horizontal ranges of 4L and 8L at depth ranges of only 8L. As the source moves further to 16L R_H and goes deeper to 16L R_D , the broadside inaccuracies became wider but are still partially accurate for the rest of the source positions around the array. For deeper source positions around 32L R_D , the geometry is accurate for narrow bearings only, and in general terms is discarded as being inaccurate. When the source moves further to 128L R_H , the SRE increases in some wide areas and a progressive lack of accuracy is shown. At such far distances, the array geometry is accurate for a few narrow bearings only, and in general terms it is considered to be inaccurate. In summary, the long square array geometry was found to be partially accurate for horizontal ranges from 4L (30m) up to 64L (480m) with depth ranges of up to 16L (120m) R_D .

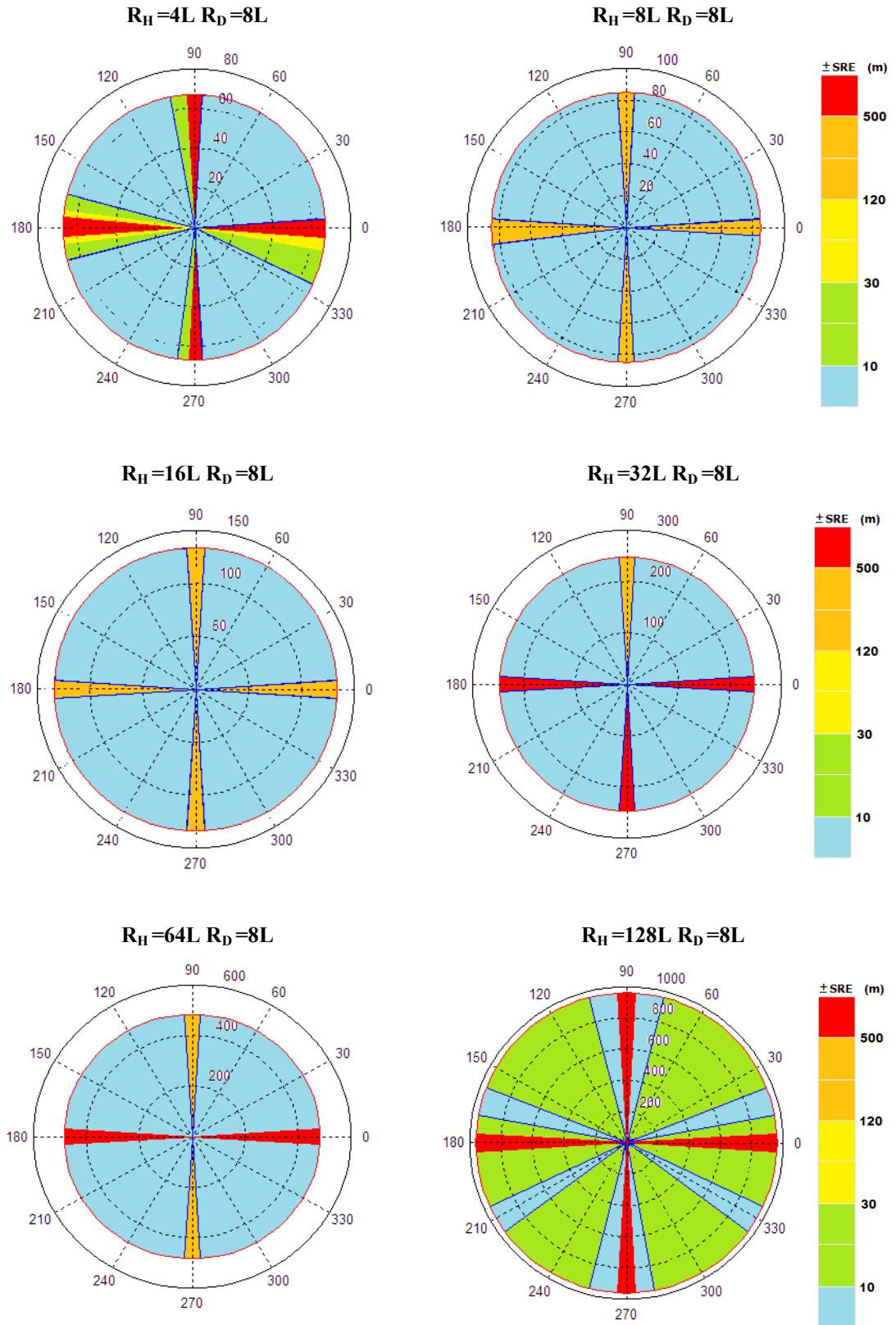


Figure 4.15: Long-Square-Array ($4L R_H$ to $128L R_H$). From horizontal ranges of $4L$ (30m) up to $64L$ (480m) the long-square geometry was found to be partially accurate. As the source moves further, on a horizontal range to $128L$ ($\sim 1\text{km}$), the detrimental effects on source range are noticeable.

4.5.3 Comparison Short Vs Long Aperture

A comparison of both apertures, short versus long, is shown in Table 4.6. The long-aperture is able to reach sources located at approximately $64L$ (0.5km) with partial accuracy. However, in comparison with its own aperture $16L$ (120m), it is able to reach range sources at only *four times* its aperture. The maximum depth range is only $16L$ (120m). The short-aperture is not able to locate any source range with sufficient accuracy.

	Short-Aperture (L)							Long-Aperture (16L)						
$R_D \backslash R_H$	L	2L	4L	8L	16L	32L	64L	L	2L	4L	8L	16L	32L	64L
8L	O	O	O	O	O	O	O	O	O	●	●	●	●	●
16L	O	O	O	O	O	O	O	O	O	O	O	●	●	●
32L	O	O	O	O	O	O	O	O	O	O	O	O	O	O
64L	O	O	O	O	O	O	O	O	O	O	O	O	O	O

O	Inaccurate	80% SRE $> \pm 10\text{m}$
●	Partially Accurate	80% SRE $< \pm 10\text{m}$
●	Accurate	100% SRE $< \pm 10\text{m}$

Table 4.6: Comparison table of Short Vs Long Aperture for the Square Geometry

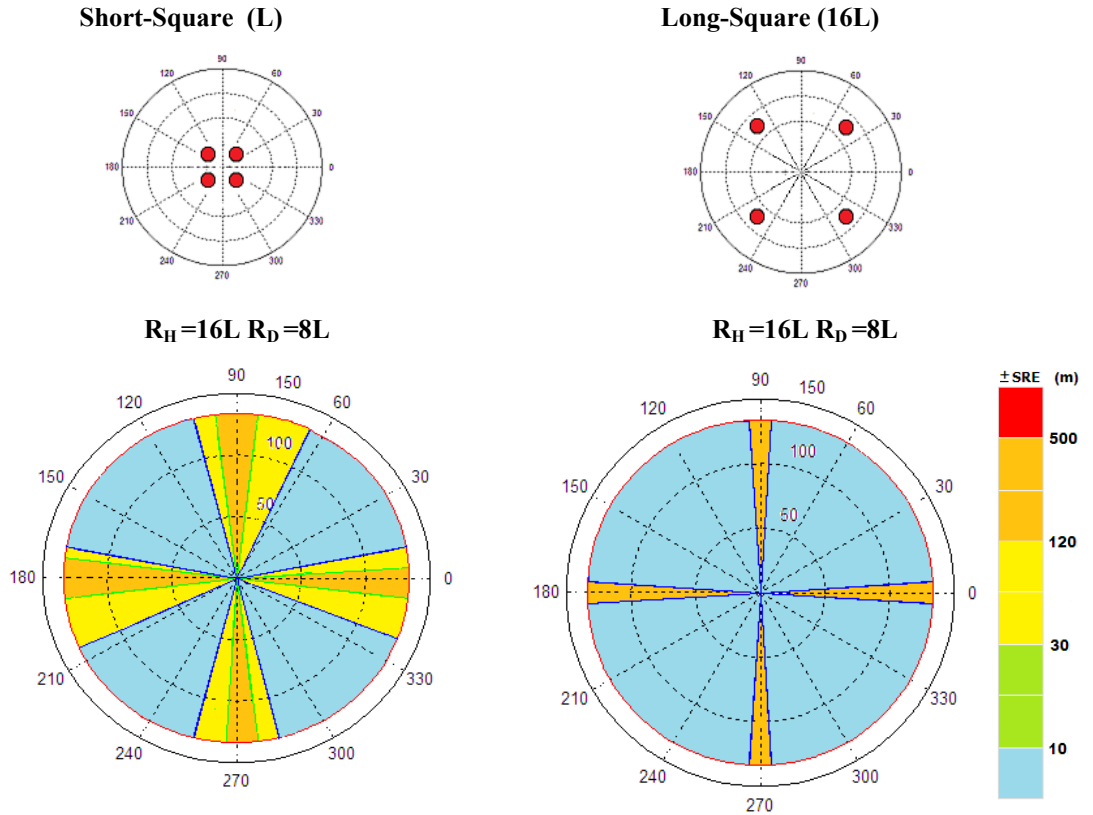


Figure 4.16: Short Vs Long aperture of a Square array ($16LR_H$ and $8LR_D$). The effects of increasing the aperture of the array geometry are clearly seen on the comparison of these two plots. A longer aperture decreases the SRE and improves its accuracy.

In Figure 4.16, the source was fixed at $16L R_H$ and $8L R_D$ for both apertures. When using the long-aperture, the broadside inaccuracies are reduced considerably. It can be seen that the long aperture is more accurate than the short one. However, no matter how far from or close to the source could be from the array, the square geometry will always have a lack of accuracy to locate source positions that are on broadside to its pairs or receivers.

4.6 Y-shape-Array

The Y-shape array-configuration, which also has four receivers, is peculiar in that receivers r_2 , r_3 and r_4 are referred to the same centre receiver r_1 . Each arm $\{(r_1, r_2), (r_1, r_3), (r_1, r_4)\}$ also has the same length (Figure 4.17).

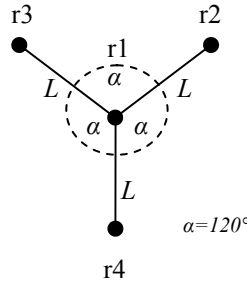


Figure 4.17: Superior view of a planar *Y-shape* array of 4 elements

4.6.1 Short Aperture (L)

The first aim of the Y-shape array experimental simulations is to investigate the behaviour of a short-aperture by varying R_H and R_D by the power of 2^n times L . The complete series of simulations is presented in Table 4.4. The general specifications for each of the following simulations in this section are shown in Table 4.7.

Figures 4.18 and 4.19 show the results of the experimental simulations. The short Y-shape array is completely accurate for horizontal ranges from L (7.5m) to $16L$ (120m) with depth ranges up to $32L$ (240m). There are no broadside inaccuracies and the SRE is definitely smaller than using a square-geometry (Figure 4.18). These are among the most important improvements that the Y-shape geometry has over the square-geometry. Then by $32L R_H$ the geometry is accurate for $8L R_D$ (60m) only. When the source

moves deeper, the array becomes partially accurate for depth ranges of $16L$ (120m) and $32L$ (240m). After that, the array-configuration becomes inaccurate for any further depth and horizontal source ranges (Figure 4.20).

Y-Array		$n = \{0, 1, \dots, 7\}$ $m = \{3, 4, \dots, 6\}$
Aperture length	A	Short (L)
Num. receivers	i	4
Receivers depth	r_d	L
Num. sources	S_V	100
Horizontal Range	R_H	$2^n L$
Depth Range	R_D	$2^m L$

Table 4.7: Simulation Specifications for Short Aperture

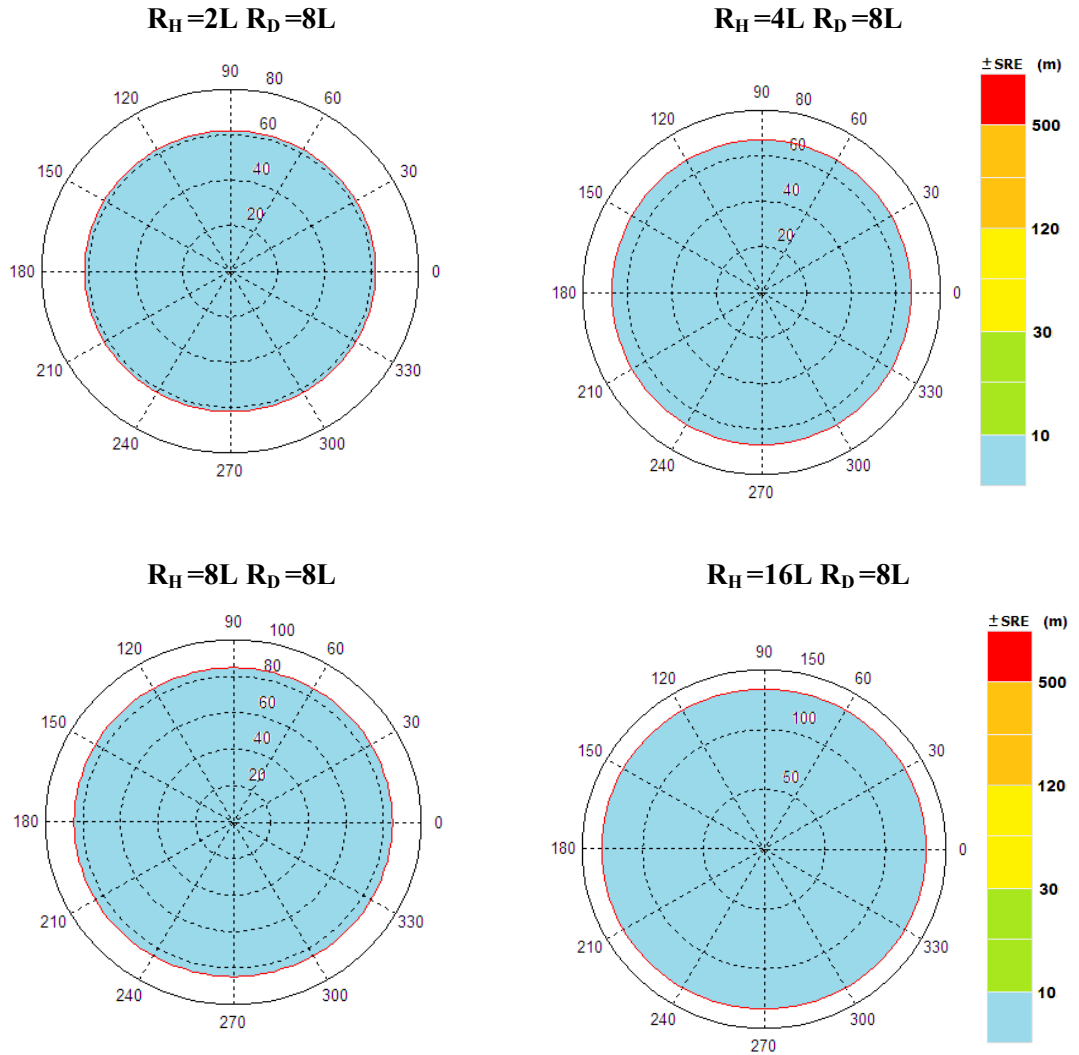


Figure 4.18: Short-Y-Array ($2LR_H$ to $16LR_H$). It was found to be completely accurate from horizontal ranges of $1L$ (7.5m) to $16L$ (120m) covering depth ranges for up to 240m ($32L$).

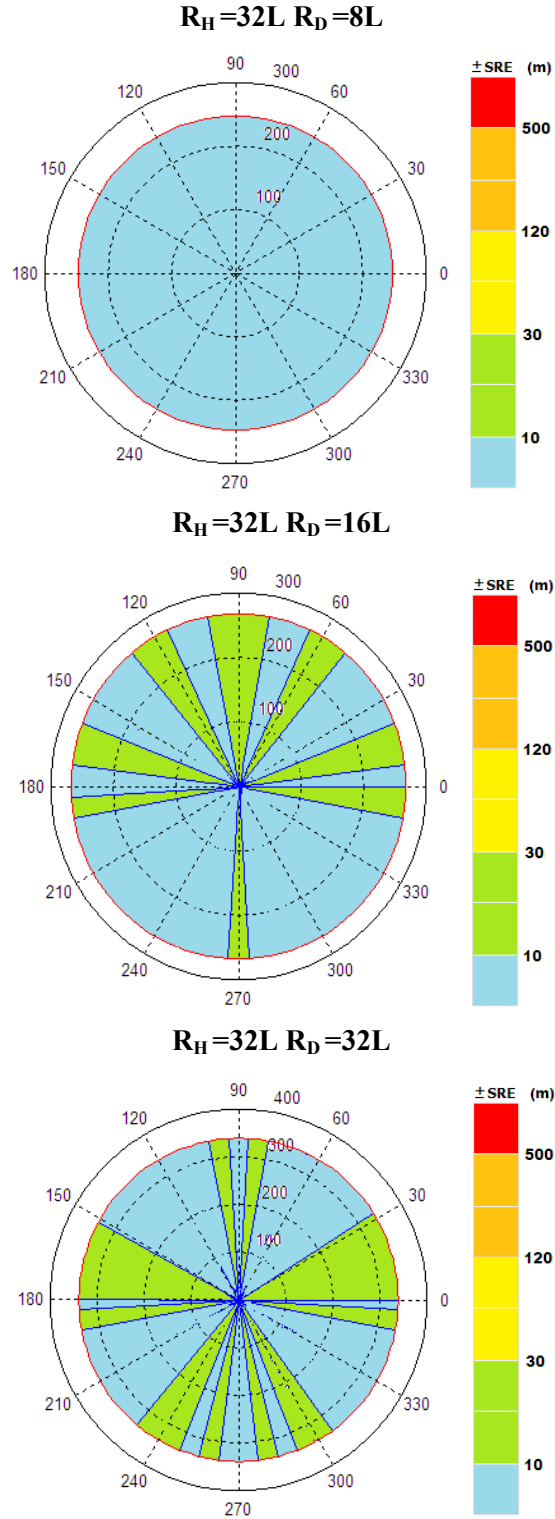


Figure 4.19: Short-Y-Array ($32L R_H$). The array is completely accurate for depth ranges of $8L$ (60m) and partially accurate for depth ranges of $16L$ (120m) and $32L$ (240m). After that, it becomes inaccurate for any source range.

In summary, the short Y-shape array geometry was found to be completely accurate for horizontal source ranges from $1L$ (7.5m) up to $16L$ (120m) at a maximum depth range of $32L$ (240m).

4.6.2 Long Aperture (16 L)

The second group of experimental simulations includes the same array geometry but with a longer aperture (16L). The general specifications for each of the following experimental simulations in this section are shown in Table 4.8.

Y-Array		$n = \{0, 1, \dots, 7\}$ $m = \{3, 4, \dots, 6\}$
Aperture length	A	Long (16L)
Num. receivers	i	4
Receivers depth	r_d	L
Num. sources	S_V	100
Horizontal Range	R_H	$2^n L$
Depth Range	R_D	$2^m L$

Table 4.8: Simulation Specifications for Long Aperture

By varying R_D and R_H by the power of 2^n times L, a series of simulations was performed, as shown in Table 4.4. The most relevant results are shown in Figures 4.20 and 4.21.

The long Y-shape array results are completely accurate for short horizontal ranges of 1L (7.5m) reaching depth ranges of up to 64L (480m). It is also able to reach horizontal ranges from 2L (15m) up to 32L (240m) at depth ranges no greater than 32L (240m) (Figure 4.20).

Although it remains completely accurate at horizontal ranges of 64L (480m), it does not do it for depth ranges greater than 8L (60m) (Figure 4.21). As the source moves to deeper and further horizontal ranges, the location accuracy decreases, becoming completely inaccurate.

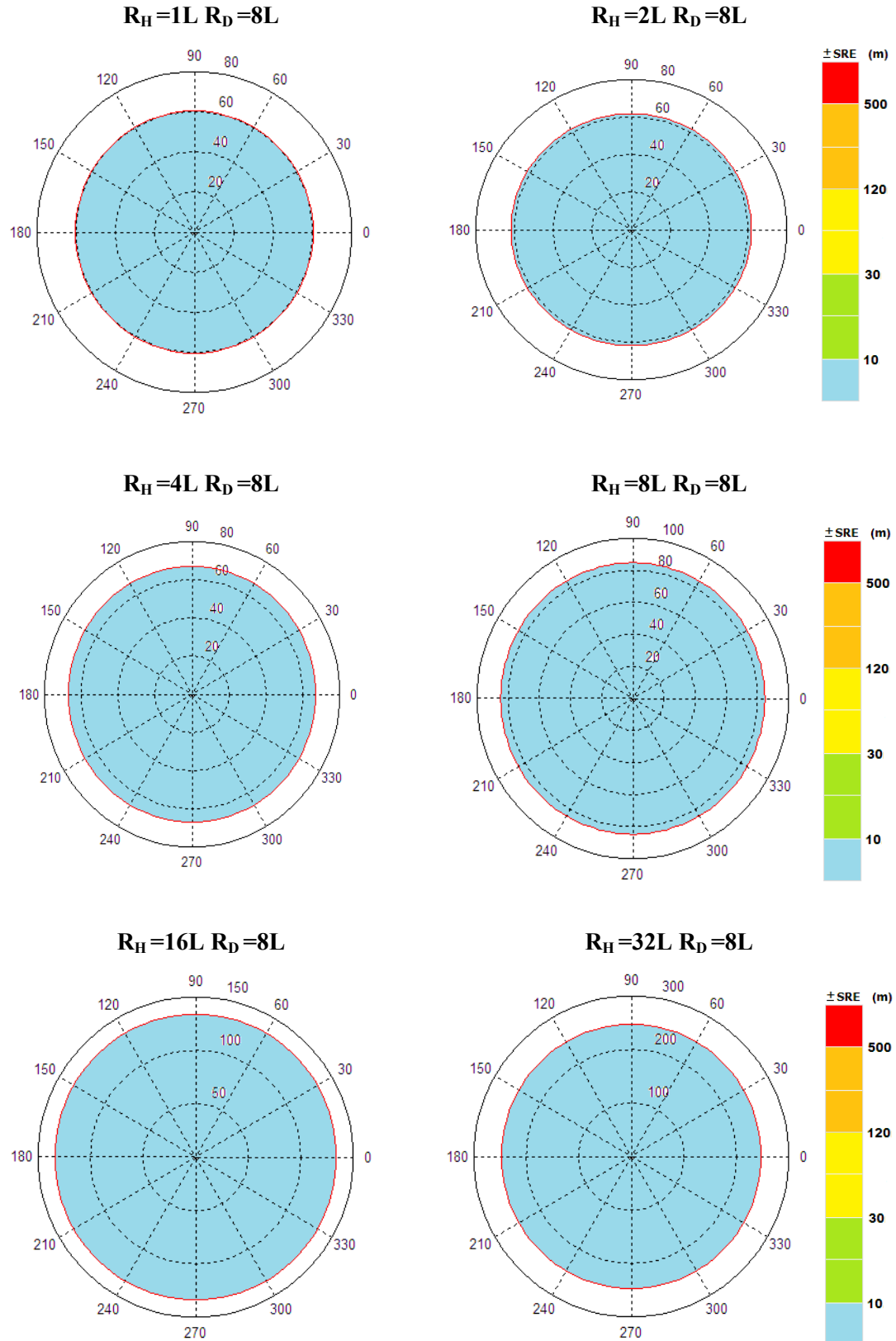


Figure 4.20: Long-Y-Array ($1L_{R_H}$ and $32L_{R_H}$). The array is completely accurate for horizontal ranges from $1L$ to $32L$ with an average maximum depth range of $240m$ ($32L$).

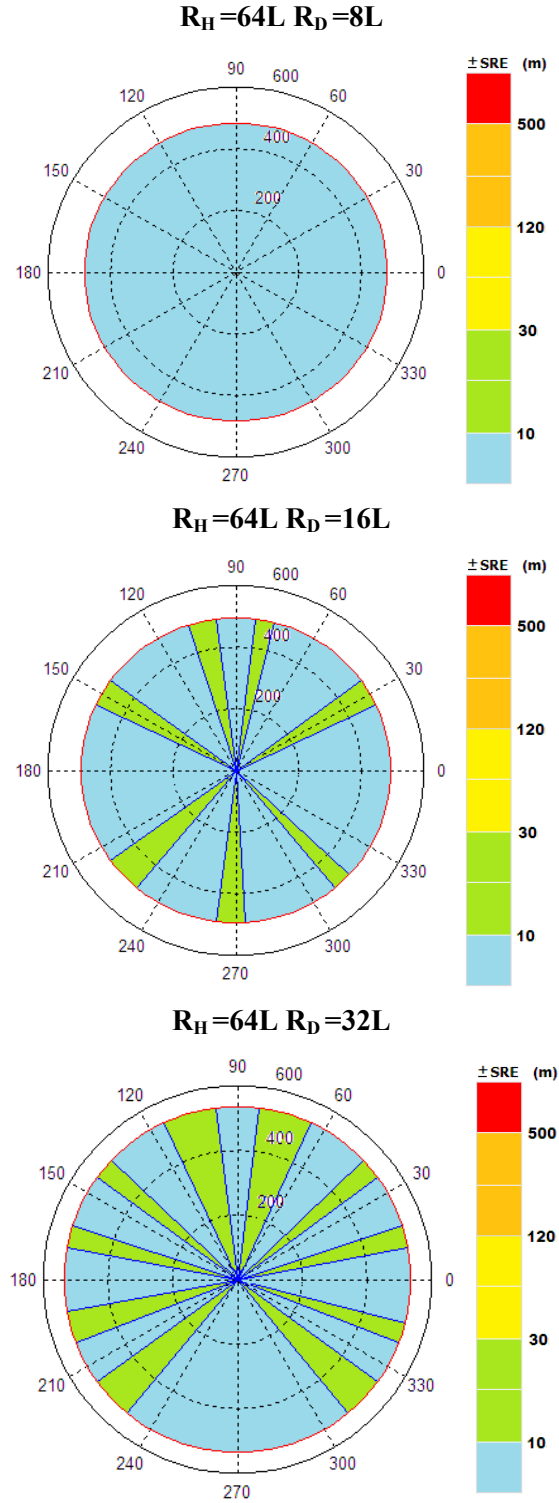


Figure 4.21: Long-Y-Array (64LR_H). The array is completely accurate for depth ranges of 8L (60m) and partially accurate for depth ranges of 16L (120m) and 32L (240m). After that, it becomes inaccurate for any source range.

4.6.3 Comparison Short Vs Long Aperture

A general comparison of both apertures, short versus long, is shown in Table 4.9 and Figure 4.22. A particular scenario is shown with the source fixed at $32L R_H$ and $16L R_D$.

	Short-Aperture (L)							Long-Aperture (16L)						
$R_D \backslash R_H$	L	2L	4L	8L	16L	32L	64L	L	2L	4L	8L	16L	32L	64L
8L	●	●	●	●	●	●	○	●	●	●	●	●	●	●
16L	●	●	●	●	●	○	○	●	●	●	●	●	●	○
32L	●	●	●	●	●	○	○	●	●	●	●	●	●	○
64L	○	○	○	○	○	○	○	●	○	○	○	○	○	○

○ Inaccurate 80% SRE $> \pm 10m$
 ○ Partially Accurate 80% SRE $< \pm 10m$
 ● Accurate 100% SRE $< \pm 10m$

Table 4.9: Comparison table of Short Vs Long Aperture for the Y-shape Geometry

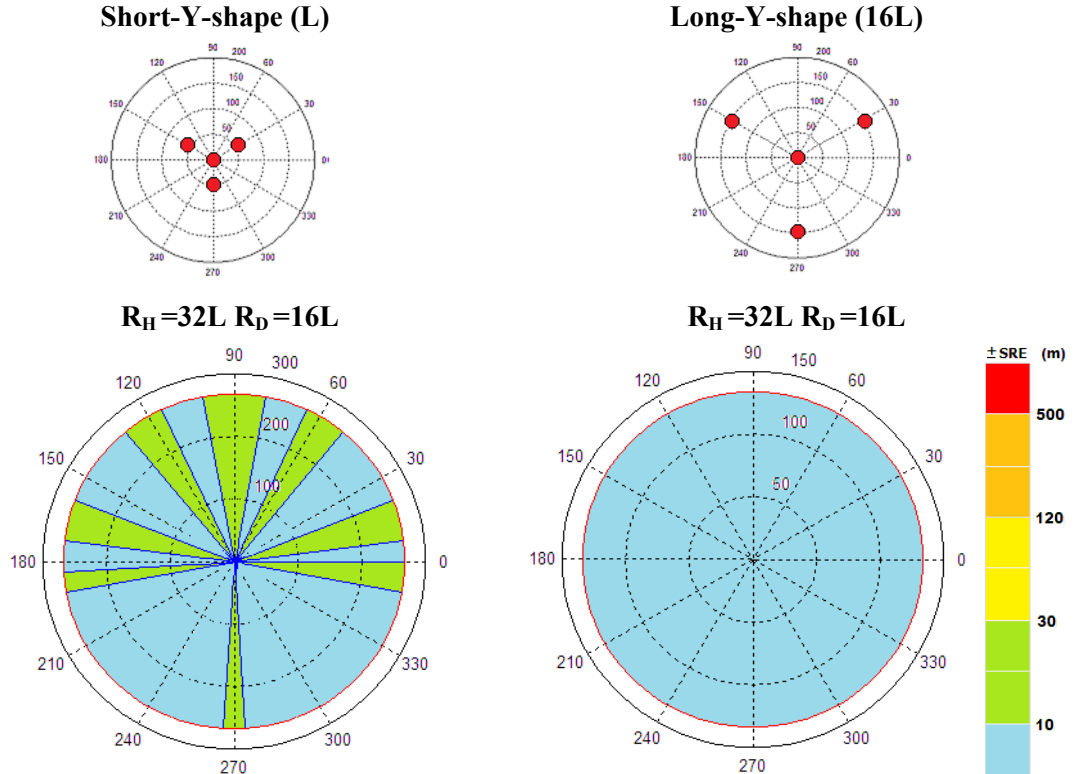


Figure 4.22: Short Vs Long aperture of a Y-shape array ($32L R_H$ and $16L R_D$). In the same way as happened with the Square array, a longer aperture decreases the SRE and improves its accuracy.

The short-aperture array is accurate for only a determined number of source range estimations. The short-aperture has a maximum R_H location of 32L (240m). The long-aperture has a maximum R_H location of 64L (~0.5km). In terms of maximum horizontal range location, the long-aperture is twice as accurate when locating further sources. When looking at the ratio of maximum horizontal range versus aperture, it is noticeable that the long-aperture is only accurate for four times (4:1) its own aperture. The short-aperture is accurate for thirty two times (32:1) its own aperture.

4.7 Comparison Square Vs Y-shape

The Square and Y-shape array configurations are two basic examples of the effects that the array geometry of four elements has in source range estimation of an idealized scenario. Table 4.10 shows a summary of the results of the experimental simulations described in this chapter.

Short-Aperture

	Square Array							Y-shape Array						
$R_D \backslash R_H$	L	2L	4L	8L	16L	32L	64L	L	2L	4L	8L	16L	32L	64L
8L	O	O	O	O	O	O	O	●	●	●	●	●	●	O
16L	O	O	O	O	O	O	O	●	●	●	●	●	●	O
32L	O	O	O	O	O	O	O	●	●	●	●	●	●	O
64L	O	O	O	O	O	O	O	O	O	O	O	O	O	O

Long-Aperture

	Square Array							Y-shape Array						
$R_D \backslash R_H$	L	2L	4L	8L	16L	32L	64L	L	2L	4L	8L	16L	32L	64L
8L	O	O	●	●	●	●	●	●	●	●	●	●	●	●
16L	O	O	O	O	●	●	●	●	●	●	●	●	●	●
32L	O	O	O	O	O	O	O	●	●	●	●	●	●	●
64L	O	O	O	O	O	O	O	●	O	O	O	O	O	O

O Inaccurate 80% SRE $> \pm 10m$
 ● Partially Accurate 80% SRE $< \pm 10m$
 ● Accurate 100% SRE $< \pm 10m$

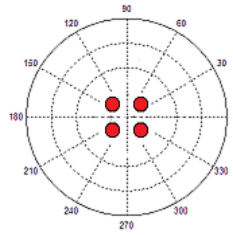
Table 4.10: Comparison table of Square Vs Y-shape Geometries (short and long apertures)

Although the Square array is the simplest and easiest configuration to deploy, it fails to reach with accuracy source positions that are located on the broadside of each pair of receivers. Certainly, a long aperture improves the partial accuracy to reach further sources up to $64L$. Nevertheless, the broadside inaccuracies are always present. The square geometry is only partially accurate to reach sources found at maximum depth ranges of $16L$, and since most cetaceans are able to dive to greater depths, the square geometry runs the risk of becoming useless for many scenarios.

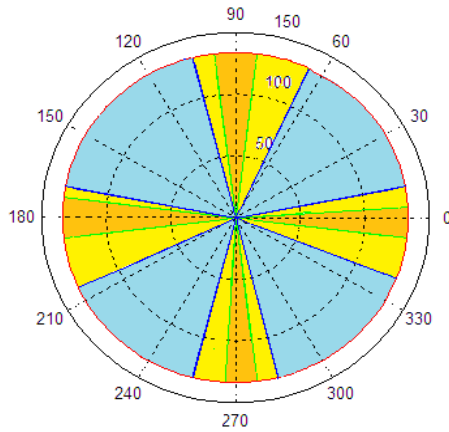
The Y-shape array has the same number of receivers as the Square array. However, these are arranged with a different geometry. Such changes are sufficient to eliminate the inaccuracies that each pair of receivers of the square geometry has. The Y-shape array is in terms of accuracy, superior to the square geometry on both apertures, short and long.

Figure 4.23 shows the same source scenario of $16L$ R_H and $8L$ R_D using four different array configurations: Short-Square (L), Long-Square ($16L$), Short-Y-shape (L) and Long-Y-shape ($16L$). It also shows a clear example of the effects associated with each array configuration in source range estimation. Two main conclusions are reached: (1) No matter what type of aperture-array is used, the Square array will always lack complete accuracy. (2) The long aperture of any array geometry decreases the slant range error and improves its accuracy.

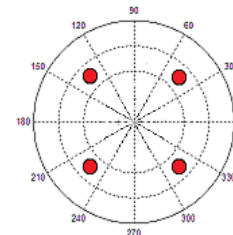
Short-Square (L)



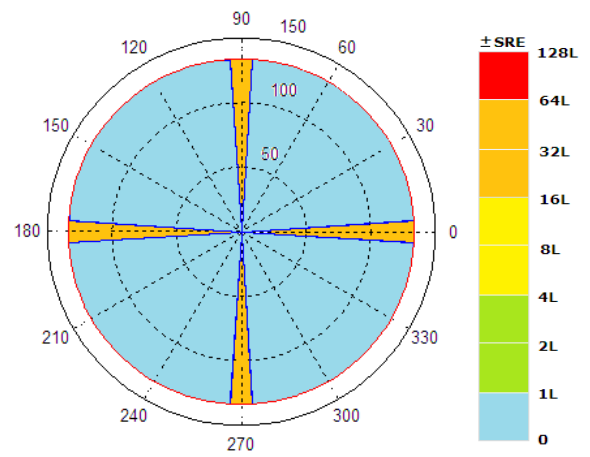
$$R_H=16L \quad R_D=8L$$



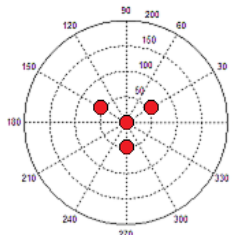
Long-Square (16L)



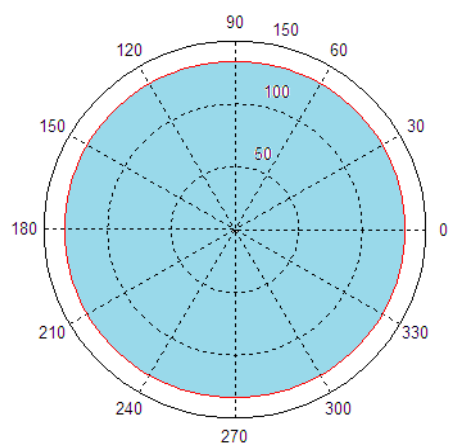
$$R_H=16L \quad R_D=8L$$



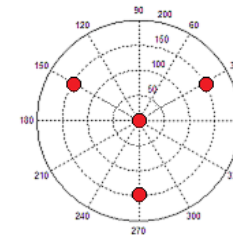
Short-Y-shape (L)



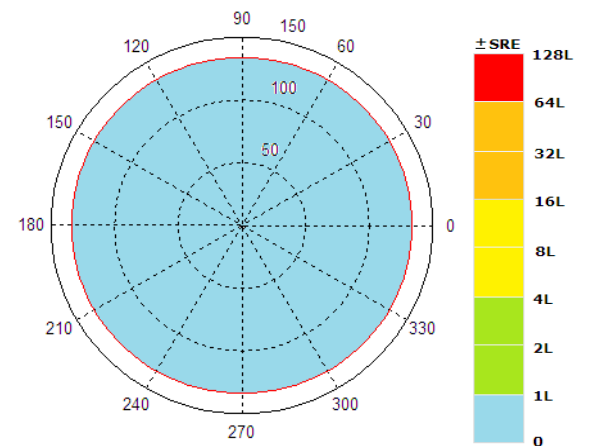
$$R_H=16L \quad R_D=8L$$



Long-Y-shape (16L)



$$R_H=16L \quad R_D=8L$$



Short-Y-shape (L)

Long-Y-shape (16L)

Figure 4.23: Comparison of Square Vs Y-shape array ($16LR_H$ and $8LR_D$). Short and Long apertures.

4.8 Other Array-Configurations

Typical array geometries of four receivers that would be practical to deploy in a two-linear towed array are also considered in this section. The array geometries are *Trapezium*, *Triangular*, and *Shifted-pair*, as shown in Figure 4.24.

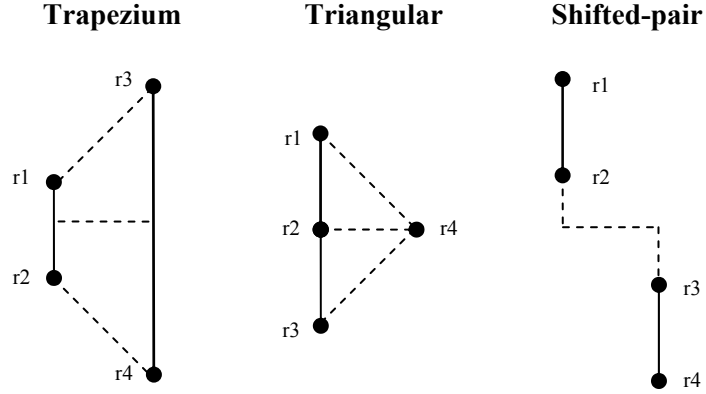


Figure 4.24: Five typical array geometries of elements.

The performance of each geometry is investigated by using the same number of experimental simulations shown in Table 4.4 and the same specifications as Square and Y-shape geometries (see Tables 4.3 and 4.7). The pair of hydrophones used are $\{(r_1, r_2), (r_1, r_3), (r_1, r_4)\}$.

4.8.1 Trapezium-Array

Trapezium-array is a quadrilateral geometry with only two opposite sides parallel. Two hydrophones are deployed in each arm of the linear towed array. The length of the right pair (r_3, r_4) is three times the length of the left pair (r_1, r_2) (Figure 4.25).

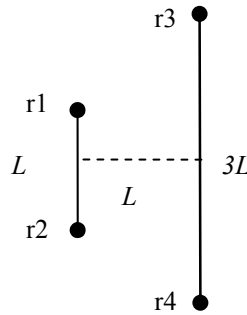


Figure 4.25: Superior view of a planar *Trapezium* array of 4 elements

Table 4.11 and Figure 4.26 show a summary of the simulation results obtained.

	Short-Aperture (L)							
$R_D \backslash R_H$	L	2L	4L	8L	16L	32L	64L	128 L
8L	O	O	O	●	●	O	O	O
16L	O	O	O	O	O	O	O	O
32L	O	O	O	O	O	O	O	O
64L	O	O	O	O	O	O	O	O

O Inaccurate 80% SRE $> \pm 10m$
 ● Partially Accurate 80% SRE $< \pm 10m$
 ● Accurate 100% SRE $< \pm 10m$

Table 4.11: Summary of the Simulation Results for the Trapezium Geometry

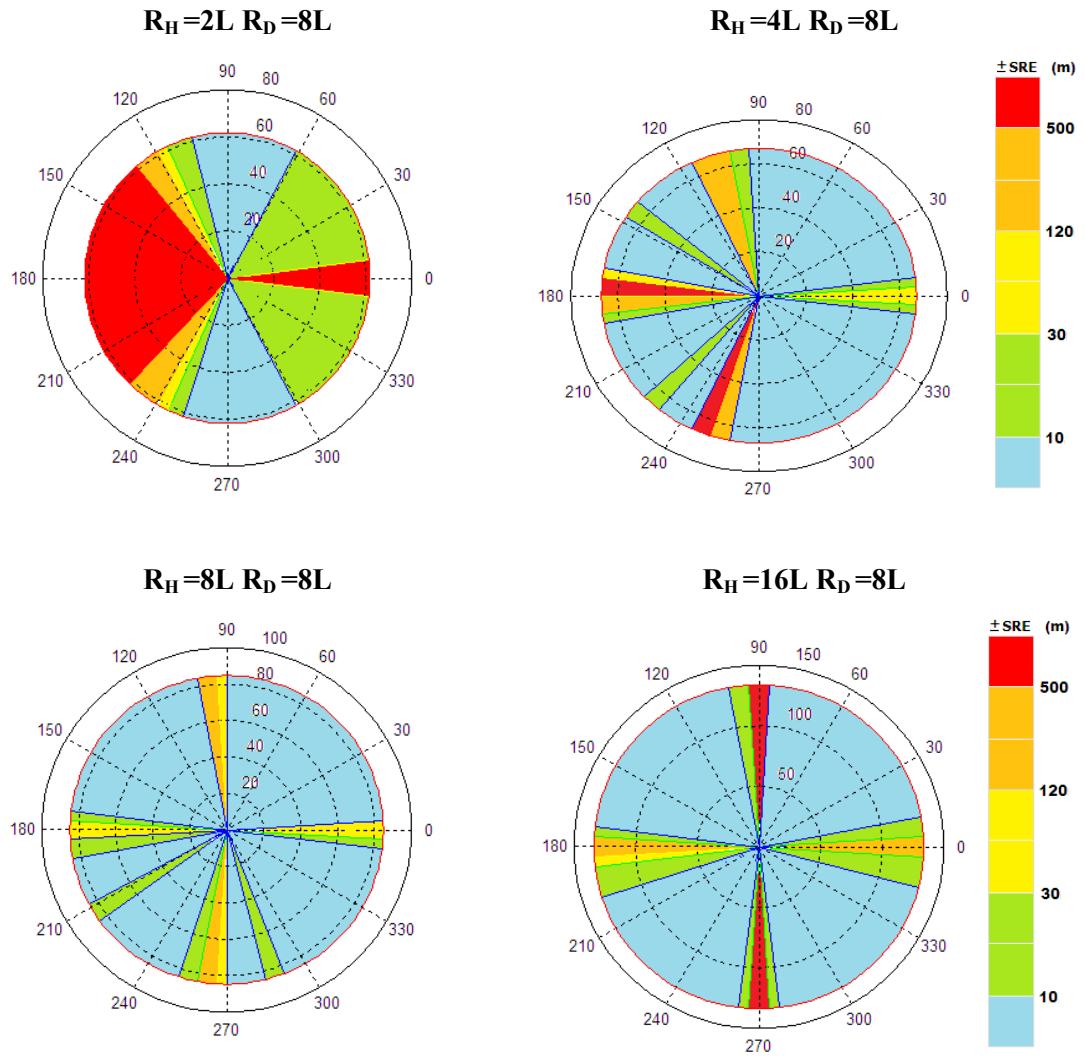


Figure 4.26: Trapezium-Array ($2LR_H$ to $16LR_H$). It is only partially accurate from horizontal ranges of $4L$ (7.5m) to $16L$ (120m) covering depth ranges for up to $8L$ (60m).

This geometry resulted in most cases being inaccurate. It is only partially accurate for horizontal ranges from $8L$ to $16L$ and depth ranges up to $8L$. As happens in the square geometry, the broadside condition is always present. There is no major performance in its accuracy when increasing the array-aperture. It constitutes a non-recommendable array geometry to deploy.

4.8.2 Triangular-Array

The *Triangular geometry* has three hydrophones deployed in one arm of the linear towed array and a single hydrophone in the other arm. The length for each pair of hydrophones is the same (Figure 4.27). Table 4.12 and Figure 4.28 show a summary of the simulation results obtained.

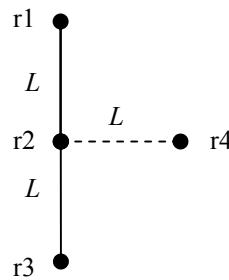


Figure 4.27: Superior view of a planar *Triangular* array of 4 elements

	Short-Aperture (L)							
$R_D \backslash R_H$	L	2L	4L	8L	16L	32L	64L	128 L
8L	●	●	●	●	O	O	O	O
16L	O	O	O	O	O	O	O	O
32L	O	O	O	O	O	O	O	O
64L	O	O	O	O	O	O	O	O

O	Inaccurate	80% SRE $> \pm 10m$
●	Partially Accurate	80% SRE $< \pm 10m$
●	Accurate	100% SRE $< \pm 10m$

Table 4.12: Summary of the Simulation Results for the Triangular Geometry

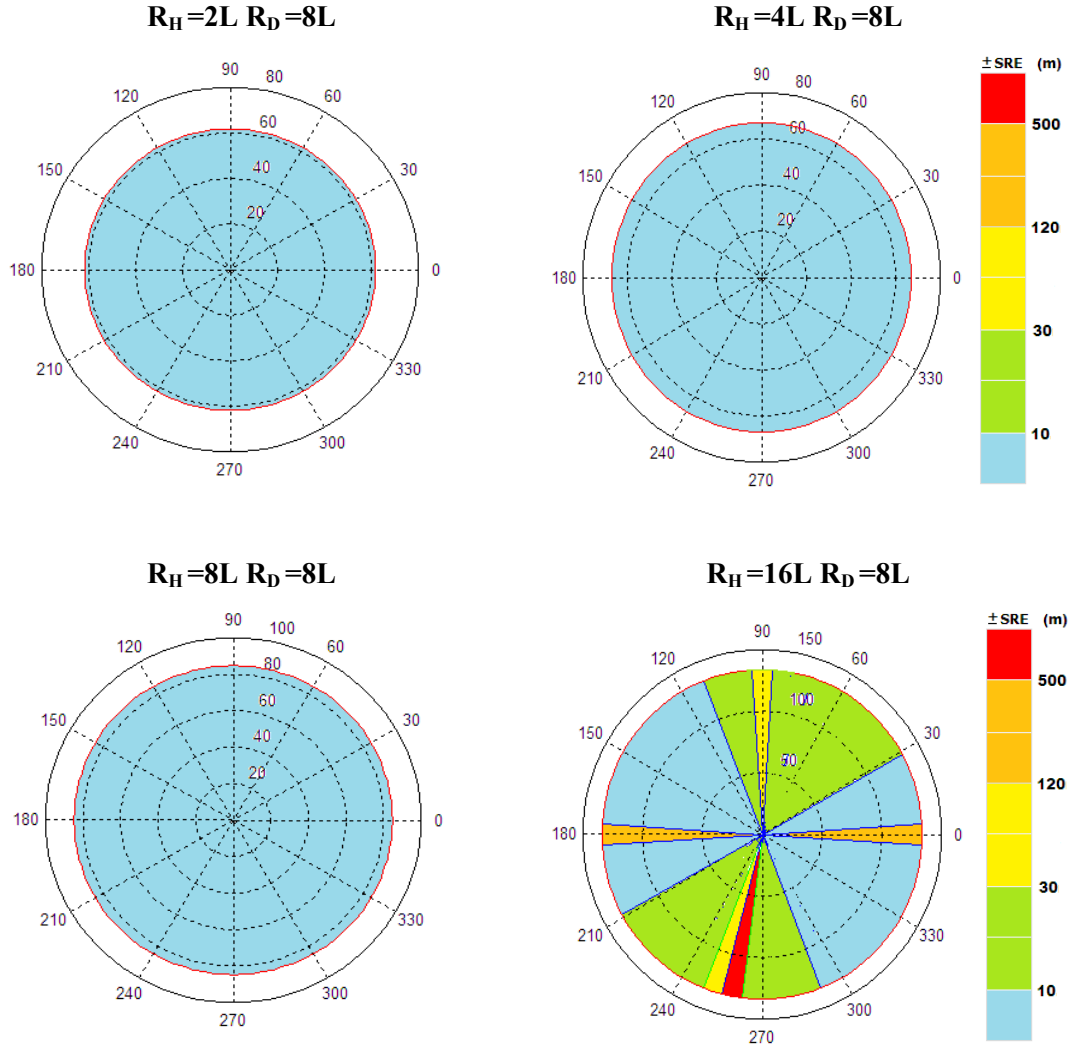


Figure 4.28: Triangular-Array ($2LR_H$ to $16LR_H$). It is completely accurate from horizontal ranges of L (7.5m) to $8L$ (60m) covering depth ranges for up to $8L$ (60m). Then, it becomes inaccurate for further horizontal and depth ranges as shown in the inferior-right plot.

Unlike the trapezium geometry, the triangular geometry is completely accurate from horizontal ranges of $1L$ to $8L$ covering only depth ranges for up to $8L$. Some inaccuracies as the broadside condition become present when the source reaches the $16L$ R_H . A longer aperture-array helps to improve its accuracy to reach longer horizontal source ranges. However, its major limitation is its inaccuracy when reaching deeper source positions. It constitutes a recommendable array geometry to deploy only for shallow sources (i.e. 60m) with short horizontal ranges (i.e. 60m).

4.8.3 Shifted-pair-Array

The *Shifted-pair geometry* is similar to a square geometry, but with the exception that one side-pair of hydrophones is shifted at least one length-pair, as shown in Figure 4.29.

Table 4.13 and Figure 4.30 show a summary of the simulation results obtained.

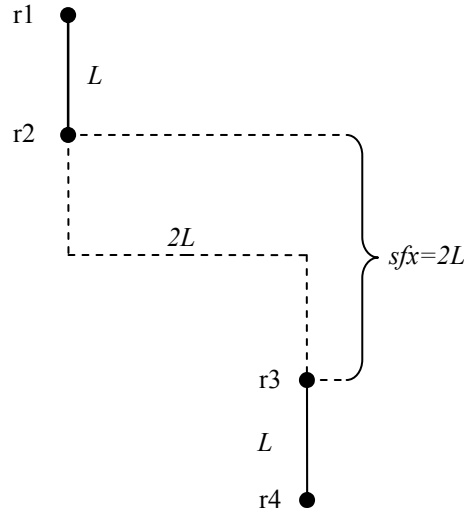


Figure 4.29: Superior view of a planar *Trapezium* array of 4 elements

$R_D \backslash R_H$	Short-Aperture (L) $sfx=2L$							Long-Aperture (16L) $sfx=32L$						
	L	2L	4L	8L	16L	32L	64L	L	2L	4L	8L	16L	32L	64L
8L	●	●	●	●	●	○	○	●	●	●	●	●	○	○
16L	●	●	●	●	●	○	○	●	●	●	●	●	○	○
32L	●	●	●	●	●	○	○	●	●	●	●	●	○	○
64L	○	○	○	○	○	○	○	●	●	●	●	●	○	○

○	Inaccurate	80% SRE $> \pm 10m$
◐	Partially Accurate	80% SRE $< \pm 10m$
●	Accurate	100% SRE $< \pm 10m$

Table 4.13: Summary of the Simulation Results for the Shifted-pair Geometry

The results from the performance of this geometry are very interesting. Unlike the square geometry which resulted in being totally inaccurate when using a short aperture, the *shifted-pair* geometry is accurate for reaching a broad range of source locations. The key factor of its accuracy is defined by the *shifted distance* (sfx) between hydrophone pairs (r_1, r_2) and (r_3, r_4). To accomplish a source range estimation with enough accuracy, sfx must have at least the value of one length of the hydrophone pair.

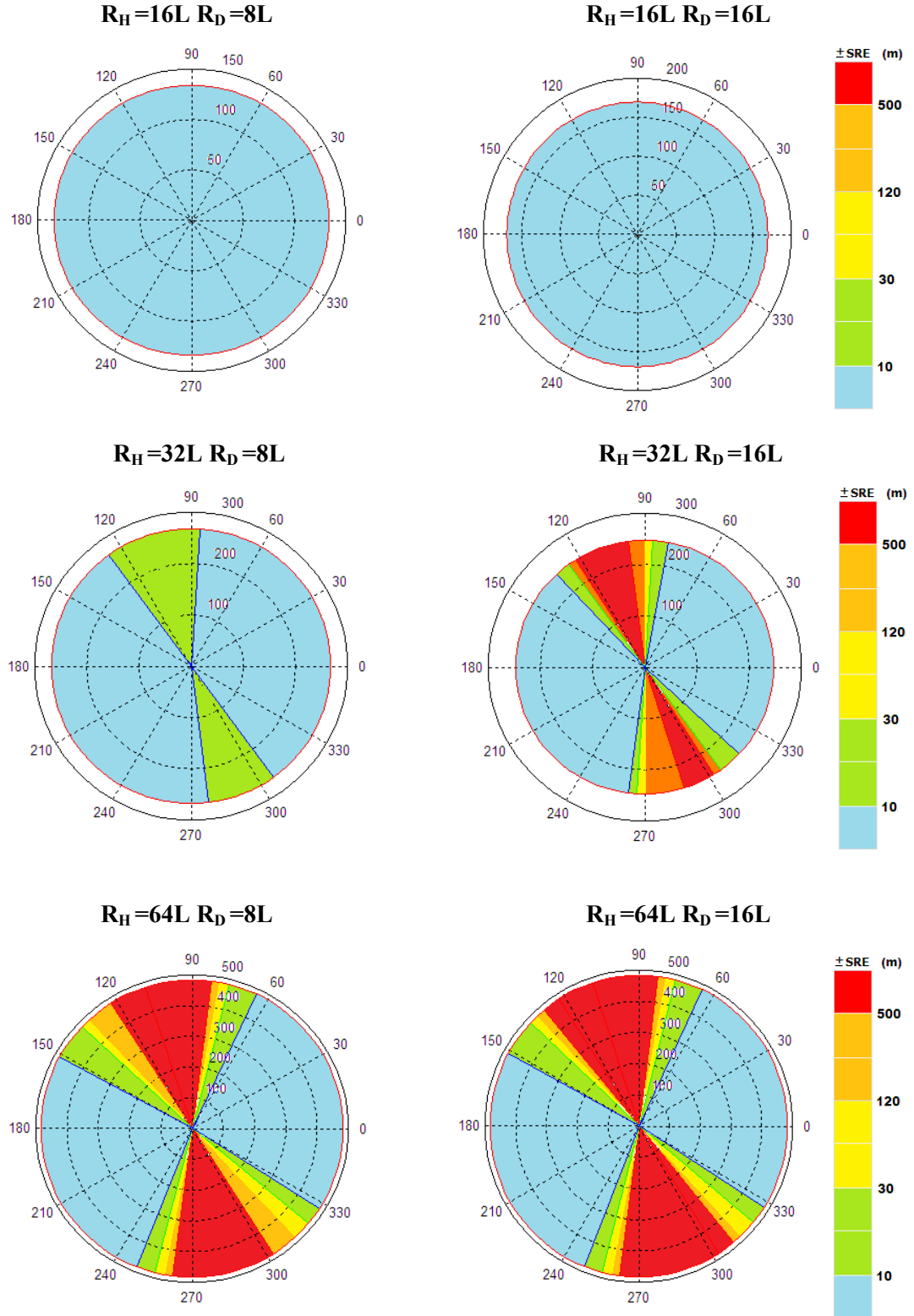


Figure 4.30: Short Shifted-pair ($16LR_H$ to $64LR_H$). The left column corresponds to depth source ranges of $8L$ ($60m$). The right column corresponds to depth source ranges of $16L$ ($120m$). The geometry is accurate for horizontal ranges of up to $16L$ ($120m$) and only partially accurate for horizontal ranges of $32L$ ($240m$). It becomes inaccurate for further horizontal ranges.

If the sfx is zero or less than the length of the hydrophone pair, the results are less accurate, being accurate up to horizontal ranges of $8L$ only.

If sfx is equal to or bigger than the length of the hydrophone pair, the *short* array-geometry is accurate when reaching horizontal ranges of $16L$, as shown in Table 4.13.

If instead of using a short-aperture (L) a long-aperture ($16L$) is used, the *long* array-geometry is accurate for reaching deeper ranges of up to $64L$. The partial accuracy is increased to horizontal ranges of $64L$, as shown in Figure 4.31.

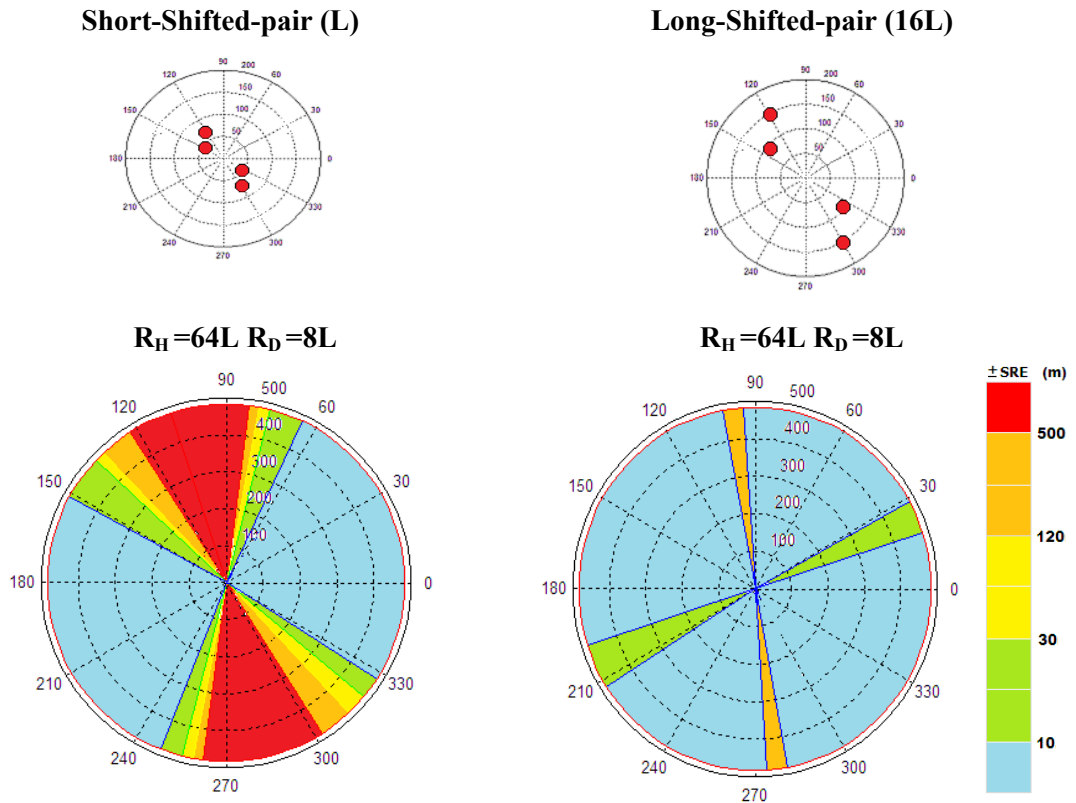


Figure 4.31: Comparison of a Short Vs Long array-aperture at source ranges of $64LR_H$ and $8LR_D$.

Two of the advantages of the *shifted-pair* over the *Y-shape* geometry are its capability to reach deeper source ranges ($64L$) when using a long aperture array and its simplicity for deployment. Nevertheless, in terms of horizontal source ranges, the *Y-shape* geometry continues to be more accurate than the *shifted-pair* and any other array geometry of 4 elements presented in this thesis.

4.8.4 Circular-Array

Other array-configuration also attempted in this thesis is the *Circular geometry* (Figure 4.32) with five receivers and four pair of receivers. The radius of the virtual circle is L_0 . Each of the two groups of pairs $\{(r_1, r_2), (r_1, r_3)\}$ and $\{(r_1, r_4), (r_1, r_5)\}$ has the same length respectively. The radius of the virtual circle is L .

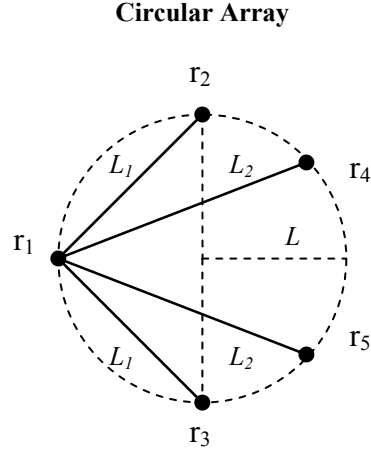


Figure 4.32: Superior view of a planar *Circular* array of 5 elements

Figure 4.33 shows an experimental simulation using the specifications of Table 4.14. The horizontal source range had a noticeable improvement against any other of the previous geometries. A long circular array of 5 elements appears to offer a greater range capability [109].

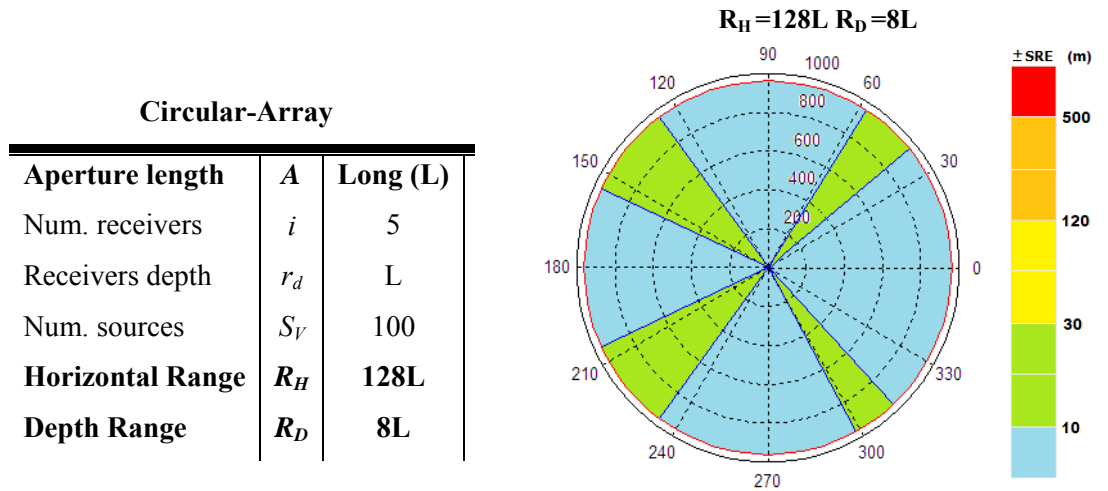


Figure 4.33: Long-Circular-Array ($128LR_H$ $8LR_D$). This array-configuration is partially accurate for reaching ranges of $128L$ (~1km).

Table 4.14: Simulation Specifications for a Circular array

4.8.5 Summary

Tables 4.15 and 4.16 show a summary of the five array geometries of the four elements described previously. Table 4.15 focuses on those source ranges reached with 100% accuracy ($SRE < \pm 10m$). Table 4.16 focuses on those source ranges reached with 80% accuracy ($SRE < \pm 10m$). To determine which array-configuration offers the best performance, it is important to analyse the advantages and disadvantages. In a real scenario, there will be times when a source range accuracy of less than $\pm 10m$ becomes an important factor – i.e. mitigation purposes, – and there will be other times when a less accurate source range location is adequate – i.e. population studies. There will be occasions where there is a need to track deep source dive profiles (e.g. 500m) and occasions where the shallow waters (e.g. 60m) is the main concern. The author considers four fixed source ranges to serve as an example measure. A “subjective score” (0 to 10) is allocated to each geometry.

The metric values are, 32L (240m) for horizontal long ranges, 8L (60m) for horizontal short ranges, 64L (480m) for deep waters and 8L (60m) for shallow waters.

100% Accuracy ($SRE < \pm 10m$)										
Source Ranges	Y-shape	S	Shifted-pair	S	Triangular	S	Trapezium	S	Square	S
RH Long	32L	10	16L	5	8L	2.5	-	0	-	0
RH Short	8L	10	8L	10	8L	10	-	0	-	0
RD Deep	32L	5	32L	5	8L	1.2	-	0	-	0
RD Shallow	8L	10	8L	10	8L	10	-	0	-	0
Score (S)		8.8		7.5		5.9		0		0

R_H Horizontal Range Long (32L) Short (8L)
 R_D Depth Range Deep (64L) Shallow (8L)

Table 4.15: Summary of Maximum and Minimum Accurate Source Ranges

80% Accuracy ($SRE < \pm 10m$)										
Source Ranges	Shifted-pair	S	Y-shape	S	Trapezium	S	Triangular	S	Square	S
RH Long	32L	10	32L	10	16L	5	8L	2.5	-	0
RH Short	8L	10	8L	10	8L	10	8L	10	-	0
RD Deep	64L	10	32L	5	8L	1.2	8L	1.2	-	0
RD Shallow	8L	10	8L	10	8L	10	8L	10	-	0
Score (S)		10		8.8		6.6		5.9		0

R_H Horizontal Range Long (32L) Short (8L)
 R_D Depth Range Deep (64L) Shallow (8L)

Table 4.16: Summary of Maximum and Minimum Partially-Accurate Source Ranges

The array-configuration with 100% accuracy and the highest score given is the Y-shape array (8.8); in second place is the shifted-pair array (7.5) and in third place the triangular array (5.9). The trapezium and square arrays perform poorly because of their limited capability in partial and total inaccuracy, respectively. For shallow water scenarios and horizontal short ranges, the triangular geometry is an appropriate array-configuration with a score of 10 (Table 4.15).

The array-configuration with 80% accuracy and the highest score given is the shifted-pair array (10); in second place (8.8) is the Y-shape array and in third place (6.6) the trapezium array (6.6). The triangular array occupies the fourth place (5.9) and the square array is left again in last place because of its inaccurate capability of reaching source ranges. For shallow water scenarios and horizontal short ranges, the trapezium array is also considered as an appropriate array-configuration with score of 10. It is left as an intermediate option for horizontal long ranges (Table 4.16).

4.9 Choice of Pair Combinations

To investigate whether the performance of the geometries presented in the last sections (4.5 - 4.8) improves with different choices of pair combinations, this section examines the influence of two pair combinations.

The number of possible pair combinations that a receiver-array can have is given by the binomial coefficient (also known as the “choose function”) [129].

$$C_n^k = \binom{n}{k} = \frac{n!}{k!(n-k)!} \quad (4.4)$$

where n is the number of receivers and k is the size of each set of combinations.

For instance, from (4.2) it is found that four receivers have *six* pair-combinations $\{(r_1, r_2), (r_1, r_3), (r_1, r_4), (r_2, r_3), (r_2, r_4), (r_3, r_4)\}$. Since the minimal number of pairs necessary to get a 3D source location is a pair combination of three, the total number of *choices* with three pair-combinations is *twenty*. Any of these pair combinations could be used to make the hyperboloids converge into one solution.

Nevertheless, since each choice of pair combination changes the geometry distribution of the pair of hydrophones, *three* particular choices were investigated as exemplar pair-combinations:

$$C1 = \{(r_1, r_2) (r_1, r_3) (r_1, r_4)\}$$

$$C2 = \{(r_1, r_2) (r_2, r_3) (r_3, r_4)\}$$

$$C3 = \{(r_4, r_1) (r_4, r_2) (r_4, r_3)\}$$

A percentage graph is used to show the results achieved. The vertical axis shows the percentage of the sources located within $\pm 10m$. The horizontal axis shows the different horizontal source ranges for a fixed depth range of $8L$ ($60m$). $C1$, $C2$ and $C3$ constitute the three different choices of pair combinations used in each simulation.

4.9.1 Square Geometry

When using a *square geometry*, choice C2 shows a better performance over choices C1 and C3. Choice C2 has an improvement of 5% on average over the other choices. Nevertheless, that improvement is not sufficient to make the array-geometry more accurate. All experimental simulations remain under 80% of accuracy (Figure 4.34).

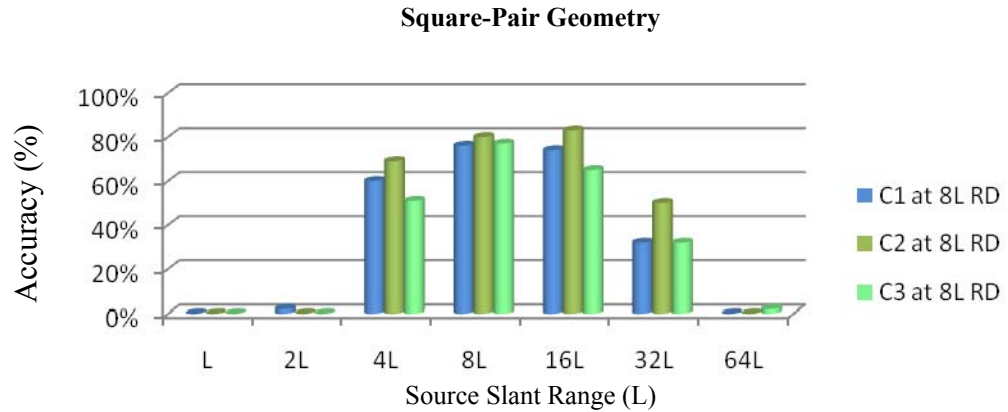


Figure 4.34: Pair-Combination Comparison of the Square Geometry. All experimental simulations remain under 80% of accuracy, making the the array-geometry inaccurate.

4.9.2 Triangular Geometry

When using a *triangular geometry*, choice C2 shows a slightly better performance over choices C1 and C3. For horizontal source ranges of L to 8L, choice C2 has a slightly improvement of only 2.5% on average. Then, by 16L and onwards the accuracy of the array starts to decrease, no matter what choice of pair-combination is used. By 32L, the triangular geometry is found below 80% of accuracy (Figure 4.35).

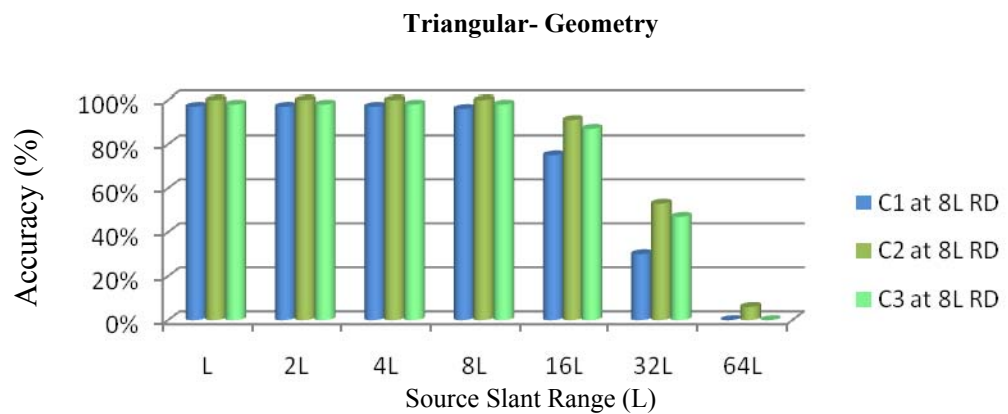


Figure 4.35: Pair-Combination Comparison of the Triangular Geometry. Choice C2 shows a slightly better performance over choices C1 and C3.

4.9.3 Trapezium Geometry

When using a *trapezium geometry*, choices C1, C2 and C3 show a more redundant performance. Each of them presents similar results, sometimes having a slightly better performance over the others, but in general terms the difference is minimal. The trapezium geometry is only partially accurate for horizontal source ranges of 8L and 16L (Figure 4.36).

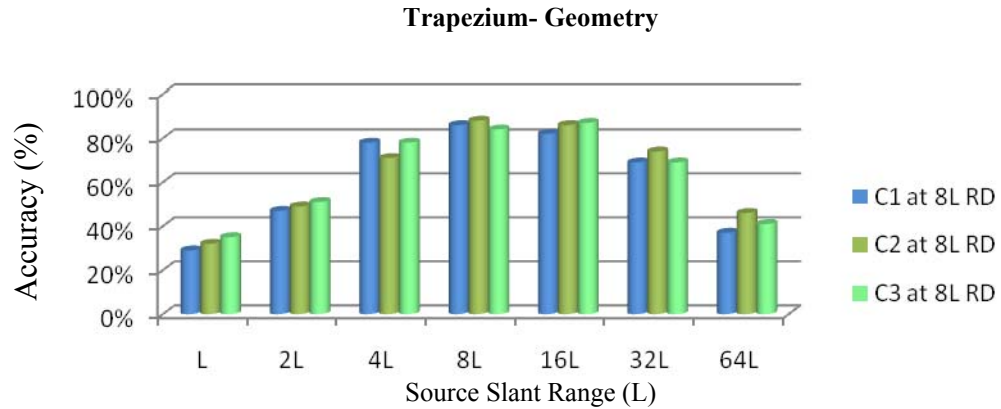


Figure 4.36: Pair-Combination Comparison of the Trapezium Geometry. Redundant performance and partially accurate for horizontal source ranges of 8L and 16L.

4.9.4 Shifted-pair Geometry

When using a *shifted-pair geometry*, the performance of the three choices is totally redundant. The average variation between choices C1, C2 and C3 is nil. At slant ranges of 32L and onwards, the accuracy of the array starts to decrease and some minor variation in the choice of pair-combination is visible (Figure 4.37).

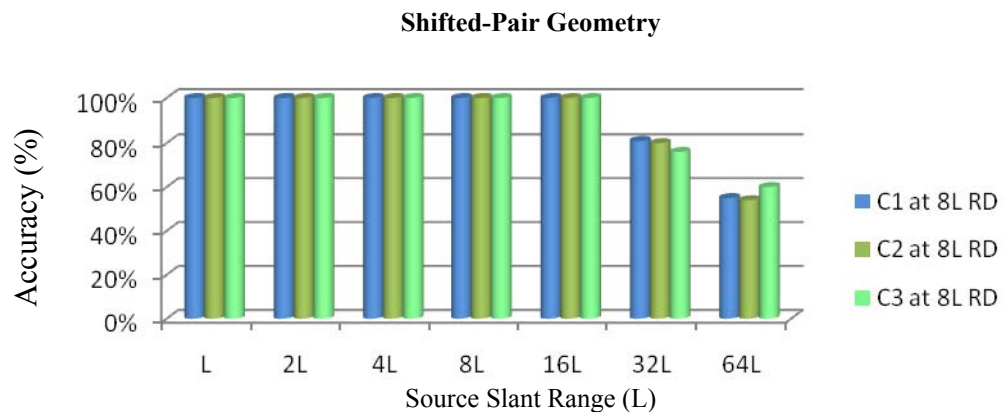


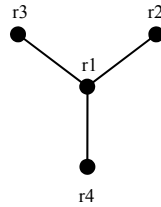
Figure 4.37: Pair-Combination Comparison of the Shifted-pair Geometry. It shows a performance totally redundant and accurate up to horizontal source ranges of 16L.

Therefore, since no significant change on the array performance of the shifted geometry is found, a particular preference on the choice of pair combinations is discarded.

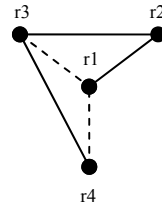
4.9.5 Y-shape Geometry

When using a *Y-shape geometry*, the choice of pair-combination becomes significantly important. Figure 4.38 shows the geometry distribution of the three choices of pair combinations

Pair-combination C1



Pair-combination C2



Pair-combination C3

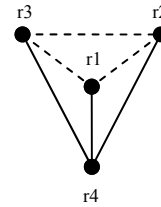


Figure 4.38: Geometry Distribution of the Three Choices of Pair-Combinations of a Y-shape Array.

Although for source ranges of L to $16L$ the performance variation is relatively small (only 2%) when reaching horizontal source ranges of $32L$, the improvement is of C1 over C2 and C3 is bigger than 60%. The inaccuracy with C2 and C3 at source ranges of $32L$ and further comes from the existence of broadside conditions that do not exist when using choice C1. Unlike the shifted geometry, the preference of using a particular choice of pair combination (e.g. C1) instead of another choice improves significantly the accuracy range of the array geometry (Figure 4.39).

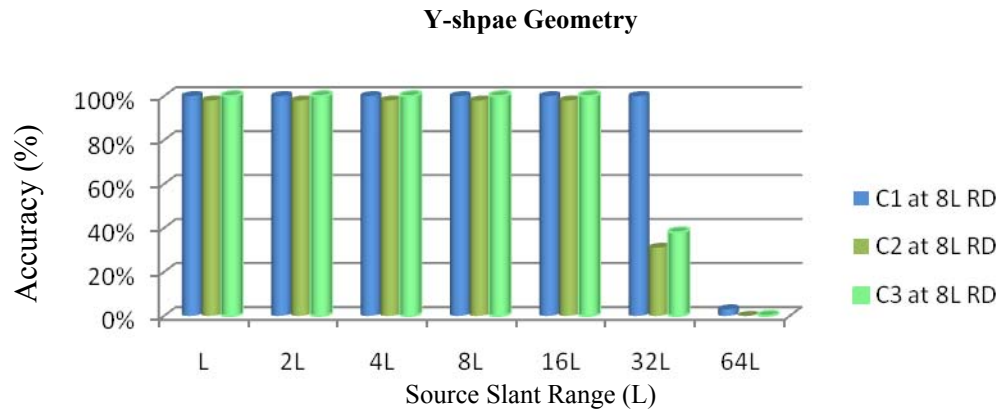


Figure 4.39: Pair-Combination Comparison of the Y-shape Geometry. Unlike other geometries, the preference of using choice C1 improves significantly its accuracy.

4.9.6 Summary

In general terms, the choice of different pair combinations becomes redundant, having a minor effect on source range estimation of the array geometry chosen. Although there are major effects for some source ranges on array-geometries such as Y-shape, in most cases those improvements are not significantly important to have a positive effect to increase the degree of accuracy up to 80%. The array-geometry and the array-aperture are issues of major importance when choosing an appropriate array-configuration.

4.10 Source Tracking Simulations

Each of the previous simulations is based on a constant slant range for a group of static synthetic source positions that cover 360° of the array deployment. On this section, the slant range is not constant, and the horizontal and depth range vary for each individual source position. A synthetic source tracking profile of sperm whale is used as an exemplar simulation.

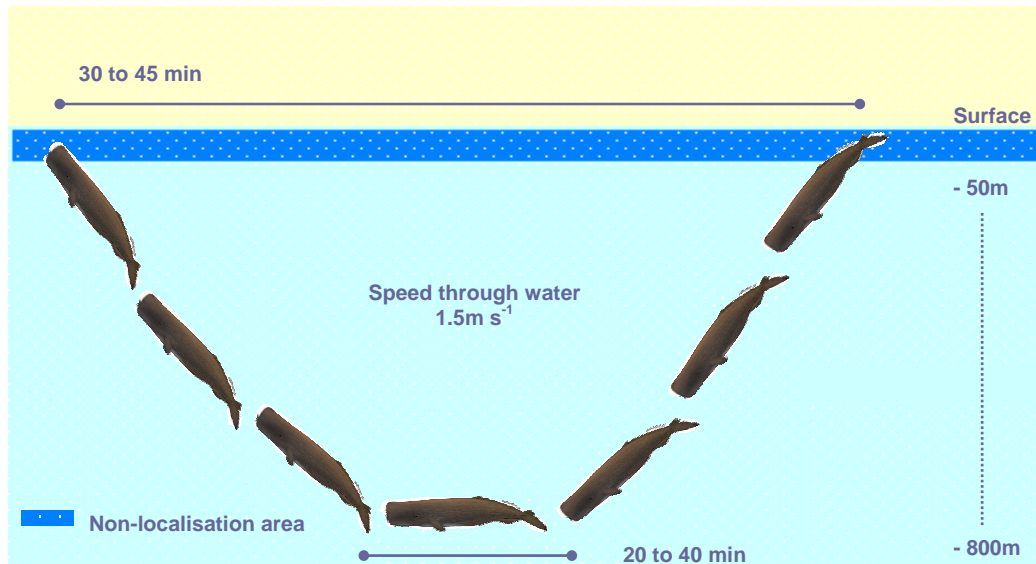


Figure 4.40: Typical Sperm Whale Dive Profile. Including average speed, depth, time duration and non-localisation area.

According to the literature [4, 31, 87, 168], the Sperm whale becomes an active source (making vocalisations) at depths of approximately 50m and greater [139]. Although such species are capable of reaching depths of 2000m, the literature [2, 48, 49] shows

typical depth profiles of 400 to 1200m (800m average) with duration of 30 to 45 minutes (Figure 4.40). The dives have an average speed of 1.15m/s with a pitch angle of 53.3 degrees for the descents, and it ascends slightly faster with 1.33m/s with a pitch angle of 56.6 degrees. The normal dives on horizontal line occurred at 1.5m/s. [4, 98].

4.10.1 Sperm whale dive profile

Based on a typical sperm whale dive profile, a hundred different source positions are chosen and plotted as shown in Figure 4.41. Since the hundred source positions are considered static, none *Doppler* effects are assumed (see page 51).

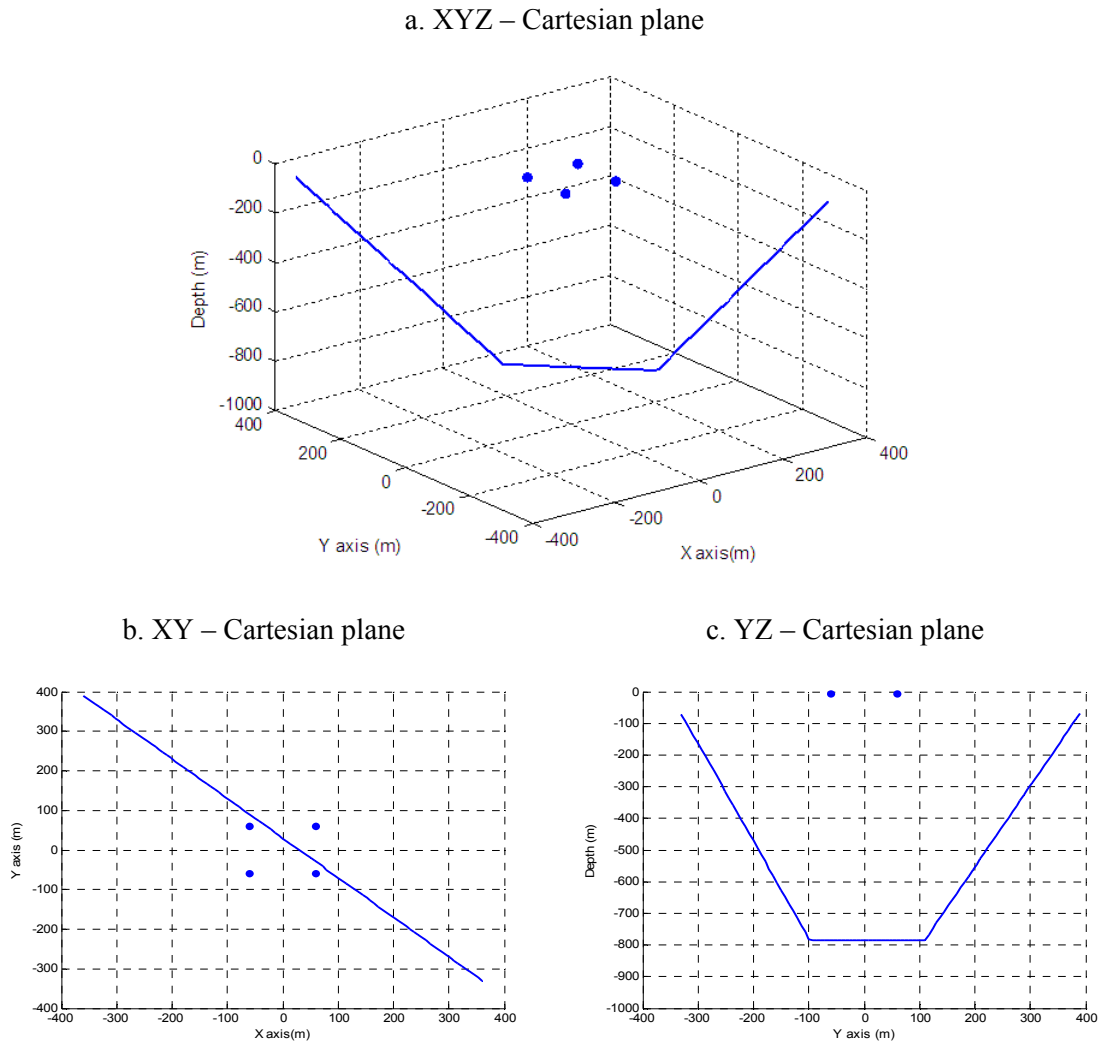


Figure 4.41: Typical Synthetic Source Dive Profile. The source tracking line follows a diagonal direction from left to right, covering a volume of approximately 800m^3 .

Three array configurations, Square, Shifted-pair and Y-shape, in their two categories, short and long aperture respectively, are placed at the centre of the source tracking line

at the three-dimensional Cartesian coordinates (0, 0, -L). Thus when the source passes by, the range distance between array and source is not only the closest horizontal range but is also the deepest at the vertical range. The general specifications for each of the following experimental simulations on this section are shown in Table 4.17.

Array Configuration

Geometry		Square		Y-shape		Shifted-pair	
Aperture length	A	Short (L)	Long (16L)	Short (L)	Long (16L)	Short (L)	Long (16L)
Num. receivers	i	4	4	4	4	4	4
Receivers depth	r_d	L	L	L	L	L	L
Num. sources	S_V	100	100	100	100	100	100

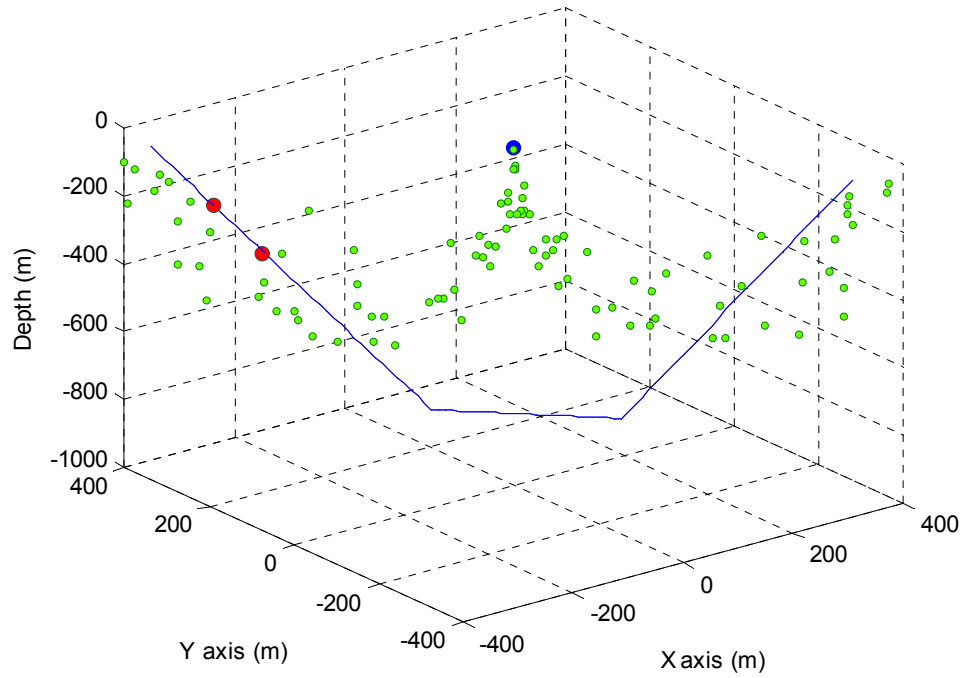
Table 4.17: Source Tracking Simulation Specifications

4.10.2 Short-Square Array

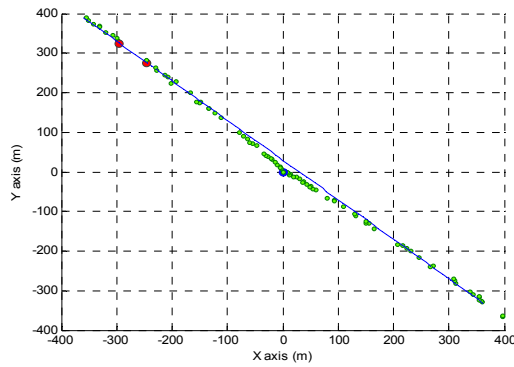
The first array-configuration to be tested is the Short-Square array. As expected, most of its results are inaccurate. The circles in red represent all the source locations found within $\pm 10\text{m}$. The circles in green constitute all the inaccurate source-locations. The circles in blue are the receivers. The blue line corresponds to the synthetic source dive profile. From 100 source positions, only 2 are accurate. The rest of the source locations are found scattered around the synthetic tracking source line with a SRE that increases as the source descends to greater depths (Figure 4.42). The same source dive profile but with a variation on the azimuth angle is also attempted. The results are also totally inaccurate (Figure 4.43). Two additional attempts with completely different source dive profiles are also simulated. The first one is 300m less deep with a long descent and a short ascent. The second one has also a lower depth with a series of three consecutive short descents and ascents. Nevertheless, none of the source positions is located accurately for either the first or second scenarios (Figure 4.44). Once again, the inaccuracy of the short-square-array is proved, giving clear evidence of the useless capabilities of this array-configuration.

— Source Dive Profile ● Array-Configuration ● Accurate Source Loc ● Inaccurate Source Loc

a. 3D view (XYZ)



b. Superior view (XY)



c. Depth view (YZ)

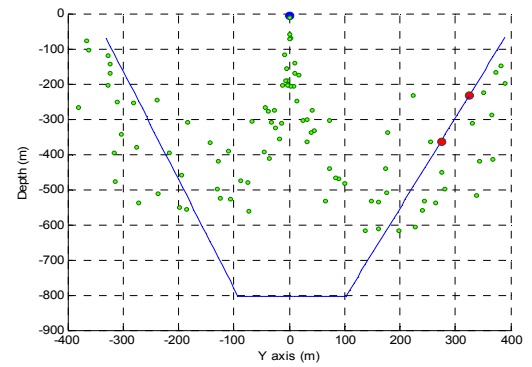


Figure 4.42: Effects of a Short-Square Array on a Source Dive Profile (a, b, c). The source locations are found scattered around the dive profile with a SRE that increases as the source descends to greater depths.

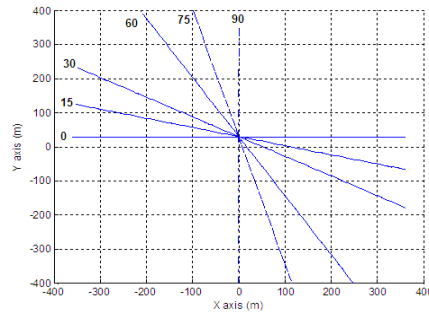
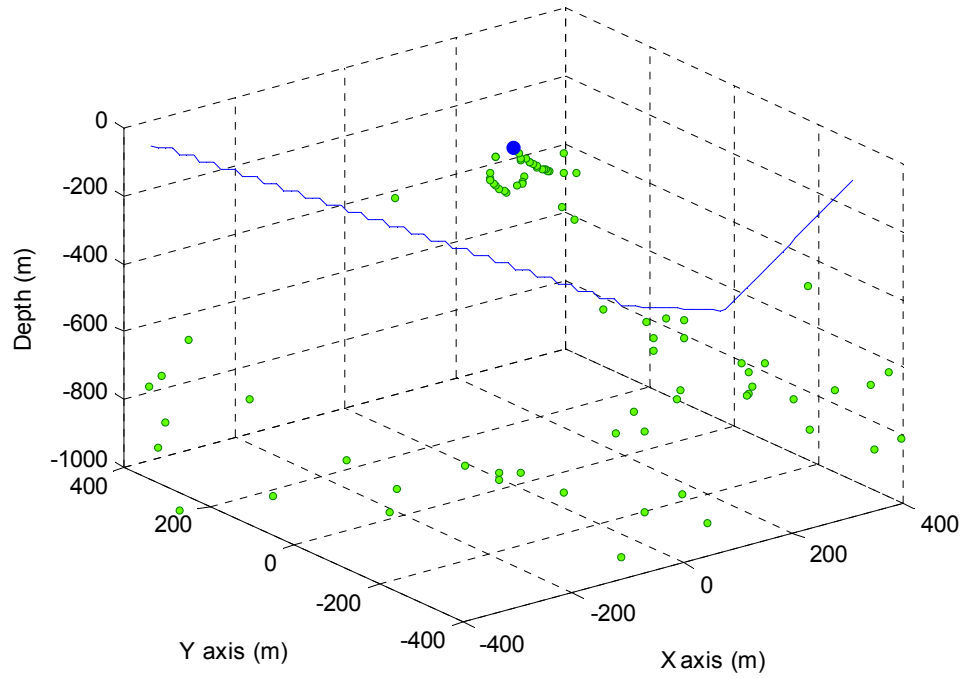


Figure 4.43: Additional simulations with a different azimuth angle (0° , 15° , 30° , 60° , 75° , 90°) produce inaccurate results.

— Source Dive Profile ● Array-Configuration ● Accurate Source Loc ● Inaccurate Source Loc

a. 3D view (XYZ) – Source Dive Profile 2



b. 3D view (XYZ) – Source Dive Profile 3

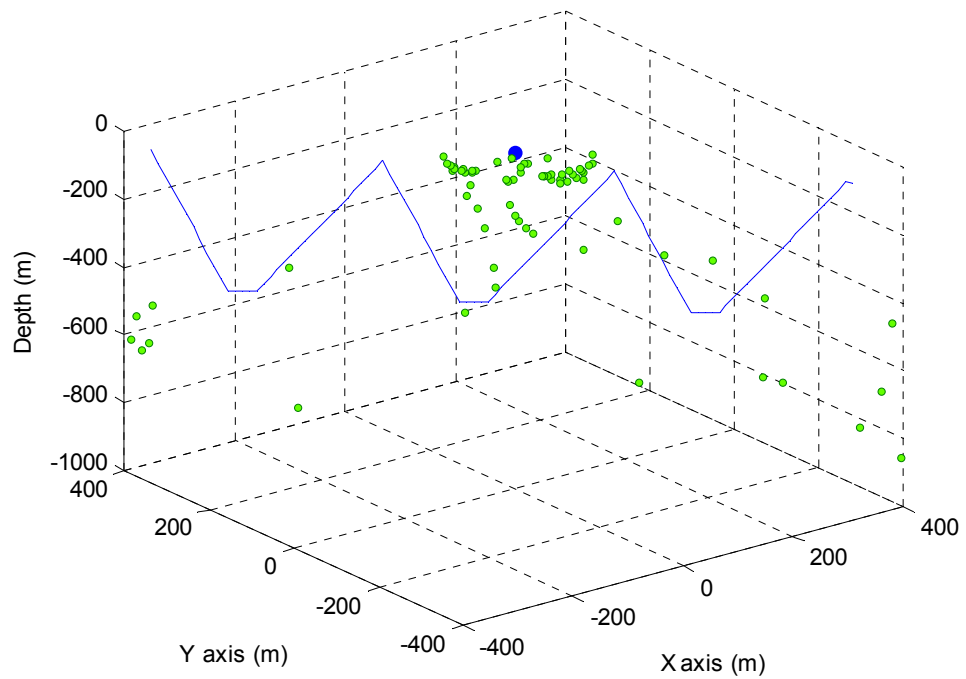


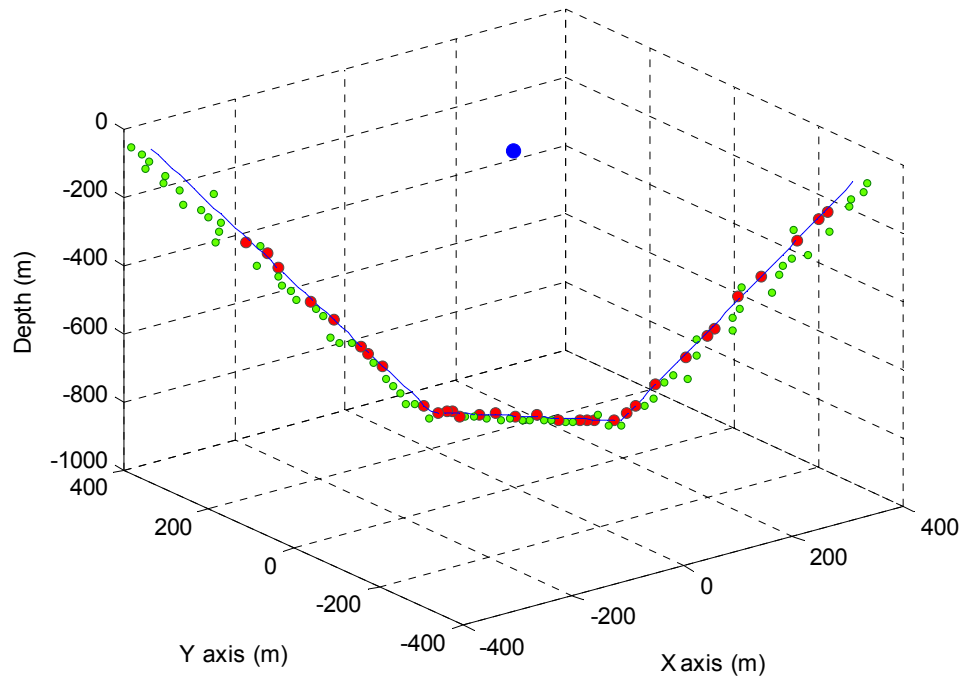
Figure 4.44: Effects of a Short-Square Array on additional two Source Dive Profiles (2 & 3). None of the source positions is located accurately for either the second or third dive profile.

4.10.3 Short-Y-shape Array

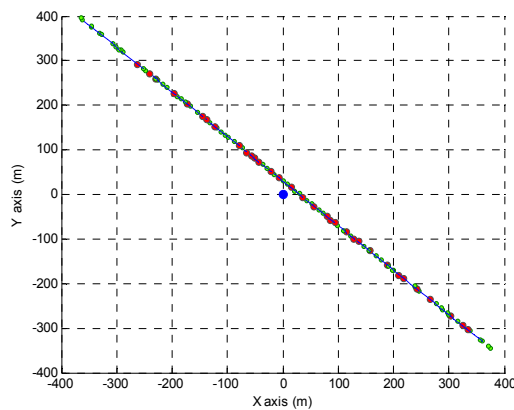
The short-Y-shape array is 45% accurate (Figure 4.45). Although it is not able to locate the majority of the sources, it is able to track the dive profile with relative accuracy. This simulation also represents a noticeable result, since half of the synthetic sources positioned on deep ranges ($\sim 800\text{m}$) are located within $\pm 10\text{m}$.

— Source Dive Profile ● Array-Configuration ● Accurate Source Loc ● Inaccurate Source Loc

a. 3D view (XYZ)



b. Superior view (XY)



c. Depth view (XZ)

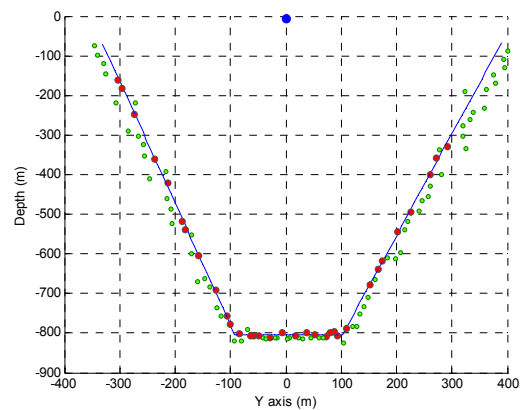


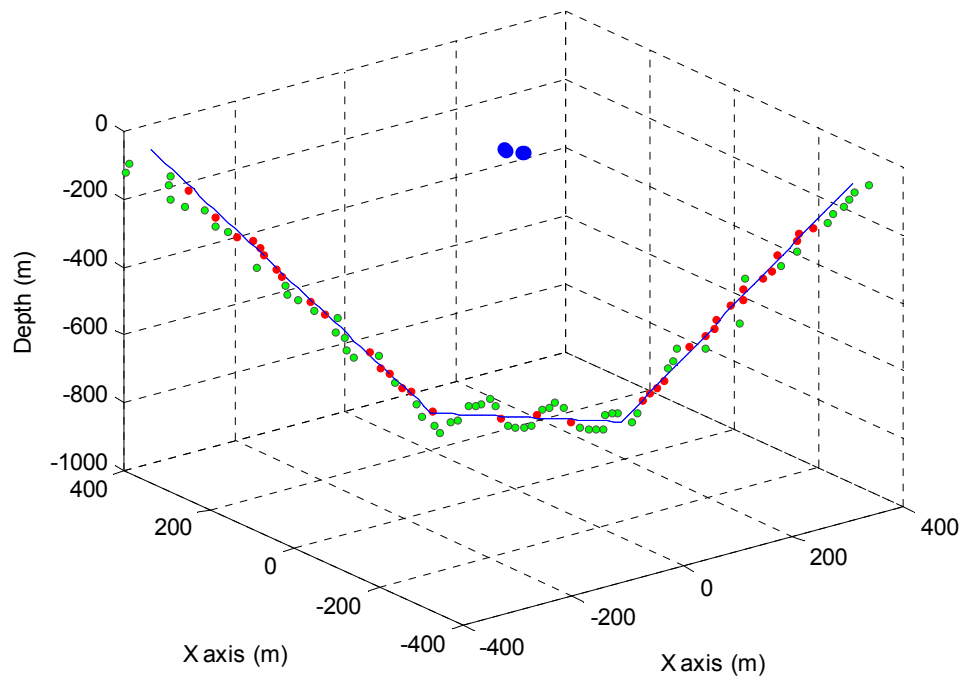
Figure 4.45 Effects of a Short-Y-shape Array on a typical Source Dive Profile. It offers 45% accuracy.

4.10.4 Short-Shifted-pair Array

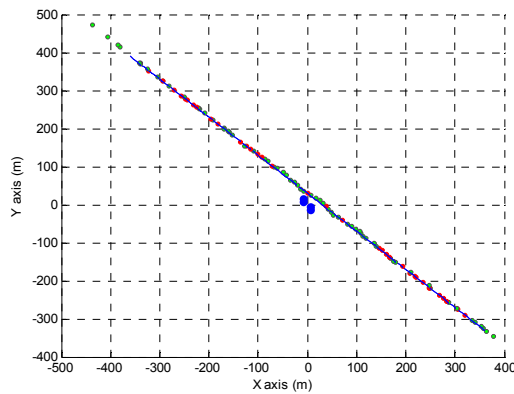
The Short-Shifted-pair array is 35% accurate (Figure 4.46). This is 10% less accurate than the Y-shape array. Its major problem is found when it tracks shallow (60-200m) and deep (750m-800m) source positions. Nevertheless, since most of the inaccurate source locations are within ± 30 m, the array still is able to track the whole dive profile.

— Source Dive Profile ● Array-Configuration ● Accurate Source Loc ● Inaccurate Source Loc

a. 3D view (XYZ)



b. Superior view (XY)



c. Depth view (XZ)

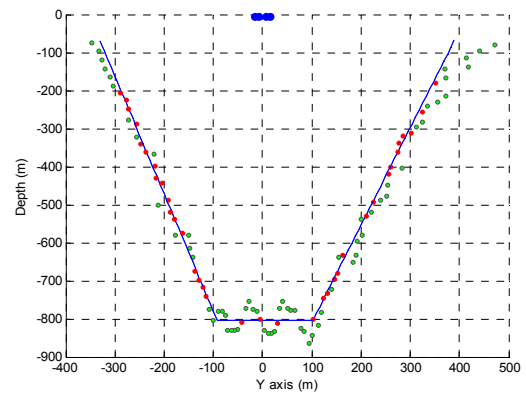


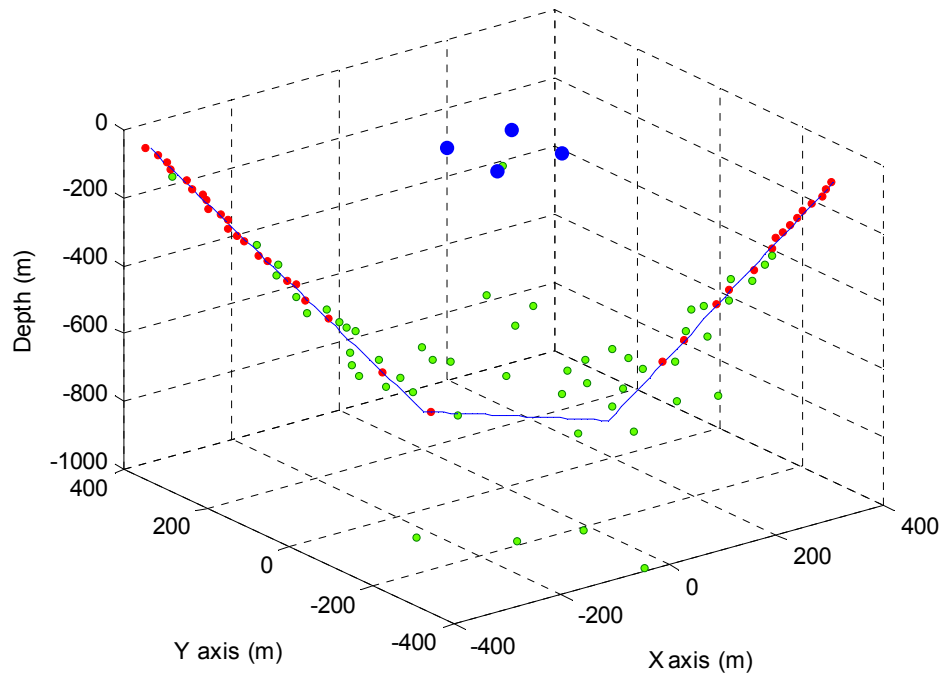
Figure 4.46 Effects of a Short-Shifted Array on a Source Dive Profile. It offers 35% accuracy.

4.10.5 Long-Square Array

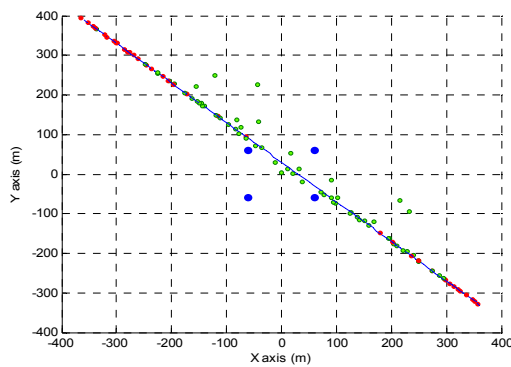
Certainly, the Long-Square has a better performance than the short-Square. However, it is still under 80% accurate. It is able to locate 43% of the total source positions. Its major problem is found when it tracked source positions that are over the barrier of 300m depth. It is only when the source ascends to shallow waters that the array-configuration is able to track the dive profile once again (Figure 4.47).

— Source Dive Profile ● Array-Configuration ● Accurate Source Loc ● Inaccurate Source Loc

a. 3D view (XYZ)



b. Superior view (XY)



c. Depth view (XZ)

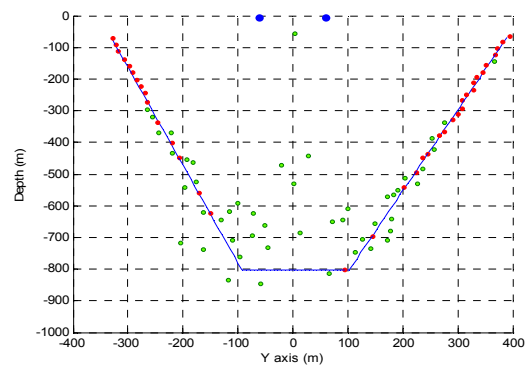


Figure 4.47: Effects of a Long-Square Array on a Source Dive Profile. It offers 43% accuracy.

To show the inaccuracy of this array when the source travels on a broadside line to the pair of receivers, an additional source dive profile (green) is simulated, as shown in Figure 4.48.

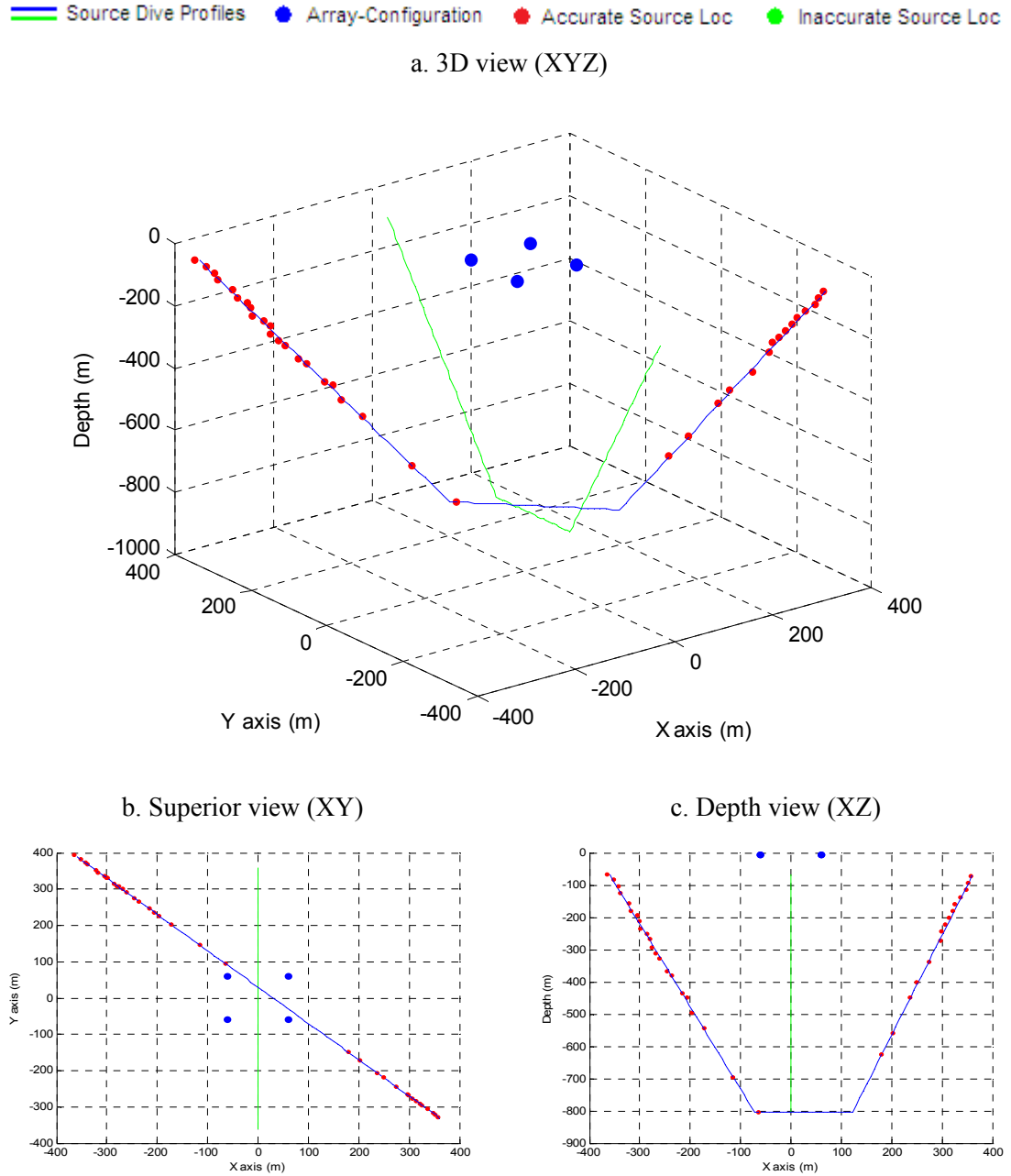


Figure 4.48: Effects of a Long-Square Array tested with a second Source Dive Profile (green). When using a Square geometry, the broadside effects cause a complete uncertainty.

The results show complete inaccuracy when locating any source position along the dive profile. Although this scenario would rarely occur, because the source tends to vary its direction, this experimental simulation shows how inaccurate it could be if we were to rely completely on the results given by a square geometry.

To confirm that this array-configuration can be more accurate than the others, a second source dive profile (green), pointing at 90 degrees with respect the X-axis, is simulated, as shown in Figure 4.50.

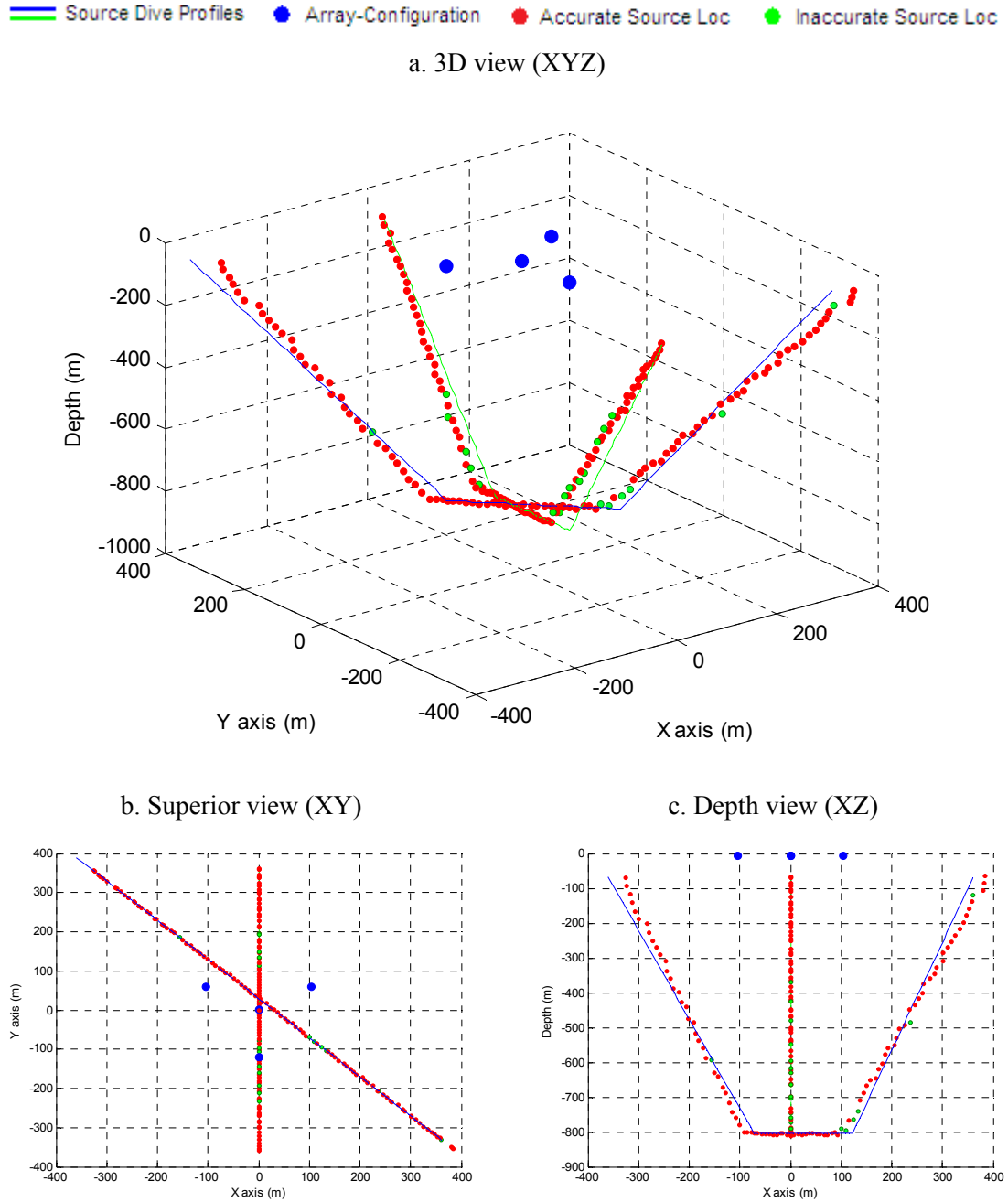


Figure 4.50: Effects of a Long-Y-shape Array tested with a second Source Dive Profile (green). It offers 87% accuracy, showing that when using a Y-shape geometry the broadside uncertainties are minority.

On this second dive profile, the Long-Y-shape is able to find 87% of the source positions. As shown in previous sections, the Y-shape array is also accurate for locating sources on broadside positions.

4.10.7 Long-Shifted-pair Array

The Long-Shifted array is 82% accurate. Unlike the Short-Shifted array which is unable to locate sources at depth positions of 800m, the long array has a noticeable improvement. Figure 4.51 shows only two inaccurate source locations at such depth.

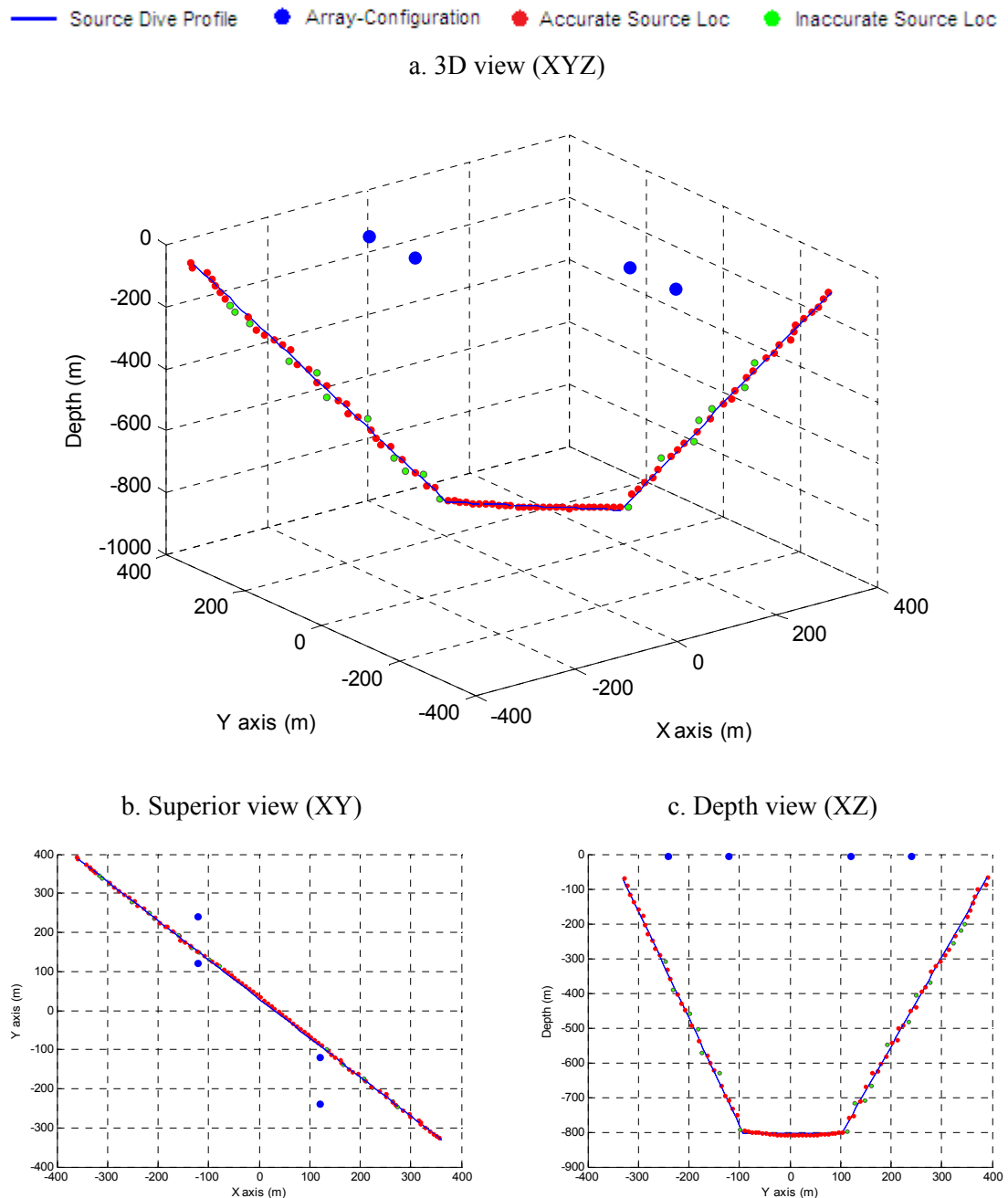


Figure 4.51: Effects of a Long-Shifted-pair Array on a Source Dive Profile. It offers 82% accuracy

A final simulation of a second source dive profile (green), pointing at 90 degrees with respect the X-axis, is also simulated to investigate the effect of the broadside conditions on the Long-Shifted-pair array (Figure 4.52).

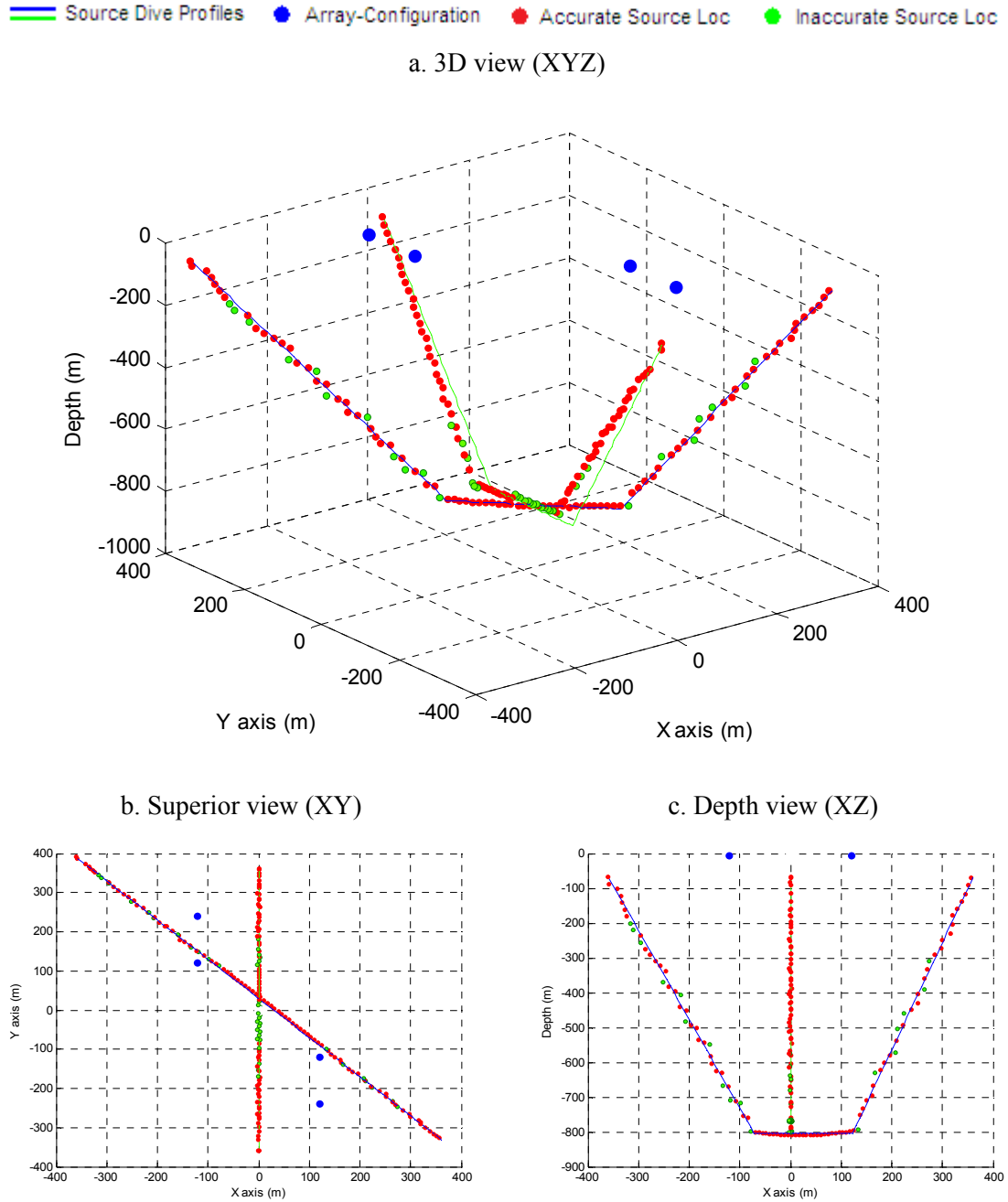


Figure 4.52: Effects of a Long-Shifted-pair Array tested with a second Source Dive Profile. It offers 72% accuracy, showing that when using a Shifted-pair geometry the broadside uncertainties are minority.

On this second dive profile, the Long-Shifted-pair is 72% accurate, 15% less accurate than the Y-shape. Nevertheless, it can be considered sufficiently accurate to track the entire dive profile. This also confirms that the broadside conditions have a minor effect on its accuracy performance.

4.10.8 Discussion

In general terms, these experimental simulations show that long aperture-arrays such as Y-shape and Shifted-pair can be accurate for locating sources within a volume of 800m^3 . The use of a short-aperture reduces the chances of tracking all the source positions.

From the three array geometries, the Y-shape proves to be the most accurate. The short-square array configuration is certainly not recommended for use. A long-square array could be considered as only partially accurate for depth source ranges of up to 300m, not including any of the broadside positions to the pair of receivers. The Y-shape and shifted-pair arrays overcome the problem of broadside source locations and constitute recommendable array geometries to use when that occurs.

Although the course of the source dive profile may vary in a number of ways, the group of these exemplar simulations provides an insight to the reader that will help to foresee the effects associated with a particular array configuration while tracking a source dive profile.

4.11 Array Positioning-Error

The accuracy of source location also depends on the precision of the receiver positions [157, 158]. When deploying a linear towed array, the receiver elements suffer the effects of the vessel's speed and manoeuvres variation. In geometric terms, it is said that the array suffers of an Offset-positioning-Error (*OpE*) and Angle-positioning-Error (*ApE*). To investigate the performance of each array-geometry, synthetic *OpE* and *ApE* is introduced in each receiver-position on the Cartesian plane XY and modelled by using the Matlab simulator. The synthetic *positioning-error* is introduced in the Shifted-pair and the Y-shape geometries only. Square and trapezium are not included, because their lack of accuracy exists already, even though non positioning-error is assumed. The general simulation specifications are shown in Table 4.18.

Array Positioning-Error		
Aperture length	A	Short (L)
Num. receivers	i	4
Num. sources	S_V	100
Horizontal Range	R_H	L
Depth Range	R_D	8L

Table 4.18: Simulation Specifications with Array Positioning-Error

4.11.1 Offset-Positioning-Error (OpE)

A progressive and identical increase of synthetic *OpE* is introduced to each of the receiver elements until the array becomes inaccurate to locate more than the 80% of the source positions with a SRE of less than $\pm 10\text{m}$.

For values of $OpE < \pm 30\text{m}$, both array geometries remain accurate. However, for values of $OpE \geq \pm 30\text{m}$, both geometries start to present inaccuracies when locating all the source positions. Figure 4.53 shows the different array positions on the plane XY when adding three different *OpE* values ($\pm 10\text{m}$, $\pm 20\text{m}$ and $\pm 30\text{m}$) respectively to a fixed shifted-pair array located on the Cartesian coordinates (0,0).

Shifted-pair

Superior view of a Towed Array

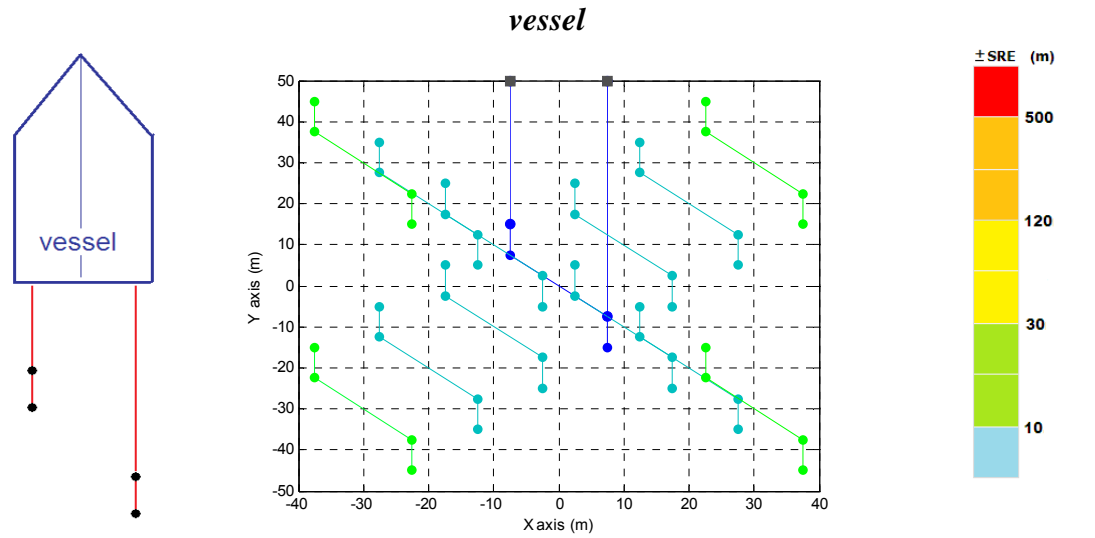


Figure 4.53: Different scenarios of a Towed Shifted-pair Array with OpE (0 to $\pm 30m$) on XY axes

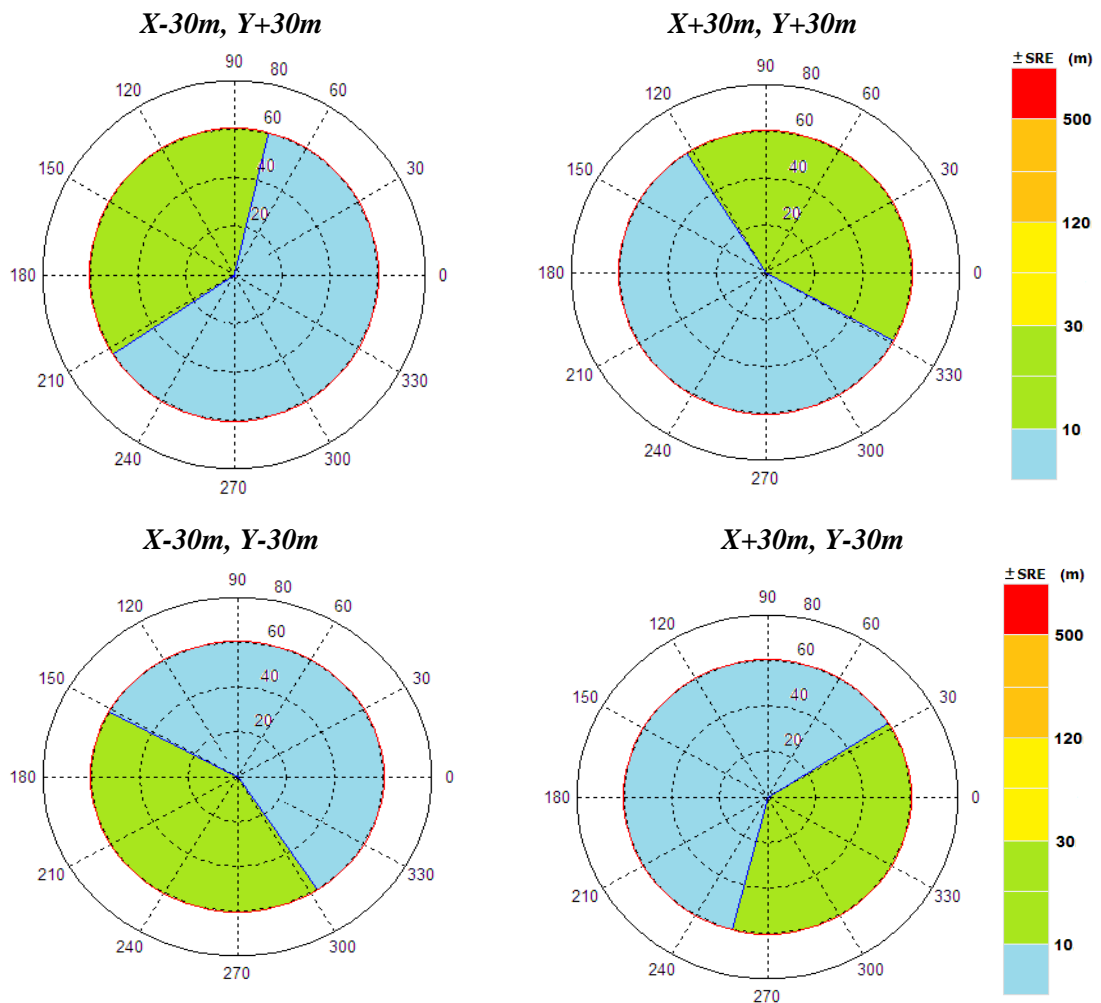


Figure 4.54 Effects of $\pm 30m$ OpE on the performance of a Shifted-pair array. 60% accurate ($SRE \leq \pm 10m$)

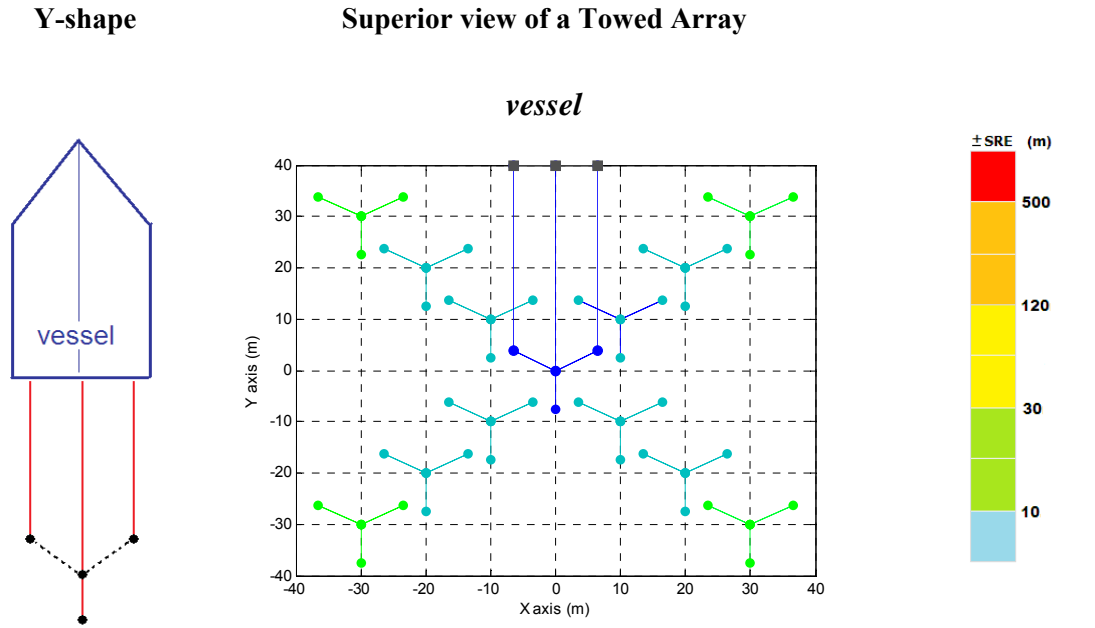


Figure 4.55: Different scenarios of a Towed Y-shape-pair Array with OpE (0 to $\pm 30m$) on XY axes

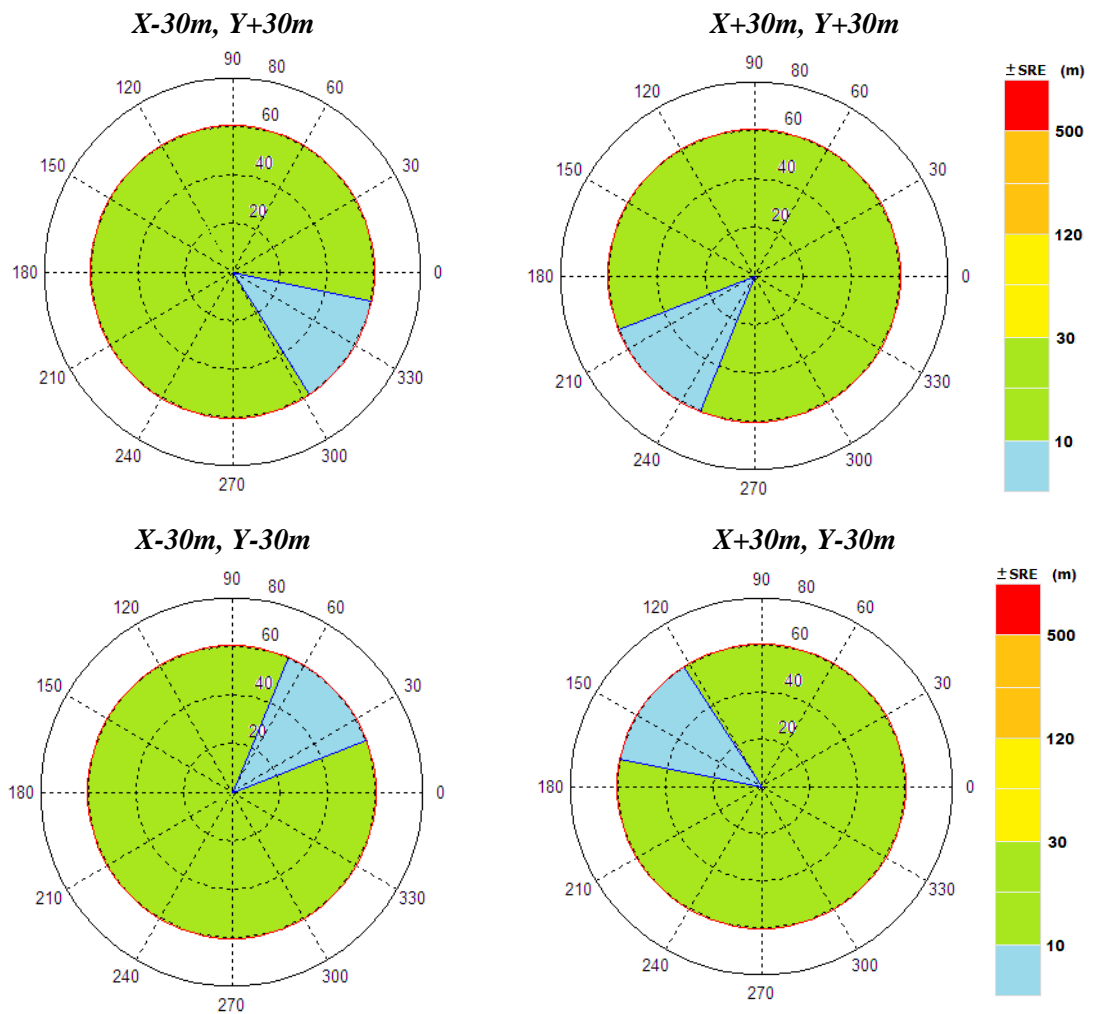


Figure 4.56: Effects of $\pm 30m$ OpE on the performance of a Y-shape array. 15% accurate ($SRE < \pm 10m$)

Figure 4.54 shows the performance of the array when a value of $\pm 30\text{m}$ OpE is added to each quadrant of the Cartesian plane. In each case, the array is 60% accurate ($SRE < \pm 10\text{m}$), being 40% inaccurate ($\pm 10\text{m} \leq SRE < \pm 30\text{m}$) for source positions found on the offset area. Figure 4.55 shows the several Y-shape array positions for OpE values of $\pm 10\text{m}$, $\pm 20\text{m}$ and $\pm 30\text{m}$ respectively. Unlike the shifted-pair, the Y-shape array shows a major inaccuracy on its performance (Figure 4.56). It is only 15% accurate ($SRE < \pm 10\text{m}$) and being 85% inaccurate ($\pm 10\text{m} \leq SRE < \pm 30\text{m}$) for source positions found on the offset area.

In summary, the shifted-pair array has a better performance when OpE is present. Receiver positions with OpE precision values of $\pm 0.5\text{m}$, $\pm 10\text{m}$, and $\pm 20\text{m}$ could be ignored if a tolerance SRE of less than $\pm 10\text{m}$ is accepted.

4.11.2 Angle-Positioning-Error (ApE)

Three common scenarios are simulated. The scenarios are classified into three types. Scenario A occurs when the vessel is moving in a straight line. Scenario B occurs when the vessel is turning to port (left). Scenario C occurs when the vessel is turning to starboard (right) (Figure 4.57).

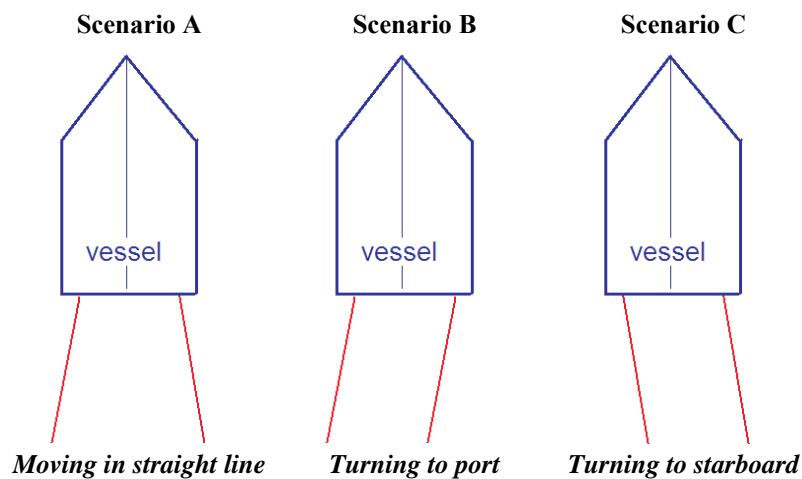


Figure 4.57: Three Different Scenarios of a Towed Array

In the three scenarios, the vessels manoeuvre is the main cause of an *Angle-positioning-Error (ApE)* when towing a linear array. The angle referred to is the angle created between the vessel and each linear array as shown in Figure 4.58a. For a static scenario in which the linear arrays do not swing, the angle is 0° , but in a real scenario the array may swing up to an angle of 90° . The distance between vessel and the first receiver position is twice the distance separation of the receivers ($2L$) (Figure 4.58b).

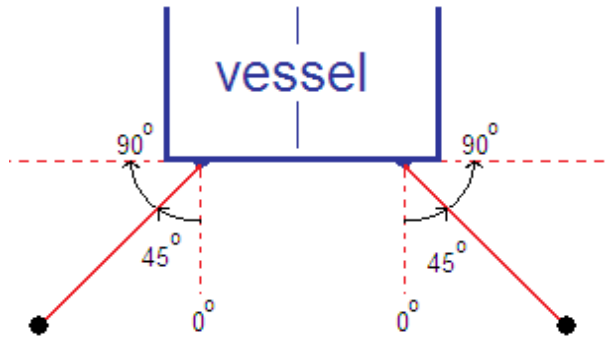


Figure 4.58a: Exemplar diagram of the angle-positioning-error (ApE) when towing two linear arrays.

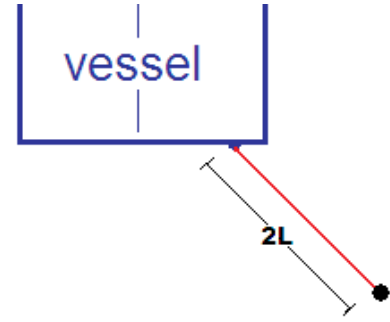


Figure 4.58b: Length between vessel and first receiver position $2L$ (15m).

Experimental simulations with *ApE* from 0° to 90° in increments of 5° for each different scenario are performed. Figures 4.59 to 4.61 show the results obtained for each scenario when a towed *Shifted-pair* array is deployed.

Scenario S-A shows a vessel moving in a straight line. When this occurs, it has the tendency to cause the linear arrays to swing up to 90° as the worst case (Figure 4.59). The greater the *ApE*, the less accurate the array-geometry becomes to locate a source position. For instance, if both arrays swing up to no more than 25° , the shifted-pair array remains, having a lower SRE of less than $\pm 10\text{m}$. However, if the *ApE* reaches 70° and more, the array becomes completely inaccurate ($\text{SRE} > \pm 500\text{m}$).

Scenario S-B has been divided into three sub scenarios: S-B1, S-B2 and S-B3 (Figure 4.60). S-B1 shows a typical scenario of a vessel turning to port side with both linear arrays swinging simultaneously at the same angle. The source range accuracy is limited to less than $\pm 30\text{m}$, when turning with an angle of 45° . After that, the array geometry becomes less accurate and the SRE is bigger than $\pm 120\text{m}$. Scenario S-B2 shows a vessel turning to port side with the port linear array fixed and the starboard linear array swinging. The SRE is increased when turning with an angle range of 25° to 35° because of the overlapping of both linear arrays on the same axis. Then the SRE is

reduced to less than $\pm 30\text{m}$. Scenario S-B3 shows a vessel turning to port side with the port linear array swinging and the starboard linear array fixed. Unlike S-B2, the linear arrays never overlap within them, and the source range accuracy is limited to less than $\pm 30\text{m}$ when turning with an angle of 60° . Its performance is better than that of scenarios S-B1 and S-B2.

Scenario S-C has been divided into three sub scenarios: S-C1, S-C2 and S-C3 (Figure 4.61). S-C1 shows a typical scenario of a vessel turning to starboard with both linear arrays swinging simultaneously at the same angle. The source range accuracy is limited to less than $\pm 30\text{m}$ when turning with an angle of 35° . After that, the array geometry becomes less accurate with a SRE no bigger than $\pm 120\text{m}$. Scenario S-C2 shows a vessel turning to starboard with the port linear array fixed and the starboard linear array swinging. The SRE remains at less than $\pm 30\text{m}$ until the vessel turns with an angle of 75° . Then, the source range accuracy is limited to less than $\pm 120\text{m}$. Finally, scenario S-C3 shows a vessel turning to starboard with the port linear array swinging and the starboard linear array fixed. An SRE of less than $\pm 30\text{m}$ is limited to an ApE of 20° only. Then as the port linear array gets closer to the starboard linear array, the SRE increases to $\pm 120\text{m}$, reaching a maximum peak range error of $\pm 120\text{m}$ to $\pm 500\text{m}$.

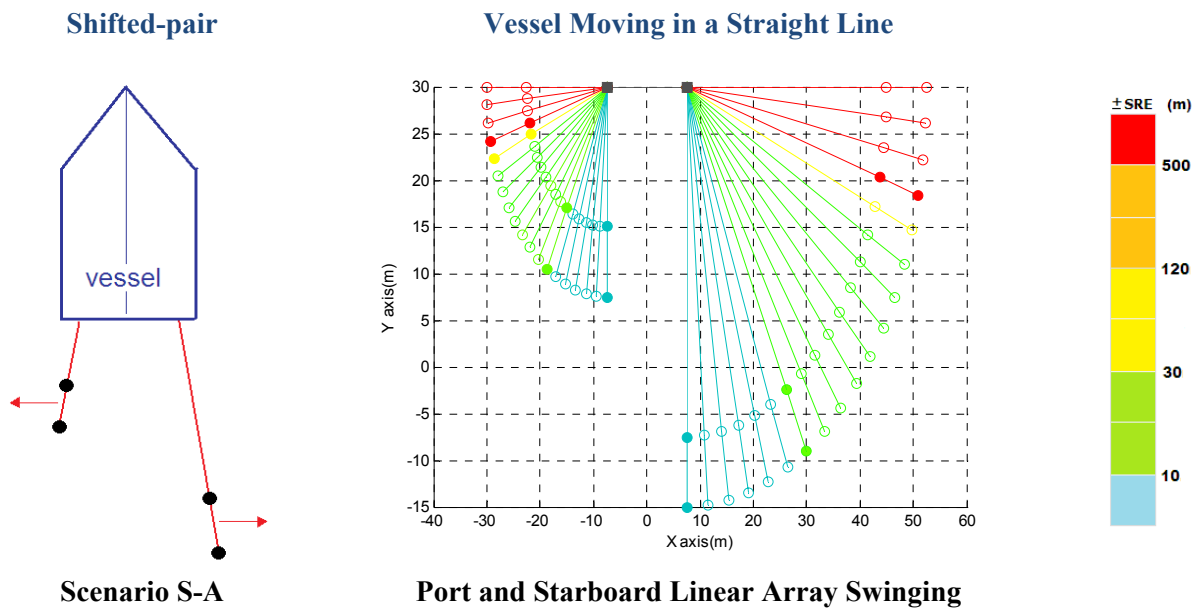


Figure 4.59: Scenarios with a Shifted-pair Array Towed to a Vessel Moving in a Straight Line

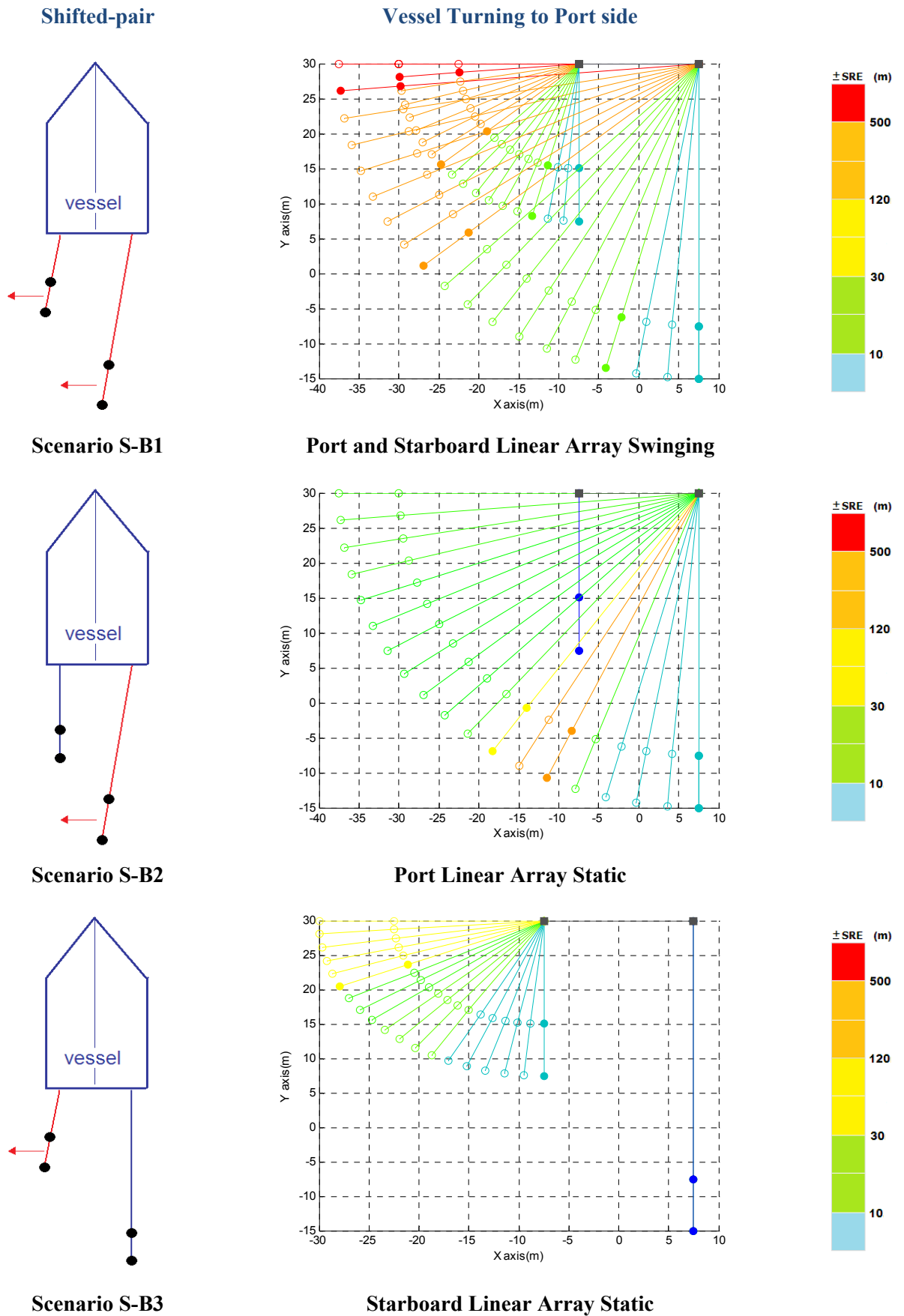
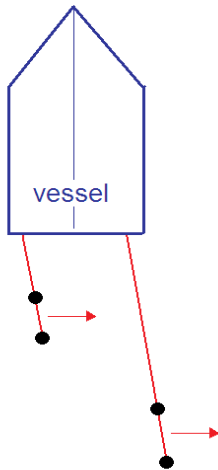
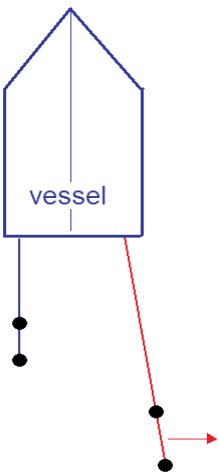


Figure 4.60: Scenarios with a Shifted-pair Array Towed to a Vessel Turning to Port

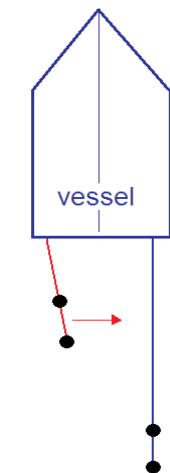
Shifted-pair



Scenario S-C1

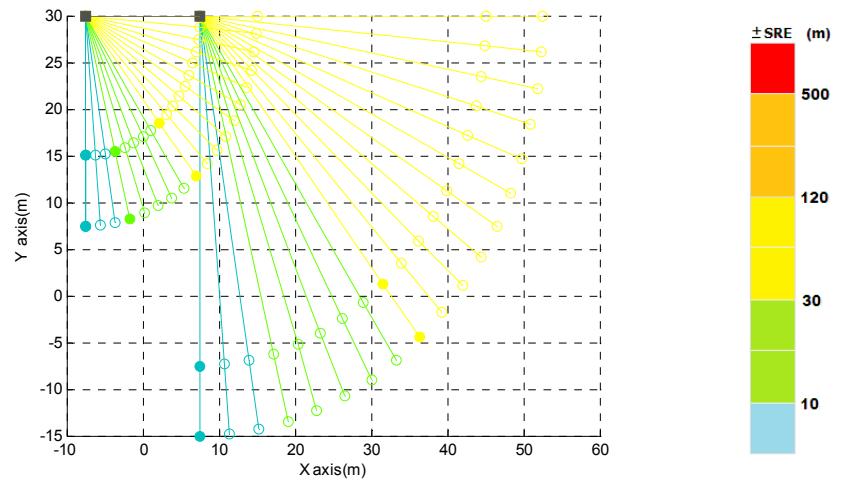


Scenario S-C2

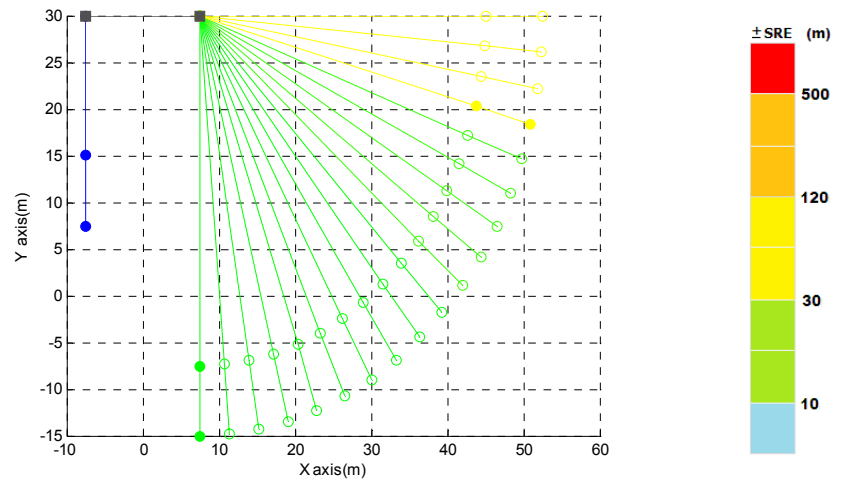


Scenario S-C3

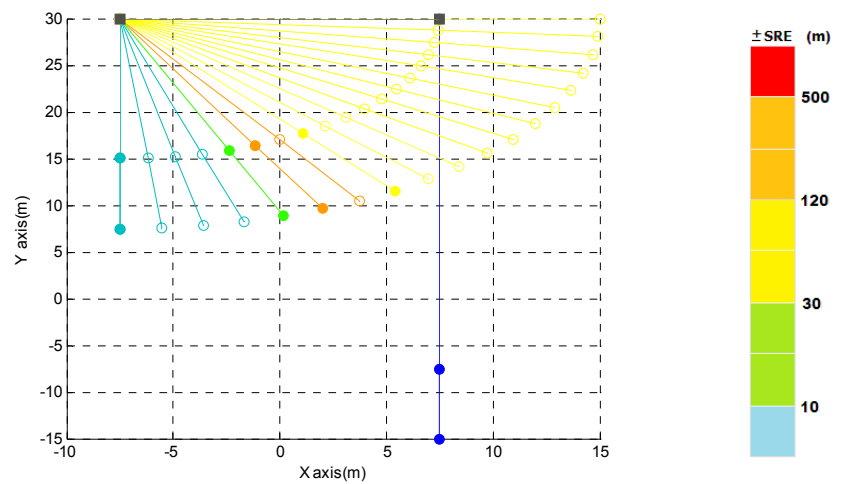
Vessel Turning to Starboard side



Port and Starboard Linear Array Swinging



Port Linear Array Static



Starboard Linear Array Static

Figure 4.61: Scenarios with a Shifted-pair Array Towed to a Vessel Turning to Starboard

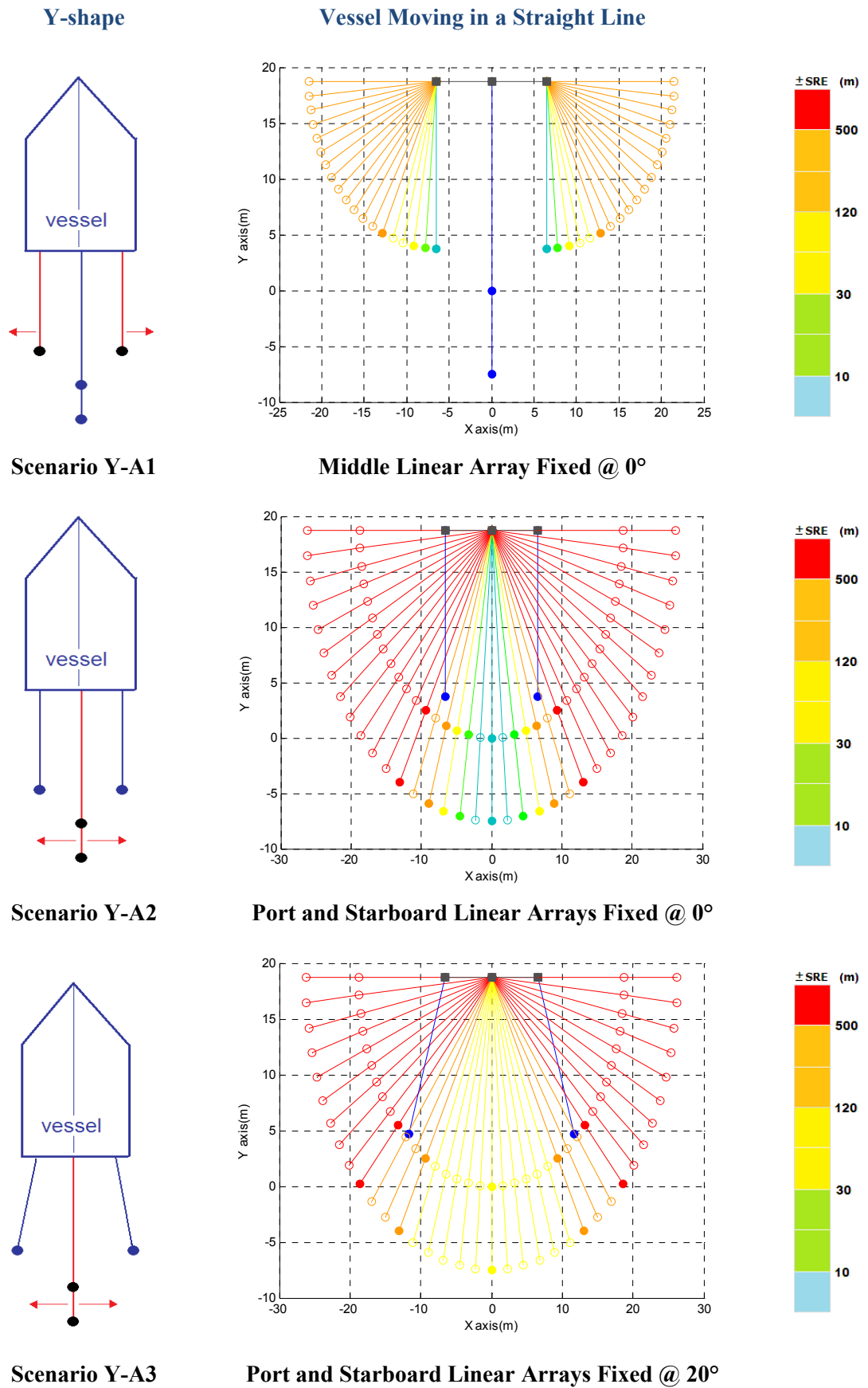


Figure 4.62: First series of scenarios with Y-shape Array Towed to a Vessel Moving in a Straight Line

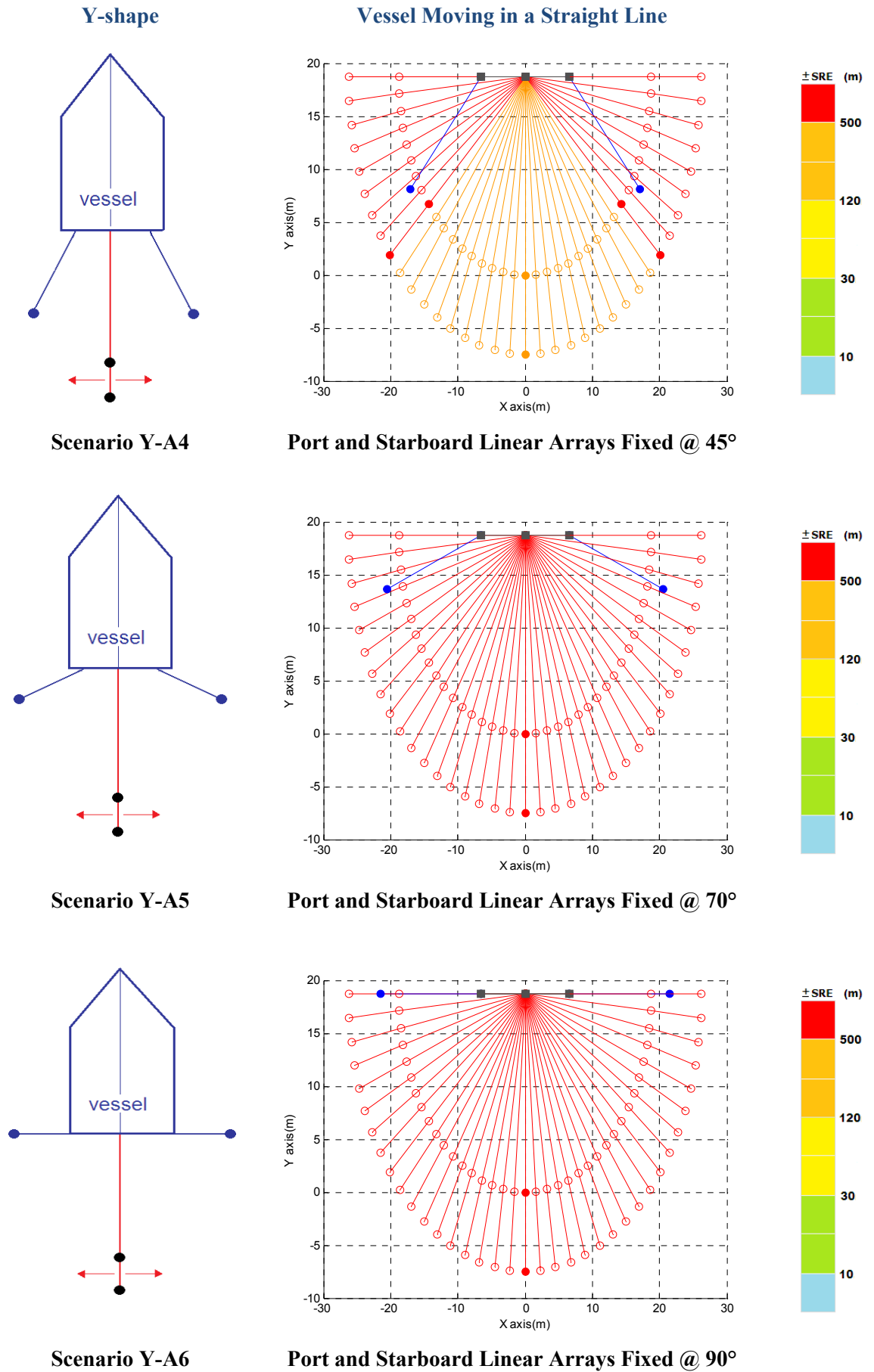


Figure 4.63: Second series of scenarios with Y-shape Array Towed to a Vessel Moving in a Straight Line

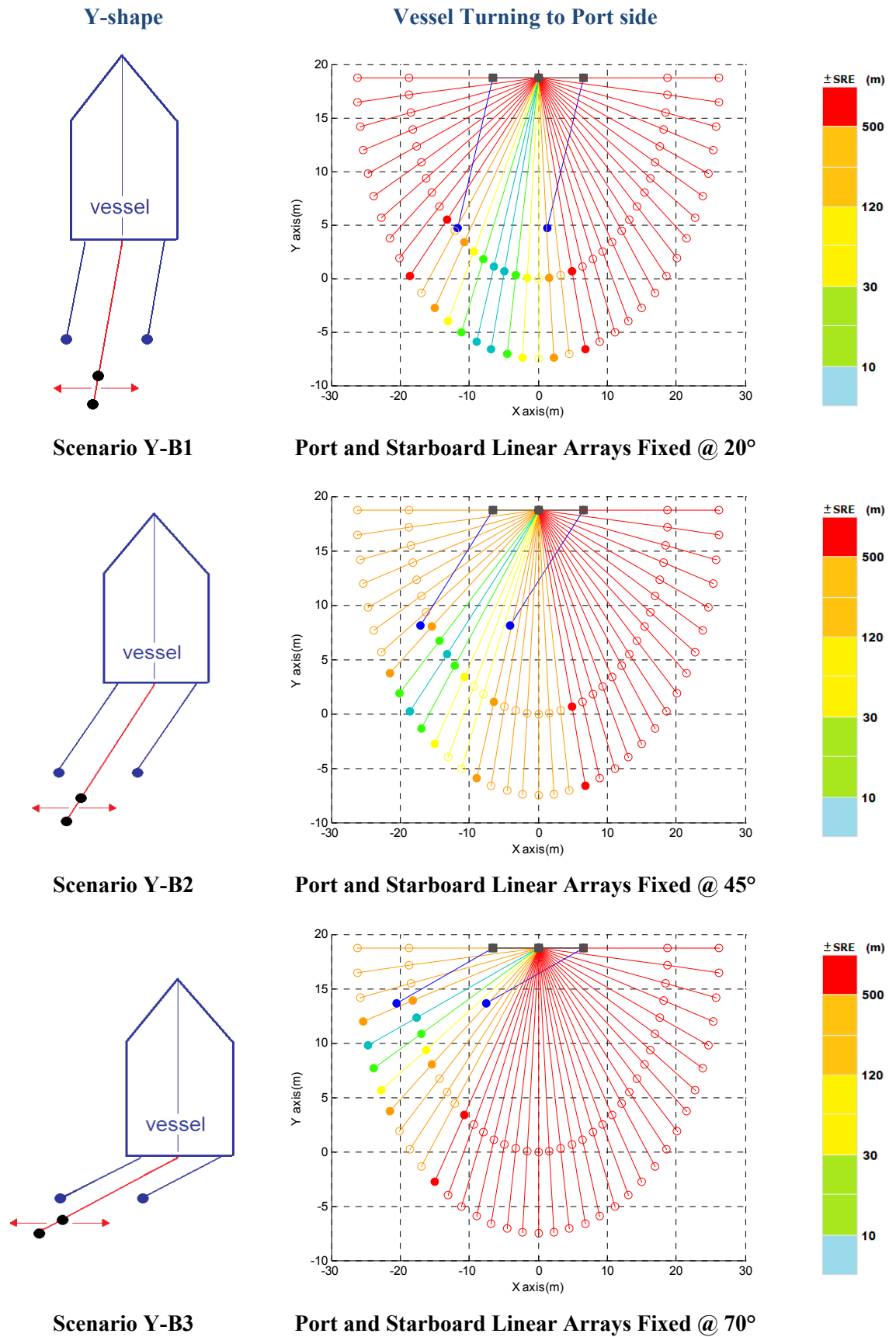


Figure 4.64: Scenarios with a Y-shape Array Towed to a Vessel Turning to Port

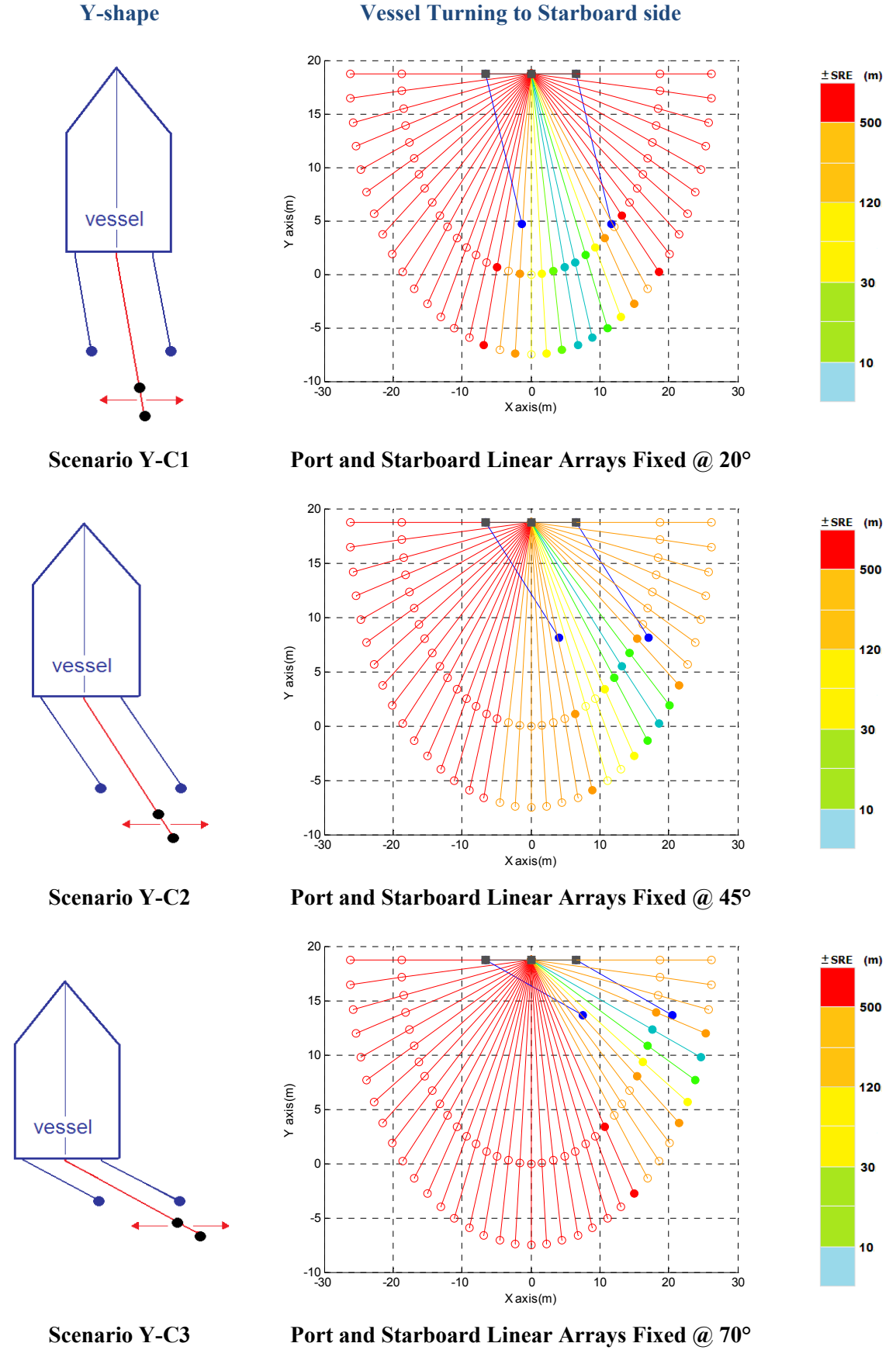


Figure 4.65: Scenarios with a Y-shape Array Towed to a Vessel Turning to Starboard

Figures 4.52 to 4.65 show the results obtained for each scenario when a towed *Y-shape* array is deployed from a vessel. Unlike the shifted-pair array, the towed deployment of a Y-shape array requires at least three linear arrays, known as port, middle and starboard respectively. Also, unlike the shifted-pair array, the possible number of scenarios with three linear arrays is bigger than would happen with two. Therefore, scenario Y-A has been divided into six sub scenarios and scenarios Y-B and Y-C into three sub scenarios respectively, a total of 12 different scenarios.

Scenario Y-A1 shows a vessel moving in a straight line, with the port and starboard linear arrays swinging and the middle linear array fixed (Figure 4.62). The source range accuracy is limited to less than $\pm 30\text{m}$ if both arrays swing up to no more than only 5° *ApE*. Then, when the swinging over takes the 25° *ApE*, the SRE becomes bigger than $\pm 120\text{m}$. Scenario Y-A2 shows an opposite scenario: a vessel moving in a straight line, but with both side linear arrays fixed at 0° and the middle array swinging from one side to the other (Figure 4.62). The source range accuracy is limited to less than $\pm 30\text{m}$ if the middle linear array swings up to no more than 10° *ApE* at any side. However, when the middle linear array swings with an angle equal to 30° *ApE* or more, the array becomes completely inaccurate ($\text{SRE} > \pm 500\text{m}$). Scenario Y-A3 shows a scenario similar to that of Y-A2 but with both side linear arrays fixed at 20° (Figure 4.62). In such a scenario, the performance of the array is affected with an SRE range of $\pm 30\text{m}$ to $\pm 120\text{m}$ when the middle linear array swings up to 25° *ApE*. Then, when the middle linear array swings further and overlaps one of the side linear arrays, the array becomes completely inaccurate ($\text{SRE} > \pm 500\text{m}$).

Scenario Y-A4 shows both side linear arrays fixed at 45° (Figure 4.63). In such a scenario, the performance of the array is affected extremely - more than in Y-A3 with an SRE bigger than $\pm 120\text{m}$ when the middle linear array swings up to 45° *ApE*. Scenarios Y-A5 and Y-A6 show both side linear arrays fixed at 70° and 90° respectively, and the middle array swinging from one side to the other (Figure 4.63). Both scenarios are completely inaccurate ($\text{SRE} > \pm 500\text{m}$) for any swinging angle of the middle linear array.

Scenario Y-B1 shows a vessel turning to port side with both side linear arrays fixed at 20° and the middle array swinging from one side to the other (Figure 4.64). The source

range accuracy is limited to less than $\pm 30\text{m}$ only when the swinging of the middle linear array is found within an angle range of 10° to 25° *ApE* on the port side. Outside of such an angle range, the array becomes less accurate. Scenario Y-B2 shows both side linear arrays fixed at 45° (Figure 4.64). A SRE of less than $\pm 30\text{m}$ is found when the middle linear array swings within an angle range of 40° to 50° *ApE* on the port side. Outside of such an angle range, the array becomes less accurate. Scenario Y-B3 shows both side linear arrays fixed at 70° (Figure 4.64). An SRE of less than $\pm 30\text{m}$ is found when the middle linear array swings within an angle range of 65° to 70° *ApE* on the port side. Outside of such an angle range, the array becomes less accurate.

Scenarios Y-C1, Y-C2 and Y-C3 show a vessel turning to starboard side with both side linear arrays fixed at 20° , 45° and 70° respectively and the middle array swinging from one side to the other. Since the three scenarios are exactly a reflection of scenario Y-B because of the geometric symmetry, the simulations reflect exactly the same results in an inverse way, as shown in Figure 4.65.

In summary, the shifted-pair array offers a higher performance of accuracy ($\text{SRE} < \pm 30\text{m}$). It is able to reach up to 65° *ApE* when the vessel moves in a straight line, up to 45° *ApE* when the vessel turns to port side and up to 35° *ApE* when the vessel turns to starboard. A lower performance comes only when both linear arrays overlap each other. In an ideal scenario, in which each linear array would move with the same angle simultaneously, the performance of the Y-shape geometry would be superior to that of any other geometry. Nevertheless, in a more realistic scenario, when the array geometry is distorted or is away from symmetry, the Y-shape array breaks down. It is more sensitive in its performance to the changes in the angle positioning error.

These simulations help as a metric to measure the sensitivity of each of the array geometries when common scenarios occur. The results are also applicable in different conditions when the array is exposed to aberrations caused by the ocean (e.g. currents). The following section discusses how changes on the depth-position of the receivers are also significant.

4.11.3 Array Depth-Motion

The ocean is never static; submarine currents, turbulence caused by propellers, and the speed of boats are among the most common causes of array depth-motion. The disturbance on each receiver position may generate significant errors in source range estimation.

For matters of simplicity, all the receivers from previous simulations have been positioned at the same depth or on the same plane. On a planar array, the angle of elevation for each of the hyperboloids never changes, because each of the pairs of receivers is found at the same depth. However, when at least one of the receivers changes its depth-position, the geometric scenario becomes volumetric with direct effects on source range estimation.

To investigate the effects of array *depth-motion* for one or more elements of the array, a series of experimental simulations using *volumetric arrays* is performed. The Y-shape with four elements was chosen as the exemplar geometry (Figure 4.66). The general specifications for the following series of experimental simulations are shown on Table 4.19. Because the source depth-position has a minimum depth range of $8L$ (60m), the *range* depth-position for each of the receivers is set within L (7.5m) and $6L$ (45m). A graphical representation of that scenario is shown in Figure 4.67.

Volumetric Y-shape Array		
Aperture length	A	Short (L)
Num. receivers	i	4
Pair of receivers		(1,2) (1,3) (1,4)
Num. sources	S_V	100
Horizontal Range	R_H	L
Depth Range	R_D	$8L$

Table 4.19: Simulation Specifications with Array Depth-Motion

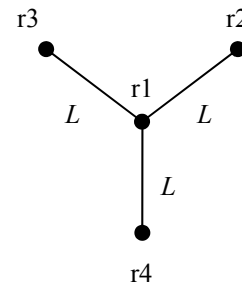


Figure 4.66: Y-shape Array Geometry

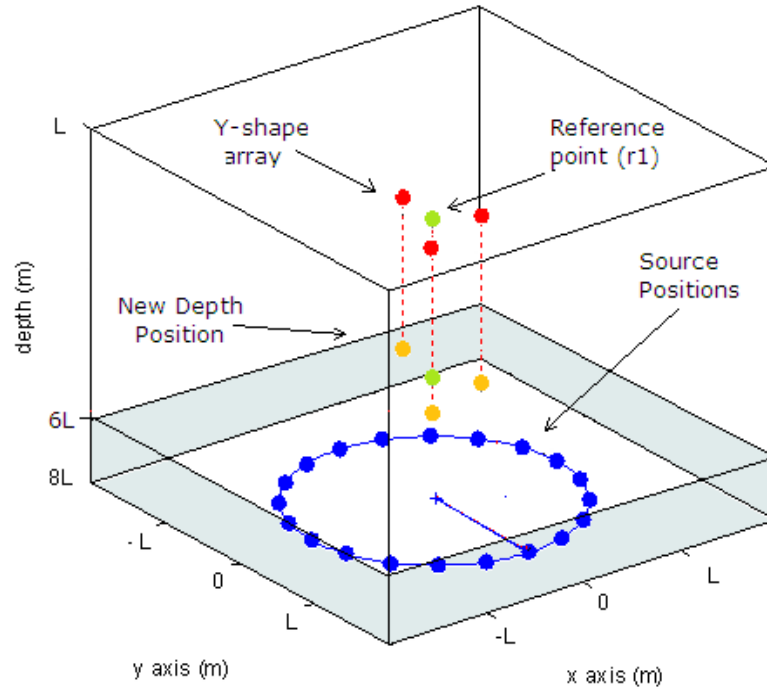


Figure 4.67: Array Depth-Motion scenario

	ONE receiver				TWO receivers				THREE receivers			
	R_1	R_2	R_3	R_4	R_1	R_2	R_3	R_4	R_1	R_2	R_3	R_4
A.	6L	L	L	L	6L	6L	L	L	6L	6L	6L	L
B.	L	6L	L	L	6L	L	6L	L	6L	6L	L	6L
C.	L	L	6L	L	6L	L	L	6L	6L	L	6L	6L
D.	L	L	L	6L	L	6L	6L	L	L	6L	6L	6L
E.					L	6L	L	6L				
F.					L	L	6L	6L				

Table 4.20 Combination of Different Experimental Simulations by varying the Depth-Position of ONE, TWO, and THREE receivers.

Table 4.20 shows the possible number of depth-motion combinations that the four receivers can have.

The first series of combinations include the depth-motion of only *one* receiver. These are divided into four different scenarios: A, B, C and D. The second series includes the depth-motion of *two* receivers at the same depth and are divided into six different scenarios: A, B, C, D, E and F. The third and last series include the depth-motion of *three* receivers with four different scenarios: A, B, C and D.

Figure 4.68 shows four scenarios with array depth-motion in *one* receiver. It results in three accurate scenarios B, C, and D, and one inaccurate scenario, A. Scenario A presents the inaccuracies with the depth-motion of R_1 to $6L$ (45m). That behaviour is also reasonable if we notice that on this scenario the three pairs of receivers have the same elevation angle, which has a direct effect on the geometric intersection between them. Scenarios B, C, D relate the accuracies with the fixed depth-motion of R_1 at $7.5m$ (L). For each simulation there is only one of the hyperboloids with an elevation angle different than zero. Scenario A has an elevation angle on pairs R_{12} , R_{13} , and R_{14} ; scenario B on pair R_{12} ; scenario C on pair R_{13} ; and scenario D on pair R_{14} .

Figure 4.69 shows six scenarios with array depth-motion in *two* receivers. Its results are accurate for the scenarios D, E and F; and inaccurate for the scenarios A, B, and C. Once again, the two accurate scenarios are related to the fixed depth-motion of R_1 at L (7.5m). The three inaccurate scenarios are related to the depth-motion of R_1 at $6L$ (45m). All the scenarios include two pairs of receivers with an elevation angle different from zero. Scenario A has an elevation angle on pairs R_{13} and R_{14} ; scenario B on pairs R_{12} and R_{14} ; scenario C on pairs R_{12} and R_{13} ; scenario D on pairs R_{12} and R_{13} ; scenario E on pairs R_{12} and R_{14} ; and scenario F on pairs R_{13} and R_{14} .

Figure 4.70 shows four scenarios with array depth-motion in *three* receivers. Its results are partially accurate for the scenario D, and inaccurate for the scenarios A, B and C. The scenarios A, B and C relate their inaccuracies to the depth-motion of R_1 at $6L$ (45m). Scenario D relates its inaccuracies to the angle elevation of the three pair of receivers. Scenario A has one elevation angle on pair R_{14} ; scenario B on pair R_{13} ; scenario C on pair R_{12} ; and scenario D on pairs R_{12} , R_{13} , and R_{14} .

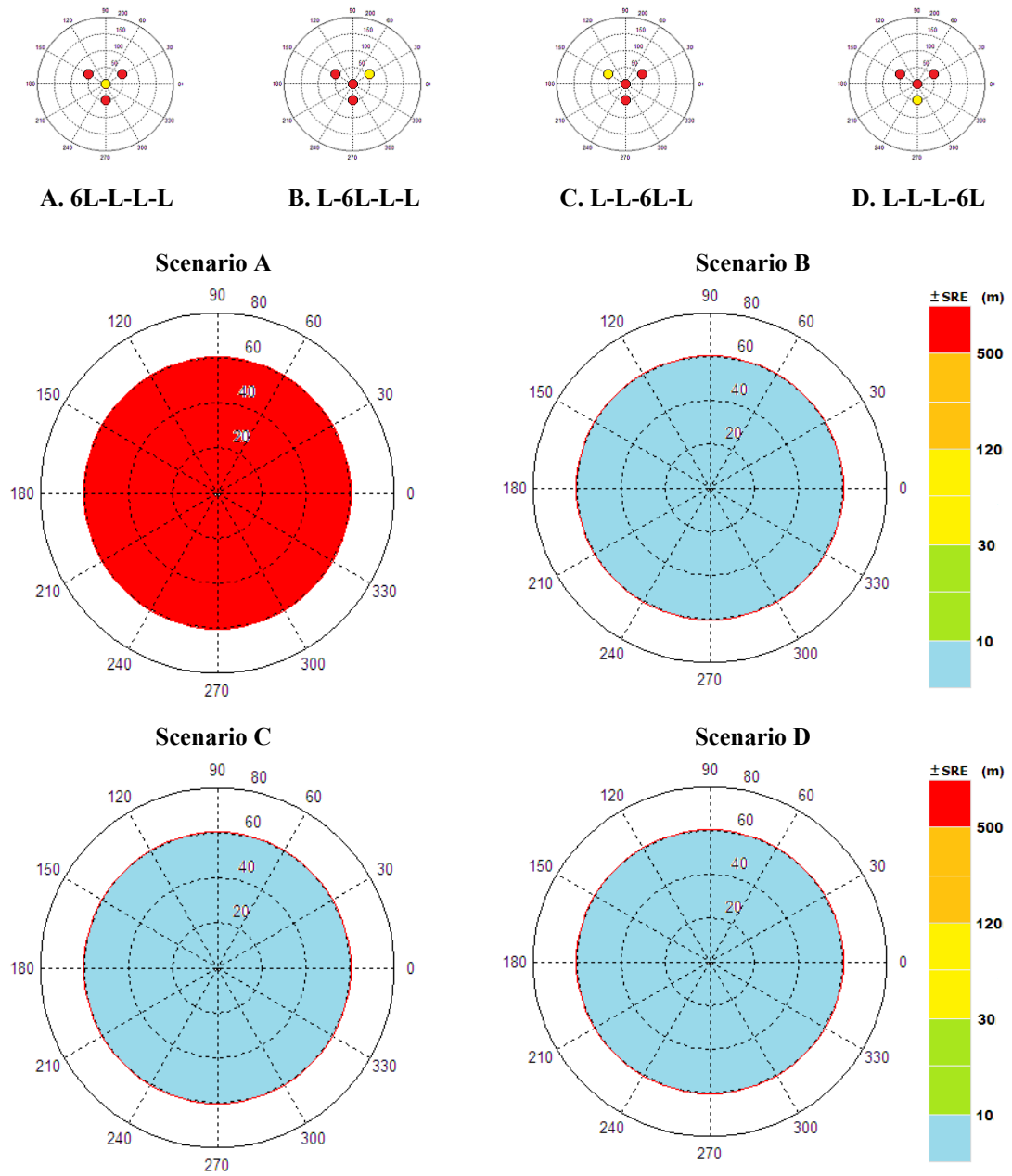


Figure 4.68: Four scenarios with depth-motion in ONE receiver (yellow). Notice that the scenario A, which has the receiver reference (R_1) at a greater depth (6L), is the most sensitive to the effects of the array depth-motion.

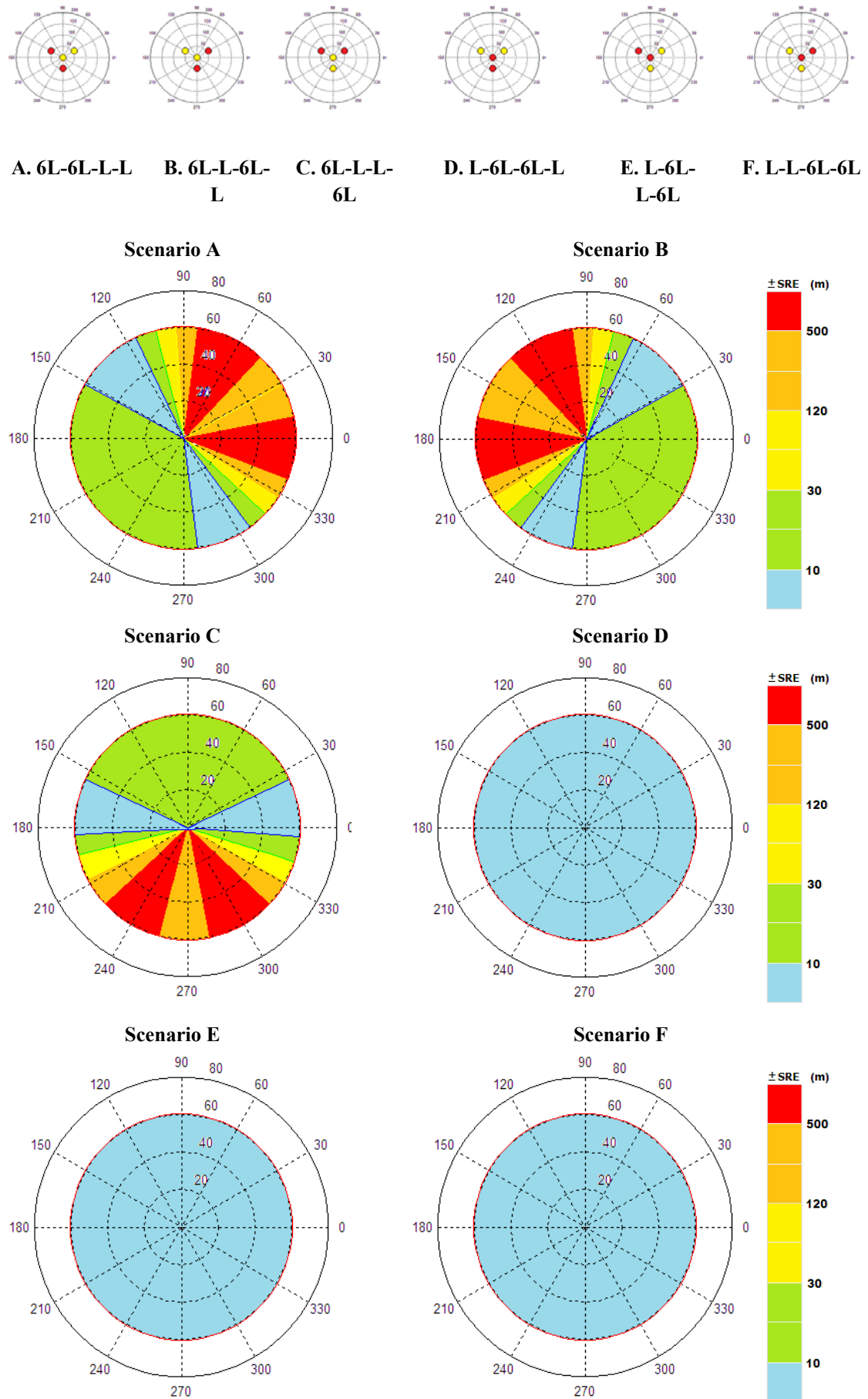


Figure 4.69: Six scenarios with depth-motion in TWO receivers (yellow). Scenarios A, B and C with the

receiver reference (R_1) at a greater depth ($6L$) suffer of inaccurate variations.

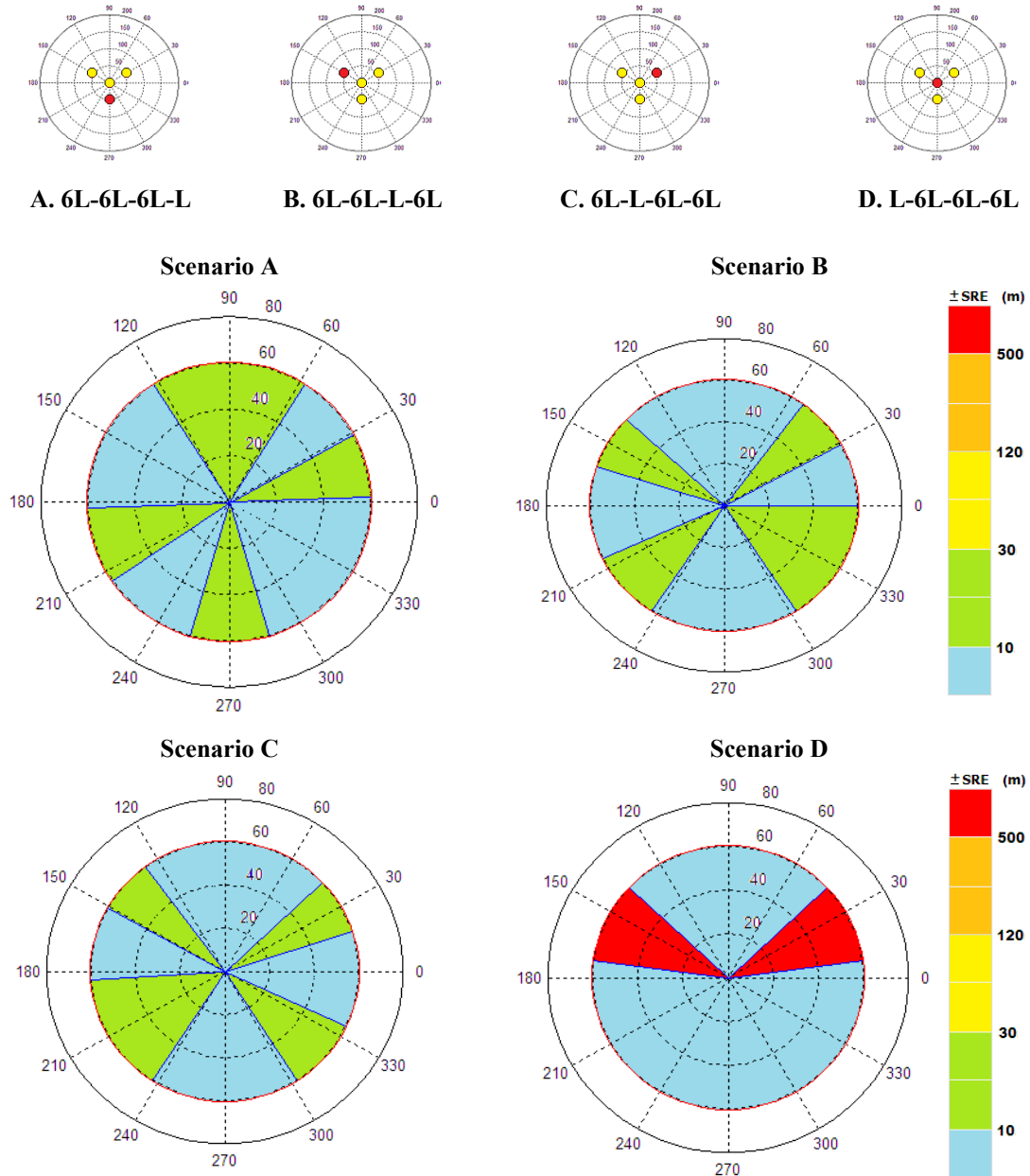


Figure 4.70: Four scenarios with depth-motion in THREE receivers (yellow). Notice that is only the scenario D with the receiver reference (R_1) at a fixed depth (L) that results partially accurate. Scenarios A, B, and C result inaccurate in several bearings.

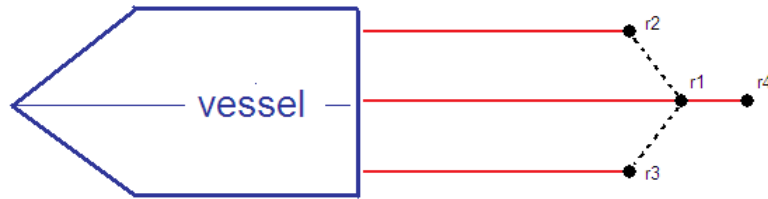
Table 4.21 shows the total number of possible receiver depth-combinations. There are six possible accurate combinations. The first three relate to the depth-motion of only one receiver. The following three relate to the depth-motion of two receivers. None of the simulations results is accurate when a depth-motion of three receivers is assumed. It is worth noting that there is no inaccuracy when all the receivers have a depth-motion below $4L$ (30m), no matter their combination. However, bearing inaccuracies result when the reference receiver R_1 has a depth-motion greater than $4L$ (30m).

Array Depth-Motion

No	R ₁	R ₂	R ₃	R ₄	# Receivers
1.	L	6L	L	L	1
2.	L	L	6L	L	1
3.	L	L	L	6L	1
4.	L	6L	6L	L	2
5.	L	6L	L	6L	2
6.	L	L	6L	6L	2

Table 4.21: Summary of the Accurate Combinations for Array Depth-Motion

To consider a more realistic scenario of a towed array with three lines, Figure 4.71 shows a diagram of a Y-shape array towed by a boat. R_2 is towed by a first line; R_1 and R_4 by a second line; and R_3 by a third line. If that scenario is implemented, the number of possible receiver depth-combinations of Table 4.21 would decrease to only three, as shown in Table 4.22.

**Figure 4.71:** Towed array of three lines for a Y-shape geometry**Towed Y-Array Depth-Motion**

No.	R ₁	R ₂	R ₃	R ₄	# receivers
1.	L	6L	L	L	1
2.	L	L	6L	L	1
3.	L	6L	6L	L	2

Table 4.22: Accurate Combinations for Array Depth-Motion of a Towed Y-shape Array.

In summary, to ensure accurate source locations with a Y-shape deployment on a towed array, a maximum receiver depth-motion of $6L$ from either R_2 or R_3 (or both) would be considered accurate. A maximum receiver depth-motion of $4L$ is conditioned only if the deployment of the middle line (R_1 - R_4) is found at inferior depths to the other two towed lines (R_2 and R_3).

4.11.4 Gaussian Array Depth-Motion

The Matlab simulator is able to generate a Gaussian array depth-motion. It is given by computing the probability distribution of each receiver depth-position. The Gaussian (normal) distribution equation [129] used is

$$\rho(x) = \frac{1}{\sigma\sqrt{2\pi}} e^{-\frac{x^2}{2\sigma^2}} \quad (4.4)$$

where

x is the media of several measurements of the receiver depth-motion
 σ represents its standard deviation.

The simulator takes an exemplar minimal number of a hundred random depth-positions for each receiver and calculates their Gaussian distribution. The result is a complete new receiver-array with different depth-positions. Table 4.23 shows the receiver positions of two simulations with Gaussian array depth-motion added to a Y-shape and Shifted-pair planar-arrays with an initial depth of L (7.5m). The array simulations use the same specifications as those shown in Table 4.19.

Synthetic Array Depth-Motion				
	R_1	R_2	R_3	R_4
A.	2.3L	2.7L	5.6L	3.2L
B.	3.9L	4.5L	L	2.6L

Table 4.23: Gaussian Array Depth-Motion Simulation Specifications.

These two random scenarios of Figure 4.72 confirm the results of the previous section. The result from scenario A is completely accurate, because the reference receiver R_1 has the lowest depth-motion. The result of scenario B is partially accurate, mainly for two reasons. First, R_1 is not the receiver with the lowest depth-motion. Secondly, R_2 is greater than $4L$.

In Figure 4.73 the results are exaggerated. None of the scenarios gave accurate results for the Shifted-pair. However, as happens with the Y-shape, the inaccuracy of scenario B is greater than that of scenario A.

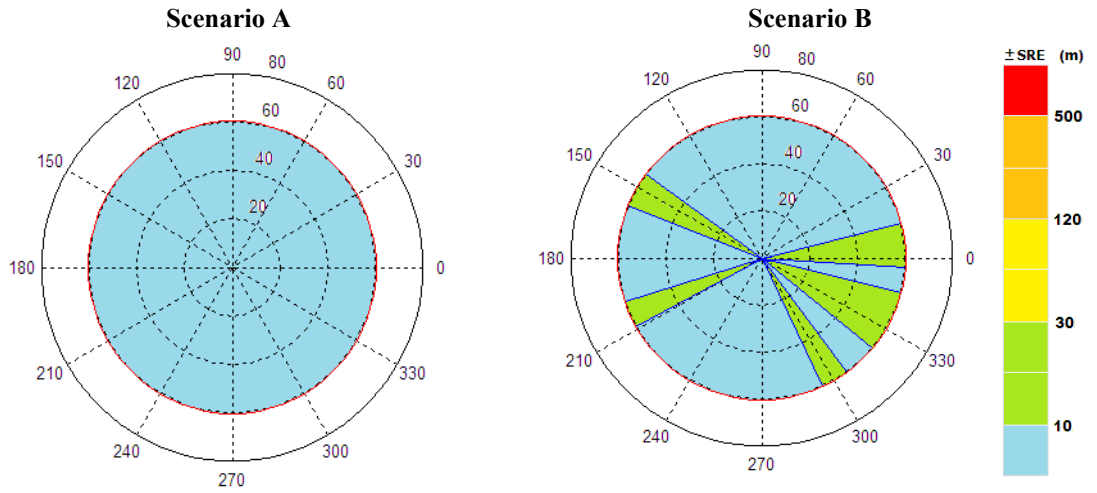


Figure 4.72: Experimental simulations with synthetic aberrations. **Y-shape array.**

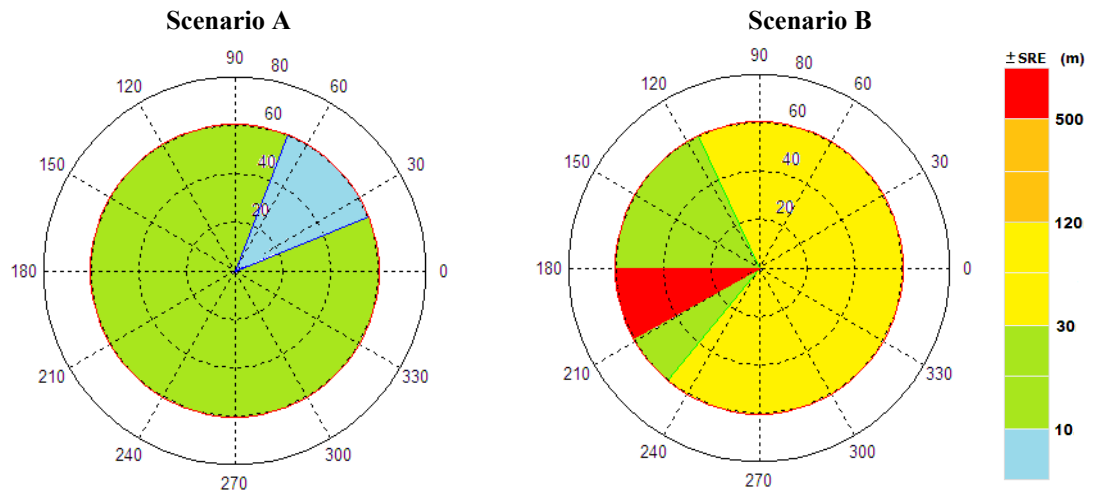


Figure 4.73: Experimental simulations with synthetic aberrations. **Shifted-pair array.**

Since different receiver depth-positions may offer a wide variety of scenarios, the previous simulations highlight the significance of the positioning-error when deploying an array-configuration.

4.12 Discussion and Summary

This chapter has introduced the general concept of array-configurations and its direct effects on source range estimation. It also provides a compilation of practical suggestions to consider before the deployment of a hydrophone array, assuming a highly idealized scenario.

The number of receivers, the geometry and the aperture between each pair of elements are among the most important features of an array-configuration. Four receivers are sufficient to give a desirable range and bearing, including azimuth and elevation angles. Although theoretically more receivers will improve the error in source range estimation, the other most important factor is the array geometry.

Depending on the number of elements, each array configuration can have a vast number of possible combinations, resulting in different geometries (e.g. square, trapezium, triangular, shifted-pair, and Y-shape) and apertures. The choice of different pair combinations becomes redundant, having a minor effect on source range estimation of the array geometry chosen. The concept of aperture is based on the minimal distance separation (L) of two elements to receive the lowest frequency produced by a Sperm whale. Assuming acoustic plane wave propagation in a homogeneous medium, L is 7.5 metres. The notation in this thesis is that a short-aperture is defined as have a distance separation equivalent to L . A long-aperture is defined with a length of $16L$. The receivers can be arranged either on a planar or in a volumetric array.

On a planar array, all the elements are deployed along a two-dimensional plane, assuming a static receiver positioning. Planar geometries find it difficult to give a completely accurate depth-source range, mainly because of the nature of the hyperboloid geometric surface. Nevertheless, the use of long apertures improves the accuracy of the depth-source range in most of the geometries. Although the number of choice of pair-combinations increases with the number of receivers, it was shown that the choice of pair combinations with four receivers has a minor effect on source range estimation in the majority of the array geometries.

In a volumetric array, the elements are deployed along a three-dimensional plane, assuming a variable receiver depth-motion. Not all the possible receiver depth-combinations produce accurate results. The choice of one receiver, as a reference deployed at the lowest possible depth, improves the accuracy when a volumetric array is used.

As mentioned before, the clearest result of these experimental simulations is that the source range estimation improves with longer apertures. However, if the ratio of range to size aperture for each array configuration is measured, it is found that such a ratio decreases for longer apertures as a result of the hyperbolic localisation error caused by the small angle between the intersections of hyperbolic surfaces. Therefore, lengthening the aperture array may be one solution to enable the assessment of a more distant source. However, in reality, this implies a more complicated deployment [150].

The square geometry is able to reach sources at a relatively long distance, depending on its aperture. This geometry is not completely accurate, owing to the inaccuracies that appear when the source is positioned on broadside to one of the receiver-pairs of the array. It also finds it difficult to locate sources at depths greater than $8L$. It constitutes a non-recommended geometry for deployment.

The Y-shape array represents a simple geometry with four elements, which provides accurate source locations for longer and deeper ranges. It does not have any of the broadside inaccuracies that the square geometry has. It only becomes inaccurate when the source lies out of its range location. The Y-shape geometry is also accurate when locating sources at a greater horizontal and depth range than the square geometry does. It also proved to be the most accurate for a typical Sperm whale dive profile. The long Y-shape array constitutes a configuration recommended for use in source locations found within a volume of 800m^3 . In towed deployments, the Y-shape array shows a minimal loss in performance only when the array geometry is able to keep its symmetry. Nevertheless, if the geometry is seriously distorted, it performs poorly. If an array depth-motion is assumed, a maximum receiver depth-motion of $4L$ is conditioned to receivers R_1 and R_4 only if their depth-position is less deep than the receivers R_2 and R_3 .

The trapezium array constitutes a non-recommendable geometry to deploy. It resulted in most cases being inaccurate. The broadside condition is always present. The triangle array is accurate only for shallow sources (i.e. 60m) with short horizontal ranges (i.e. 60m). The shifted-pair geometry has the advantage of reaching deep source ranges (64L) when using a long aperture array. Its towing deployment is easy and simple. It also proves to be less sensitive in its performance when the angle (ApE) positioning-error increases and the vessel either moves in a straight line or turns to port or starboard.

Table 4.24 shows an ultimate summary of the array geometries, shifted-pair and Y-shape. This table is similar to the one shown before (see Table 4.15). A subjective score (from 0 to 10) is given to each geometry. The new metric values are based on 100% accuracy for tracking a dive profile with an *offset-positioning-error* (OpE) of $\pm 30\text{m}$, and when an array is towed by a vessel moving in straight line, with a delta *angle-positioning-error* (ApE) of 90° . The Shifted geometry has the highest score. Assuming its higher performance and simplicity when it is towed from a vessel, it may constitute the best choice. The Y-shape geometry still constitutes the most accurate geometry in terms of reaching longer source ranges and tracking a dive source profile. However, when its symmetry is seriously distorted by OpA or ApE , it ceases to be the most accurate.

100% Accuracy ($SRE \leq \pm 10\text{m}$)

	Y-shape	Score	Shifted-pair	Score
RH Long	32L	10	16L	5
RH Short	8L	10	8L	10
RD Deep	32L	5	32L	5
RD Shallow	8L	10	8L	10
Dive Profile	45%	4.5	35%	3.5
OpA ($\pm 30\text{m}$)	15%	1.5	60%	6
ApE ($\Delta 90^\circ$) straight line	$\Delta 5^\circ$	0.6	$\Delta 65^\circ$	7.2
Score		5.9		6.7

R_H Horizontal Range Long (32L) Short (8L)
 R_D Depth Range Deep (64L) Shallow (8L)

Table 4.24: Ultimate Summary Table on the Accuracy of Array Optimization

This chapter constitutes an initial study of array optimization using a geometric hyperbolic localisation algorithm and assuming a highly idealized scenario. The following chapter discusses in detail the effects associated with a non-homogeneous medium.

Chapter 5

Non-Homogeneous Medium

Chapter five investigates the variables associated on a non-homogeneous medium. Simulation data (TDOAs) are generated through an acoustic propagation model that takes into account the *Sound Speed Profile (SSP)*. In the previous chapter, all the simulations focused on a homogeneous and idealistic medium, where it is said that the sound travels in a straight line. In this chapter, the hyperbolic algorithm is integrated in a more realistic scenario, where the sound bends as a result of refraction.

Since the hyperbolic algorithm is not designed to work on a non-homogeneous medium, inaccurate results are expected. Nevertheless, as discussed in previous chapters, the majority of people use these localisation techniques on natural environments where the sound speed is not constant. This chapter discusses the 3D geometric hyperbolic algorithm array-accuracy and its associated effects when the non-homogeneous medium is included.

5.1 Acoustic Propagation Model

The study of sound propagation in the ocean is fundamental to the understanding of all other underwater acoustic phenomena. Chapter three presented a synthesis of the basis of the underwater modelling. To include the effects of a non-homogeneous medium into the source range estimation, an integration of the output data of the acoustic propagation model into the 3D geometric hyperbolic algorithm is necessary.

5.1.1 Model Integration

The synthetic data constitutes the main input variables needed for both scenarios: homogeneous and non-homogeneous. These variables include the synthetic source position and array-configuration. While only a constant sound speed is needed to represent a homogeneous medium, the sound speed profile is an essential input variable for the acoustic propagation model into a non-homogeneous medium. Since the hyperbolic technique relies on the TDOA to create the different number of

hyperboloids, a new set of TDOA_{ssp} is obtained from the acoustic propagation model. A basic diagram of the acoustic propagation model integration into the hyperbolic algorithm is shown in Figure 5.1.

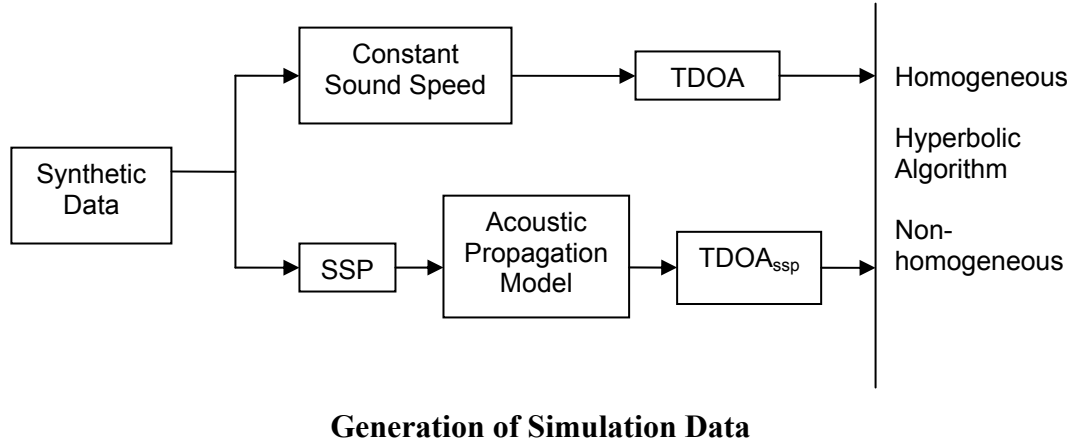


Figure 5.1 Generation of Simulation Data. Basic diagram of the acoustic propagation model integration of the hyperbolic algorithm into a non-homogeneous medium.

5.1.2 Sound Speed Profile (SSP)

The acoustic path from the source to the receiver may pass through a range of different sound speeds. Most of the experimental simulations correspond to one sound speed profile used. However, to validate those results, some experimental simulations are chosen and tested with two additional sound speed profiles. These profiles correspond to data gathered in the Gulf of Mexico 2003 by Dr. Douglas Biggs from the University of Texas [64, 65]. However, since our vocalising source scenario reaches a depth of 800m as average [2], the profiles chosen are limited to negative sound speed gradient, as shown in Figure 5.2. The sound speed in blue (SSP1) corresponds to that most used in the experimental simulations. The one in yellow (SSP2) has the highest variation of sound speed, being particularly extreme at shallow waters less than 100m in depth. The profile in red (SSP3) is the one with the lowest variation of sound speed.

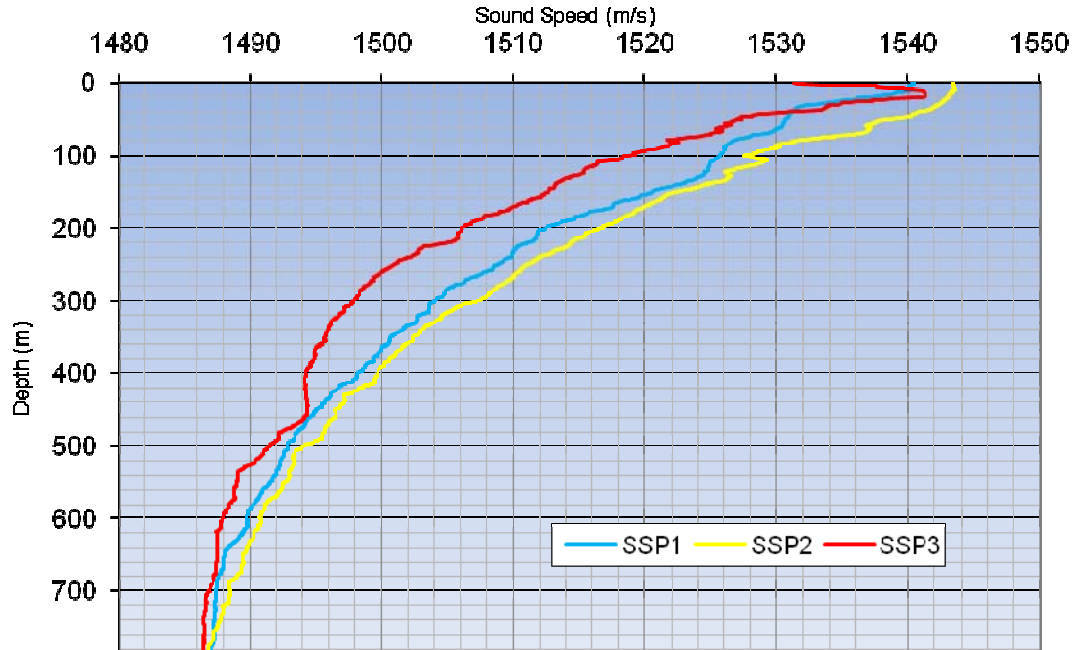


Figure 5.2: Three different sound speed profiles correspondent to the Gulf of Mexico [64, 65].

5.1.3 Bellhop Model

Because each medium has its own features that make it quite particular, is impossible to use only one model to represent the general properties of the ocean. However, since the author's aim focus is on a particular environment where the Sperm whale lives, Bellhop ray model [88] is considered as the most convenient model to simulate similar underwater sound propagation conditions in the sea. Occasionally a mixture of the models is used. Such combined techniques are referred to as hybrid approaches. Although ray-tracing techniques are theoretically applicable to fully range-dependent (3D) problems, they are rarely implemented as such.

Bellhop differs from standard ray models in using a robust variant of Gaussian beam tracing, which is a technique especially attractive for high-frequency (>500 Hz). In comparison to standard ray tracing, the method has the advantage of being free of certain ray-tracing artefacts, such as perfect shadows and infinitely high energy at caustics (Figure 5.3). Several informal attempts have been made to smooth the ray-tracing results by taking into account the inherent variation of the medium, thus achieving an answer which more closely resembles reality.

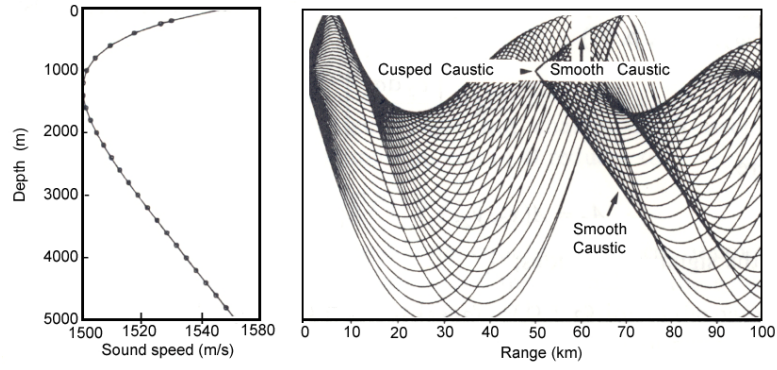


Figure 5.3: Sound speed profile and associated ray trace showing the formation of smooth and cusped caustics. (Published by [44] and adapted by [28])

Basically, the model consists of approximating a given source by a fan of beams and tracing the propagation of these beams through the medium. The quantities of interest are then computed at a specified location by summing the contributions of each of the individual beams [80]. The approach is based on the idea that a ray should be considered as a statistically varying curve with Gaussian statistics. This leads informally to associating a Gaussian intensity distribution with each ray. The ray then becomes the central ray of the Gaussian beam. The Gaussian beam is given an initial beam width and curvature at the source point, but is allowed to expand and contract or change curvature as it propagates away from the source [61].

With regard to efficiency, the Bellhop model is actually set up internally to do a full range-dependent ray trace while it allows only for a range-independent input structure as in the case of the sound speed profile. Bellhop works by assuming an initial fan of beams, each with a Gaussian intensity profile. The signal at a receiver is calculated by summing the contributions of all beams that pass close enough to the receiver to produce a non-negligible signal. The result is several *times of arrival* (TOAs) with slightly different delays but with very different amplitudes. These are used to compute the new set of TDOA_{SSP} . The highest amplitude arrival will be from the beam that has passed closest to the receiver. The more beams the user specifies, the closer he will get to the eigenray solution. The environment treated consists of an acoustic medium with water column sound speed that depends on depth. Although Bellhop can optionally be run with a bathymetry file, this option is not always used for scenarios with greater depths [88].

5.1.4 Modelling Settings

The Bellhop model is modelled by an underwater acoustic propagation modelling algorithm called AcTUP V1.6 [180]. It runs under Matlab and was written by Alec Duncan from the Centre for Marine Science and Technology at Curtin University of Technology. Matlab scripts, developed by the author of this thesis, were also used. AcTup V1.6 provides a uniform, menu-based user interface for running different models and plotting the results. Among the main input variables to include in the model are:

- source vocalising average frequency (Hz)
- source directionality angles (degrees)
- number of beams, receiver depths (m)
- horizontal range (m)
- *sound speed profile (SSP)*

For a detailed description of the acoustic propagation *Graphical Interface User (GUI)*, see the Appendix C.2 To simulate a non-homogeneous scenario favourable for our target (sperm whale), the following assumptions are considered:

- No bathymetry is included. Cetaceans like sperm whales are used to diving in deep waters where the sea bottom has little effect on the sound propagation.
- An average source frequency of 14 kHz is used because of its very high energy, according to a typical PSD for sperm whale (see Table 4.8).
- Omni-directional receivers.
- Typical sound speed profiles of 800m of depth are used.

5.2 Experimental Modelling for a Hyperbolic Algorithm

By using the new data ($TDOA_{SSP}$) as an input into the same geometric hyperbolic algorithm (used in chapter four), a new group of experimental simulations is the result. A comparison of the effects associated with the two mediums (homogeneous and non-homogeneous) on the array-accuracy to solve the source range problem is analysed through a series of simulations. Square and Y-shape array configurations are used again.

The technical specifications for the array configurations and synthetic source positions are shown in Tables 5.1 and 5.2. They are exactly the same as those shown in chapter four (see Table 4.4).

Depth Range	Horizontal Range						
8LR _D	LR _H	2LR _H	4LR _H	8LR _H	16LR _H	32LR _H	64LR _H
16LR _D	LR _H	2LR _H	4LR _H	8LR _H	16LR _H	32LR _H	64LR _H
32LR _D	LR _H	2LR _H	4LR _H	8LR _H	16LR _H	32LR _H	64LR _H
64LR _D	LR _H	2LR _H	4LR _H	8LR _H	16LR _H	32LR _H	64LR _H

Table 5.1: Synthetic source values of R_H and R_D used for the experimental simulations

Array-Configuration		n= {0, 1, ... , 7} m= {3, 4, ... , 6}	
Aperture length	A	Short (L)	Long (16L)
Num. receivers	i	4	4
Receivers depth	r_d	L	L
Num. sources	S_V	100	100
Horizontal Range	R_H	$2^n L$	$2^n L$
Depth Range	R_D	$2^m L$	$2^m L$

Table 5.2: Experimental Specifications for two *Array-Configurations*

5.2.1 Short Aperture

The first series of experimental simulations uses a short-aperture. The first array configuration to be tested is the *Square-array*. The result is a complete number of inaccurate results for any of the horizontal and depth ranges shown in Table 5.3.

	Homogeneous							Non-Homogeneous						
$R_D \backslash R_H$	L	2L	4L	8L	16L	32L	64L	L	2L	4L	8L	16L	32L	64L
8L	O	O	O	O	O	O	O	O	O	O	O	O	O	O
16L	O	O	O	O	O	O	O	O	O	O	O	O	O	O
32L	O	O	O	O	O	O	O	O	O	O	O	O	O	O
64L	O	O	O	O	O	O	O	O	O	O	O	O	O	O

- O Inaccurate 80% SRE $> \pm 10m$
 ● Partially Accurate 80% SRE $< \pm 10m$
 ● Accurate 100% SRE $< \pm 10m$

Table 5.3: Summarised table of the results correspondent to a Short-Square-Array

For instance, Figure 5.4 shows a horizontal source range of 16L and depth range of 8L. The experimental simulation on the left side corresponds to a homogenous medium. On the right side and in a square box, the same experimental simulation including a non-homogeneous medium is presented. The difference is clearly noticeable.

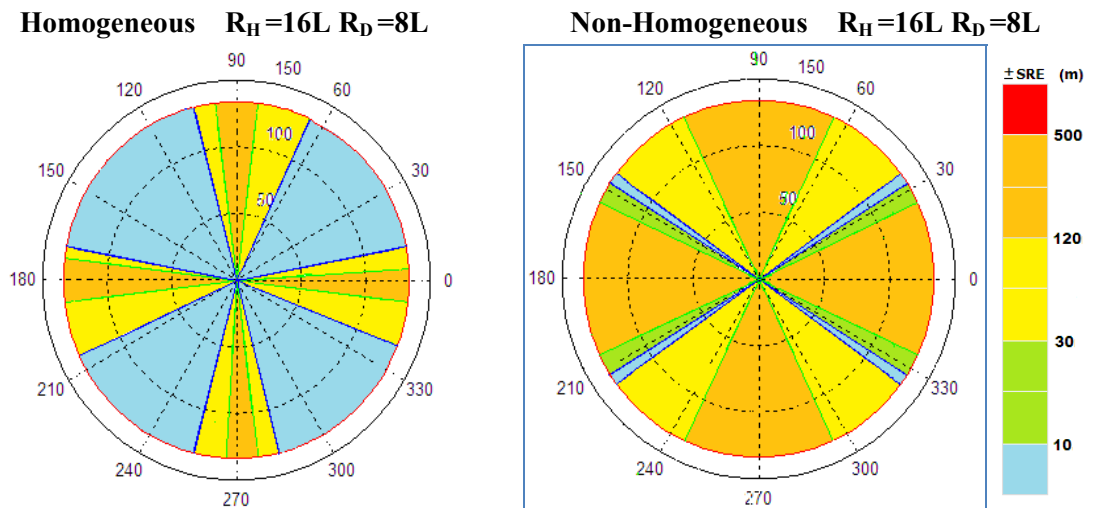


Figure 5.4: Short-Square-Array ($16L_{R_H}$ & $8L_{R_D}$). Homogeneous (left), Non-Homogeneous (right). A scale of different SRE thresholds is shown in different colours. Notice how the SRE increases in a non-homogeneous medium.





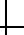





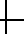





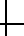

The square array inaccuracies cover a wider area in a non-homogeneous medium. In a homogeneous scenario, the accurate bearings (blue) cover 74% of the total source positions. However, when the non-homogeneous medium is present, the accuracy is

reduced to only 6% of the total source positions.. Even if the threshold of $\pm 10\text{m}$ could be increased to less than $\pm 120\text{m}$, as shown with the bearings in yellow and green, the array would still be considered to be inaccurate.

The rest of the short-aperture simulations present characteristics very similar to the one above. When using a short aperture array, the small range of TDOA values ($\pm 5\text{ms}$) is affected by the minor change of new conditions in the non-homogeneous medium. The result is a new group of TDOA_{SSP} that do not generate the correct results.

In summary, the use of square arrays with short-aperture in a non-homogeneous medium will always have negative effects on the accuracy of source range estimation.

The second array configuration to be tested is the *Y-shape array*. In a way similar to that of the square array, deploying a short-aperture array in a non-homogeneous medium results in inaccurate source locations. Table 5.4 presents a summary and a comparison of the results obtained in the two scenarios: homogeneous and non-homogeneous.

	Homogeneous							Non-Homogeneous						
$R_D \backslash R_H$	L	2L	4L	8L	16L	32L	64L	L	2L	4L	8L	16L	32L	64L
8L							O	O	O	O	O	O	O	O
16L							O	O	O	O	O	O	O	O
32L							O	O	O	O	O	O	O	O
64L	O	O	O	O	O	O	O	O	O	O	O	O	O	O



O	Inaccurate	80% $\text{SRE} > \pm 10\text{m}$
	Partially Accurate	80% $\text{SRE} < \pm 10\text{m}$
	Accurate	100% $\text{SRE} < \pm 10\text{m}$

Table 5.4: Summarised table of the results correspondent to a Short-Y-shape-Array.

For instance, consider Figure 5.5 which shows a horizontal source range of $8L R_H$ and a depth range of $8L R_D$. The homogeneous medium shows a completely accurate source range estimation. The non-homogeneous medium shows a different scenario.

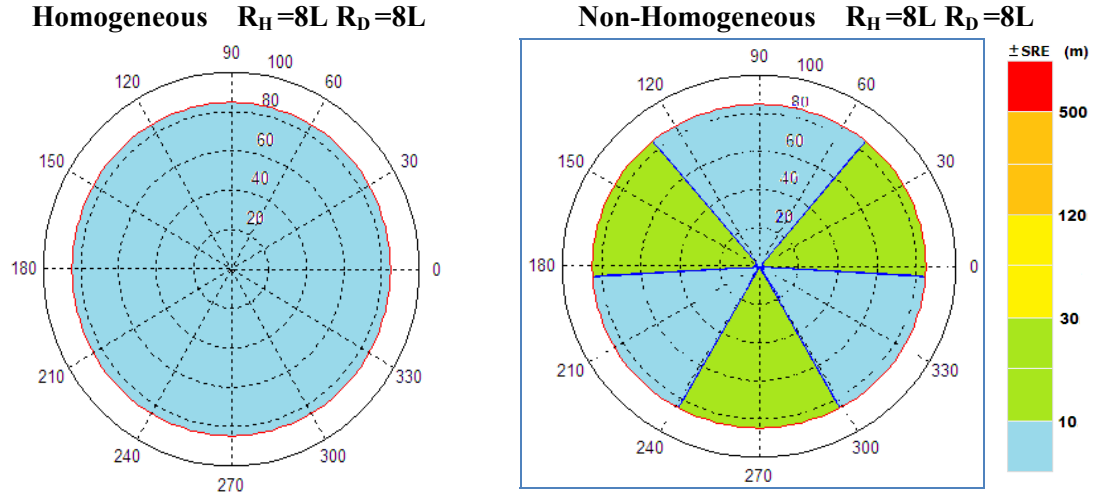


Figure 5.5: Short-Y-shape-Array ($8LR_H$ & $8LR_D$). Homogeneous (left), Non-Homogeneous (right). Two different SRE thresholds are shown (blue & green). If the threshold is increased to $\pm 30m$ SRE, the whole number of sources locations of the non-homogeneous medium could be considered as accurate.

The differences associated with the new group of $TDOA_{SSP}$ produced major effects on source range estimation of $\pm 10m$ SRE. However, if the threshold is increased only to $\pm 30m$ SRE, the array-configuration could be considered accurate for all the source positions with no inaccuracy. In our particular scenario ($\pm 10m$ SRE), the use of a Y-shape-array with short-aperture in a non-homogeneous medium gave an inaccurate result.

5.2.2 Long Aperture

The second series of experimental simulations correspond to source range estimation of the *long Square array* for both mediums. From the results, it is found that source ranges under the equivalent of $8L R_H$ are not among the most accurate locations. A summary of the results is shown in Table 5.5.

	Homogeneous							Non-Homogeneous						
$R_D \backslash R_H$	L	2L	4L	8L	16L	32L	64L	L	2L	4L	8L	16L	32L	64L
8L	O	O	◐	◐	◐	◐	◐	O	O	O	◐	◐	◐	O
16L	O	O	O	O	◐	◐	◐	O	O	O	O	O	O	O
32L	O	O	O	O	O	O	O	O	O	O	O	O	O	O
64L	O	O	O	O	O	O	O	O	O	O	O	O	O	O

O Inaccurate 80% $SRE > \pm 10m$
 ◐ Partially Accurate 80% $SRE < \pm 10m$
 ● Accurate 100% $SRE < \pm 10m$

Table 5.5: Summarised table of the results correspondent to a Long-Square-Array

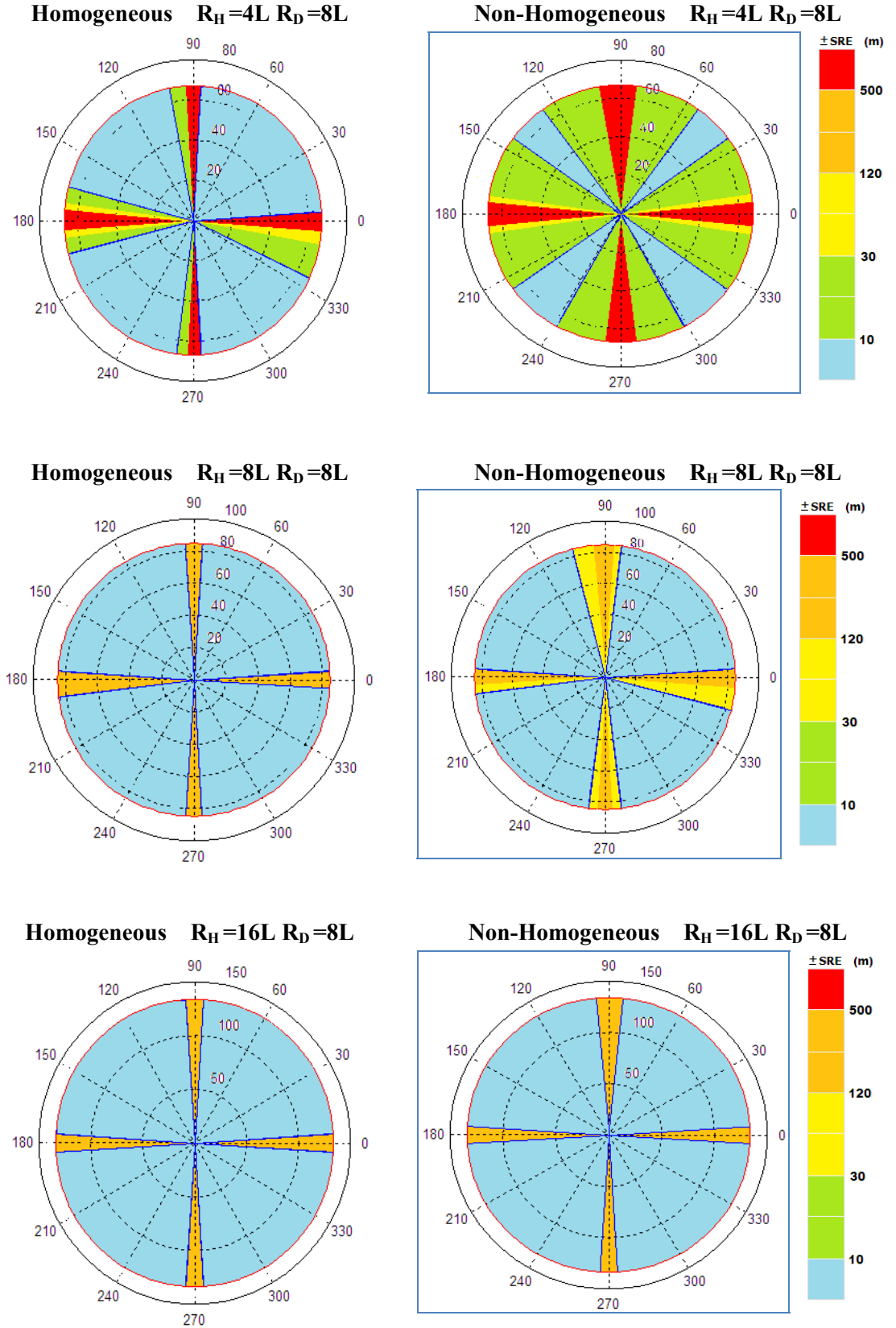


Figure 5.6: Long-Square-Array ($4L$ - $16LR_H$, $8LR_D$) Homogeneous (left), Non-Homogeneous (right). Increasing the aperture array improves the performance for a determined source range only.

For instance, consider Figure 5.6. The bearings in green show the sources found within $\pm 10\text{m} < \text{SRE} \leq \pm 30\text{m}$; in yellow those found within $\pm 30\text{m} < \text{SRE} \leq \pm 120\text{m}$; in orange those found within $\pm 120\text{m} < \text{SRE} \leq \pm 500\text{m}$; and in red those found with $\text{SRE} > \pm 500\text{m}$.

At source ranges of $4L R_H$, the long square array resulted inaccurate to localise the majority of the source positions when a non-homogeneous medium is included. When the source range increased to $8L R_H$, some of the inaccurate results ($\pm 10\text{m} < \text{SRE} \leq \pm 30\text{m}$) are reduced and the long square array became partially accurate. For source ranges of $16L R_H$ and $32L R_H$, the differences between homogeneous and non-homogeneous are too minimal. In summary, the long-square array in a non-homogeneous medium is limited to reach only with partial accuracy horizontal source ranges of the order of up to $32L R_H$ and $8L R_D$.

Unlike the short square array, source range estimation in a non-homogeneous medium improved with the *long square array*. Since a long-aperture of $16L$ (120m) generates a bigger range of TDOAs values ($\pm 80\text{ms}$), source range estimation is less inaccurate than when using a short aperture. However, the typical angles for broadside uncertainties are still present.

The next series of experimental simulations correspond to source range estimation of the *long Y-shape array*. A summary of the results is shown in Table 5.6.

$R_D \backslash R_H$	Homogeneous							Non-Homogeneous						
	L	2L	4L	8L	16L	32L	64L	L	2L	4L	8L	16L	32L	64L
8L	●	●	●	●	●	●	●	●	●	●	●	●	●	O
16L	●	●	●	●	●	●	●	●	●	●	●	●	●	O
32L	●	●	●	●	●	●	●	●	●	●	●	●	●	O
64L	●	O	O	O	O	O	O	●	O	O	O	O	O	O

O	Inaccurate	80% $\text{SRE} > \pm 10\text{m}$
●	Partially Accurate	80% $\text{SRE} < \pm 10\text{m}$
●	Accurate	100% $\text{SRE} < \pm 10\text{m}$

Table 5.6: Summarised table of the results correspondent to a Long-Y-shape-Array

The results show a significant similarity between the accuracy found in a homogeneous and a non-homogeneous mediums. Figures 5.7 show two representative results of the total number of experimental simulations. Figure 5.7a shows how although the SRE is

slightly bigger than in a homogeneous medium, all the slant ranges are found within the tolerance error of $\pm 10\text{m}$, producing accurate results.

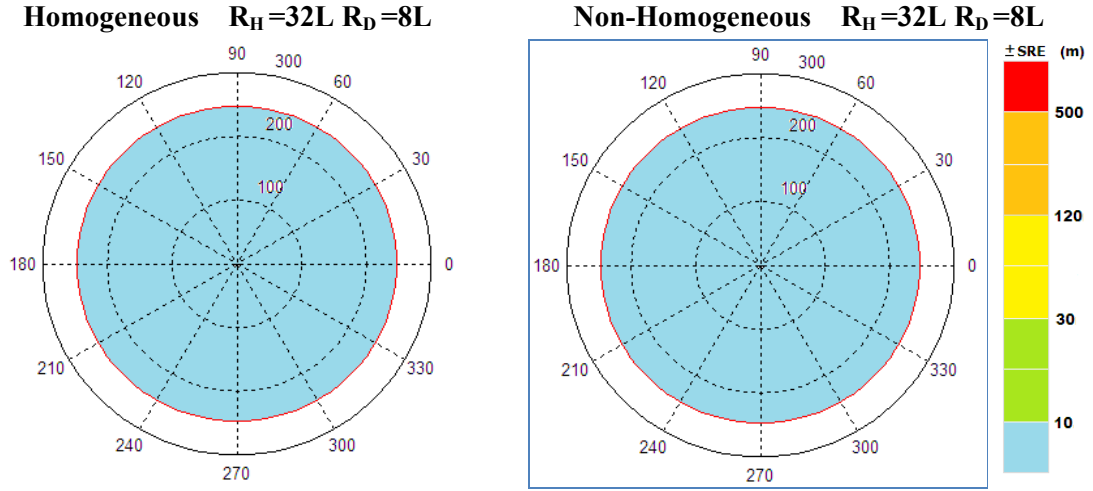


Figure 5.7a: Long-Y-shape (32LR_H, 8LR_D). Homogeneous (left), Non-Homogeneous (right).

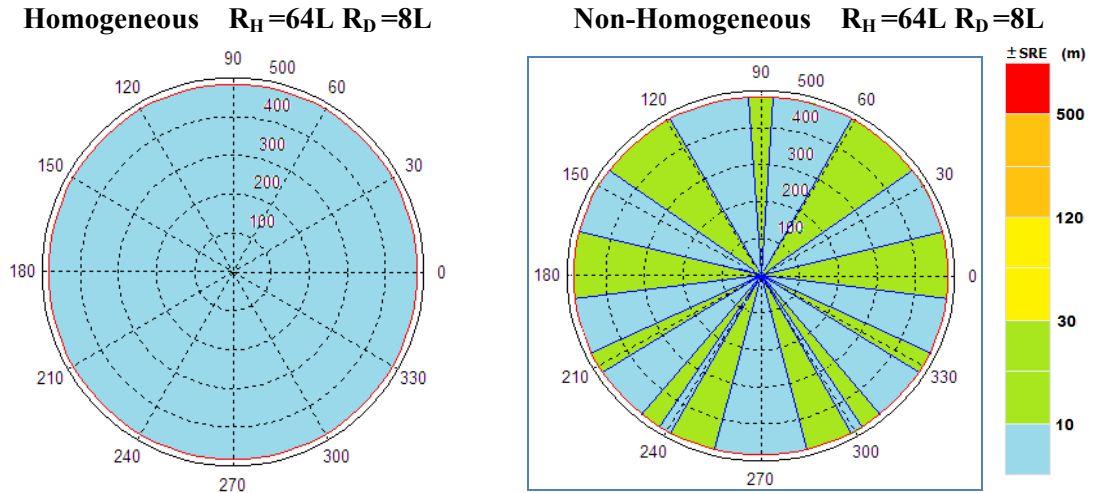


Figure 5.7b: Long-Y-shape (64LR_H, 8LR_D). Homogeneous (left), Non-Homogeneous (right).

Figure 5.7b shows how the long Y-shape array fails to produce accurate results for all the horizontal source ranges near to 64L (0.5km) and over. However, in the same way as happened in the short-aperture, if the threshold is increased only to $\pm 30\text{m}$ SRE, the array configuration could be considered accurate for all the source positions at horizontal and depth ranges of 64L. In summary, the long Y-shape array proves not to be affected greatly by a non-homogeneous medium. The longer aperture helps to minimize the deteriorating effect of the sound speed on the TDOAs.

5.2.3 The use of different SSP

For the following experimental simulations, the same horizontal source range ($32L R_H$) and two different depth ranges ($8L R_D$ and $16L R_D$) are chosen. Because the receivers are deployed at 7.5m depth and the maximum capabilities of the array configurations to reach accurate source locations in a non-homogeneous medium are limited to only 127.5m, a reduced sound speed profile is then used (Figure 5.8). For the shallow source positions at $8L R_D$, the profiles used are SSP1 and SSP2. For deeper source positions at $16L R_D$, the profiles used are SSP1 and SSP3. Two different array geometries are tested. Both array geometries have the same experimental specifications, shown in Table 5.7.

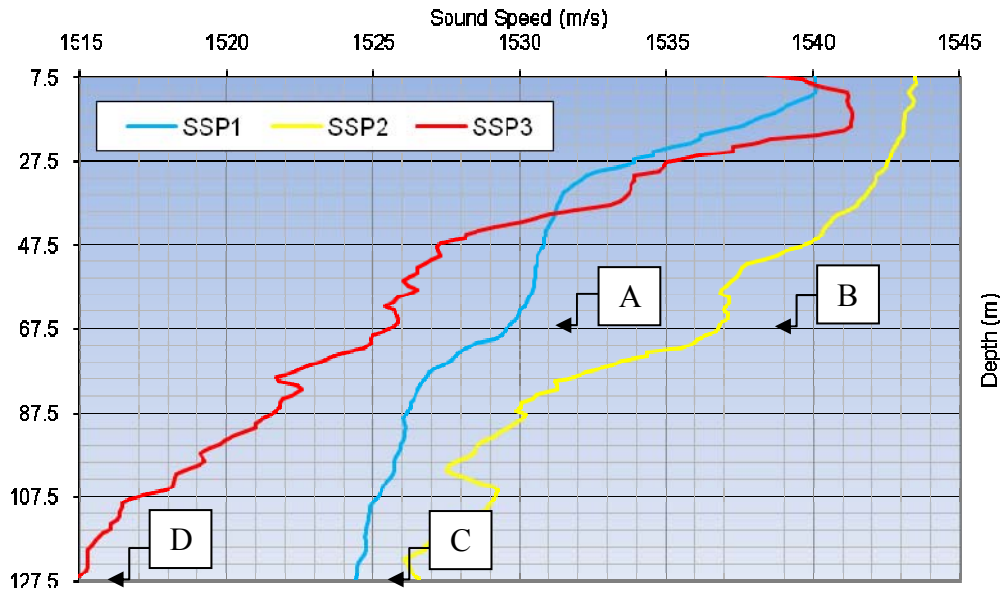


Figure 5.8: Scenario with three different sound speed profiles (SSP1, SSP2, & SSP3) and four different source positions (A, B, C & D).

Array-configuration		A	B	C	D
Sound Speed Profile		SSP1	SSP2	SSP1	SSP3
Num. receivers	i	4	4	4	4
Receivers depth	r_d	L	L	L	L
Num. sources	S_V	100	100	100	100
Horizontal Range	R_H	$32L$	$32L$	$32L$	$32L$
Depth Range	R_D	$8L$	$8L$	$16L$	$16L$

Table 5.7: Experimental Specifications of four source positions (A, B, C & D)

Figure 5.9 and 5.10 show the results of the Square and Y-shape experimental simulations respectively. On the left column, each Figure shows the same SSP and on the right column two different SSPs are shown. On the first row, two simulations with the same source position are shown (A & B). On the second row, the results of two additional simulations with a deeper source position are also shown (C & D).

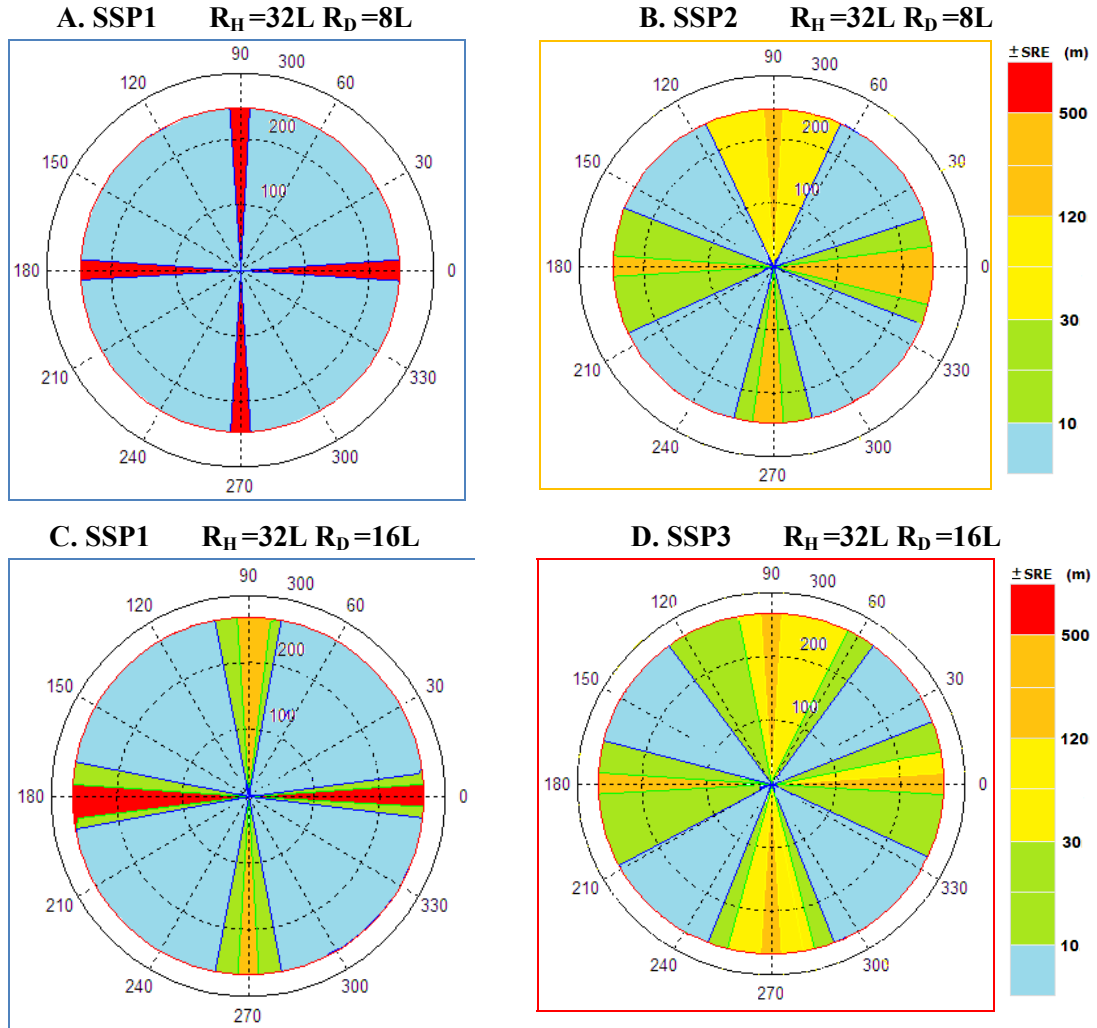


Figure 5.9: Long-Square-Array ($32LR_H$). The four scenarios show the effects associated with the use of different SSP with different source positions. SSP1 (left column), SSP2 and SSP3 (right column). Scenarios A and B ($8LR_D$), Scenarios C and D ($16LR_D$).

Figure 5.9 shows the effects on the Square geometry. Simulation B and D produce a higher number of slant ranges out of $\pm 10m$. These inaccurate slant ranges occurred when the source is found on broadside to a pair of receivers, which is considered a typical behaviour of the Square array. The differences of the three SSP are associated with the size range of speeds contained in each SSP. For instance, consider SSP3. It is

the one with the widest sound speed range (1515 - 1541m/s). Consequently, simulation D results in being the least accurate of the four scenarios.

Figure 5.10 shows the effects on the Y-shape geometry. The associated effects of different SSP correspond in all cases to accurate slant ranges. Although there are slight differences, the SRE kept within $\pm 10\text{m}$ for the four scenarios.

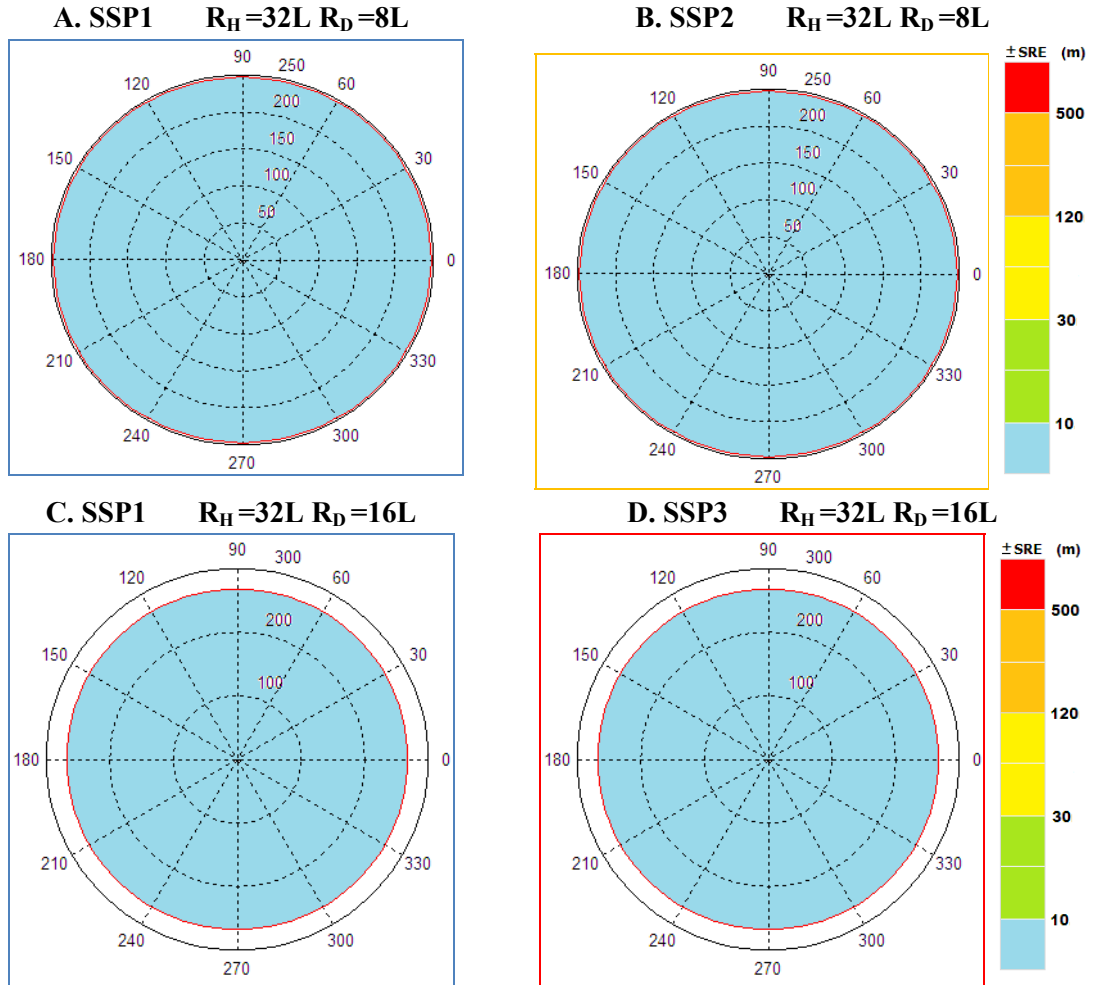


Figure 5.10: Long-Y-shape-Array ($32LR_H$). The four scenarios show the effects associated by the use of different SSP with different source positions. SSP1 (left column), SSP2 and SSP3 (right column). Scenarios A and B ($8LR_D$), Scenarios C and D ($16LR_D$).

In summary, the use of different SSP with a negative sound speed gradient produces different results on both array geometries. The *Square array* presents a relatively higher sensitivity to the variation of the SSP. The *Y-shape* is less sensitive and offers a more accurate performance.

5.2.4 Sperm whale dive profile

In chapter four, a scenario with a synthetic dive profile was simulated to test the capabilities of the two different array configurations (see Figure 4.30). The same synthetic dive profile is used in this chapter. Since the short aperture array proved to be completely inaccurate in a non-homogeneous medium, only the long aperture is used. These last series of experimental simulations also have two additional features: first, the comparison of two different SSP tracking the same source dive profile, and second, the addition of synthetic array-motion.

The Square array is the first geometry to be tested. Figure 5.11 shows a comparison of the results obtained for a long Square array on a homogeneous and non-homogeneous medium. The sources in red represent all the source locations found within the tolerance range. The sources in green constitute all the inaccurate source-locations. The blue line corresponds to the synthetic source dive profile. Whereas in a homogeneous medium the array is 43% accurate, in a non-homogeneous medium it is only 15% accurate. The 85% of inaccuracy is shown as sources scattered around the 3D Cartesian plane. Figure 5.12 shows two different 2D views of the square array in a non-homogeneous medium. Figure 12.a shows a series of source positions which, although accurate on a XY position, their depth position is found to be inaccurate. Figure 12b shows how the tracking line is lost at greater depths of 500m. The total non-existence of a pattern on the sequence of the source depth positions is also noticeable. Assuming the inaccuracies of Square array, there is no sense in going any further with additional simulations. The Square array, although used for many people, has proved its non efficiency and low performance on the accuracy of source localisation.

The Y-shape array is the second geometry to be tested. Figure 5.13 shows a comparison of both scenarios. Whereas in a homogeneous medium the array is accurate to find 94% of the source positions, in a non-homogeneous medium it is able to locate 63% of the source positions. Figure 5.14 shows the non-homogeneous scenario from two different views. It is also interesting to see that Figure 5.14a with a XY view corresponds to typical 2D views of the hyperbolic algorithm. As can be seen, such a view seems to have all source locations going along the source dive profile. However, Figure 5.14b shows how a great majority of the inaccurate source locations correspond to positions

that are deeper than 700m where the array is not sufficiently accurate. Unlike the long-square array, the long-Y-shape is able to track most of the synthetic source dive profile.

The Shifted-pair array is the third geometry to be tested. Figure 5.15 compares the homogeneous and the non-homogeneous medium. Whereas in a homogeneous medium the array is 82% accurate, in a non-homogeneous it is 64%. That represents only 1% more accurate than that of the Y-shape. Figure 5.16 shows 2D views of the array. In a similar way as happens with the Y-shape, most of the inaccurate source locations correspond to positions found at the flat bottom part of the dive profile (784m) and at horizontal ranges of less than 16L (120m) from the array. Even though a different SSP is used, the number of accurate source locations still remains very similar. For instance, consider Figure 5.17. It shows the results of two different SSP using a Y-shape array. Whereas using a SSP1 the array is only 63% accurate, by using SSP3 it is 60% accurate.

The scenario becomes different when the array-motion is assumed in long apertures. The results from various simulations with the Y-shape array show that, in order to get accurate source locations, the array depth-motion must be limited only to $\pm 1L$ on a single receiver, with the exception of the reference receiver.

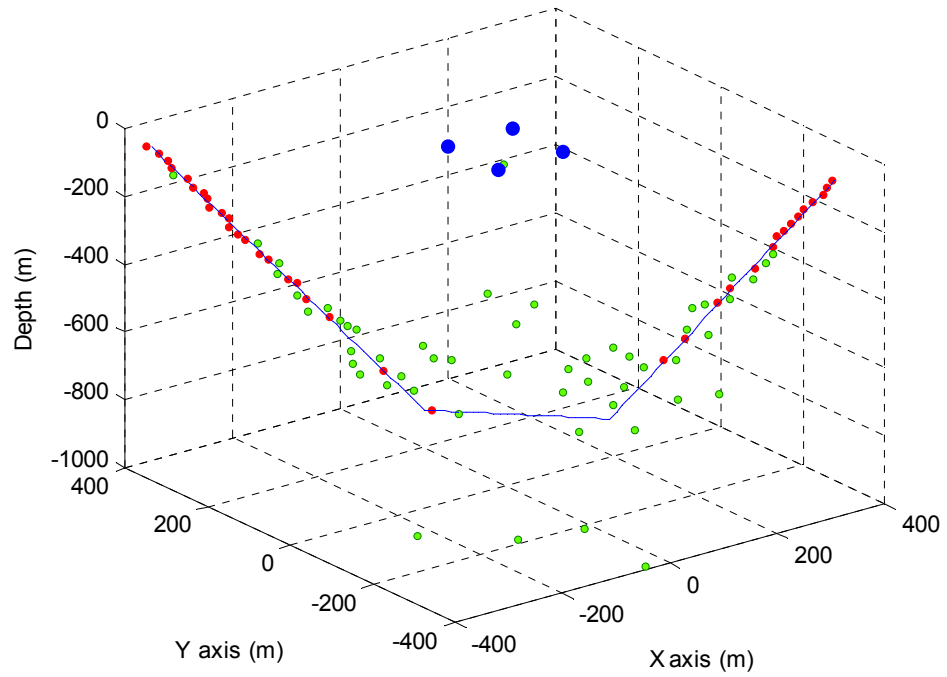
Figure 5.18 shows how the Y-shape geometry with depth-motion of $\pm 1L$ on two of the receivers causes non-accurate source locations. However, it is noticeable that the array has a trend that draws the same source dive profile with an offset on the maximum depth. Although theoretically it could be considered as inaccurate, the array still is helpful when estimating the location of a source approaching the surface.

Figures 5.19 show two simulations with a single receiver depth-motion of $\pm 1L$ and $\pm 2L$ respectively. The first simulation is considered as accurate since it is able to locate more than the 80% of the source positions (Figure 5.19a). The second simulation finds it difficult to track the bottom line of the profile, so is considered as inaccurate.

Finally, if only an array-motion on the XY axes of the four receivers is assumed, the inaccurate associated effects with array-motion decreased. Typical XY array-motion of $\pm 4L$ is under the acceptable value to expect more than the 80% of accuracy on tracking a source dive profile, only if the array geometry does not change significantly. An experimental simulation example is shown in Figure 5.20.

— Source Dive Profile ● Array-Configuration ● Accurate Source Loc ● Inaccurate Source Loc

a. XYZ – Cartesian plane - Homogeneous medium



b. XYZ – Cartesian plane - Non-homogeneous medium

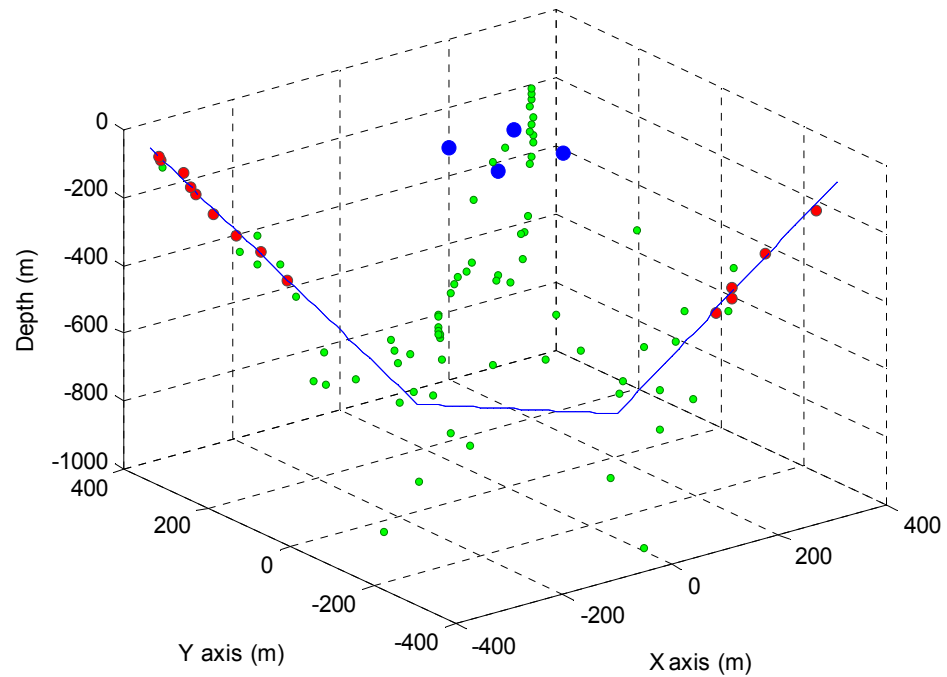
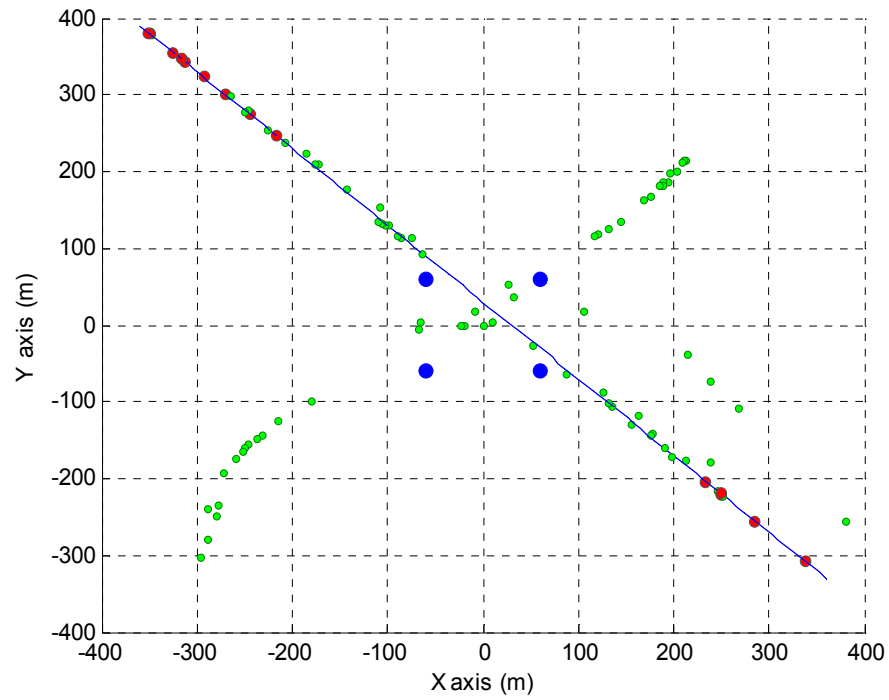


Figure 5.11: Comparison of a Long-Square Array tracking a synthetic Source Dive Profile in two different mediums (Homogeneous medium Vs Non-homogeneous medium).

— Source Dive Profile ● Array-Configuration ● Accurate Source Loc ● Inaccurate Source Loc

a. XY – Cartesian plane - **Non-Homogeneous medium**



b. XY – Cartesian plane - **Non-homogeneous medium**

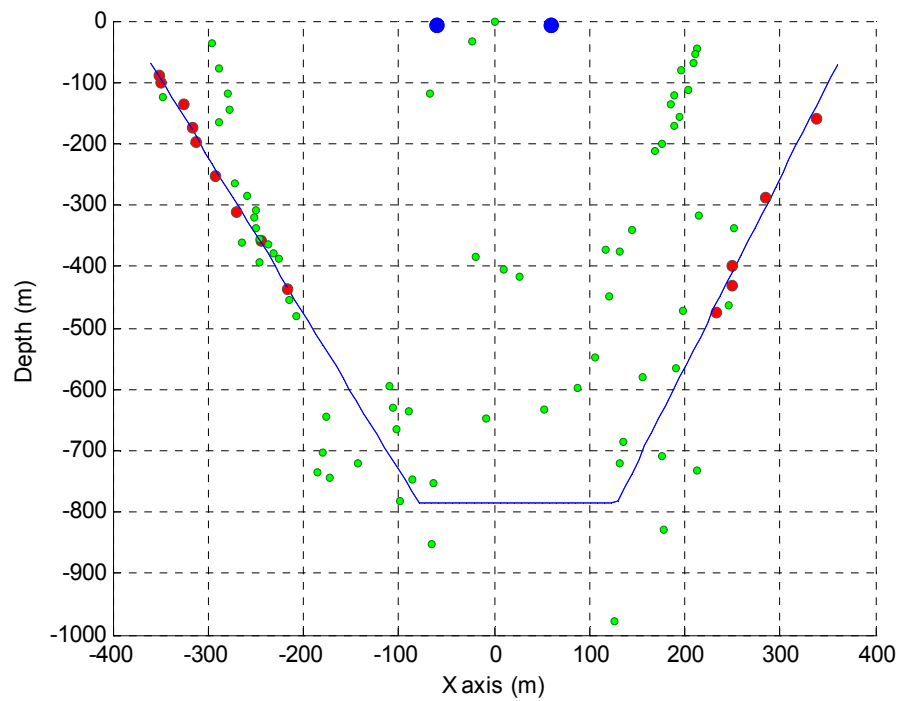
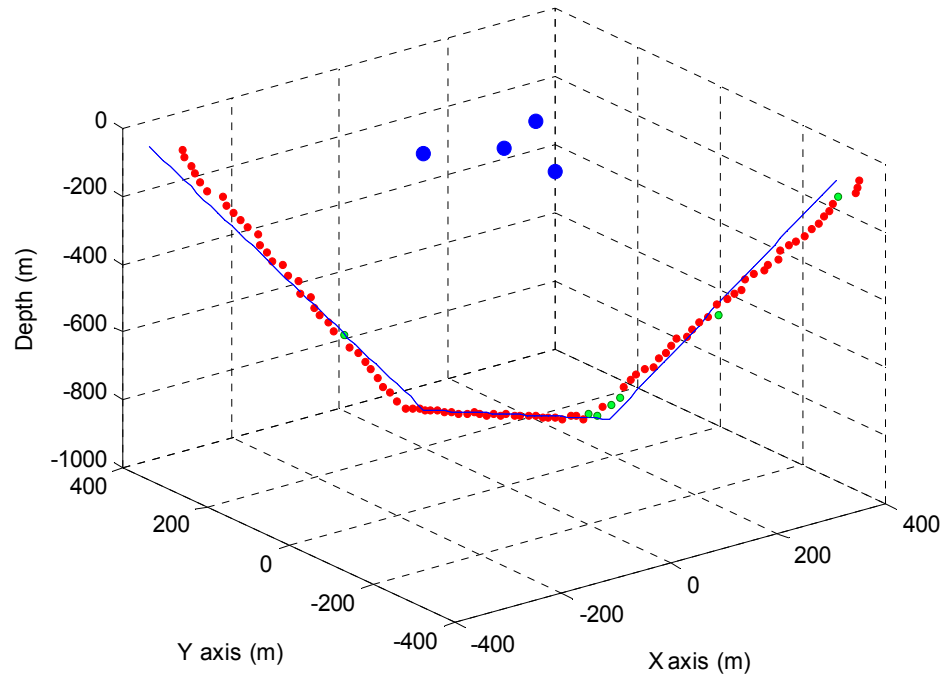


Figure 5.12: 2D views of a Long-Square Array tracking a synthetic Source Dive Profile in a non-homogeneous medium.

— Source Dive Profile ● Array-Configuration ● Accurate Source Loc ● Inaccurate Source Loc

a. XYZ – Cartesian plane - **Homogeneous medium**



b. XYZ – Cartesian plane - **Non-homogeneous medium**

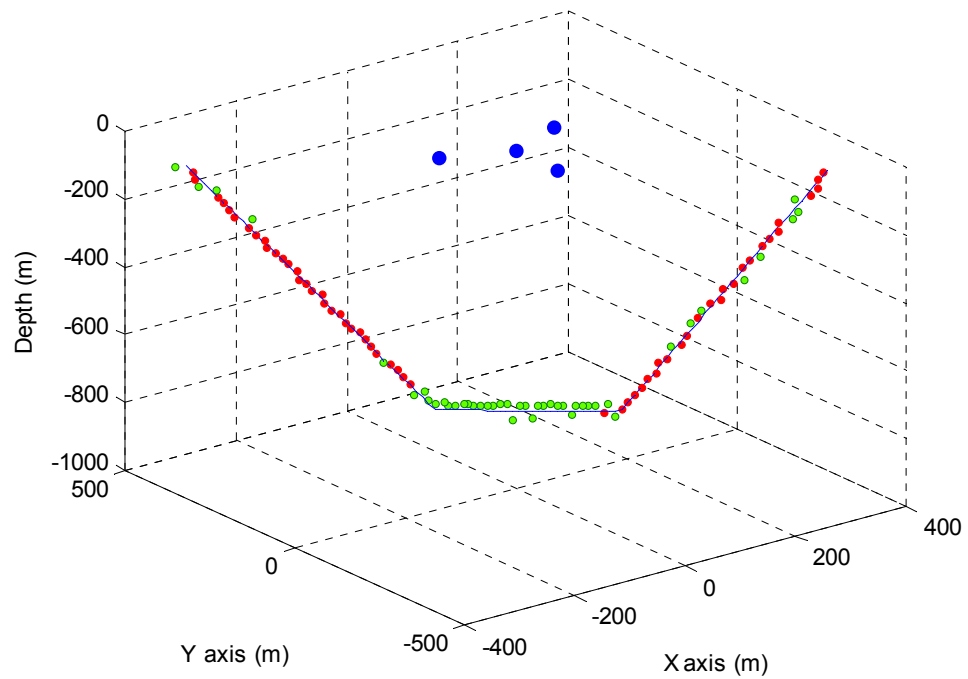
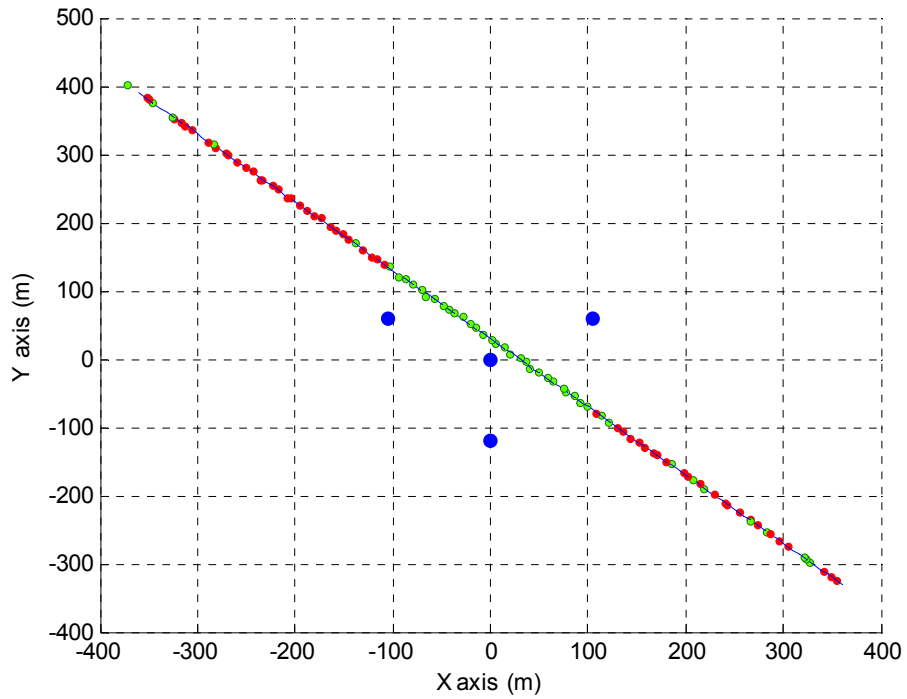


Figure 5.13: Comparison of a Long-Y-shape Array tracking a synthetic Source Dive Profile in two different mediums. For this particular scenario, the non-homogeneous medium is 31% less accurate than a Homogeneous medium.

— Source Dive Profile • Array-Configuration • Accurate Source Loc • Inaccurate Source Loc

a. XY – Cartesian plane - **Non-Homogeneous medium**



b. XZ – Cartesian plane - **Non-homogeneous medium**

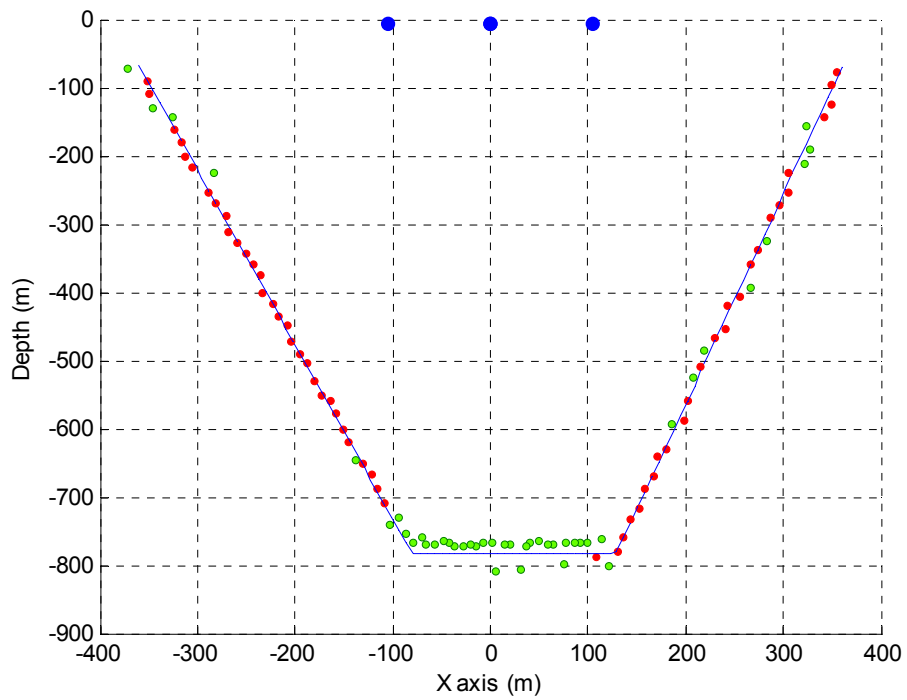
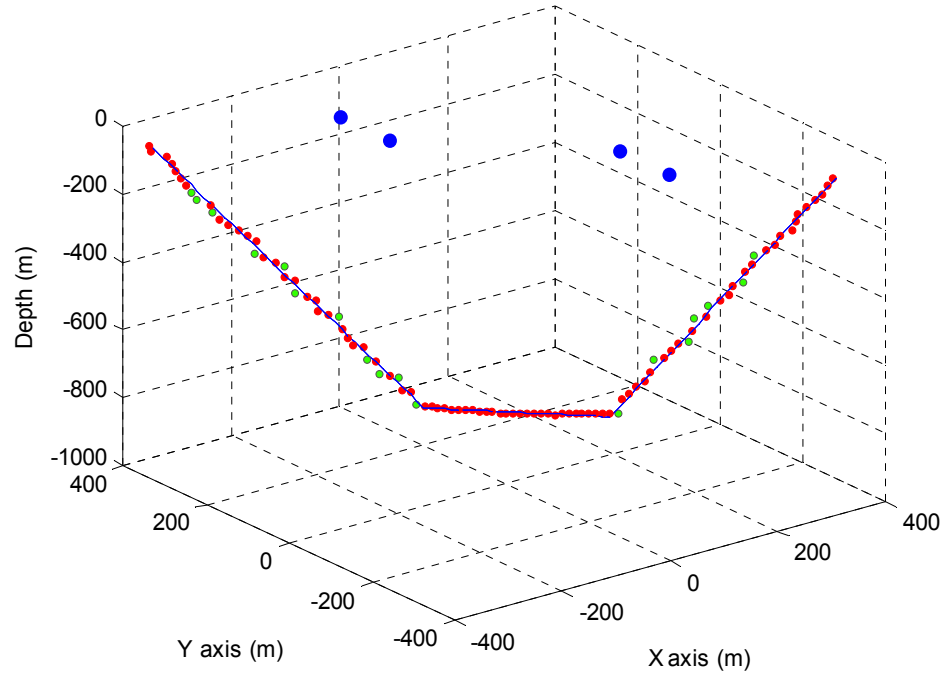


Figure 5.14 2D views of a Long-Y-shape Array tracking a synthetic Source Dive Profile in a non-homogeneous medium. Most of the inaccurate locations correspond to positions deeper than 700m.

— Source Dive Profile ● Array-Configuration ● Accurate Source Loc ● Inaccurate Source Loc

a. XYZ – Cartesian plane - **Homogeneous medium**



b. XYZ – Cartesian plane - **Non-homogeneous medium**

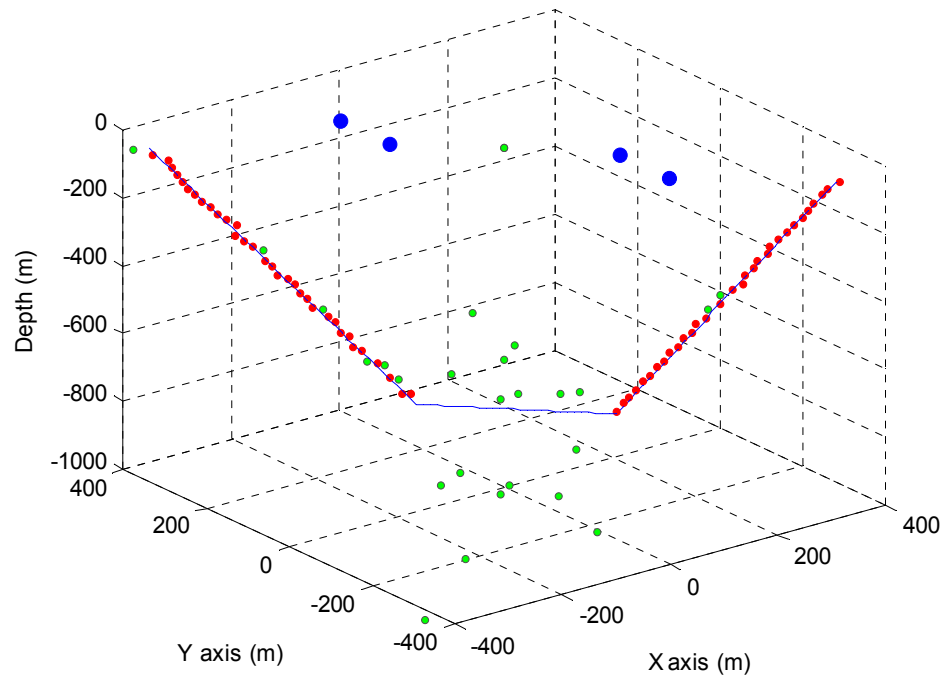
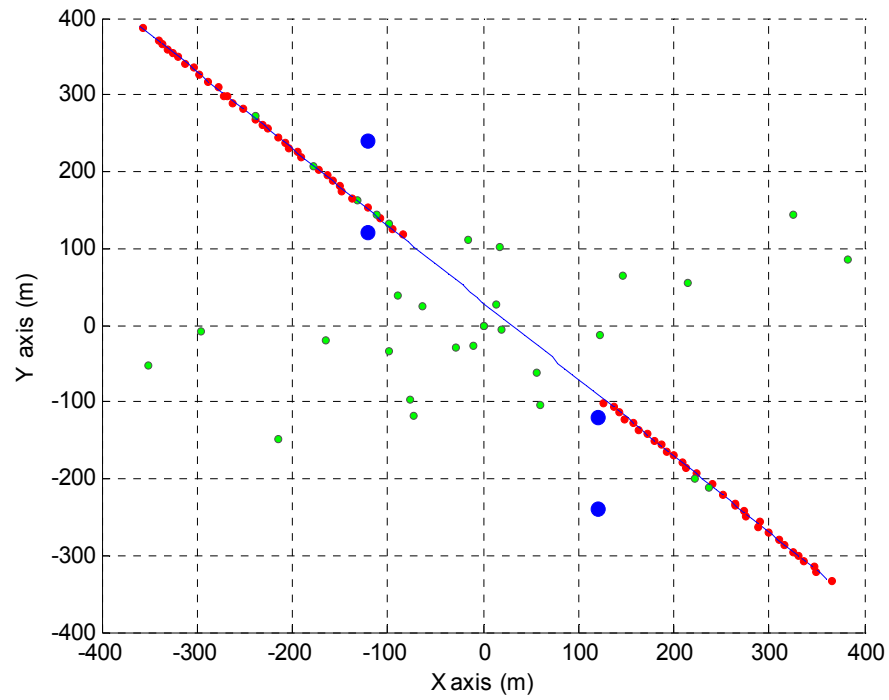


Figure 5.15: Comparison of a Long-Shifted-pair Array tracking a synthetic Source Dive Profile in two different mediums. For this particular scenario, the non-homogeneous medium is 18% less accurate than a Homogeneous medium.

— Source Dive Profile ● Array-Configuration ● Accurate Source Loc ● Inaccurate Source Loc

a. XY – Cartesian plane - **Non-Homogeneous medium**



b. XZ – Cartesian plane - **Non-homogeneous medium**

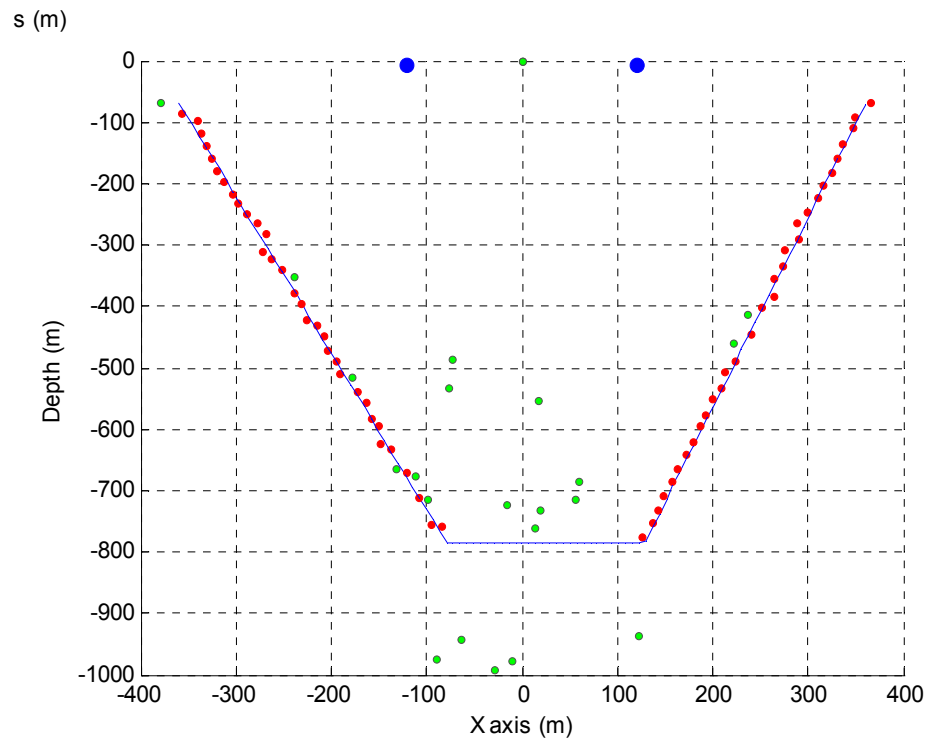
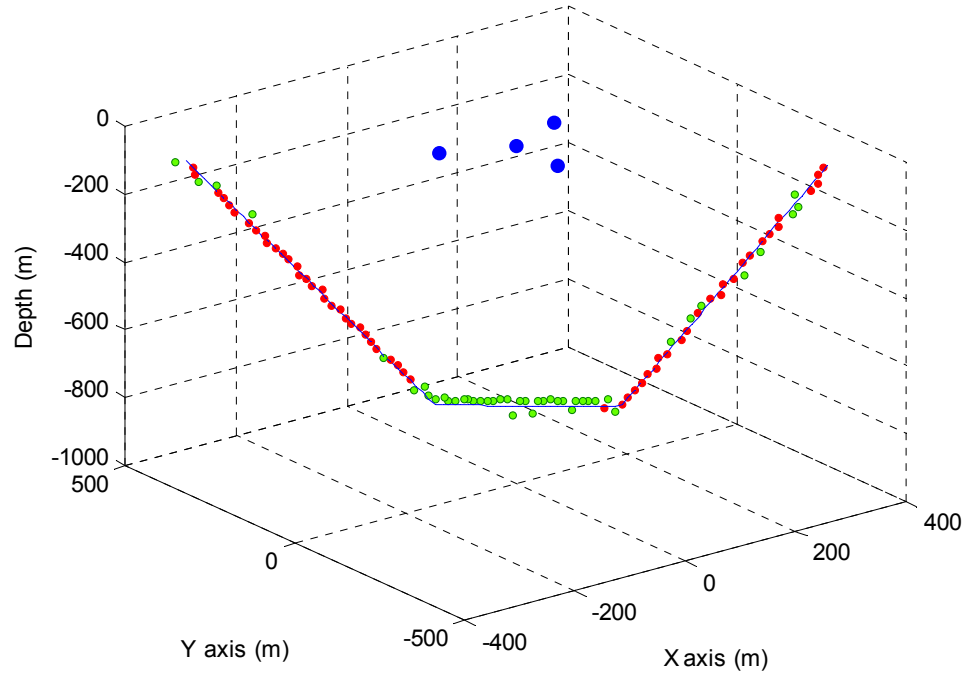


Figure 5.16 2D views of a Long-Shifted-pair Array tracking a synthetic Source Dive Profile in a non-homogeneous medium.

— Source Dive Profile ● Array-Configuration ● Accurate Source Loc ● Inaccurate Source Loc

a. XYZ – Cartesian plane - **Non-Homogeneous medium using SSP1**



b. XYZ – Cartesian plane - **Non-homogeneous medium using SSP3**

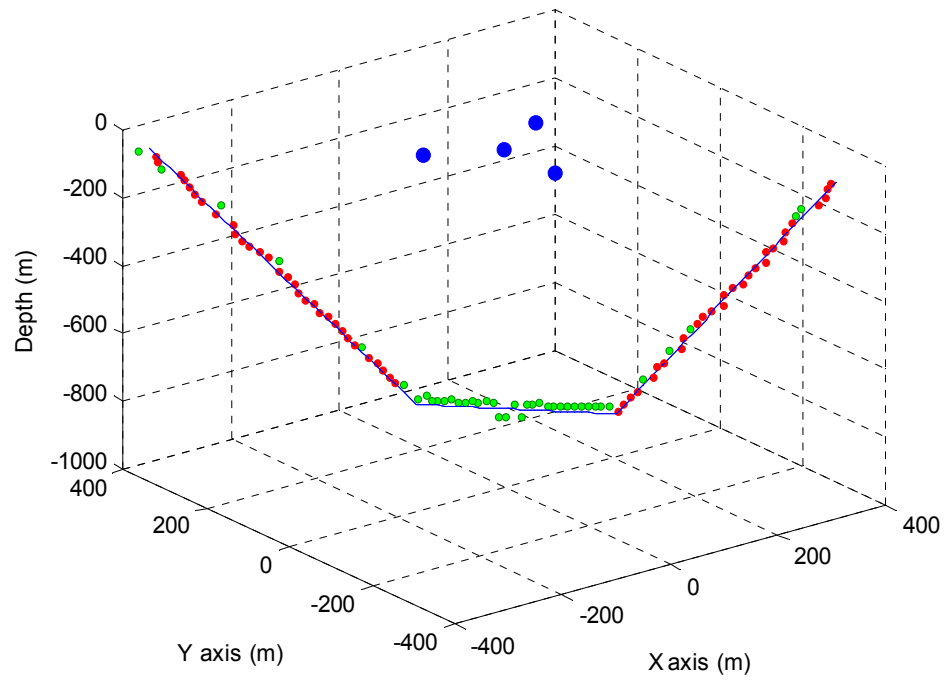
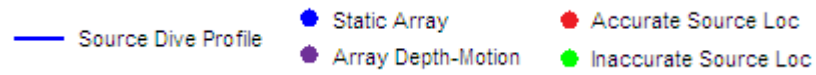
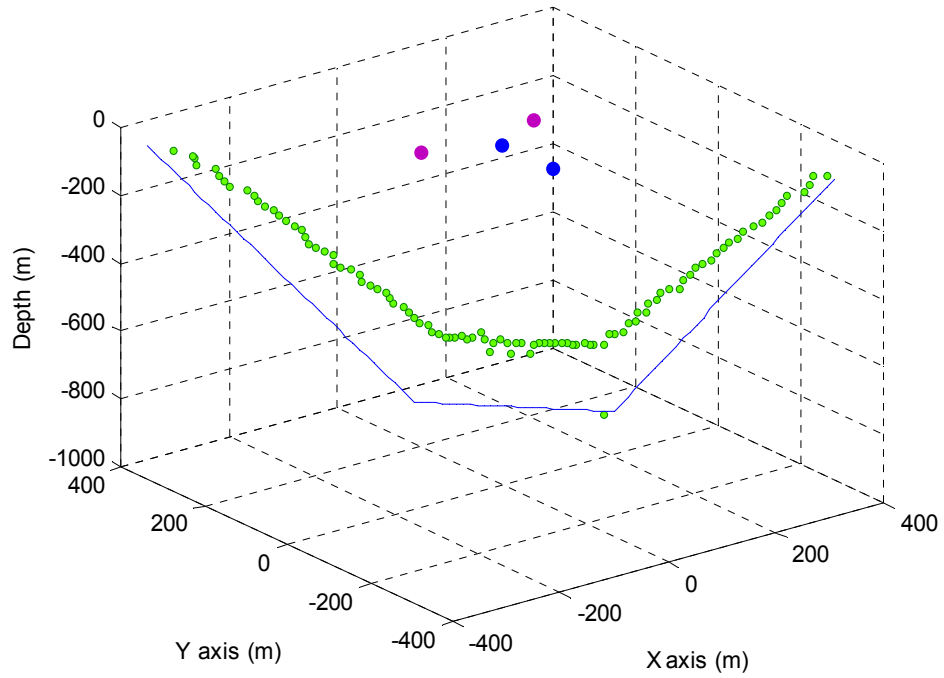


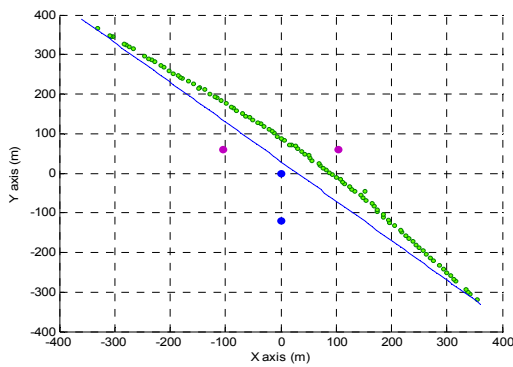
Figure 5.17: Comparison of a Long-Y-shape Array tracking a synthetic Source Dive Profile with two different SSP (SSP1 Vs SSP3). Both scenarios show a greater similarity.



a. XYZ – Cartesian plane - Array Depth-Motion of $\pm 1L$ on TWO receivers



b. XY– Cartesian plane



c. XZ – Cartesian plane

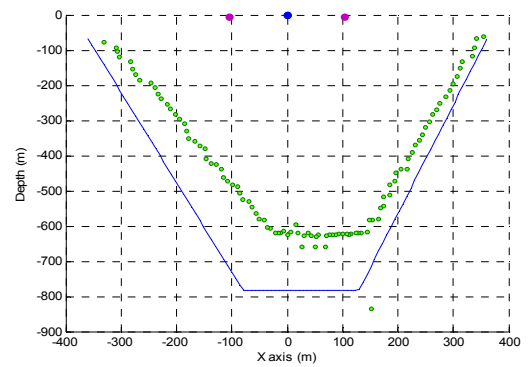
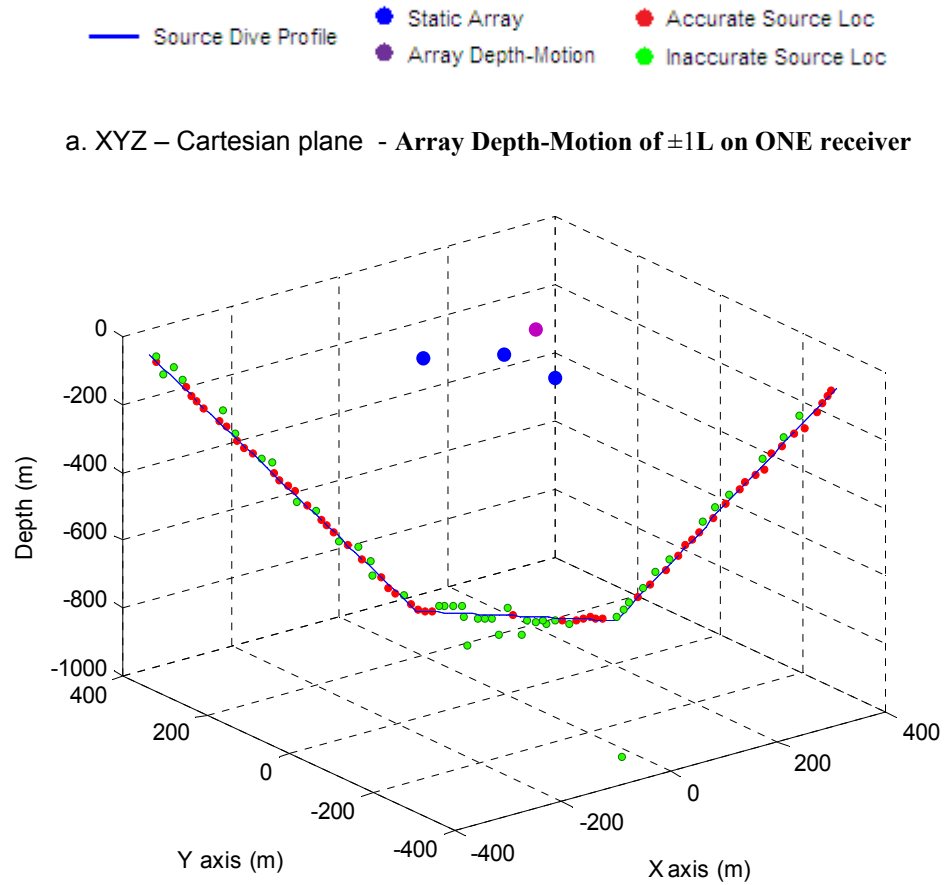


Figure 5.18: Typical array depth-motion of $\pm 1L$ on TWO or more receivers causes inaccurate source locations when tracking a typical source dive profile.



b. XYZ – Cartesian plane - Array Depth-Motion of $\pm 2L$ on ONE receiver

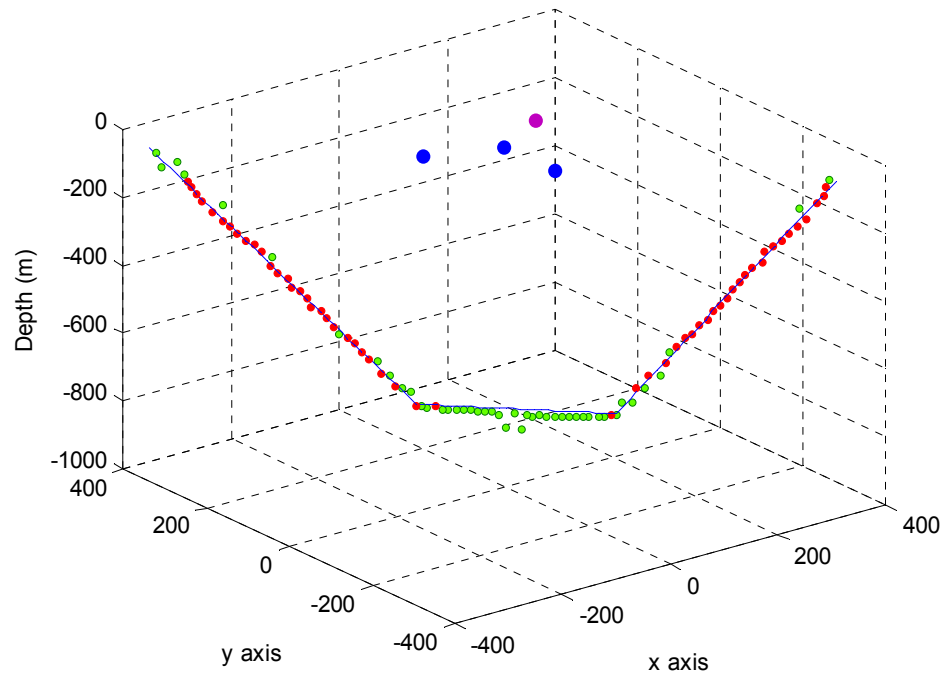


Figure 5.19: Typical array depth-motion of $\pm 1L$ on ONE receiver constitutes a maximum acceptable value to expect more than the 80% of accuracy on tracking a source dive profile.

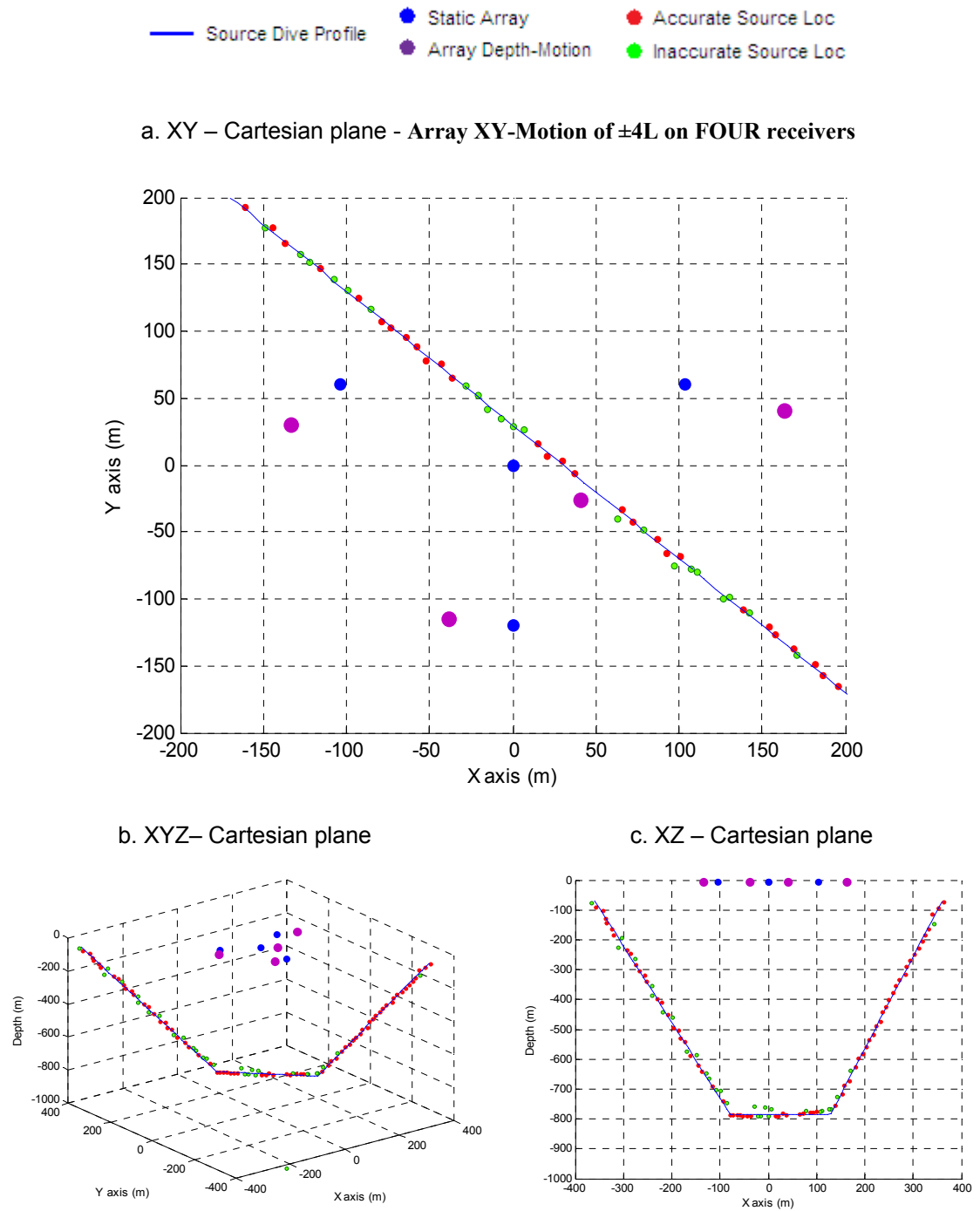


Figure 5.20: Typical XY array-motion of $\pm 4L$ on the FOUR receivers constitutes a maximum acceptable value to expect more than the 80% of accuracy on tracking a source dive profile.

5.3 Discussion and Summary

Using a non-homogeneous medium has indeed negative effects on source range estimation of both short and long apertures. However, a long-aperture will inherently have a better accuracy because of the range of received TDOA. On average, a short-aperture (L) array produces TDOAs of the order of $\pm 5\text{ms}$, whereas a long-aperture ($16L$) array generates TDOAs of $\pm 80\text{ms}$.

Although the accuracy improves with the long square array, the typical broadside ambiguities of the square array are exaggerated. The long Y-shape array is accurate for vocalising sources at horizontal and depth ranges of the order of $\sim 0.25\text{km}$ ($32L$) with a tolerance error of $\pm 10\text{m}$. This is slightly smaller than in the homogeneous medium (see Table 5.6). The propagation model is set up internally to do a full range-dependant ray trace. Therefore, some properties of the ocean of the medium vary as functions of range and azimuth from the receiver. As the range increases, the hyperbolic technique is more sensitive to such variations and a lack of accuracy is visible.

This chapter shows that for long arrays such as those typically deployed in PAM there is a significant difference in performance as a result of using different array geometries. By using a square-geometry, the geometric hyperbolic algorithm gives a degraded performance. Therefore, since the user does not have any control of all the external variables, it would not be recommended to use a type of array-configuration (e.g. Square array) that offers low accuracy, even in the most ideal scenarios.

An appropriate array-configuration (e.g. long Y-shape or Shifted-pair) can reduce the error found in a non-homogeneous medium. Even the variations of different SSP would have reduced effects on source range estimation. Nevertheless, since the array-motion has deteriorating effects, careful attention must be given, allowing only array-motion on the XY axes no greater than $\pm 4L$ and a depth-motion on Z axis of no greater than $\pm 1L$ for any single receiver without including the reference receiver.

Chapter 6

Conclusions and Further Work

The effectiveness of an underwater acoustic localisation technique is a function of many physical variables which are themselves dependant on the particular field scenario and experimental programme. In this thesis, the author decided to focus on the major factor controlling performance, namely the *array-configuration*.

The hyperbolic technique was chosen because of its simplicity and adaptability. It is the most commonly used algorithm in cetacean research and mitigation. Such a method relies on the TDOA between array elements to establish a source location. Although the sound propagation channel may contribute to inaccuracy in source locations, the *number of receivers*, the *array-geometry* and the *array-aperture* are by far the most important variables. A major contribution of this thesis is a set of guidelines on the design and deployment of a hydrophone array configuration for sperm whale range estimation.

In order to define the aperture of a hydrophone array, the frequency of the cetacean vocalisation in question must be considered. For instance, this thesis defines a *short aperture* as one with length of $L=7.5$ metres and a *long aperture* as one with $16L$. To avoid any aliasing frequency, the *ideal* separation distance of two receivers must be related to half of the cetacean vocalisation wavelength. Any distance separation superior to that will assure the inclusion of the complete frequency range of the cetacean. Since this thesis focuses on the Sperm whale (*Physeter macrocephalus*), the measure L constitutes the ideal separation distance for its minimal frequency of 100 Hz. The accuracy of source range estimation is based on the tolerance of the slant range error ($SRE < \pm 10\text{m}$). A coloured bar is used as a metric to compare the accuracy of different array-configurations.

A linear-array suffers the effects of the right/left ambiguity and is not suitable for 3D source range estimation. On the other hand, a planar-array offers a wide variety of planar geometries on the horizontal Cartesian plane. *Four* receivers are sufficient to generate *three independent TDOAs* through which the intersection of hyperboloid surfaces gives a desirable directional (azimuth and elevation) and slant range

information of the source location. However, since array-geometry has a direct effect on source range estimation, it is advisable to take into account all the possible uncertainties when choosing an array-geometry. For instance, *endfire* and *broadside* are two different scenarios of a spatial array worthy of note, as they represent a spatial uncertainty. They limit the performance for some array geometries.

The *Square*, *Trapezium* and *Triangle* geometries constitute a representative example of such spatial uncertainty. These common array deployments are particularly vulnerable to the broadside effect, which creates uncertainties in their performance. Therefore, they are not recommendable geometries to be deployed. The same recommendation applies when two linear arrays (with two receivers per line) are towed by a vessel in a parallel line. For instance, consider the array deployments from the Gulf of Mexico discussed in chapter one (see Figure 1.14). They resulted in two different scenarios, as shown in Figure 6.1.

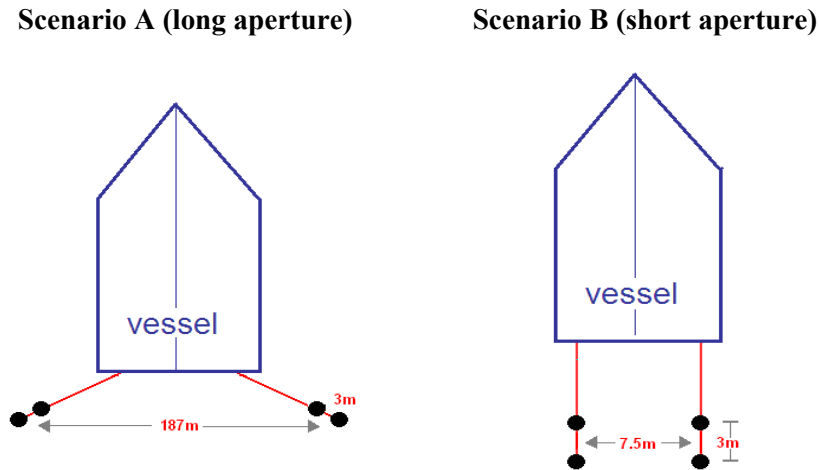


Figure 6.1: Scenarios of two linear arrays towed by a vessel in the Gulf of Mexico

The distance separation between port and starboard pair of receivers, 187m for scenario A and 7.5m for scenario B, made them susceptible to the broadside effects. Nevertheless, this problem can be solved by increasing the length of one linear array, so the geometry becomes a shifted-pair of hydrophones (see Figure 4.29). The *Shifted-pair* array helps to create an array that is less sensitive to the broadside effects when deploying a towed array from a vessel. Unlike the *Y-shape*, which breaks down when the array geometry is distorted or is away from symmetry, the Shifted-pair minimizes the receiver positioning error. For instance, when angle-positioning-error (ApE) of 45°

is present and the vessel either moves in a straight line, or turns to port or starboard, the Shifted-pair proves to be less sensitive than the Y-shape. Only in the case that offset-positioning-errors (OpE) are bigger than $\pm 20\text{m}$ on XY axes, both geometries would become affected by having a lower performance with SRE bigger than $\pm 10\text{m}$.

The *choice of different pair-combinations* becomes redundant in four of the five geometries investigated in this thesis. It is only the Y-shape geometry that relies on a particular pair-combination $\{(r1, r2), (r1, r3), (r1, r4)\}$ to give its most accurate performance. If distant and more accurate source locations are required, the Y-shape geometry would perhaps be the best choice. However, it depends on a fixed deployment capability (e.g. sonobuoys or fixed platforms) to keep its geometric symmetry.

The *array depth-motion* is directly related to the depth at which the source (cetacean vocalisations) becomes active. Since the geometric hyperbolic algorithm works better with planar arrays to produce 3D source range estimation, an array depth-motion of $\pm 2L$ is considered to be less sensitive, only if the depth position of the receivers is kept separate by at least $4L$ (30m) from where the source becomes active. Array depth-motion superior to $\pm 2L$ increases the sensitivity of the array, resulting in inaccurate source locations. One should consider having the reference receiver at the lowest possible depth from the other receivers at all times.

A non-homogeneous medium tends to have more deteriorating effects on source range estimation for short-apertures than for long-apertures. Furthermore, on a short-aperture array, the TDOA between individual elements are of such magnitude that the effects associated with the sound speed profile (SSP) are comparable with those of the TDOAs. This makes the array extremely sensitive, and results in inaccurate slant ranges. On the other hand, long aperture arrays tend to be less sensitive to the SSP. Since a long-aperture generates large TDOAs, a better resolution is obtained and an increment on the accuracy is achieved. For example, in a non-homogeneous medium, the Short Y-shape Array is found to be inaccurate at any range. However, when a long Y-shape or Shifted Array is used, a completely different scenario is obtained. On one hand, the long Y-shape is able to reach vocalising sources for ranges of up to $32L R_H$ and $32L R_D$ with complete accuracy ($\text{SRE} < \pm 10\text{m}$). On the other hand, the long Shifted-pair is also

accurate to reach vocalising sources with shorter ranges of up to $16L$ R_H and deeper ranges of up to $64L$ R_D .

Modelling the underwater sound propagation also helps to determine whether a particular source is localisable at specific dive profile. The *source dive profile* constitutes the best example to illustrate the accuracy of an array-configuration using the geometric hyperbolic algorithm in a non-homogeneous scenario. Whereas the long square geometry fails to locate the majority of the source positions, the long Y-shape and Shifted-pair geometries are able to track a complete synthetic source dive profile, being less sensitive to the variation of the sound speed. They fail only when they are used to reach source depths greater than 700m. This is a typical problem of the hyperbolic algorithm, especially when the array depth-motion is greater than $\pm 1L$. In summary, although the hyperbolic technique was ideally created to work in homogeneous mediums, the technique is more sensitive to changes on the array depth-motion than to changes in the sound speed.

In chapter I, it was stated that recently implemented mitigation measures for a safety zone included the reducing of sonar power by at least 6dB whenever a marine mammal is detected and located within 1,500 metres of the vessel, by 10 dB at 750m, and shut it down completely at 500m. Nevertheless, none of the array-configurations studied in this thesis reached slant ranges of at least 500m with an accuracy of $\pm 10m$ in a non-homogeneous medium. Therefore, to comply with the mitigation guidelines, the design of a hydrophone array-configuration for such an application is proposed. Based on the previous research exposed in this thesis and on the use of the Matlab simulator, the author concludes that a planar Shifted-pair geometry with an aperture-length of $30L$ and tolerance error of $\pm 15m$ is able to reach an animal within 1,500 metres of horizontal range and 750m deep, as shown in Figure 6.2.

In most cases there is a compromise amongst the aperture-array and the SRE accuracy. Thus, an array-configuration used for mitigation purposes and one for researching purposes will require differing specifications. Whereas one array could need to have an aperture of $30L$ and SRE accuracy of $\pm 15m$, another could be sufficient by having an aperture of L and SRE accuracy of less than $\pm 10m$.

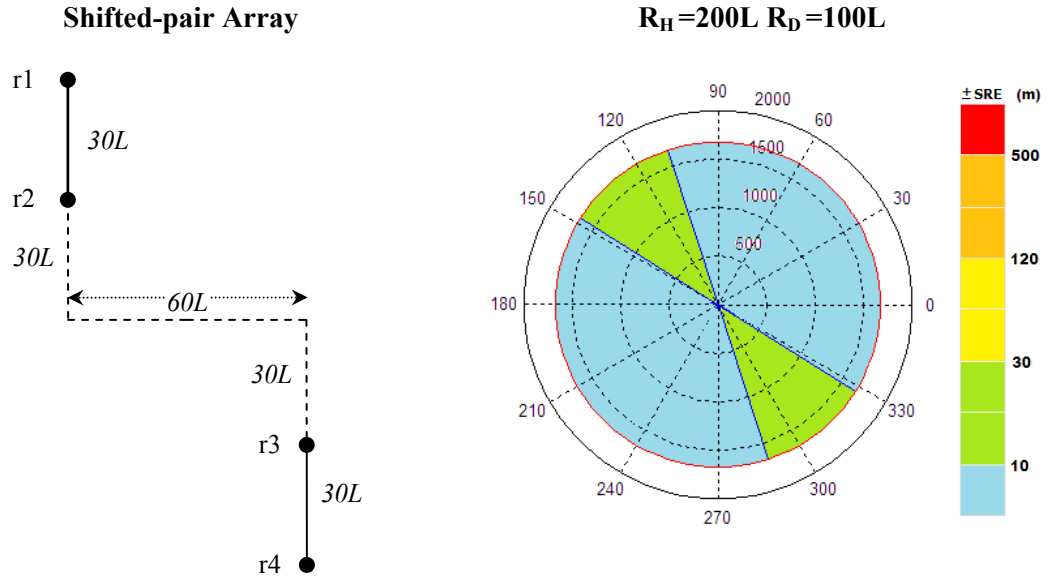


Figure 6.2: In an ideal medium the Shifted-pair Array-Configuration, with an aperture-length of $30L$ (225m) is able to comply with the mitigation guidelines, reaching ranges of up to $200L R_H$ (1500m) and $100L R_D$ (750m) with an accuracy of $\pm 15m$.

This thesis has concentrated only on the significance of the influence of array-configurations by modelling five basic array geometries of four receivers, shifted-pair, square, trapezium, triangular and Y-shape. Since the tendency for accurate source location may constitute an array-geometry with more than four receivers, further work would include the exploration of additional array-configurations.

It would also be appropriate to conduct detailed simulations in dynamic scenarios. That would include the assumption of moving platforms and a moving source. This scenario would introduce the Doppler effects from three different perspectives: (1) for a moving constant-frequency source, (2) for a moving observer, and (3) for both source and receiver moving through a uniform medium.

The issue of multipath should also be addressed. This would include shallow and large range scenarios. It is acknowledged that shallow water is a high reverberation medium; then a continuous echo caused by scattering of the source signal is expected. Additional sound speed profiles with positive gradient should also be included.

Further investigations on the presence of more than one vocalising source would improve the performance of the array-configuration, including perhaps an automated discrimination algorithm. Moreover, the inclusion of other many cetacean species

would offer a wide range of scenarios in which the Matlab simulator can also be applicable.

Further work should also include a study of compatibility when using the array-configurations in other PAM cetacean localisation techniques, like those discussed in sections 2.1.4 to 2.1.7.

The overall system has been validated mainly with theoretical and simulating data. Field and experimental data will contribute to validating the whole system with real data, including other particular scenarios that were not investigated in this thesis.

This thesis has concentrated on sperm whale distance assessment only, ignoring the positive or negative effect of the previous stages of detection and recognition. To assess a more robust algorithm for PAM cetacean localisation, additional algorithms would require merging this thesis with those two stages, including an error treatment of the source location angle.

Appendix A

Underwater Acoustic Concepts

This first appendix presents a synthesis of basic underwater acoustic concepts and propagation modelling techniques.

A.1 SOUND

Sound is a wave of pressure variations propagating through a medium. Acousticians have adopted a logarithmic scale for sound intensities, which is denoted in decibels (dB). Decibel measurements represent the ratio between a measured pressure value and a reference pressure value. The logarithmic nature of the scale means that each 10 dB increase is a ten-fold increase in power. Humans perceive a 10 dB increase in noise as a doubling of sound level, or a 10 dB decrease in noise as halving a sound level [41].

However, because of the different densities and different decibels standards, sound with the same intensity in air and in water would be approximately 63 dB quieter than in air. The ocean, together with its boundaries, forms a remarkably complex medium for the propagation of sound. It possesses an internal structure and a peculiar upper and lower surface which creates many diverse effects upon the sound emitted from an underwater source. In travelling through the sea, an underwater sound signal becomes delayed, distorted, and attenuated [148].

A.1.1 Sound Speed

The single most important acoustical variable in the ocean is sound speed. In the waveguide it plays the same role as the index of refraction does in optics. The sound speed (c) in the ocean is an increasing function of temperature (T), salinity (S) and pressure, the last being a function of depth (z). A simplified expression of this dependence is

$$c = 1449.2 + 4.6T - 0.055 T^2 + 0.00029 T^3 + (1.34 - 0.01 T)(S - 35) + 0.016z \quad (\text{A.1})$$

For most cases, the above equation is sufficiently accurate. The speed of sound increases with increasing temperature, salinity, and pressure. In the ocean, the sound speed between the source and hydrophone varies with source location. The actual time for sound to reach a hydrophone on the bottom from the surface depends on the sound speed along a ray path, which is not straight because it bends as a result of refraction. Refraction is a dominant feature of deep water sound transmission.

If the ray paths were straight, the sound speed would be the same for all source locations. But the bending changes the sound speed, and in the real ocean, it normally varies both horizontally and vertically, the most pronounced gradients usually being vertical.

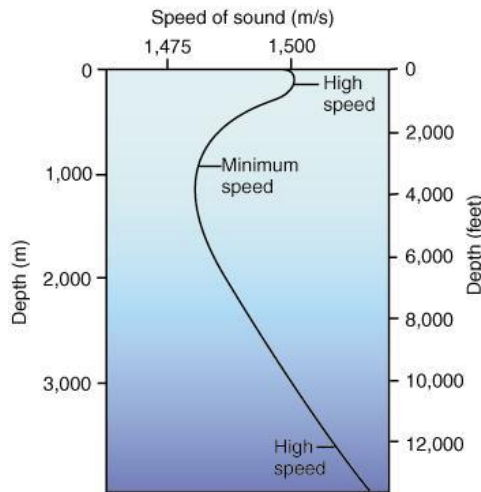


Figure A.1: Typical sound-speed profile

A typical sound speed profile is shown in Figure A.1. The acoustic path from the source to the receiver may pass through a range of different horizontal sound speeds. The surface layer extends to a depth of 150m and is usually associated with a well-mixed layer of isothermal water. Below the mixed layer lies the thermocline, a region of the water column in which the temperature decreases rapidly with depth and is also characterized by a negative sound speed gradient. It extends its limits to 1000m. Below the thermocline and extending to the ocean floor is the deep isothermal layer. This layer has a nearly constant temperature in which the speed of sound increases with depth because of the effect of pressure on sound speed. Between the negative sound speed gradient and the positive gradient is a sound speed minimum. The depth corresponding to it is referred to as the sound channel axis [16].

A.1.2 Transmission Loss

The standard unit of measure of underwater acoustic propagation is acoustic intensity I , which is defined as the sound power P_{ac} per unit area A . The average intensity I of a plane wave is given by

$$I = \frac{p^2}{\rho c} \quad (\text{A.2})$$

Where p is the pressure (N/m²), ρ is the density (kg/m³) of sea water and c the sound speed (m/s) in sea water. The product ρc is commonly referred to as the acoustic impedance (kg/m²s). The acoustic intensity units are W/m² (watts per square metre).

Transmission Loss (TL) can be defined as ten times the log (base 10) of the ratio of the reference intensity (I_{ref}) measured at a point 1 m from the source, to the intensity (I), measured at a distant point. Since the standard metric unit for pressure is 1 micro Pascal, which is equivalent to 10⁻⁶ Newtons/m², the SL units are abbreviated *dB re 1 μ Pa*.

$$TL = 10 \log \frac{I_{ref}}{I} \quad (\text{A.3})$$

In an unbounded medium the signal experiences a *spherical* spreading TL which is defined as $20 \log r$, where r is the unit reference distance. On the other hand, in a medium bounded because of the sea floor and surface, the TL is related to *cylindrical* spreading of $10 \log r$ [61]. Transmission loss (TL) has conventionally been plotted for each frequency and source-receiver location as a function of range, as illustrated in Figure A.2. In this example, the depth of the source and receiver are 60m and 25m respectively. The sound speed profile corresponds to waters in the Gulf of Mexico. The source frequency modelled is 14 kHz.

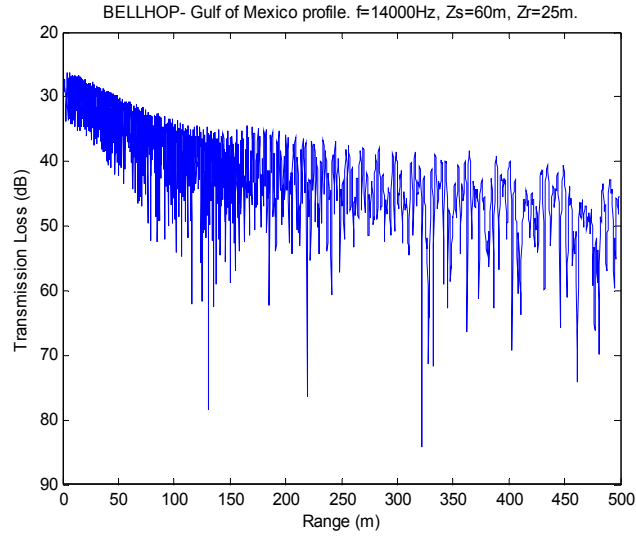


Figure A.2: TL as a function of range

The TL can also be displayed in the entire range-plane for all receiver positions (depth), given a fixed source depth as it is shown in Figure A.3.

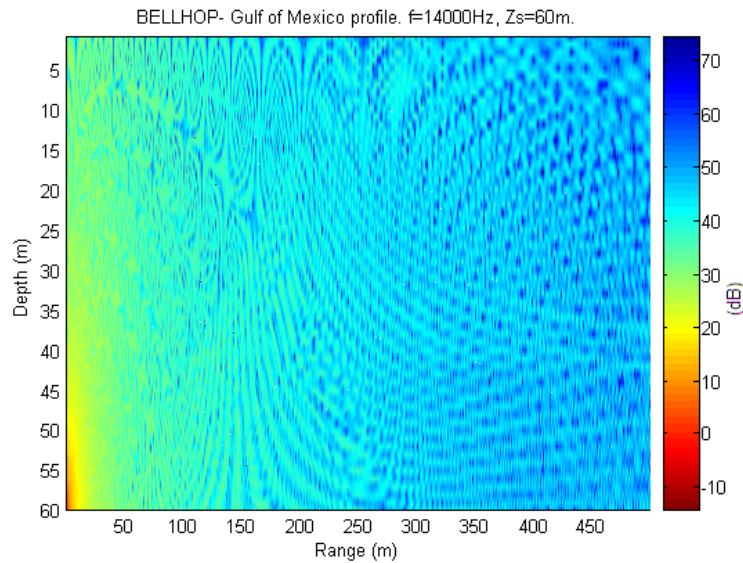


Figure A.3: TL as function of range and receiver depth

The acoustic TL is subdivided into three categories: coherent, incoherent and semicoherent transmission loss. A *Coherent Transmission Loss* associates a phase and intensity with each eigenray. On the other hand, an *Incoherent Transmission Loss* ignores them. While the coherent transmission loss may represent a result which is so detailed that it could never be observed in reality, the incoherent calculation can

smoothe out features which are quite stable even at high frequencies. An intermediate solution which retains features that are insensitive to the detailed environmental knowledge but smoothes out other features which are not possible to predict is called *Semicoherent Transmission Loss* [61]. Figure A.4 shows the three types of TL plots by modelling a source frequency of 100Hz located at a depth of 270m and a receiver at a depth of 45m.

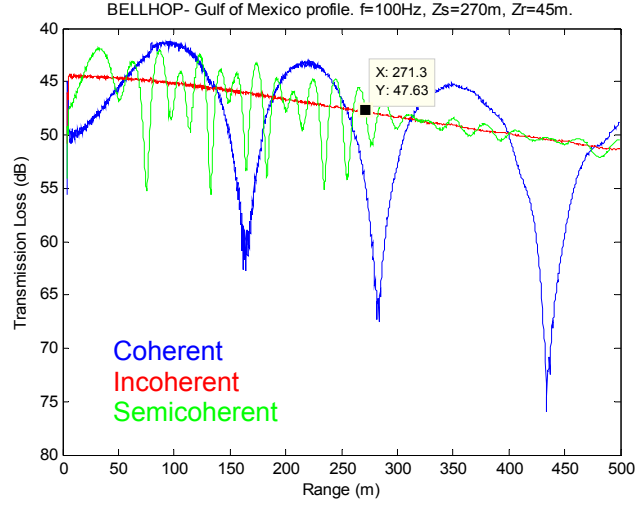


Figure A.4: Representation of the different TL calculations
(computed with Matlab software)

Owing to attenuation, TL is represented in the sonar equations in terms of an attenuation coefficient α with the units of dB/m. The two primary causes of attenuation are viscous friction and ionic relaxation phenomena

Thus, the combined effect of spreading and absorption are given by

$$TL = 20\log(R) + \alpha R \quad (A.4)$$

The measured transmission losses are often at variance owing to the combined effects of other complicating factors such as multiple path propagation, refraction effects, or diffraction and scattering of sound by particulates, bubbles and plankton within the water column.

Whilst it is possible to derive theoretical expressions to account for these processes, it is simpler to combine them in a single term called the transmission anomaly (A). Thus, the one-way transmission loss becomes:

$$TL = 20\log(R) + \alpha R + A \quad (\text{A.5})$$

A.1.3 Ambient Noise

The acoustic signal also becomes distorted as a result of ambient noise. In the source-path-receiver model, ambient noise is present in the medium along the path, and it is present at any receiver location. A spectrum of ambient noise in the open ocean is shown in Figure A.5.

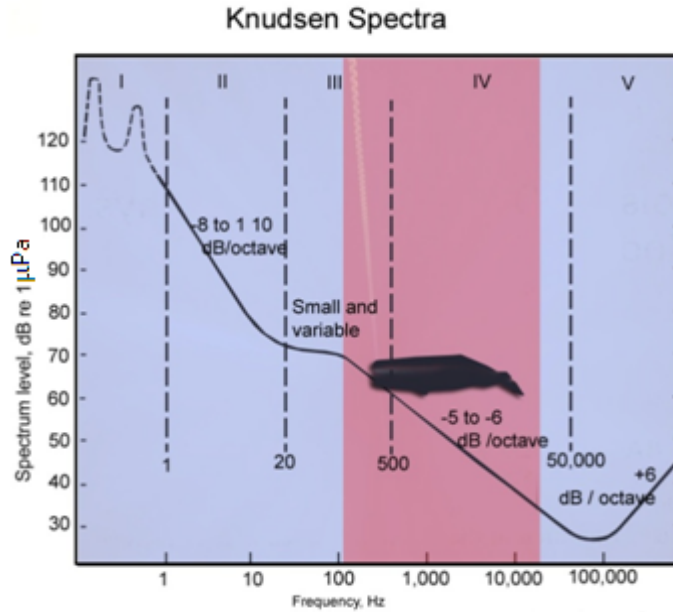


Figure A.5: Knudsen spectra. General spectrum of deep-sea noise showing five frequency bands of differing spectral slopes [148].

This spectrum is composed of segments of different slope, each exhibiting a different behaviour. A number of frequency bands in the spectrum can be associated with readily identifiable noise sources. Five frequency bands are indicated in vertical columns. Band I, lying below 1 Hz, is associated with noise of hydrostatic origin or with seismic activity. Band II is characterized by a spectral slope of -8 to -10 dB/octave. The most

probable source noise in deep water appears to be oceanic turbulence. In Band III, the ambient noise spectrum flattens out and the noise appears to be dominated by distant shipping traffic. Band IV contains the Knudsen spectra having a slope of -5 to -6 dB/octave in which the noise originates at the ocean surface near the point of measurement. Band V is dominated by thermal noise originating in the molecular motion of the sea, and is uniquely characterized by a positive spectrum having a slope of +6dB/octave [33].

The correspondent frequency band (100 Hz to 30 kHz) of the Sperm whale vocalisation overlaps with frequency bands III and IV of the Knudsen spectra. This means an ambient noise within 70 and 35 dB re 1 μ Pa of noise level. The level at which the signal becomes audible against the background noise is termed the *masked threshold*.

A.1.4 Directionality and Source Level

The amount of sound radiated by the source is specified by the parameter *source level* (*SL*). It is defined as the intensity of the radiated sound in decibels relative to the intensity of a plane wave of rms pressure 1 μ Pa, referred to 1.0 meters from the acoustic centre of the source in the direction of the target.

The transmitting *directivity index* (*DI*) of a source is the difference, measured at a point on the axis of the beam pattern, between the level of sound generated by the source and the level that would be produced by a non-directional source radiating the total amount of acoustic power. Directionality is highly desirable, for it enables the direction of arrival of a signal to be determined, and at the same time, reduces noise relative to the signal, arriving in other directions [148].

Echolocation sounds emitted by toothed whales are highly directional. Since directionality generally follows the ratio of transmitter cross section to wavelength; with an aperture on the order of 1m and wavelengths on the order of 0.1 m (3.4 kHz), directionality in sperm whales is as good as, or better than, that of dolphins, which also have a pronounced directionality [102].

The lack of knowledge of direction of the acoustic axis of the whales precludes any statement about the *maximum capability* of the SL and DI. However, some guidance can be obtained by means of the theory of a vibrating plane piston in an infinite baffle. The piston model predicts behaviour of the transmitter somewhat similar to that of a low-pass filter with the cut-off frequency being inversely proportional to the off-axis angle [5, 6, 7, 102, 103].

To get recordings near the whales requires deep water hydrophones, which are costly and difficult to handle. Once recordings have been made, SL determination involves a series of processes. The probability that a whale complies and directs its clicks towards one of the hydrophones can be increased with the number of hydrophones deployed, and by increasing the time spent recording. However, the observation underlines the importance of the completely uncontrollable condition of having whales pointing towards the array during measurements of maximum levels. The maximum levels reported on the literature are the ones that the hydrophones can register.

Studies of sperm whales using large-aperture array techniques -200m of distance separation between elements-, found SL between 202 and 223 dB re 1 μ Pa, showing a pronounced directionality, with maximum recorded source levels exceeding 220 dB re 1 μ Pa and spectral emphasis above 10 kHz [102, 103, 121, 144, 173]. Sperm whales, pilot whales, and presumably some other species with relatively strong calls are detectable at distances > 1km [121]. Watkins detected sperm whale sounds at distances of 10 km [121]. Studies from [103] reveal monopulsed clicks, with source levels up to 236 dB re 1 μ Pa (rms), and with centroid frequencies of 15 kHz. That indicates a half-angle and half-power beam width of about 4 degrees. The directional index of sperm whale clicks was calculated to be 27 dB.

A.1.5 Signal-to Noise Ratio

The difference between the signal level and the ambient noise level is calculated by the Signal-to Noise Ratio (SNR) criteria. The main factors affecting detection of a sound signal in the presence of background noise are related as follows

$$\text{SNR} = \text{RL} - N_r \quad (\text{A.6})$$

where SNR = Signal-to-Noise Ratio (dB)
 N_r = Noise level (natural + man-made) at receiver
 RL = Received level of a sound signal

$$\text{RL} = \text{SL} - \text{TL} + G \quad (\text{A.7})$$

where SL = source level of sound signal
 TL = transmission loss from source to the receiver
 G = gain factor

A.1.6 Sonar Equations

The SONAR (Sound Navigation and Ranging) is a sensing strategy which measures features of an environment (or medium) by the way in which that environment transmits, reflects and/or absorbs acoustic waves.

It is customary to define a critical SNR that defines whether a target is present or absent. This parameter is defined as the detection threshold (DT). This is probably the most commonly implemented form of the sonar equations. In an active sonar system, the return signal will be increased by the source level, directivity index and target strength but reduced by the two-way transmission loss and noise level. Thus, the echo to noise ratio as determined by the sonar is:

$$\text{SL} + \text{DI}_s + \text{TS} - 2\text{TL} - (\text{NL} - \text{DI}) = \text{DT} \quad (\text{A.8})$$

The Target Strength (TS) is the amount of signal reflected by the target. The intensity of an acoustic signal reduces with range. This observed reduction in the acoustic signal with distance from the source is caused by the combined effects of spreading and attenuation and is accounted for by the Transmission Loss term (TL). The Noise Level (NL) refers to the ambient noise. Notice also that a distinction has been made in the

equation above between the directivity of the source (DI_s) that focuses on the source energy and the directivity index (DI) of the hydrophone that reduces the effective NL. This is an essentially a steady state, isotropic (equal in all directions) sound which is generated by, amongst other things, wind, waves, biological activity and shipping. In order to improve efficiency, most acoustic sources are designed to focus the acoustic energy into a narrower beam. Here the source level (SL) is a measure of the acoustic intensity of the signal measured one metre away from the source. All of the parameters are expressed on a logarithmic scale in decibels (dB).

In the passive case, the sonar itself is the source (SL), the target strength (TS) becomes irrelevant, and the transmission loss (TL) term is one-way. Notice that DI_{TS} in this case refers to the directivity of target-source. The passive sonar equation is:

$$SL + DI_{TS} - TL - (NL - DI) = DT \quad (A.9)$$

In summary, noise is likely to be the primary limitation on the source detectability. Many human activities that reach source levels of the order of 175 dB are likely to reduce the detection of sperm whales [121]. However, even if it is detectable, this still does not guarantee that it can be accurately localisable.

Appendix B

Algebraic Solution of the Source Location Problem

B.1 Synthetic TDOA

In the three dimensional space, the mathematical equation that describes the magnitude of a straight line segment that connect two points is given by

$$d = \sqrt{d_x^2 + d_y^2 + d_z^2} \quad (\text{b.1})$$

If the locations of the source vector $(s_x \ s_y \ s_z)$ and receiver vector $(r_x \ r_y \ r_z)$ are already known, the same basic equation is used to determine the distance d_{sr} between them.

$$d_{sri} = \sqrt{(r_{xi} - s_x)^2 + (r_{yi} - s_y)^2 + (r_{zi} - s_z)^2} \quad i = 1, 2, 3, n_r \quad (\text{b.2})$$

where n_r is the total number of receivers

Then if the sound speed ss of the medium is also known, we are able to compute the *time of arrival* (TOA) τ for each receiver r_i of the array.

$$\tau_i = \frac{d_{sri}}{ss} \quad (\text{b.3})$$

By subtracting τ_1 from the other TOAs, the *time difference of arrival* (TDOA) δ is computed.

$$\delta_{li} = \tau_i - \tau_1 \quad (\text{b.4})$$

B.2 Algebraic Solution

A synthesis of the source-localisation methods used by Watkins and Schevill [164] and Spiersberger and Firstrup [130] was published in 2001 [134, 158]. It describes the relation between the TDOA and the locations of the source and the receivers. It also gives “the same mathematical form for the 2D and 3D array systems”. From equation (b.2) and (b.3) we have

$$(r_{xi} - s_x)^2 + (r_{yi} - s_y)^2 + (r_{zi} - s_z)^2 = ss^2 \tau_i^2 \quad (\text{b.5})$$

Solving for τ_i from (b.4)

$$\tau_i = \delta_{li} + \tau_1 \quad (\text{b.6})$$

substituting (b.6) in (b.5)

$$(r_{xi} - s_x)^2 + (r_{yi} - s_y)^2 + (r_{zi} - s_z)^2 = ss^2 (\delta_{li} + \tau_1)^2 \quad (\text{b.7})$$

Equation (b.7) describes the relation between the TDOA and the locations of the source and the receivers. The total number of equations is equal to the number of receivers in the array. By placing the vector r_1 at the origin of the coordinate system (0, 0, 0) and solving for equation (b.7) we have

$$s_x^2 + s_y^2 + s_z^2 = ss^2 \tau_1^2 \quad (\text{b.8})$$

Now, if equation (b.8) is subtracted from the $n_r - 1$ remaining equations (b.7) the result is

$$2[r_{x(i)}s_x + r_{y(i)}s_y + r_{z(i)}s_z] + 2ss^2 \delta_{l(i)} \tau_1 = r_{x(i)}^2 + r_{y(i)}^2 + r_{z(i)}^2 - ss^2 \delta_{l(i)}^2 \quad (\text{b.9})$$

$$i = 2, \dots, n_r$$

Rewriting equation (b.9) in matrix notation, we have an equation which was designed to use five or more receivers

$$Am = b \quad (b.10)$$

where the i th (from $i > 1$) row of matrix \mathbf{A} is given by

$$2[r_{x(i)} + r_{y(i)} + r_{z(i)} + ss^2 \delta_{l(i)}] \quad (b.11)$$

the i th (from $i > 1$) row of matrix \mathbf{b} is given by

$$b_i = r_{x(i)}^2 + r_{y(i)}^2 + r_{z(i)}^2 - ss^2 \delta_{l(i)}^2 \quad (b.12)$$

Thus, solving for the \mathbf{m} vector which contains the source coordinates (s_x, s_y, s_z) and τ_1 , we have

$$m = A^{-1}b \quad (b.13)$$

However, for four receivers the equation (b.10) is rewritten as

$$2Rs + 2ss^2 \delta \tau_1 = b \quad (b.14)$$

where \mathbf{R} represents the receiver matrix

$$R = \begin{bmatrix} r_{x(2)} & r_{y(2)} & r_{z(2)} \\ r_{x(3)} & r_{y(3)} & r_{z(3)} \\ r_{x(4)} & r_{y(4)} & r_{z(4)} \end{bmatrix} \quad (b.15)$$

\mathbf{s} the source vector

$$s = [s_x, s_y, s_z]^T \quad (b.16)$$

and δ is the TDOA vector

$$\delta = [\delta_{12}, \delta_{13}, \delta_{14}]^T \quad (\text{b.17})$$

where the superscript **T** denotes transpose

Thus, solving for **s** from (b.14)

$$s = \frac{1}{2} R^{-1} b - s s^2 \delta \tau_1 R^{-1} \quad (\text{b.18})$$

From (b.8) a relationship can be written

$$s^T s = s s^2 \tau_1^2 \quad (\text{b.19})$$

Substituting (b.18) in (b.19) it is solved for τ_1

$$\tau_1 = \frac{s s a_2 \pm \sqrt{s s^2 a_2^2 - (s s^2 a_3 - 1) a_1}}{2 s s (s s^2 a_3 - 1)} \quad (\text{b.20})$$

where

$$a_1 = (R^{-1} b)^T (R^{-1} b) \quad a_2 = (R^{-1} \tau)^T (R^{-1} b) \quad a_3 = (R^{-1} \tau)^T (R^{-1} \tau)$$

Substituting (b.20) in (b.18), a solution for the source location **s** is obtained. Two positive solutions correspond to two possible source positions [158]. However, if one of the solutions follows an ambiguous region, this one can be ignored.

When using five receivers, the ambiguous solutions of equation (b.18) are eliminated. If more receivers are used, they are divided into groups of 4 or 5 using equation (b.13).

Important also is the fact that equation (b.13) ignores any contribution to the source position error from the inaccuracies in sound velocity, TDOAs, and receiver position measurements, respectively.

Appendix C

Matlab Graphical User Interfaces (GUI)

A Matlab GUI simulator was designed to analyze the accuracy of a source location for arbitrary passive acoustic array configuration. The simulator uses the geometric hyperbolic algorithm as the main localisation method. It has been developed in such a way that the final result is given in a graphical 3D representation. The simulator uses a constant sound speed for a homogeneous medium, and incorporates an acoustic propagation model for a non-homogeneous scenario (Figure C.1).

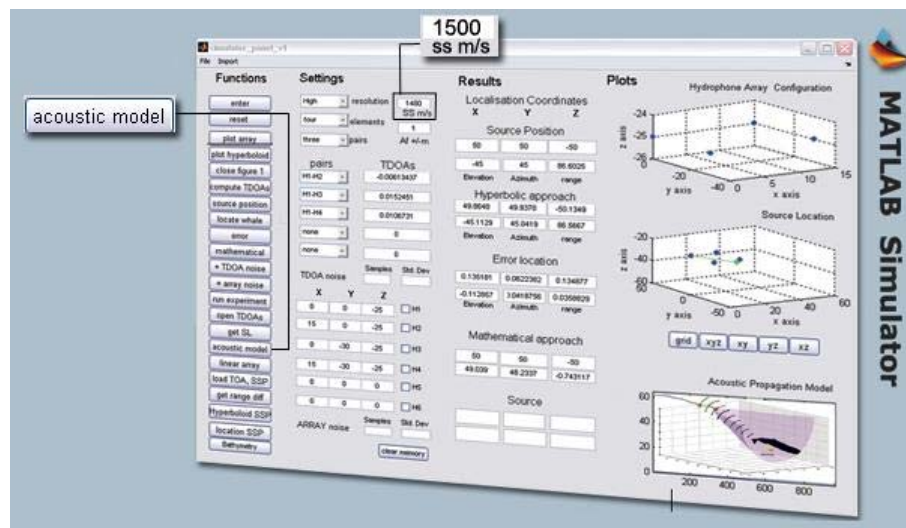


Figure C.1: Matlab GUI Simulator

C.1. Simulator

C.1.1 Settings

The user is able to set the number of receivers, the number of pair of receivers and the constant sound speed value. For real data, a TDOA section for a set of input variables is available. For synthetic data, the TDOA section is left blank and the system gets back the synthetic set of TDOA.

Settings

High resolution 1485 SS m/s

four elements 1

three pairs Af +/-m

pairs TDOAs

H1-H2 -0.118412698

H1-H3 -0.107959184

H1-H4 -0.071428571

none 0

none 0

Figure C.2: Settings and TDOAs

C.1.2 Receivers

The user is able to choose the desirable number of receivers (maximum 6) and their position in the 3D Cartesian plane XYZ.

X	Y	Z	
0	0	-0.49	<input checked="" type="checkbox"/> H1
-182.18	97.02	-0.5	<input checked="" type="checkbox"/> H2
-143.4	96.389	-0.5	<input checked="" type="checkbox"/> H3
-148.31	31.661	-0.5	<input checked="" type="checkbox"/> H4
0	0	0	<input type="checkbox"/> H5
0	0	0	<input type="checkbox"/> H6

ARRAY noise Samples Std. Dev

Figure C.3: Receivers Position

The simulator also has an array noise feature. The simulator generates a random number of samples with a standard deviation previously defined by the user. The result is a new array that has implicit a Gaussian distribution or *white noise* simulating the array motion produced mainly by the ocean currents.

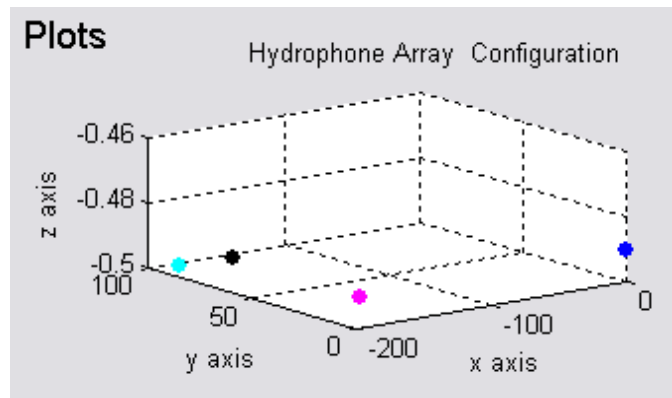


Figure C.4: 3D Receiver Array

A 3D plot of the receiver array allows the user to visualize the array geometry chosen.

C.1.3 Control Panel

The Control Panel includes all the different functions programmed in Matlab. Each button calls to one or various functions. The control panel is divided into three sections.

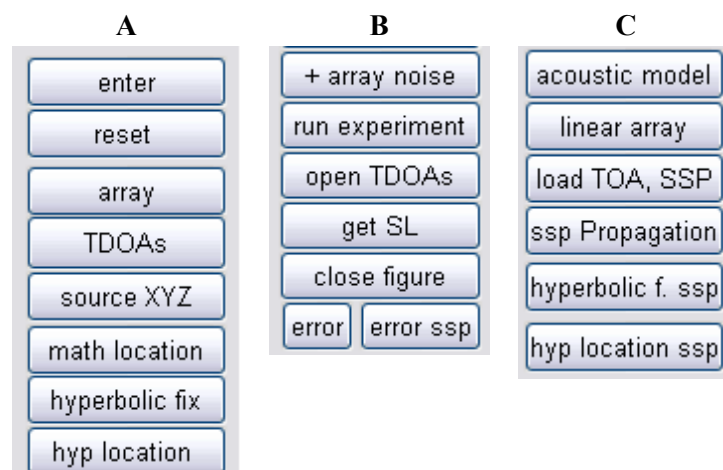


Figure C.5: Control Panel Sections

Section A

- **Enter**
Set all the data given by the user into the global and local variables of the system
- **Reset**
Set to zero all the local variables.
- **Array**
It generates a plot of the receiver array.
- **TDOAs**
If synthetic data are being used, they compute the set of TDOA correspondent to the number of pair of receivers selected. This function needs a previous source position set by the user.
- **Source**
Computes the correspondent range and bearing of the source chosen.
- **Math Location**
It computes the source location by using the algebraic solution. It requires the receiver positions, the set of TDOA, and sound speed as main input variables.
- **Hyperbolic fix**
It computes the stages 1 and 2 of the geometric hyperbolic localisation algorithm
- **Hyp Location**
It computes stages 3 and 4 of the geometric hyperbolic localisation algorithm.

Section B

- **Array Noise**

It adds Gaussian noise to the receiver array.

- **Run experiment**

It runs a series of different kinds of experiments previously programmed.

- **Open TDOAs**

It adds a group of TDOAs from a file that contains a list of TDOAs for different events.

- **Get SL**

It gets the source location from a group of different events.

- **Close Figure**

It closes the current Figure.

- **Error**

It computes the source location error on a homogeneous medium.

- **Error SSP**

It computes the source location error on a non-homogeneous medium.

Section C

- **Acoustic Model**

It accesses the acoustic propagation model menu

- **Linear array**

It converts the volumetric array into a linear array

- **Load TOA, SSP**

It loads the time of arrival matrix and the sound speed profile from a previous file generated by the acoustic propagation model.

- **SSP Propagation**

It gives the range difference of arrival between the source and receivers.

- **Hyperbolic f. ssp**

It computes stages 1 and 2 of the geometric hyperbolic localisation algorithm with the integration of a sound speed profile.

- **Hyp Location ssp**

It computes stages 3 and 4 of the geometric hyperbolic localisation algorithm with the integration of a sound speed profile.

C.1.4 Results

The source localisation is given in Cartesian Coordinates (X, Y, Z) and in Polar Coordinates, (Azimuth, Elevation, Range).

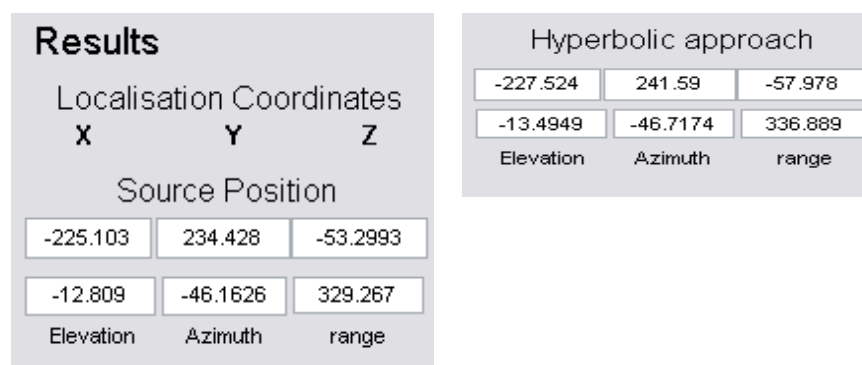


Figure C.6: Synthetic source position and its hyperbolic estimate location.

C.1.5 Plots

All the plots are given in 3D. This feature allows the user to make a virtual journey into each point of the hyperboloid geometric surfaces. Each simulation is saved with all the parameters and local variables generated. The user is able to call back any previous simulation and use the data for a posterior analysis and study.

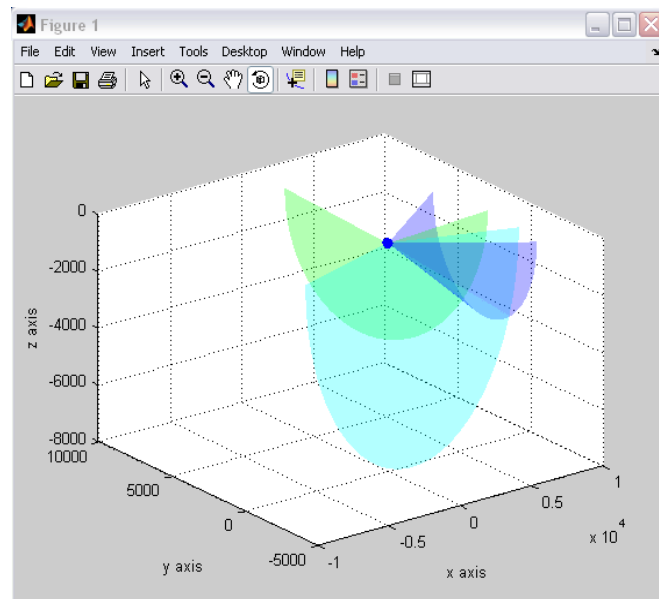


Figure C.7: 3D plot of the intersection of three hyperboloid geometric surfaces

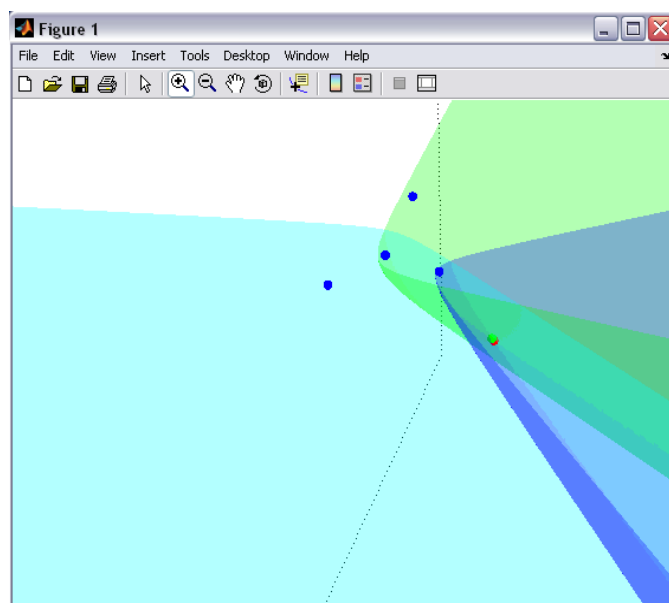


Figure C.8: Zoom in window showing the hyperboloid intersection

C.2 Acoustic Propagation Model

The acoustic propagation modelling software AcTUP V1.6 [62, 134] uses a GUI that starts up with a default run definition to let the user run a general propagation model. For a more detailed configuration, the user can modify the different variables according to the modelling problem. Among the different propagation parameters to modify are the frequency(s), source depth, receiver depth(s), minimum and maximum range, resolution and the environment file which includes the sound speed profile (Figure C.9).

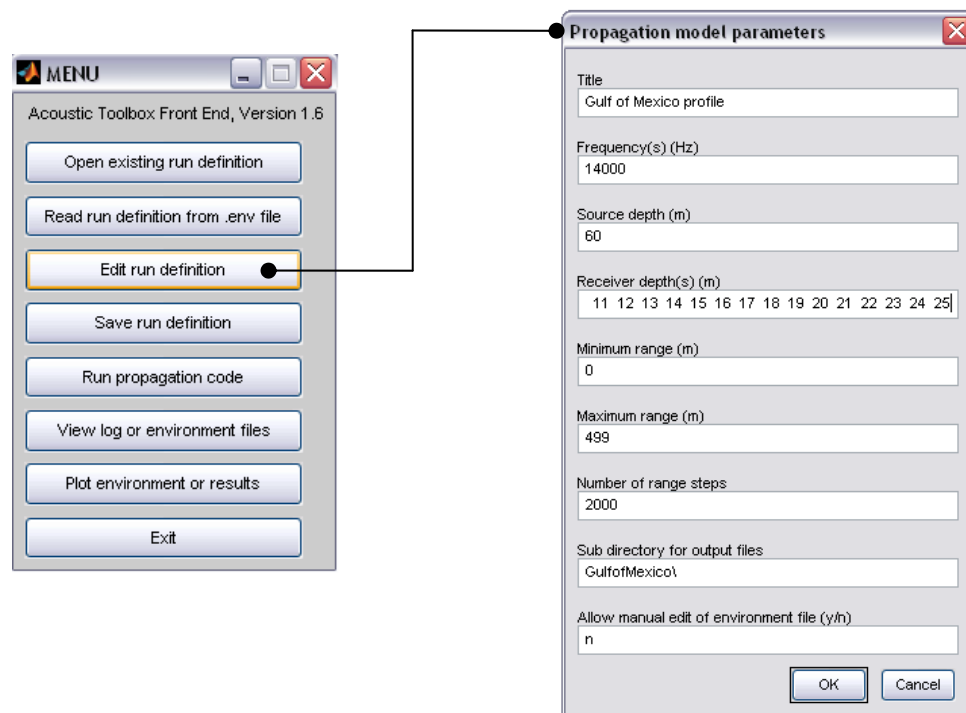


Figure C.9: Propagation Model Parameters

The AcTUP V1.6 GUI provides a uniform, menu-based user interface for running and plotting the results of the next modelling techniques:

- kraken (normal mode model)
- krakenc (complex normal mode model)
- scooter (fast-field model)
- bellhop (gaussian beam tracing)
- bounce (bottom reflection coefficient from geoacoustic model)

This makes the use of these models much quicker and easier, and is especially useful for running models at multiple frequencies or for comparing the results of applying different models to the same problem (Figure C.10).

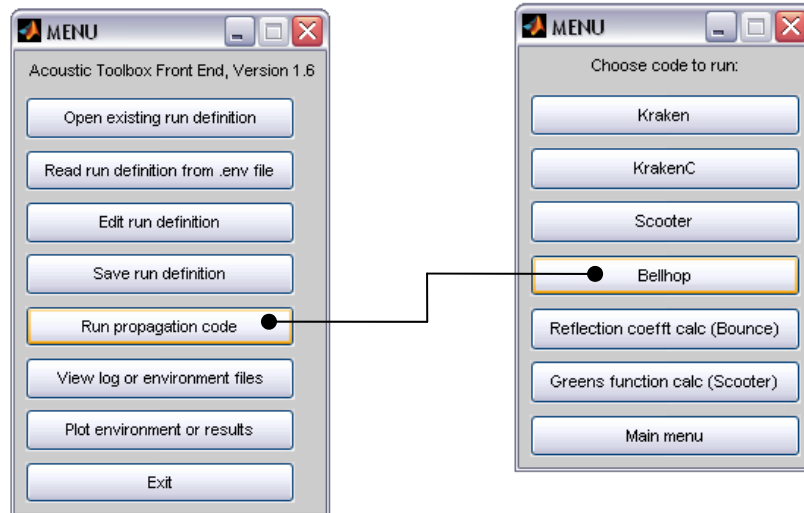


Figure C.10: Acoustic Propagation Modelling Techniques

The AcTUP V1.6 GUI offers access to set specific parameters of the modelling techniques. The user is able to model the ray-tracing path, the amplitude-delay signals, and the TL which can be coherent, incoherent or semicoherent. The final resolution depends on the number of beams and the angle the rays projected from the source (Figure C.11).

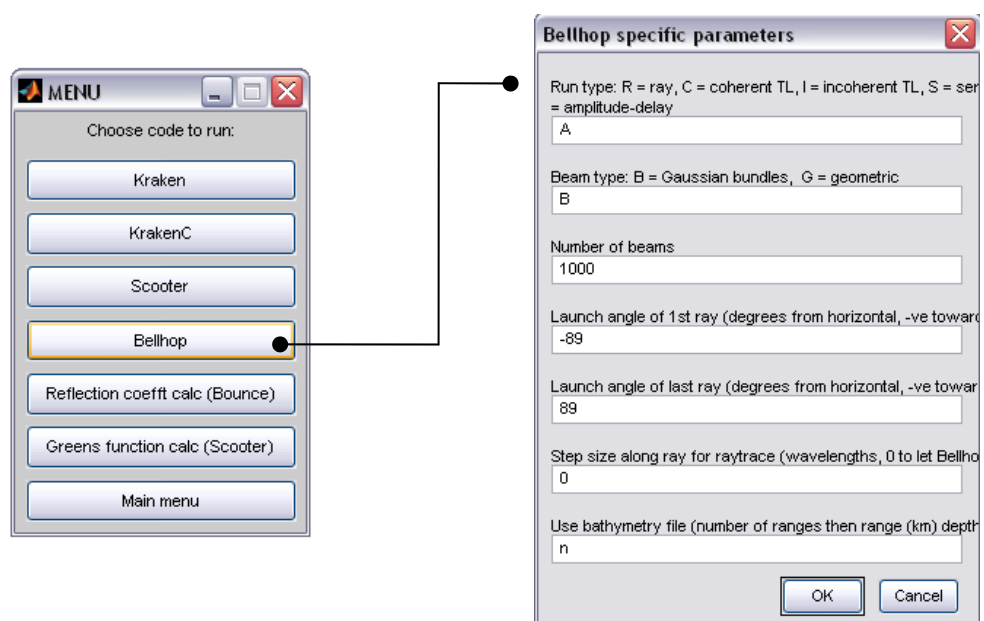


Figure C.11: Bellhop Setting Parameters

References

- [1] Adam O., Lopatka M. and Motsch J., 2003, *The 'fanning out' shape in the acoustic signature of sperm whales*, Proceedings of the workshop on Detection and Localisation of Marine Mammals using Passive Acoustics, Journal of the Canadian Acoustical Association, 32 (2).
- [2] Amano M. and Yoshioka M., 2003, *Sperm whale diving behavior monitored using a suction-cup-attached TDR tag*, Marine Ecology Progress Series, 258, 291-295.
- [3] Andersen S., 1970, *Auditory sensitivity of the harbour porpoise Phocoena phocoena*, Invest. Cetacea, 2:260-263.
- [4] Andre M., Johansson T., Delory E. And Van der Schaar M., 2005, *The Sperm Whale mid-range sonar: detecting low reflective objects*, Tecni-Acustica.
- [5] Au W.W.L, Penner R.H. and Turl C.W., 1987, *Propagation of beluga echolocation signal*, Journal of the Acoustical Society of America, 82(2): 807-813.
- [6] Au W.W.L., 1993, *The sonar of dolphins*, New York Springer-Verlag.
- [7] Au W.W.L., Moore P.W.B. and Pawloski D., 1986, *Echolocation transmitting beam of the Atlantic bottlenose dolphin*, Journal of the Acoustical Society of America, 80(2): 688-691.
- [8] Backus R.H., and Schevill W.E., 1966, *Physeter clicks*, Whales, dolphins, and porpoises, Univ. Calif. Press, Berkeley, 789.
- [9] Baker G.J. and Bonin Y.R.M., 2001, *GPS Equipped Sonobuoy*, Defence Research Establishment Atlantic, Canada.
- [10] Beerens S.P., IJsselmuide S.P.V. and Robert M.K., 2004, *Detection classification and localisation of marine mammals using the passive acoustic capabilities of an LFAS system*, Proceedings of the Seventh European Conference on Underwater Acoustics, Delft, The Netherlands.
- [11] Berrow S.D, *An assessment of the frameworks, legislation and monitoring required to develop genuinely sustainable whale watching*, Shannon Dolphin and Wildlife Foundation, Merchants Quay, Kilrush, Co. Clare: 1-12.

- [12] Blackwell S.B. and Greene J.C.R., 2004, *Drilling and operational sounds from an oil production island in the ice-covered Beaufort Sea*. Journal of the Acoustical Society of America, 5: 3199-3211.
- [13] Bocquet M., Loyez C. and Benlarbi-Delai A., 2005, *Using Enhanced-TDOA Measurement for Indoor Positioning*, IEEE Microwave and wireless components letters, 15(10):612-614.
- [14] Bradbury J.W. and Vehrencamp S.L., 1998, *Principles of Animal Communication*, Sinauer Associates, Inc.
- [15] Brady W.G., Mansfield M.J., 1961, *Analytic Geometry*, Little Brown and Company.
- [16] Burdic W.S., 1991, *Underwater Acoustic System Analysis*, 2nd edition, Prentice Hall, New Jersey.
- [17] Cato D.H., 1998, *Simple methods of estimating source levels and locations of marine animal sounds*, Journal of the Acoustical Society of America, 104(3): 1667-1671.
- [18] Chabot D., 1988, *A quantitative technique to compare and classify humpback whale (Megaptera novaeanglie) sounds*, Ethology 77: 89-102.
- [19] Clark C.W. and Clark J.M., 1980, *Sound playback experiments with southern right whales, Eubalaena australis*, Science 207:663-664.
- [20] Clark D.S., Flattery J., Gisiner R., Schilling J., Sledzinski T. and Trueblood R., 1994, *MMATS: Acoustic localization of whales in real time over large area*, Journal of the Acoustical Society of America, 96: 3250.
- [21] Clark C.W., Marler P. and Beeman K., 1987, *Quantitative analysis of animal vocal phonology: An application to swamp sparrow song*, Ethology 76:101-115.
- [22] Clarke M.R., 1978, *Structure and proportions of the spermaceti organ in the sperm whale*, J. Mar. Biol. Assn, 58, 1-17.
- [23] Cummings W.C. and Holliday D.V., 1985, *Passive acoustic location of bowhead whales in a population census off Point Barrow, Alaska*, Journal of the Acoustical Society of America, 78: 1163–1169.
- [24] Cummings W.C. and Holliday D.V., 1987, *Sound and source levels from bowhead whales off Point Barrow, Alaska*, Journal of the Acoustical Society of America, 82: 814–821.

- [25] Cummings W.C. and Thompson P.O., 1994, *Characteristics and seasons of blue and finback whales along the U.S. west coast as recorded at SOSUS stations*, Journal of the Acoustical Society of America, 95: 2853.
- [26] Cummings W.C., Thompson P.O. and Cook R, 1968, *Underwater sounds of migrating gray whales, Eschrichtius glaucus (Cope)*, Journal of the Acoustical Society of America, 44: 1278–1282.
- [27] Cunningham A. and Thomas B., 2005, *Target Motion Analysis Visualisation*, In Proc. Asia Pacific Symposium on Information Visualisation, Sydney, Australia, CRPIT, 45, 81-90.
- [28] D'Spain G.L., Kuperman W.A., Hodgkiss W.S. and Berger L.F., 1995, *Three-dimensional localization of a blue whale using broadband matched-field processing for range and depth, and plane-wave adaptive beamforming for azimuth*, Journal of the Acoustical Society of America, 97(5):3353.
- [29] Diatschenko V., Stoy J.R., Brown W.K. and Ledoux A.N., 1998, *Passive acoustic method of measuring the effective internal diameter of a pipe containing flowing fluids*, TEXACO INC, United States, Patent 5756898.
- [30] Dobbins P.F. and Nowacek D.P., 2007, *Passive azimuth localization of dolphin whistles using acoustically small sensors*, Proceedings of the Institute of Acoustics, Fourth International Conference on Bio-Acoustics, Loughborough, UK, 29(3):149-156.
- [31] Douglas L.A., Dawson, S.M. and Jaquet N., 2005, *Click rates and silences of sperm whales at Kaikoura, New Zealand*, Journal of the Acoustical Society of America, 118:523-529.
- [32] Edds P.L., 1988, *Characteristics on finback Balaenoptera physalus vocalisations in the St. Lawrence Estuary*, Bioacoustics 1(2/3): 131-149.
- [33] Etter P.C., 1996, *Underwater Acoustic Modeling*, 2nd edition, E & FN SPON.
- [34] Evans P.G.H, 1987, *The natural history of whales and dolphins*, Christopher Helm, London.
- [35] Falk J., Handel P. and Janson M., 2003, *Effects of frequency and phase errors in electronic warfare TDOA direction-finding systems*, IEEE Transactions on Acoustics, Speech, Signal Processing, 118-123.
- [36] Fernández A., Arbelo M., Deaville R., Patterson I.A.P., Castro P., Baker J.R., Degollada E., Ross H., Herráez P., Pocknell A., Rodriguez E., Howie F.,

- Espinosa A., Reid R., Jaber J., Martín, V., Cunningham A. and Jepson, P., 2004, *Pathology: Whales, sonar and decompression sickness*, Nature, 428: 1-2.
- [37] Fernández A., Edwards J.F., Rodríguez F., Espinosa de los Monteros A., Herráez P., Castro, P., Jaber J.R., Martín V., and Arabelo M., 2005, *Gas and fat embolic syndrome involving a mass stranding of beaked whales (Family Ziphiidae) exposed to anthropogenic sonar signals*, Veterinary Pathology, 42: 446-457.
- [38] Frantzis A., 1998, *Does acoustic testing strand whales?* Nature, 392: 29.
- [39] Freitag L.E. and Tyack P.L., 1993, *Passive acoustic localization of the Atlantic bottlenose dolphin using whistles and echo location clicks*, Journal of the Acoustical Society of America, 93, 2197–2205.
- [40] Fristrup K.M., 1992, *Characterizing acoustic features of marine animal sounds*, Woods Hole Oceanographic Institution, WHOI-92-04, Woods Hole, MA.
- [41] Gates M.R., 2008, *Order granting in part and denying in part plaintiffs' motion for preliminary injunction; and order setting injunction*, The United States District Court for the District of Hawaii 100: 1-84.
- [42] Gillespie D. and Chappell O., 2002 *An automatic system for detecting and classifying the vocalisation of harbour porpoises*, Bioacoustics, 13(1): 36-61.
- [43] Gillespie D. and Leaper R., 1996, *Detection of sperm whale (Physeter macrocephalus) clicks and discrimination of individual vocalisations*, European Research on Cetaceans 10: 87-91.
- [44] Gillespie D., 2004, *Detection and classification of right whale calls using an 'edge' detector operating on a smoothed spectrogram*, Proceedings of the workshop on Detection and Localisation of Marine Mammals using Passive Acoustics, Journal of the Canadian Acoustical Association, 32 (2).
- [45] Giraudet P. and Glotin H., 2006, *Real-time 3D tracking of whales by echo-robust precise TDOA estimates with a widely-spaced hydrophone array*. Applied Acoustics, 67, 1106-1117.
- [46] Gisiner R.C., 1998, *Workshop on: the effects of anthropogenic noise in the marine environment*, Workshop Proceedings, Arlington, Virginia, 19-57.
- [47] Gordon J.C., 1987, *The behaviour and ecology of sperm whales off Sri Lanka*, PhD Thesis, University of Cambridge.
- [48] Gordon J., 1990, *A simple photographic technique for measuring the length of whales from boats at sea*, Rep. International Whaling Commission. 40: 581-588.

- [49] Gordon J., 1995, *The acoustic world of sperm whales*, Eur. Res. Cetaceans 9:29-33.
- [50] Gray A., 1997, *Modern Differential Geometry of Curves and Surfaces with Mathematica*, CRC Press, 2nd edition, Florida.
- [51] Greene C.R., McLennan M.W., Norman R.G. and Richardson W.J., 2004, *Bowhead whale call localization using DIFAR technique*, Proceedings of the workshop on Detection and Localisation of Marine Mammals using Passive Acoustics, Journal of the Canadian Acoustical Association, 32 (2).
- [52] Hall J.D. and Johnson C.S., 1972, *Auditory thresholds of a killer whale *Orcinus orca* Linnaeus*, Journal of the Acoustical Society of America, 51(2): 515-517.
- [53] Hilbert D. and Cohn-Vossen S., 1999, *Geometry and the Imagination*, Chelsea, New York.
- [54] Hoor R.T., 1996, *Array Redundancy for Active Line Arrays*, IEEE Transactions on Image Processing, 5(7): 1179-1183.
- [55] Howland P., 2005, *Passive radar systems*, IEE Proceedings-Radar Sonar Navigation, 152(3): 105-106.
- [56] Janik V.M. and Parijs V., 2000, *A two-dimensional acoustic localization system for marine mammals*, Marine Mammal Science 16(2): 437-447.
- [57] Jaquet N.S., Dawson, et al., 2001, *Vocal behavior of male sperm whales: Why do they click?*, Journal of the Acoustical Society of America, 109(5): 2254-2259.
- [58] Jensen F.B. and Ferla C.M., 1988, *Numerical solutions of range-dependent benchmark problems in ocean acoustics*, SACLANT Undersea Res. Ctr, Rept, 141.
- [59] Jensen F.B. and Krol H., 1975, *The use of the parabolic equation method in sound propagation modelling*, SACLANT ASW Res. Ctr, Memo, 72.
- [60] Jensen F.B., 1982, *Numerical models of sound propagation in real oceans*, Proc. MTS/IEEE Oceans 82 Conference, 147-154.
- [61] Jensen F.B., Kuperman W.A., Porter M.B. and Schmidt H., 1994, *Computational Ocean Acoustics*, American Institute of Physics.
- [62] Jepson P.D., Arbelo M., Deaville R., Patterson I.A.P., Castro P., Baker J.R., Degollada E., Ross H.M., Herraiz P., Pocknell A.M., Rodriguez F., Howie F.E., Espinosa A., Reid R.J., Jaber J.R., Martín V., Cunningham A.A. and Fernandez A., 2003, *Gas-bubble lesions in stranded cetaceans*, Nature, 425: 575-576.

- [63] Jepson P.D., Deaville R., Petterson A.P., Pocknell A.M., Ross H.M., Baker J.R., Howie F.E, Reid R.J., Collof A. and Cunningham A.A., 2005, *Acute and chronic gas bubble lesions in cetaceans stranded in the United Kingdom*, Veterinary Pathology, 42: 291-305.
- [64] Jochens A.E. and Biggs D.C., 2004, *Sperm Whale Seismic Study in the Gulf of Mexico; Annual Report*, OCS Study MM 2003-069.
- [65] Jochens A.E., Biggs D.C., et al., 2006, *Sperm Whale Seismic Study in the Gulf of Mexico; Summary Report*, OCS Study MM 2006-034.
- [66] Johansson A. T. and White P. R., 2004, *Detection and Characterization of Marine Mammal Calls by Parametric Modelling*, Proceedings of the workshop on Detection and Localisation of Marine Mammals using Passive Acoustics, Journal of the Canadian Acoustical Association, 32 (2).
- [67] Johnson C.S., 1967, *Sound detection thresholds in marine mammals*, Marine bio-acoustics, 2:353.
- [68] Johnson J.S., 2001, *Executive summary, final overseas environmental impact statement and environmental impact statement for surveillance towed array sensor system low frequency active (SURFASS LFA) sonar*, Department of Navy, Arlington, VA.
- [69] Kerman B.R., 1993, *Natural Physical Sources of Underwater Sound*, Proceedings of the Conference on 'Natural Physical Sources of Underwater Sound', Cambridge, UK.
- [70] Ketten D.R., 1997, *Structure and function in whale ears*, Bioacoustics, 8, 103-135.
- [71] Ketten D.R., 2002, *Marine Mammal Auditory Systems: A Summary of Audiometric and Anatomical Data and Implications for Underwater Acoustic Impacts*, Polarforschung 72 (2/3): 79-92, (erschienen 2004).
- [72] Ketten D.R., 2005, *Beaked Whale Necropsy Findings for Strandings in the Bahamas, Puerto Rico, and Madeira, 1999-2002*, Woods Hole Oceanographic Institution, Technical Report WHOI-2005-09, Woods Hole, MA.
- [73] Ketten D.R., Arruda J., Cramer S., Yamato M., Zosuls M., Mountain D., 2007, *How low can they go: Functional analysis of the largest land and marine mammal ears*, 17th Biennial Conference on the Biology of Marine Mammals, Cape Town, South Africa.

- [74] Ketten D.R., Rowles T., Cramer S., O'Malley J., Arruda J. and Evans, P.G.H., 2003, *Cranial trauma in beaked whales*, Proceedings of the Workshop on Active Sonar Cetaceans, ECSN, 42:21-27.
- [75] Klima M., 1995, *Cetacean phylogeny and systematics based on the morphogenesis of the nasal skull*, Aquatic Mammals 21(2):79-89.
- [76] La Cour B.R. and Linford M.A., 2004, *Detection and classification of North Atlantic right whales in the Bay of Fundy using independent component analysis*, Proceedings of the workshop on Detection and Localisation of Marine Mammals using Passive Acoustics, Journal of the Canadian Acoustical Association, 32 (2).
- [77] Lang S.W., Duckworth G.L. and McClellan J.H., 1981, *Array Design for MEM and MLM Array Processing*, ICASSP-81 Proceedings, IEEE International Conference on Acoustics, Speech and Signal Processing, Atlanta, 145-148.
- [78] Laplanche C. Adam O. Lopatka M. and Motsch J., 2005, *Male sperm whale acoustic behavior observed from multipaths at a single hydrophone*, Journal of the Acoustical Society of America, 118(4): 2677-2687.
- [79] Laplanche C., Adam O. and Motsch J., 2004, *Accuracy in the localization of sperm whales resident in the Strait of Gibraltar using one hydrophone*, Proceedings of the workshop on Detection and Localisation of Marine Mammals using Passive Acoustics, Journal of the Canadian Acoustical Association, 32 (2).
- [80] Laurinolli M.H., Hay A.E., Desharnais F. and Taggart C.T., 2004, *Localization of North Atlantic Right whale sounds in the bay of fundy using a sonobuoy array*. Marine Mammal Science 19(4): 708-723.
- [81] Levenson C., 1974, *Source level and bistatic target strength of the sperm whale (Physeter catodon) measured from an oceanographic aircraft*, Journal of the Acoustical Society of America, 55(5): 1100-1103.
- [82] Lewis T., Gillespie D., Gordon J. and Chappell O., 1999, *Acoustic Cetacean Monitoring TO 1999 – Summary Report*, Birmingham Research and Development, A report to Shell UK Ltd.
- [83] Ljungblad D.K., Scoggins P.D. and Gilmartin W.G., 1982, *Auditory thresholds of a captive eastern Pacific bottle-nosed dolphin, Tursiops spp.*, Journal of the Acoustical Society of America, 72(6):1726-1729.

- [84] Lo K.W. and Ferguson B.G., 2000, *Broadband Passive Acoustic Technique for Target Motion Parameter Estimation*, *IEEE Transactions on Aerospace and Electronic Systems*, 36(1):163-175.
- [85] Lockyer C., 1991. *Body composition of sperm whale, Physeter catodon, with special reference to the possible function of fat depots*, *Rit Fisk*, 12: 124.
- [86] MacCurdy E., 1942, *The Notebooks of Leonardo da Vinci*, Garden City, NY.
- [87] Madsen P.T., Payne R., Kristiansen N.U., Wahlberg M., Kerr I. and Mohl B., 2002, *Sperm whale sound production studied with ultrasound time/depth-recording*, *The Journal of Experimental Biology* (205): 1899-1906.
- [88] Maggi A.L. and Duncan A.J., 2005, *AcTUP (LITE) Installation and User Guide*, Centre for Marine Science & Technology , Curtin University, Australia, 13.
- [89] Mantis S.D., 2001, *Localization of Wireless Communication Emitters Using Time Difference of Arrival (TDOA) Methods in Noisy Channels*, Master's thesis, Naval Postgraduate School Monterey Ca, USA.
- [90] Mason T., Priestley D. and Reeve D.E., 2007, *Monitoring near-shore shingle transport under waves using a passive acoustic technique*, *Journal of the Acoustical Society of America*, 122(2): 737-746.
- [91] Matthews J., 2004, *Detection of frequency-modulated calls using a chirp model*, *Proceedings of the workshop on Detection and Localisation of Marine Mammals using Passive Acoustics*, *Journal of the Canadian Acoustical Association*, 32 (2).
- [92] McDonald M.A., 2004, *DIFAR hydrophone usage in whale research*, *Proceedings of the workshop on Detection and Localisation of Marine Mammals using Passive Acoustics*, *Journal of the Canadian Acoustical Association*, 32 (2): 155-160.
- [93] McHugh R., McLaren D. and Wilson M., 2005, *Underwater Sound*, *Acta Acustica*, *Journal of the European Acoustics Association*, 1, 51-60.
- [94] Mellinger D.K., 2001, *Ishmael 1.0 User's Guide*. NOAA Tech. Report OAR-PMEL-120, NOAA.
- [95] Mellinger D.K., 2004, *A comparison of methods for detecting right whale calls*, *Proceedings of the workshop on Detection and Localisation of Marine Mammals using Passive Acoustics*, *Journal of the Canadian Acoustical Association*, 32 (2).
- [96] Milinkovitch M.C., Orti G. and Meyer A., 1993, *Revised phylogeny of whales by mitochondrial ribosomal DNA sequences*, *Nature* 361:346-348.

- [97] Miller P.J.O., Biassoni N., Samuels A. and Tyack P.L., 2000, *Whale songs lengthen in response to sonar*. *Nature*, 405:903.
- [98] Miller P.J.O., Johnson M.P., Tyack P.L., Terray E.A., 2004, *Swimming gaits, passive drag and buoyancy of diving sperm whales *Physeter macrocephalus**, *The Journal of Experimental Biology* 207: 1953-1967.
- [99] Mitchell S. and Bower J., 1995, *Localization of animal calls via hyperbolic methods*, *The Journal of the Acoustical Society of America*, 97(5): 3352-3353.
- [100] Mohl B. and Wahlberg M., 2001, *A large-aperture array of nonlinked receivers for acoustic positioning of biological sound sources*, *The Journal of the Acoustical Society of America*, 109(1): 434-437.
- [101] Mohl B., 1968, *Auditory sensitivity of the common seal in air and water*, *J. Aud. Res.* 8(1):27-38.
- [102] Mohl B., Wahlberg M., Madsen P.T., Miller L.A. and Surlykke, A., 2000, *Sperm whale clicks: Directionality and source level revisited*, *Journal of the Acoustical Society of America*, 107(1): 638-648.
- [103] Mohl B., Wahlberg, M., Madsen P.T., Heerfordt A. and Lund A., 2003, *The monopulsed nature of sperm whale clicks*, *Journal Acoustical Society of America*, 114(2): 1143-1154.
- [104] Moore S.E. and Schusterman R.J., 1987, *Audiometric assessment of northern fur seals, *Callorhinus ursinus**, *Marine Mammal Science*, 3(1):31-53.
- [105] Morfey C. L., 2001. *Dictionary of Acoustics*, Academic Press.
- [106] Morrissey R.P., Ward J., DiMarzio N. Jarvis S. and Moretti D.J., 2006, *Passive acoustics detection and localization of sperm whales in the Tongue of the Ocean*, *Applied Acoustics*, 10, 1016.
- [107] National Research Council, 2005, *Marine Mammal Populations and Noise*, The National Academies Press.
- [108] Nowacek D.P., Thorne, L.H., Johnston, D.W., and Tyack P.L., 2007, *Responses of cetaceans to anthropogenic noise*, *Mammal Society, Mammal Review*, 37 (2): 81-115.
- [109] Nutall A.H., 2001, *Approximations to Directivity for Linear, Planar, and Volumetric Apertures and Arrays*, *IEEE Journal of Oceanic Engineering*, 26(3): 383-398.

- [110] Paradiso J.A., Leo C.K., Checka N., and Hsiao K., 2002, *Passive Acoustic Knock Tracking for Interactive Windows*, ACM CHI Conference, Minneapolis, USA.
- [111] Pham D.T., Ji Z., Yang M., Wang Z. and Al-Kutubi M., 2007, *A Novel Human-Computer Interface Based on Passive Acoustic Localisation*, Springer Berlin / Heidelberg.
- [112] Pinkowski B., 1994, *Robust Fourier descriptors for characterizing amplitude-modulated waveform shapes*, Journal of the Acoustical Society of America, 95: 3419-3423.
- [113] Porter M. and Bucker H.P., 1987, *Gaussian beam tracing for computing ocean acoustic fields*, Journal of the Acoustical Society of America, 82(4): 1349-1359.
- [114] Potter J. and Delory E., 1998, *Noise sources in the sea and the impact for those who live there*, Proceedings of the Acoustics and Vibration Asia'98 Conference, Singapore.
- [115] Proakis J.G. and Manolakis D.G., 1988, *Introduction to Digital Signal Processing*, Macmillan Publishing Company, New York.
- [116] Rabiner L.R., and Juang, B.H., 1993, *Fundamentals of Speech Recognition*, Prentice Hall, Englewood Cliffs, NJ.
- [117] Ramani N., and Patrick, P.H., 1992, *Fish detection and identification using neural networks*, IEEE Journal of Ocean Engineering, 17: 364-368.
- [118] Rayleigh L., 1909, *On the Perception of the Direction of Sound*, Proc. R. Soc. A. 83:61-64.
- [119] Rice D.W., 1998, *Marine mammals of the world - systematics and distribution*, Society for Marine Mammalogy, Special Publication, 4: 1-231.
- [120] Richards S.D., Miles D.A., Clarke T. and Harland E.J., 2007, *Passive acoustic localization of marine mammals from mobile platforms*, Proceedings of the Institute of Acoustics, Fourth International Conference on Bio-Acoustics, Loughborough, UK, 29(3):133-140.
- [121] Richardson W.J., Greene C.R., Malme C.I. and Thomson D.H., 1995, *Marine Mammals and Noise*, Academic Press.
- [122] Santoro A.K., Marten K.L., and Cranford T.W., 1989, *Pygmy sperm whale sounds (Kogia breviceps)*, 8th Biennial Conference on the Biology of Marine Mammals, Pacific Grove, California.

- [123] Shiao T-J., 2001, *Optimal array design and sensitivity for mode filtering. 141st Meeting: Acoustical Society of America. Underwater Acoustics: Time Reversal and Propagation*, Michigan, USA, Journal of the Acoustical Society of America 109(5):2496.
- [124] Simard Y., Bahoura M. And Roy N., 2004, *Acoustic detection and localization of whales in Bay of Fundy and St. Lawrence estuary critical habitats*, Proceedings of the workshop on Detection and Localisation of Marine Mammals using Passive Acoustics, Journal of the Canadian Acoustical Association, 32 (2):107-116.
- [125] Simmonds M.P. and Lopez-Jurado L.F., 1991, *Whales and the military*, Nature, 351: 448.
- [126] Simons D.G., Van Moll C. and Snellen M., 2004, *A two-stage method for determining the position and corresponding precision of marine mammal sounds*, Proceedings of the workshop on Detection and Localisation of Marine Mammals using Passive Acoustics, Journal of the Canadian Acoustical Association, 32 (2):117-124.
- [127] Sindt J.C. and Theije P.A.M., 2004, *Target localisation with multistatic systems*, Proceedings of the Seventh European conference on Underwater Acoustics, 5-8. Society of Marine Mammalogy Special Publication, 4:231.
- [128] Southall B.L., Bowles A.E., Ellison W.T., Finneran J.J., Gentry R.L., Greene Jr., C.R., Kastak D., Ketten D.R., Miller J.H., Nachtigall P.E., Richardson W.J., Thomas J.A., and Tyack P.L., 2007. *Marine mammal noise exposure criteria: Initial scientific recommendations*. Aquatic Mammals 33(4): 411-521.
- [129] Spiegel M.R., Schiller J.J. and Srinivasan R.A., 2000, *Theory and Problems of Probability and Statistics*, Schaum's series, McGraw Hill, 2nd edition.
- [130] Spiesberger J.L. and Fristrup K.M., 1990, *Passive Localization of Calling Animals and Sensing of their Acoustic Environment Using Acoustic Tomography*, The American Naturalist, 135: 107-153.
- [131] Spiesberger J.L. and Wahlberg M., 2002, *Probability density functions for hyperbolic and isodiachronic locations*, Journal of the Acoustical Society of America, 112(6): 3046-3079
- [132] Spiesberger J.L., 1998, *Linking auto- and cross-correlation functions with correlation equations: Application to estimating the relative travel times and*

- amplitudes of multipath*, Journal of the Acoustical Society of America, 104(1): 300-312.
- [133] Spiesberger J.L., 1999, *Locating animals from their sounds and tomography of the atmosphere: Experimental demonstration*, Journal of the Acoustical Society of America, 106(2): 837-846.
- [134] Spiesberger J.L., 2001, *Hyperbolic location errors due to insufficient numbers of receivers*, Journal of the Acoustical Society of America, 109(6): 3076-3079.
- [135] Spiesberger J.L., 2004, *Geometry of locating sounds from differences in travel time: Isodiachrons*, Journal of the Acoustical Society of America, 116(5): 3168-3177.
- [136] Spiesberger J.L., 2005, *Probability distributions for locations of calling animals, receivers, sound speeds, winds, and data from travel time differences*, Journal of the Acoustical Society of America, 118(3): 1790-1800.
- [137] Stafford K.M., Fox C.G. and Clark D.S., 1988, *Long-range acoustic detection and localization of blue whale calls in the northeast Pacific ocean*, Journal of the Acoustical Society of America, 104(6): 3616-3625.
- [138] Stafford, K. M., Fox, C. G., and Mate, B. R., 1994, *Acoustic detection and location of blue whales (*Balaenoptera musculus*) from SOSUS data by matched filtering*, Journal of the Acoustical Society of America, 96, 3250-3251.
- [139] Teloni V., Mark J.P., Miller J.O.P., Madsen P.T., 2008, *Shallow food for deep divers: Dynamic foraging behavior of male sperm whales in a high latitude habitat*, Journal of Experimental Marine Biology and Ecology 354 (2008) 119-131.
- [140] Terhune J.M. and Ronald K., 1972, *The harp seal, *Pagophilus groenlandicus*. The underwater audiogram*, Canadian Journal of Zoology. 50(5):565-569.
- [141] Thode A., 2004, *The use of acoustic multipath for localization of sperm whales*, Journal Acoustic Society of America, 116(4): 2606.
- [142] Thode A., 2004, *Tracking sperm whale (*Physeter macrocephalus*) dive profiles using a towed passive acoustic array*, Journal of the Acoustical Society of America, 116(1): 245-253.
- [143] Thode A., D'Spain G.L. and Kuperman W.A., 2000, *Matched-field processing, geoacoustic inversion, and source signature recovery of blue whale vocalizations*, Journal of the Acoustical Society of America, 107(3): 1286-1300.

- [144] Thode A., Mellinger D.K., Stienessen S., Martinez A., and Mullin K., 2002, *Depth-dependent acoustic features of diving sperm whales (Physeter macrocephalus) in the Gulf of Mexico*, Journal of the Acoustical Society of America, 112(1): 308-321.
- [145] Thode A., Norris T. and Barlow J., 2000, *Frequency beamforming of dolphin whistles using a sparse three-element towed array*, Journal of the Acoustical Society of America, 107(6): 3581-3584.
- [146] Thomsen F., Ludemann K., Kafemann R. and Piper W., 2006, *Effects of offshore wind farm noise on marine mammals and fish, biola*, Hamburgh, Germany on behalf of COWRIE Ltd.
- [147] Tiemann C.O., Porter M.B., 2004, *Localization of marine mammals near Hawaii using an acoustic propagation model*, Journal of the Acoustical Society of America, 115(6): 2834-2843.
- [148] Urick R.J., 1983, *Principles of Underwater Sound*, 3rd edition, McGraw-Hill.
- [149] Vagle S., Ford J.K.B., Erickson N., Hall-Patch N. and Kamitakahara G., 2004, *Acoustic recording systems for baleen whales and killer whales on the west coast of Canada*, Proceedings of the workshop on Detection and Localisation of Marine Mammals using Passive Acoustics, Journal of the Canadian Acoustical Association, 32 (2).
- [150] Vallarta J., McHugh R. and Record P., 2007, *The effect of different array-configurations on the accuracy of passive acoustic location of cetaceans*, Proceedings of the Institute of Acoustics, Fourth International Conference on Bio-Acoustics, Loughborough, UK, 29(3):141-148.
- [151] Van IJsselmuide S.P. and Beerens S.P., 2004, *Detection and classification of marine mammals using an LFAS system*, Proceedings of the workshop on Detection and Localisation of Marine Mammals using Passive Acoustics, Journal of the Canadian Acoustical Association, 32 (2).
- [152] Vincent H., 2001, *Models, Algorithms, and measurements for underwater acoustic positioning*, PhD Thesis, University of Rhode Island, Kingston.
- [153] Vincent H.T., 2000, *Geodetic position estimation for underwater acoustic sensors*, US Patent No. 6,028,823.
- [154] Vincent H.T., 2002, *Method and system for determining underwater effective sound velocity*, US Patent No. 6,388,948.

- [155] Wahlberg M., 1999, *Positioning accuracy of a large-aperture hydrophone array for sperm whale research*, Journal of the Acoustical Society of America, 105(2): 1318.
- [156] Wahlberg M., 2002, *The acoustic behaviour of diving sperm whales observed with a hydrophone array*, Journal of Experimental Marine Biology and Ecology 281: 53-62.
- [157] Wahlberg M., 2004, *Comparing a linear with a non-linear method for acoustic localization*, Proceedings of the workshop on Detection and Localisation of Marine Mammals using Passive Acoustics, Journal of the Canadian Acoustical Association, 32 (2):125-131.
- [158] Wahlbergh M., Mohl B and Madsen P.T., 2001, *Estimating source position accuracy of a large-aperture hydrophone array for bioacoustics*, Journal of the Acoustical Society of America, 109(1): 397-406.
- [159] Walker R.A., 1963, *Some intense, low-frequency, underwater sounds of wide geographic distribution, apparently of biological origin*, Journal of the Acoustical Society of America, 35, 1816–1824.
- [160] Walter M.X., Zimmer M.P.J., D’Amico A. and Tyack P.L., 2003, *Combining Data From a Multisensor Tag and Passive Sonar to Determine the Diving Behavior of a Sperm Whale (Physeter macrocephalus)*, IEEE Journal of Oceanic Engineering 28(1),: 13-28.
- [161] Watchtower B.T.S, 1995, *The Earth—Both Amazing and Beautiful*, Journal Awake! 11/22, 10.
- [162] Watchtower B.T.S, 1997, *Water-Lifeblood of the Planet*, Journal Awake! 8/22, 3
- [163] Watkins W. A., Daher, M.A., Fristrup, K.M., and Howald, T.J., 1993 *Sperm whales tagged with transponders and tracked underwater by sonar*. Marine Mammal Science. 9: 55-67.
- [164] Watkins W.A. and Schevill W.E., 1972, *Sound source location by arrival-times on a non-rigid three-dimensional hydrophone array*, Deep-Sea Research 19: 691-706.
- [165] Watkins W.A., 1980, *Acoustics and the behaviour of sperm whales*, Animal sonar systems, Plenum, New York, 1135.
- [166] Watkins W.A., 1981, *Activities and underwater sounds of fin whale*, Scientific Reports of the Whales Research Institute, 33:83-117.

- [167] Watkins W.A., and Schevill W.E., 1977, *Sperm whale codas*, Journal of the Acoustical Society of America, 62(6): 1485-1490.
- [168] Watwood S., Miller P.O.J., Johnson M.P., Madsen P.T. and Tyack P.L., 2006, *Deep-diving foraging behaviour of sperm whales (Physeter macrocephalus)*, J. Anim. Ecol. 75, 826-835.
- [169] Weilgart L.S., and Whitehead H., 1988, *Distinctive vocalisations from mature male sperm whales (Physeter macrocephalus)*, Canadian Journal of Zoology, 66(9): 1931-1937.
- [170] Weisstein E.W., *Circle-Line Intersection*, MathWorld Wolfram Web Resource, <http://mathworld.wolfram.com/Circle-CircleIntersection.html> (28/01/09).
- [171] White P.R., Liegton T.G., Finfer D.C., Powles C. and Baumann O.N., 2006, *Localisation of sperm whales using bottom-mounted sensors*, Applied Acoustics, 67, 1074-1090.
- [172] Whitehead H., 2003, *Sperm whales: Social Evolution in the Ocean*, University of Chicago Press.
- [173] Whitney W., 1968, *Observations of sperm whale sounds from great depths*, Marine Physical Laboratory, Scripps Institute of Oceanography 1-9.
- [174] Wiggins S.M., McDonald M.A., Munger L.M., Moore S.E. and Hildebrand J.A., 2004 *Waveguide propagation allows range estimates for North Pacific right whales in the Bering Sea*, Proceedings of the workshop on Detection and Localisation of Marine Mammals using Passive Acoustics, Journal of the Canadian Acoustical Association, 32 (2): 146-154.
- [175] Wilson D.K. and Thomson D.W., 1994, *Acoustic tomographic monitoring the atmospheric surface layer*, Journal Atm. Oceanic Technology 11, 751-76.
- [176] Winn H.E. and Winn L.K., 1978, *The song of the humpback whale Megaptera novaeangliae in the West Indies*, Mar. Biol., 47, 97-114.
- [177] Woodhouse J.H., and Dziewonski A.M., 1984, *Mapping the upper mantle Three-dimensional modelling of Earth structure by inversion of seismic waveforms*, Journal Geophys Res. 89, 5953-5986.
- [178] Xiao L. and Collins T., 2005, *In-air passive acoustic source localization in reverberant environments*, IPROMS conference, 503-508.
- [179] Zimmer W.M.X., Jonson M.P., and Tyack P.L., 2004, *3-D reconstruction of sperm whale traces during foraging dives using visual, acoustic and tag data*,

Proceedings of the workshop on Detection and Localisation of Marine Mammals using Passive Acoustics, Journal of the Canadian Acoustical Association, 32 (2).

[180] <http://www.cmst.curtin.edu.au/products/actoolbox/> (28/01/2009)

[181] <http://www.pamguard.org> (28/01/2009)